AN INVESTIGATION ON FORCE MODIFICATION FACTORS IN COLD-FORMED STEEL STRUCTURES

by

Macit Yurtsever

M.Sc., Structural Engineering, Istanbul Technical University, 2005

Submitted to the Institute for Graduate Studies in
Science and Engineering in partial fulfillment of
the requirements for the degree of
Doctor of Philosophy

Graduate Program in Civil Engineering

Boğaziçi University

2020

To my daughters Bilge and İpek

ACKNOWLEDGEMENTS

I would like to express my sincere thanks first and foremost to my advisor and thesis supervisor, Prof. Dr. Serdar Soyöz. His devotion, perseverance and guidance throughout this whole thesis has been truly phenomenal. He has always been very encouraging and incredibly helpful even in very difficult circumstances. My gratitude is simply hard to put into words, he has been the main and the biggest reason I have come to complete this study.

I would also like to present my gratefulness to Assoc. Prof. Serdar Selamet and Assoc. Prof. Barlas Özden Çağlayan for their valuable input and supervision. Their advice has almost been life-saving at times.

It goes without saying that I owe a heartfelt appreciation to Akşan Yapı, and especially Taner Mermut for their contribution during this journey. Without the moral support, help and enthusiasm I received from him and Hasan Yel, this study could have been a difficult task.

In addition, I would like to offer my sincerest thanks to Oğuz Şenkardeşler, who accompanied me during all of the experiments, and helped me improve my technical knowledge on testing equipment. I also wish to thank Burak Karabulut, Emre Aytülün and Semih Gönen for their help and support throughout this study.

It would be disgraceful of me for not mentioning the great efforts of the laboratory personnel, Hasan Şenel and Hamdi Ayar. Their hard work and dedication has been absolutely monumental.

Last but not least, I would like to show the best of my gratitude to my wife, Eda Çelik Yurtsever, for her immense support, motivation and patience. Time and time again she pulled me through difficult times, and I cannot thank her enough for being there for me. I also wish to include my whole family members to this humble thank list, for their unconditional support and joy of living.

Besides my two little daughters, to whom I hope to be an inspiration someday, I also wish to dedicate this thesis to the deceased Ahmet Boyacı. He has been highly influential to me in becoming a civil engineer, and I cannot repay him for his help and devotion during the early years of my education.

ABSTRACT

AN INVESTIGATION ON FORCE MODIFICATION FACTORS IN COLD-FORMED STEEL STRUCTURES

Cold-formed steel (CFS) structures are a new feature in the recently effectuated 2018 Turkish Seismic Code (TSC). Their seismic design philosophy and other regulations are described within the Code. In the scope of this thesis, the Force Modification Factors defined in the Code for CFS structures are examined. Experimental and analytical studies are carried out on a real-life CFS building to investigate if the defined coefficients are practically applicable. The building chosen for this study is a two-story twin-villa type of building in Enez (Edirne) region. An Ambient Vibration Test is implemented to obtain the characteristic modal periods of the building. Then the building is thoroughly modelled in computing environment as close to reality as possible. In order to analyze the nonlinear behavior of the structure, performance analysis is conducted and the results are evaluated. Two additional laboratory experiments are carried out to determine the important structural parameters used in the analysis. The samples used in the experiments are 2.40 m x 2.40 m shear walls with X-braces on both sides, and are sheathed (on both sides) with OSB panels in one and with gypsum panels in the other. In the experiments, the behavior of a standard wall panel with double X-braces and double sheathing is investigated generally. Also a mathematical relationship is determined for the connections between the bracing and the frame members. The results obtained from the performance analysis of the analytical model and the force modification factors given in the 2018 TSC are then compared. The objective of the studies conducted within the scope of this thesis is to come up with a concluding remark on whether the given factors are reliable enough in practice. Obviously, experimental and analytical studies carried out on only one building are not sufficient to compare the order of the factors. Here, the sole intent is to get a reasonable idea about the rank of these coefficients and to provide an insight for future works that aim to study the same subjects in more detail.

ÖZET

HAFİF ÇELİK YAPILARIN DEPREM YÜKÜ KATSAYILARI ÜZERİNE BİR İNCELEME

Bu tez kapsamında, 2018 Deprem Yönetmeliği ile birlikte ulusal tasarım şartnamelerimizde kendine yer bulan hafif çelik binalar ve Yönetmelikte bunlar için tanımlanmış olan Taşıyıcı Sistem Davranış Katsayıları ve Dayanım Fazlalığı Katsayıları incelenmiştir. Tanımlanan katsayıların pratikte uygulanabilir olup olmadığının irdelenmesi adına, gerçek bir hafif çelik bina üzerinde deneysel ve analitik çalışmalar yapılmıştır. Bu çalışma için seçilen bina Enez (Edirne) yöresinde çokça yapılı bulunan ikiz villa tipi iki katlı bir binadır. Ortamsal Titreşim Deneyi (Ambient Vibration Test) yapılarak binanın karakteristik modal periyotları bulunmuş ve gerçeğine en yakın sonuçları verecek şekilde bilgisayar ortamında modellenmiştir. Ardından lineer olmayan yapı davranışını incelemek üzere, performans analizi yürütülmüş ve elde edilen sonuçlar değerlendirilmiştir. Analizde kullanılacak önemli yapısal parametrelerin belirlenmesi için ayrıca laboratuvar ortamında iki ayrı deney daha yapılmıştır. Deneylerde kullanılan numuneler, her iki yüzünde X-çaprazları olan ve birinde OSB, diğerinde alçıpan ile her iki tarafından kaplanan 2.40 m x 2.40 m ölçülerinde duvar panelleridir. Deneylerde hem genel olarak çift X-çaprazlı ve çift kaplamalı standart bir duvar panelinin tekrarlı yükler altındaki davranışı incelenmiş, hem de çapraz elemanlar ile çerçeve elemanları arasındaki bağlantılar için matematiksel bir ilişki belirlenmiştir. Bina modelinin performans analizinden elde edilen sonuçlar 2018 Deprem Yönetmeliğinde verilen deprem yükü katsayıları ile karşılaştırılmıştır. Tez kapsamında yapılan çalışmaların amacı, tanımlanan katsayıların pratikte yeterince güvenilir olup olmadığına ilişkin bir yorum yapabilmektir. Elbette sadece bir adet bina üzerinde yapılan deneysel ve analitik çalışmalar, verilen katsayıların mertebesini kıyaslamak açısından tek başına yeterli değildir. Burada yalnızca bu katsayıların mertebesi hakkında makul bir fikir edinme ve tez kapsamında hedeflenen konuların daha detaylı olarak incelenmesi için ileriki çalışmalara ışık tutma niyeti güdülmektedir.

TABLE OF CONTENTS

ACKNOWLEDGEMENTS iv
ABSTRACT vi
ÖZET vii
TABLE OF CONTENTS viii
LIST OF FIGURES x
LIST OF TABLES xxiv
LIST OF SYMBOLS xxv
LIST OF ACRONYMS/ABBREVATIONS xxviii
1. INTRODUCTION 1
1.1. General 1
1.2. Brief Theory and Motivation 2
1.3. Literature Review 4
1.3.1. Existing Codes, Standards and Software 5
1.3.2. Review on the Research 6
1.4. Scope and Objective of the Thesis 31
1.5. Thesis Overview 32
2. AMBIENT VIBRATION TEST AND ANALYTICAL CALIBRATION OF A REAL-LIFE STRUCTURE 34
2.1. Introduction 34
2.2. General Information about the Building and Experiment 34
2.3. Evaluation of the Experimental Data 36
2.4. Analytical Verification and Calibration 37
2.5. Corrections and Improvements to the Analytical Model 40
3. CYCLIC TESTS AND NONLINEAR MODELLING OF PANELS 45
3.1. General Information about the Experiments 45
3.2. Test Results for the Specimen with Gypsum Boards 48
3.3. Analytic Verification for the Specimen with Gypsum Boards 52
3.3.1. Updated Definition for Brace-to-Frame Links 56
3.3.2. Updated Definition for Plastic Hinges 57
3.4. Test Results for the Specimen with OSB Boards 62

3.5. Analytic Verification for the Specimen with OSB Boards....66
4. PERFORMANCE ASSESSMENT OF THE FINALIZED FE MODEL....67
4.1. Introduction....67
4.2. Performance-Based Analyses: Introduction....67
4.3. Performance-Based Analyses: Results....70
4.4. Evaluation of the Force Modification Factors....74
5. ADDITIONAL ANALYSES WITH VARIABLE PROPERTIES....81
5.1. Introduction....81
5.2. Gravity Loading Variations....82
5.3. OSB Shear Panel Variations....84
5.4. Gypsum Shear Panel Variations....86
5.5. Connection Rigidity Variations....88
6. CONCLUSIONS AND FUTURE WORKS....91
6.1. List of Conclusions....91
6.2. List of Future Works....96
REFERENCES....98
APPENDIX A: TECHNICAL DOCUMENTATION (REPRESENTATIVE DRAWINGS) OF THE PROJECT BUILDING....102
APPENDIX B: AMBIENT VIBRATON TEST RESULTS OF THE PROJECT BUILDING....109
APPENDIX C: IMAGES & RESULTS FROM THE LAB EXPERIMENT #1....117
APPENDIX D: IMAGES & RESULTS FROM THE LAB EXPERIMENT #2....129
APPENDIX E: PLASTIC HINGE PROPAGATION WITHIN THE STRUCTURAL MODEL....140
APPENDIX F: CAPACITY SPECTRA WITH LARGER SCALES....149

LIST OF FIGURES

Figure 1.1. General cold-formed steel sections [1]. 1

Figure 1.2. The schematic view of the tested prototype and the testing instrumentation [14]. 8

Figure 1.3. Finite element idealizations [15]. 9

Figure 1.4. Modal shapes for the first three structural modes of the full-scale building, obtained through FE modelling [15]. 10

Figure 1.5. The comparison between the results of the Simplified Method and Easley's Method [17]. 12

Figure 1.6. FE modelling options for double-story walls [18]. 13

Figure 1.7. The general view of a representative wall specimen, and typical connection details including track reinforcement [20]. 15

Figure 1.8. The general view and the corner detail of the wall specimen with elastic light (WLE) bracing configuration [20]. 16

Figure 1.9. The general view and the corner detail of the wall specimen with dissipative light (WLD) bracing configuration [20]. 16

Figure 1.10. The general view and the corner detail of the wall specimen with dissipative heavy (WHD) bracing configuration [20]. 16

Figure 1.11. (a) Net section failure for WLE specimen, (b) brace yielding mechanism for WLD specimen, (c) and (d) brace yielding mechanism for WHD specimen [20]. 17

Figure 1.12. (a) Net cross-section fracture for WLE specimen, (b) net cross-section fracture for WLD specimen, and (c) strap yielding mechanism for WHD specimen [20]. 17

Figure 1.13. Test results for single connections: (a) force-deformation curves, and (b) failure modes for SLE, SLD and SHD specimens [20]. 18

Figure 1.14. (a) Specimen configurations, (b) and (c) test results, and (d) failure modes for CLE, CLD and CHD frame-to-strap connection specimens [20]. 18

Figure 1.15. The reference model used for element idealization [21]. 19

Figure 1.16. The development of chord stud model in OpenSees [21]. 20

Figure 1.17. Extensive results and comparisons obtained from the analytical studies [21]. 21

Figure 1.18. Screw models used in the analytical studies [22]. 22

Figure 1.19. The pushover curve of the one-story representative model with performance point assessment [22]. 23

Figure 1.20. Visuals of the specimens and the actuator [23]. 24

Figure 1.21. The effect of varying stud and/or steel sheathing thickness (a) on lateral load capacity, and (b) on ductility [24]. 26

Figure 1.22. The effect of fastener spacing (a) on lateral stiffness, and (b) on ductility [24]. 27

Figure 1.23. Typical testing rigs and subsequent test results for various CFS SFRS [25]. 27

Figure 1.24. (A) Construction phases of the test building, for which shake table tests are conducted, and (B) relevant analysis models with varying levels of detail [26]. 29

Figure 1.25. Development of the force-displacement relationship from surrogate fastener-based models [26]. 29

Figure 1.26. Natural periods of the test building at various construction phases, obtained by shake table tests [26]. 30

Figure 1.27. Pushover analysis results of the test building, performed for various construction phases [26]. 31

Figure 2.1. The location of the tested building. 34

Figure 2.2. Some images of the typical mirror-villa used for AVT. 35

Figure 2.3. Sensor layout on the upper floor slab. 35

Figure 2.4. Sensor placement on the upper floor slab. 36

Figure 2.5. Sensor layout and placement on the upper floor ceiling. 36

Figure 2.6. Windowed and filtered results of the Fast Fourier Transformation. 37

Figure 2.7. Some images from the analytical model of the building. 38

Figure 2.8. A sample force-deformation curve of the link elements used for the connections in between frame elements (studs, girders and braces) [22]. ...39

Figure 2.9. A sample force-deformation curve of the link elements used for the connections between frames and shell elements (OSB panels) [22]. 39

Figure 2.10. Graphical representation of the loads applied on the structure. 39

Figure 2.11. Sample force-displacement curves for some of the updated frame-to-frame and frame-to-panel connections (link elements). 41

Figure 2.12. Force-deformation definition for the link elements to be used at locations where the second floor studs meet the first floor studs. 41

Figure 2.13. Allowable tensile and compressive stress limits defined for timber types [27]. 43

Figure 2.14. The principal stress levels in the OSB panel elements after pushover analyses in (a) X-direction, (b) in Y-direction. 43

Figure 3.1. CFS frame with braces on both sides, during the assembly of the specimens. 45

Figure 3.2. The test specimens with (a) gypsum boards, and (b) OSB boards. 46

Figure 3.3. (a) Specimen dimensions, and (b) stud/girder sections. 46

Figure 3.4. Sensor and strain gauge orientations. 47

Figure 3.5. Test Method C: CUREE Basic Loading Protocol (applied actuator displacements). 47

Figure 3.6. The local damage in (a) the upper portion, and (b) the lower portion of the panels. 48

Figure 3.7. The local damage in (a) general, and (b) specific parts on the CFS frame. .49

Figure 3.8. Hysteretic force-displacement curve of the test specimen. 50

Figure 3.9. Time-history of the sensors and strain gauges (a) on the actuator side of the specimen, and (b) on the opposite (outer) side of the specimen. 51

Figure 3.10. Time-history of the strain gauge attached to the upper brace. 52

Figure 3.11. The graphical representation of the analytical model for the test specimen.53

Figure 3.12. A detailed representation of the analysis model with (a) link elements, and (b) plastic hinge assignments. 53

Figure 3.13. Sensitivity analysis for the numerical model of the test specimen.....55

Figure 3.14. The proposed force-deformation curves for the brace connections. 56

Figure 3.15. Cross-section definition in GBTUL software.....58

Figure 3.16. Selection of the available buckling mode types in GBTUL software. 58

Figure 3.17. The definition of the other analysis parameters: solution type, support conditions, loading, member length etc.....59

Figure 3.18. Analysis results page of GBTUL software.....60

Figure 3.19. A sample stress-strain relationship defined for stud members. 61

Figure 3.20. Resultant pushover curve compared with the experimental data. 61

Figure 3.21. Superimposed hysteresis curves for both experiments.....62

Figure 3.22. The local damage in OSB panels. 63

Figure 3.23. General view of the local damage in CFS frame elements. 63

Figure 3.24. The local damage in the upper girder and the nearby braces. 64

Figure 3.25. The local damage in the middle portion of the upper girder. 64

Figure 3.26. A broken piece of steel, most probably from the heavily damaged mid-point of the upper girder. 65

Figure 3.27. Time-history of the sensors and strain gauges (a) on the actuator side of the specimen, and (b) on the opposite (outer) side of the specimen. 66

Figure 3.28. Resultant pushover curve tryouts for the modified model of the specimen, compared with the experimental data. 66

Figure 4.1. Sample hinge definition for studs. 68

Figure 4.2. The resultant pushover curve in X-direction. 70

Figure 4.3. The resultant pushover curve in Y-direction. 70

Figure 4.4. Deformed shape after pushover analysis in X-direction. 71

Figure 4.5. Deformed shape after pushover analysis in Y-direction. 71

Figure 4.6. Representative hinge progression at analysis steps 23 and 27, respectively. 72

Figure 4.7. Significant event progression and the proposed structural damage levels. ..72

Figure 4.8. Performance assessment in X-direction. 1

Figure 4.9. Performance assessment in Y-direction. 77

Figure 5.1. Pushover curves of analysis models with varying gravity loads. 82

Figure 5.2. Bilinear EEEP Curve evaluation for varying gravity loads.....82

Figure 5.3. Pushover curves of analysis models with varying OSB panel thickness. 85

Figure 5.4. Bilinear EEEP Curve evaluation for varying OSB panel thickness. 85

Figure 5.5. Pushover curves of analysis models with varying gypsum panel thickness.87

Figure 5.6. Bilinear EEEP Curve evaluation for varying gypsum panel thickness. 87

Figure 5.7. Pushover curves of analysis models with varying connection stiffness.....89

Figure 5.8. Bilinear EEEP Curve evaluation for varying connection stiffness. 89

Figure 6.1. The variation of ductility with respect to varying seismic weight ratios. 92

Figure 6.2. The variation of ductility with respect to gypsum or OSB thickness.....93

Figure 6.3. The variation of the ductility ratio with respect to connection stiffness. 94

Figure A.1. First floor plan (wall numbering) of Enez villa (provided by the manufacturer company for educational purposes). 102

Figure A.2. T001 and T009 wall configurations for representative purposes (provided by the manufacturer company for educational purposes).....103

Figure A.3. T003 and T006 wall configurations for representative purposes (provided by the manufacturer company for educational purposes).....103

Figure A.4. Second floor plan (wall numbering) of Enez villa (provided by the manufacturer company for educational purposes). 104

Figure A.5. T101 and T111 wall configurations for representative purposes (provided by the manufacturer company for educational purposes).....105

Figure A.6. T104 and T117 wall configurations for representative purposes (provided by the manufacturer company for educational purposes).....105

Figure A.7. First floor girder plan of Enez villa (provided by the manufacturer company for educational purposes). 106

Figure A.8. Roof level truss plan of Enez villa (provided by the manufacturer company for educational purposes). 107

Figure A.9. CM-02, CM-04 and CM-05 truss configurations for representative purposes (provided by the manufacturer company for educational purposes). 108

Figure B.1. Live on-site monitoring of the ambient vibration test at Enez villa. 109

Figure B.2. Full AVT records and consequent FFT decompositions of Channel-1 readings. 109

Figure B.3. Full AVT records and consequent FFT decompositions of Channel-2 readings. 110

Figure B.4. Full AVT records and consequent FFT decompositions of Channel-3 readings. 110

Figure B.5. Full AVT records and consequent FFT decompositions of Channel-4 readings. 111

Figure B.6. Full AVT records and consequent FFT decompositions of Channel-5 readings. 111

Figure B.7. Full AVT records and consequent FFT decompositions of Channel-6 readings. 112

Figure B.8. Full AVT records and consequent FFT decompositions of Channel-7 readings. 112

Figure B.9. Full AVT records and consequent FFT decompositions of Channel-8 readings. 113

Figure B.10. Full AVT records and consequent FFT decompositions of Channel-9 readings. 113

Figure B.11. Full AVT records and consequent FFT decompositions of Channel-10 readings. 114

Figure B.12. The resultant FFT decompositions of all the channels in X-direction. 115

Figure B.13. The resultant FFT decompositions of all the channels in Y-direction. 116

Figure C.1. General view of the test pad in the Structures Laboratory of Boğaziçi University. 117

Figure C.2. General view of the assembled CFS frame with bracings. 117

Figure C.3. General view of the completed test specimen being attached to the testing rig. 118

Figure C.4. Local damage observed on each side of the upper corners of the gypsum panels after the test. 118

Figure C.5. Local damage observed on the lower corners of the gypsum panels after the test. 119

Figure C.6. General view of the damage observed in the frame elements after the test. 120

Figure C.7. Local damage observed in upper corner brace connections. 120

Figure C.8. Local damage observed in the lower corner brace connections. 121

Figure C.9. Local damage observed on the intermediate studs. 121

Figure C.10. Local damage observed on the exterior girders. 122

Figure C.11. General view of the resultant hysteresis curve obtained after the test. 122

Figure C.12. Time-history sketches of the sensors and gauges on the actuator-side of the test specimen. 123

Figure C.13. Time-history sketches of the sensors and gauges on the free-side of the test specimen. 124

Figure C.14. Uplift of the studs vs. actuator displacement. 125

Figure C.15. Uplift of the studs vs. actuator force. 125

Figure C.16. Strains in the stud on the free-side of the test specimen vs. actuator displacement. 126

Figure C.17. Strains in the stud on the actuator-side of the test specimen vs. actuator displacement. 126

Figure C.18. Strains in the brace on the free-side of the specimen (lower corner) vs. actuator displacement. 127

Figure C.19. Strains in the brace on the actuator-side of the specimen (lower corner) vs. actuator displacement. 127

Figure C.20. Strains in the brace on the free-side of the specimen (upper corner) vs. actuator displacement. 128

Figure D.1. General view of the test specimen (with OSB panels mounted). 129

Figure D.2. Local damage observed on each side of the upper corners of the OSB panels after the test. 130

Figure D.3. Local damage observed on each side of the upper corners of the OSB panels (continued). 131

Figure D.4. General view of the damage observed in the frame elements after the test. 131

Figure D.5. Local damage observed in the upper corner elements.....132

Figure D.6. Local tearing observed in the upper girder, along with the broken piece. .133

Figure D.7. Local damage observed in the lower corner elements.....133

Figure D.8. Time-history sketches of the sensors and gauges on the actuator-side of the test specimen. 134

Figure D.9. Time-history sketches of the sensors and gauges on the free-side of the test specimen. 135

Figure D.10. Uplift of the studs vs. actuator displacement.....136

Figure D.11. Uplift of the studs vs. actuator force. 136

Figure D.12. Strains in the stud on the free-side of the test specimen vs. actuator displacement. 137

Figure D.13. Strains in the stud on the actuator-side of the test specimen vs. actuator displacement. 137

Figure D.14. Strains in the brace on the free-side of the specimen (lower corner) vs. actuator displacement. 138

Figure D.15. Strains in the brace on the actuator-side of the specimen (lower corner) vs. actuator displacement. 138

Figure D.16. Strains in the brace on the free-side of the specimen (upper corner) vs. actuator displacement. 139

Figure E.1. Plastic hinge progression at the 4th step of the pushover analysis in Y-direction. 140

Figure E.2. Plastic hinge progression at the 23rd step of the pushover analysis in Y-direction. 140

Figure E.3. Plastic hinge progression at the 27th step of the pushover analysis in Y-direction. 141

Figure E.4. Plastic hinge progression at the 43rd step of the pushover analysis in Y-direction. 141

Figure E.5. Plastic hinge progression at the 47th step of the pushover analysis in Y-direction. 142

Figure E.6. Plastic hinge progression at the 50th step of the pushover analysis in Y-direction. 142

Figure E.7. Plastic hinge progression at the 120th step of the pushover analysis in Y-direction.....143

Figure E.8. Plastic hinge progression at the 121st step of the pushover analysis in Y-direction.....143

Figure E.9. Plastic hinge progression at the 127th step of the pushover analysis in Y-direction.....144

Figure E.10. Plastic hinge progression at the 160th step of the pushover analysis in Y-direction.....144

Figure E.11. Plastic hinge progression at the 161st step of the pushover analysis in Y-direction.....145

Figure E.12. Plastic hinge progression at the 162nd step of the pushover analysis in Y-direction.....145

Figure E.13. Plastic hinge progression at the 163rd step of the pushover analysis in Y-direction.....146

Figure E.14. Plastic hinge progression at the 170th step of the pushover analysis in Y-direction.....146

Figure E.15. Plastic hinge progression at the 178th step of the pushover analysis in Y-direction.....147

Figure E.16. Plastic hinge progression at the 180th step of the pushover analysis in Y-direction.....147

Figure E.17. Plastic hinge progression at the 186th step of the pushover analysis in Y-direction.....148

Figure E.18. Plastic hinge progression at the 188th step of the pushover analysis in Y-direction. 148

Figure F.1. Pushover curves of the analysis models with varying gravity loads. 149

Figure F.2. Performance assessment for varying gravity loads. 150

Figure F.3. Pushover curves of analysis models with varying OSB panel thickness. ..151

Figure F.4. Performance assessment for varying OSB panel thickness. 152

Figure F.5. Pushover curves of analysis models with varying gypsum panel thickness. 153

Figure F.6. Performance assessment for varying gypsum panel thickness. 154

Figure F.7. Pushover curves of analysis models with varying screw thickness. 155

Figure F.8. Performance assessment for varying screw thickness. 156

LIST OF TABLES

Table 1.1. Force modification factors as described in AISI S213. 3

Table 1.2. Force modification factors as described in TSC 2018.....4

Table 1.3. Modal parameters of the full-scale building, (a) obtained by FE modelling, and (b) obtained by ambient vibration tests [15]. 10

Table 1.4. Structural behavior factors for WLE, WLD and WHD wall configurations [20]. 19

Table 1.5. The ultimate shear strength and the relevant strength reduction factor of each specimen [22]. 22

Table 2.1. Structural modal periods obtained for various modelling options. 40

Table 2.2. Structural modal periods after updated link properties. 42

Table 4.1. Modal periods after updating the link properties of the brace connections..67

LIST OF SYMBOLS

a_1	Modal spectral acceleration for the first natural mode of a SDFS
A	Area of the screws
A_{ref}	Area of a reference set of screws
C_d	Deflection amplification factor
d	Displacement (or deformation); screw diameter
d_1	Modal spectral displacement for the first natural mode of a SDFS
$d_1^{(p)}$	Modal spectral displacement for the first natural mode of a SDFS, obtained from (the ith step of) a pushover analysis
d_{ref}	Diameter of a reference set of screws
D	Overstrength factor, as defined in TSC 2018
D_{el}	Displacement at elastic limit
D_{max}	Seismic Design Category for maximum seismic loads, as defined in FEMA P695
D_{min}	Seismic Design Category for minimum seismic loads, as defined in FEMA P695
D_{ult}	Ultimate displacement
D_{yield}	Displacement at yield
F	Force
F_a	Acceleration-based (short-periods) site coefficient
F_{el}	Force value at elastic limit
F_{max}	Peak value of the force
F_u	Ultimate force or ultimate strength
F_v	Velocity-based (long-periods) site coefficient
F_y, F_{yield}	Yield force
g	Gravitational acceleration; gravity loads (superimposed dead loads)
h	Horizontal distance between the two end studs
H	Height of the structure; height of the shear wall

I , I_E	Earthquake importance factor of the structure
K_e	Lateral stiffness of a shear wall
L	Width of the shear wall
M	Mass of the story
n_s	The number of screws connecting the board to one of the end studs
n_t	The number of screws connecting the board to one of the tracks
P	Gravity load(s) or compressive force
P_{el}	Compressive force value at elastic limit
P_{nl}	The critical (buckling) load of a single stud
P_{peak}	The peak value of base shear (or force)
P_{ult}	Ultimate force level, defined for a simplified finite element model
P_{yield}	The base shear (or force) value at yield
q	Seismic force reduction factor; live loads
R	Response modification factor; structural behavior factor
R_a	Seismic force reduction factor
R_d	Ductility-related force modification factor, reflecting the capability of a structure to dissipate energy through inelastic behavior
R_o	Overstrength-related force modification factor, accounting for the dependable portion of reserve strength in a structure
S	Construction stage (number)
S_a	Spectral (response) acceleration
$S_{a(peak)}$	The peak value of spectral (response) acceleration
S_{ay}	Spectral (response) acceleration at yield
S_{D1}	Design spectral response acceleration parameter at 1-sec. period (5% damping)
S_{del}	Linear elastic spectral displacement
S_{DS}	Design spectral response acceleration parameter at short periods (5% damping)
t	Panel thickness
T	Period; the fundamental period of the building

T_B	Upper corner period of the elastic design acceleration spectrum
T_i	The natural vibration period related to the ith structural mode
V	Lateral force (load)
w	Vertical distance between the top and bottom tracks
W	Dead weight of the structure
W_E	Total seismic weight (computed in accordance with TSC 2018)
X_{max}	Maximum value (of a set of data)
X_{min}	Minimum value (of a set of data)
X_{ort}	Average value (of a set of data)

δ	Deformation
Δ_e	Elastic displacement
Δ_{peak}	The displacement value at peak response acceleration level
Δ_u	Ultimate displacement
Δ_y	Yield displacement
γ_m	Factor of safety
μ , μ_k	Ductility ratio
ν	Variation coefficient
Ω_0	Overstrength factor
ξ_i	Damping ratio of the ith structural mode

LIST OF ACRONYMS/ABBREVATIONS

ADRS	Acceleration Displacement Response Spectrum
AISI	American Iron and Steel Institute
AVT	Ambient Vibration Test
ASTM	American Society for Testing and Materials
BS EN	British Standard European Norm
BYS	Bina Yükseklik Sınıfı
CFS	Cold-Formed Steel
cFSM	Constrained Finite Strip Method
CFSSWP	Cold-Formed Steel Shear Wall Panels
CHD	Dissipative Heavy Connection
CLD	Dissipative Light Connection
CLE	Elastic Light Connection
CP	Collapse Prevention
CPB	Cement Particle Board
CUFSM	Constrained and Unconstrained Finite Strip Method
CUREE	Consortium of Universities for Research in Earthquake Engineering
CUTWP	Cornell University Thin-Walled (Section) Properties
DPO	Dynamic Pushover
EEEP	Equal Energy Elastic-Plastic
FE	Finite Element
FEMA	Federal Emergency Management Agency
FFT	Fast Fourier Transform
GBT	Generalized Beam Theory
GBTUL	Generalized Beam Theory at the University of Lisbon
GWB	Gypsum Wallboard
IDA	Incremental Dynamic Analysis
IO	Immediate Occupancy
LS	Life Safety
LSD	Limit States Design
NBCC	National Building Code of Canada

NEHRP	National Earthquake Hazards Reduction Program
NP	Not Permitted
OSB	Oriented Strand Board
OT	Over-tightened (bolt)
PSD	Power Spectral Density
RELUIS-DPC	Rete dei Laboratori Universitari di Ingegneria Sismica - Dipartimento della Protezione Civile
S4R	Four-Node Shell Finite Element
SAP	Structural Analysis Program
SBMF	Special Bolted Moment Frame
SFIA	Steel Framing Industry Association
SFRS	Seismic Force Resisting System
SHD	Dissipative Heavy Single (connection element)
SLD	Dissipative Light Single (connection element)
SLE	Elastic Light Single (connection element)
ST	Standard-tightened (bolt)
TSC	Turkish Seismic Code
UT	Under-tightened (bolt)
WHD	Dissipative Heavy Wall Bracing
WLD	Dissipative Light Wall Bracing
WLE	Elastic Light Wall Bracing
WSP	Wood Structural Panels

1. INTRODUCTION

1.1. General

Cold-formed steel structures are relatively new in construction industry. Use of cold-formed steel members for construction of buildings can only be traced back as early as the 1850s in the US and UK. During the 1920s and 30s, acknowledgment of cold-formed steel as a construction material was as yet constrained, since there was not an adequate design standard, and no data on the utilization of the material in the building codes. In 1946, the first Specification for the *Design of Light Gage Steel Structural Members* was published, and in 1949, the first *Design Manual* was made available for use by design engineers. In 2007, the Limit States Design (LSD) method was incorporated into the cold-formed steel framing standards, which enabled those guidelines to be adopted in Canada and Mexico as North American standards.

Cold-formed steel is widely used in residential and light commercial building construction as well as other secondary structures such as poles and towers. Reports indicate that 40% of the steel structures built in the US are made of cold-formed steel. In Australia the same rate is 13%. Cold-formed steel frames have been successfully used in projects with a height of more than 10 stories. One recent project named SFIA Matsen Tower aims to rise 40 stories primarily on cold-formed steel. There are numerous cold-formed steel sections used in structural frames, floor and roof decks, and walls/panels (Figure 1.1).

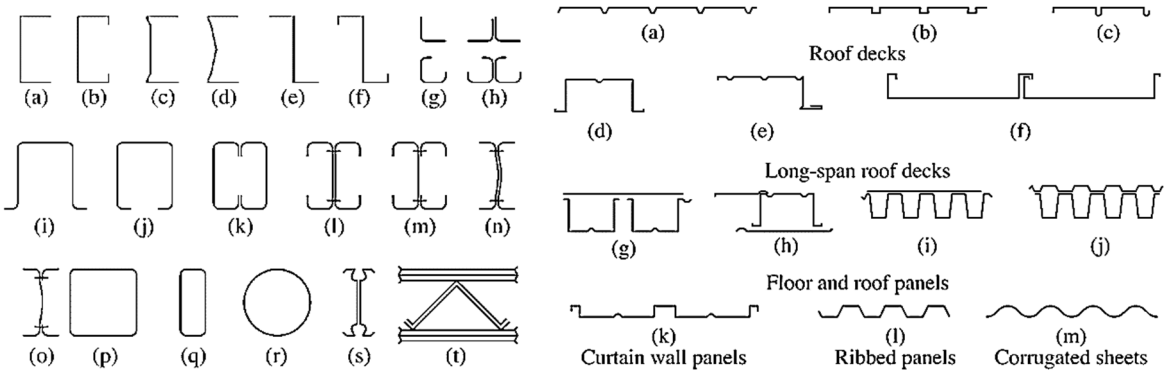

Figure 1.1. General cold-formed steel sections [1].

There are at least 14 different steel types in the cold-formed steel industry, with yield strengths ranging from 166 MPa to 552 MPa. The ratios of tensile strengt-to-yield point vary from 1.12 to 2.22. It is obvious that the material ductility is relatively poor with CFS elements. However, local buckling and post-buckling strength of members are often the major considerations in structural design. In addition, shear buckling and web crippling should also be considered in the design of beams.

Seismic performance is greatly influenced by fastener configuration and quality of connection between the CFS framing and panel material. Experimental data suggests that failure or collapse under lateral load is manifested in local buckling of steel members, rupture of sheathing edges and/or deformation of connections.

Although the seismic force acting on a cold-formed steel structure is relatively low owing to structural lightness, numerical evidence suggests that the computed drift ratios under the effect of ground motion records generally span between 5% and 10%.

1.2. Brief Theory and Motivation

Construction industry has only known cold-formed steel structures for a couple of decades now, but thanks to technological improvements and development of sophisticated testing facilities, there are already plenty of available data (codes, recommendations and other written sources) to be used in the design of such structures. Yet some of the aspects that have entered the building design codes still require more research to be finalized. Force modification factors (ductility-related and overstrength-related) are one of those aspects.

AISI S213, the North American Standard for Cold-Formed Steel Framing – Lateral Design, has been developed by the American Iron and Steel Institute Committee on Framing Standards to address the design of lateral force resisting systems to resist wind and seismic forces in a wide range of buildings constructed of cold-formed steel frames. This code, for example, defines the force modification factors (and building height limitations) according to the type of seismic force resisting system (Table 1.1).

Table 1.1. Force modification factors as described in AISI S213.

Type of Seismic Force Resisting System	R_d	R_o	Building Height (m) Limitations [1]				
			Cases Where $I_E F_a S_a(0.2)$				Cases Where $I_E F_v S_a(1.0)$
			< 0.2	≥0.2 to <0.35	≥0.35 to ≤0.75	>0.75	>0.3
Shear Walls [2]							
Screw connected shear walls: wood-based structural panel	2.5	1.7	20	20	20	20	20
Screw connected shear walls: wood based structural and gypsum panels in combination	1.5	1.7	20	20	20	20	20
Diagonal Strap Braced (Concentric) Walls [3]							
Limited ductility braced wall [4]	1.9	1.3	20	20	20	20	20
Conventional construction [5]	1.2	1.3	15	15	NP	NP	NP
Other Cold-Formed Steel SFRS(s) Not Listed Above	1.0	1.0	15	15	NP	NP	NP

1. NP = Not Permitted.
2. *Seismic Force Resisting System* specifically detailed for ductile seismic performance. *Capacity based design* approach is applied, assuming the sheathing connections act as the energy-dissipating element (See Section C5.1).
3. *Seismic Force Resisting System* specifically detailed so that all members of the bracing system are subjected primarily to axial forces. The eccentric effect due to single sided bracing is neglected for purposes of this classification, but shall be considered in accordance with C5.2.2.3.
4. *Seismic Force Resisting System* specifically detailed for ductile seismic performance. *Capacity based design* approach is applied, assuming the braces act as the energy-dissipating element (gross cross-section yielding). See Section C5.2.
5. Lateral system not specifically detailed for ductile seismic performance (*Capacity based design* approach not required. See Section C5.2).

The development of these force modification factors was based on shear wall test data using the Equivalent Energy Elastic-Plastic (EEEP) method, and the proposed *R*-values should only be used in the case of a sheathing connection failure in the shear wall, rather than chord stud failure (as stated in the code commentary).

The code also forces the designer to implement R_d and R_o values of 1.0 for systems that are not defined in the foregoing table, since their ductility and overstrength capacity have not yet been demonstrated. This alone, is a clear indication that there is still room for improvement regarding the rules defined in the design codes.

The table in the latest Turkish Seismic Code (Table 1.2) is much simpler, yet, appears to be not quite comparable to that of AISI S213, since the calculation of the seismic response modification coefficient (R or R_a, depending on the code) is given by the formula $R = R_d \times R_o$ in one code, and by Equation 1.1 in the other.

Table 1.2. Force modification factors as described in TSC 2018.

Bina Taşıyıcı Sistemi	Taşıyıcı Sistem Davranış Katsayısı R	Dayanım Fazlalığı Katsayısı D	İzin Verilen Bina Yükseklik Sınıfları BYS
D. HAFİF ÇELİK BİNA TAŞIYICI SİSTEMLERİ			
D1. Süneklik Düzeyi Yüksek Taşıyıcı Sistemler			
Deprem etkilerinin tamamının vidalı, bulonlu sac, OSB veya kontrplak (plywood) duvar panelleri ile karşılandığı süneklik düzeyi yüksek hafif çelik binalar	4	2	BYS = 8
D2. Süneklik Düzeyi Sınırlı Taşıyıcı Sistemler (Bkz.4.3.4.1)			
Deprem etkilerinin tamamının alçı levhalar içeren kaplamalı veya çaprazlı panellerle karşılandığı süneklik düzeyi sınırlı hafif çelik binalar	3	2	BYS = 8

$$R_a(T) = \frac{R}{I} \qquad T > T_B$$
$$R_a(T) = D + \left(\frac{R}{I} - D\right)\frac{T}{T_B} \qquad T \le T_B \tag{1.1}$$

It should be noted that, for the same value of the building's (first) natural modal period, the formulae in these two codes may not give the same result. Does this discrepancy between the resulting values necessarily need to be considered as a flaw for analysis and design? Which value is to be trusted? Since these structures consist of rather slender elements, slightest change in the seismic force accounted in the analysis may cause drastic differences in the structural design. These are just some of the possible questions that spring to mind when it comes to analyzing and designing a cold-formed steel structure.

More importantly, in an academic point of view, it may prove more critical to verify if the values of force modification factors defined in the codes are generally reliable in the first place. Introduction of new values and/or implementation of an adjustment coefficient may be required if it becomes evident that the factors are inadequate.

1.3. Literature Review

It is helpful and important to review similar literature in order to enlighten the studies in the scope of this thesis. Plenty of valuable and contentful reference is available covering both experimental and analytical research previously done by academics and other

professionals. There is an increasing number of written source in the field of cold-formed steel structures, and the contribution of each one is highly regarded. Thus, in this chapter, some of the papers that are closely related to the scope of this thesis are briefly outlined.

1.3.1. Existing Codes, Standards and Software

American Iron and Steel Institute (AISI) [2] appears to have become the main guidance for the design of cold-formed steel structures, inducing an increased interest on the subject in the last century. Their well-known specification AISI S213-07/S1-09(2012) refers to "North American Standard for Cold-Formed Steel Framing: Lateral Design" and is widely accepted as a reliable source. This code has been used as a reference during the experiments, evaluating the results and other calculations.

Another useful specification is "Standard Test Methods for Cyclic (Reversed) Load Test for Shear Resistance of Vertical Elements of the Lateral Force Resisting Systems for Buildings" (ASTM E2126-11) [3]. A general overview for the tests to be conducted on cold-formed steel elements is proposed in this code, which includes information about specimens, test setup, test procedure and loading protocol as well as calculations. Experimental studies in the content of this thesis have been carried out by utilizing the specifications in this code.

FEMA 440 [4] is another useful code which is prepared by the Applied Technology Council (ATC-55 Project) and specializes on the improvement of nonlinear static seismic analysis procedures. In this thesis, it has been used as a supplementary material on performance based design and as a special reference on the capacity spectrum design method provided for pushover analyses in the software SAP2000.

The final Turkish Seismic Code (TSC) 2018 [5] includes rules and other specifications for the seismic design of cold-formed structures, provided in Chapter 10 of the code. In addition, Addendums 4A and 4B provide informative data on force modification factors and modal analysis methods. Addendum 5B provides info on performance based design. The rules and other data given in the said addendums have been utilized in the scope of the analytical study of this thesis. Other than that, elastic design

spectrum proposed in the code has also been used for design purposes and performance evaluation.

CUFSM (Constrained-Unconstrained Finite Strip Method) [6], CUTWP (Cornell University Thin-Walled Section Properties) [7] and GBTUL (Generalized Beam Theory by University of Lisbon) [8] are all specialized software created by various academics which have been used to calculate the buckling modes of various CFS sections in the scope of this thesis.

MATLAB [9] is a programming platform designed specifically for engineers and scientists, which utilizes a matrix-based language that allows the most natural expression of computational mathematics. In this study, it has been used for compiling of a code with which FFT (Fast Fourier Transform) computations of ambient vibration test data are made.

SAP2000 [10] software is a structural analysis program developed by Computers and Structures, Inc. (CSI). It has been used during all analytical studies regarding the structure examined in the scope of this thesis.

1.3.2. Review on the Research

Serrette and Ogunfunmi [11] presented the detailed results on the shear behavior of light-gauge stud steel walls with dimensions of 2.44 m by 2.44 m for three different shear resisting systems. The overall test setup, based on the recommendation contained in ASTM E 72-80, features only monotonic loading procedure, in which the specimens were loaded to failure in four stages. The failure occurred as a result of excessive lateral deflection of the wall, following the yield of the tension-side X-bracing. Minor reversed bending was also observed in the end studs. The paper concludes that, while limited, this test program provided valuable information on the design of light-weight steel framed shear walls. Based on the test results, it was recommended that the percentage of shear carried by gypsum walls be limited.

Tian *et al.* [12] provided an experimental study on cold-formed steel shear panels with various configurations. The paper mainly contains experimental observations for a set

of CFS shear panels, tested on a racking device. Two loading methods based on the code BS EN 594:1996 are utilized during the experiments. The first is a 1-step loading, with which the load is applied continuously until frame failure occurs. The second is a 3-step loading, in which the test is composed of three loading stages: the stabilizing step, the stiffness step and the strength step.

The remaining part of the paper consists of theoretical analysis of the test specimens, aimed at calculating their racking stiffness. Based on these calculations, there are also comparisons between the predicted (theoretical) racking failure loads and measured failure loads, for which the results are pretty much in agreement. Some of the conclusions taken from the study are:

- A frame without bracing has 5% less racking strength compared to braced frames.
- A frame braced with thin flat steel straps (except 1-side X bracing) has nearly the same racking strength compared to a frame braced with CPB or OSB boards.
- Failure occurs on the board near screw connections for frames braced with boards. Racking strength can be increased by increasing the board thickness or decreasing the screw spacing.
- Predicting the racking performance of strap-braced frames was done by utilizing the slope-deflection method. The predicted racking failure loads for specimen types B-1 and C-1 are close to measured values. Yet, it is observed that a simple first-order elastic analysis in which yielding and post-buckling are ignored cannot predict the frame stiffness or displacement correctly.
- Using larger ratio of bracing unit width to frame length is preferable for bracing. The specimen type B-1 with single X strap bracing showed better racking performance than the specimen type C-1 with 2X strap bracing.
- Racking strength of a braced frame is almost independent of strap width. However, increasing the strap width greatly decreases the lateral deflection of the frame.
- The racking performance of a frame is based on many factors: the section design of individual members, bracing method, connection method, and strap size. All of them should be thoroughly investigated when optimizing the racking performance of the frame.

Della Corte *et al.* [13] provided and discussed the results of a numerical study on seismic deformation demand in cold-formed steel structures with sheathed shear walls. It is part of a broader study, involving the calibration of the numerical model against data from physical tests. Numerical results were elaborated so that the seismic performance of the structure under increasing seismic forces can be evaluated and an ad-hoc cyclic loading protocol for physical tests can be developed.

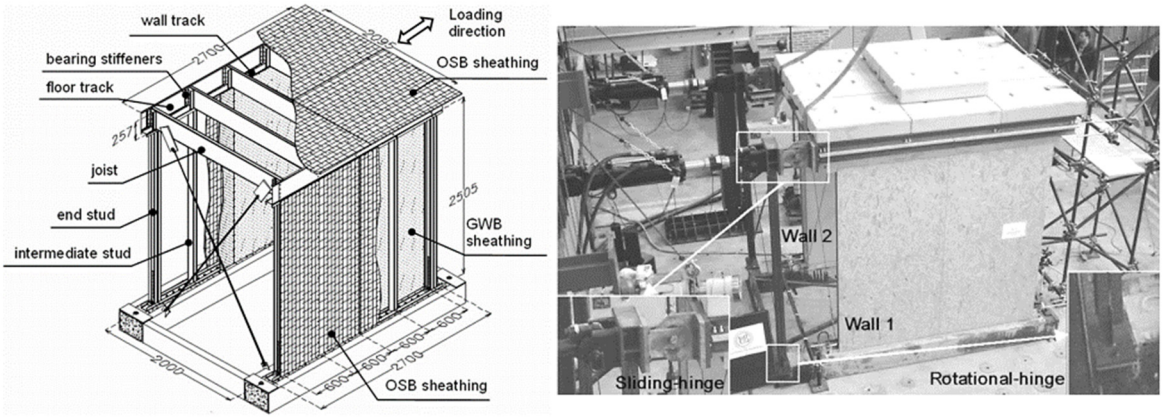

Figure 1.2. The schematic view of the tested prototype and the testing instrumentation [14].

Landolfo *et al.* [14] conducted an extensive experimental study on the seismic behavior of cold-formed steel stud shear walls. Two identical prototypes were tested: one of them was tested under monotonic loading conditions, and the other was tested under cyclic loading conditions, with a loading history extracted from a computational analysis of the deformation histories which are likely to be inflicted by typical earthquakes in Italy. The following conclusion can be drawn from the experimental results:

- All of the components of this structural system can be designed according to capacity design criteria without increasing the cost significantly, by imposing a collapse mechanism in the sheathing connections of the vertical shear wall.
- Increasing the lateral displacement during the monotonic test did not change the collapse mechanism, while the cyclic test showed minor discrepancies after the peak lateral load was achieved. After reaching the peak load, the subsequent strength degradation was observed to be higher in the cyclic test than that observed in the monotonic test.

- The lateral-load response for displacements less than those corresponding to the peak lateral load was very similar for all specimens, although major differences were observed for larger displacement values.
- No significant deformation in the OSB panel-to-frame connections was observed in neither tests.

Dubina [15] provided an extensive paper that summarizes the results and findings of monotonic and cyclic tests performed on full-scale shear panels, tests on various connection details, and in-situ ambient vibration tests on a house under construction. Analytical studies and result comparisons for test specimens were also included. In order to model the complex hysteretic behavior of the panel, and to enable further use in analytical design, simplified 2D and 3D models were created and the following idealizations were made for finite element modelling: a trilinear hysteretic model (which takes pinching effect into account) was utilized and calibrated using the experimental results, and the wall shear panel was replaced with an equivalent bar model (Figure 1.3).

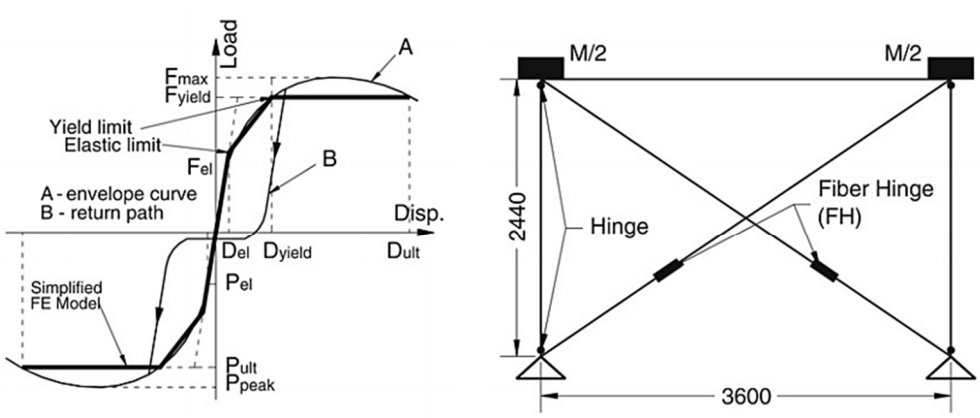

(a) Trilinear hysteretic model. (b) Modeling with equivalent bracing.

Figure 1.3. Finite element idealizations [15].

Five earthquake records were selected for the purpose of earthquake analysis, and normalized elastic spectra with a damping ratio of 5% was contrasted with Eurocode 8 elastic spectra for typical soil conditions. Incremental dynamic analysis (also known as dynamic pushover) is utilized, which is a common analysis procedure that is sensitive to both the structure and the accelerogram. Additional tests were carried out to determine the mechanical properties of the connections and to identify their effect on the behavior of the

panels. The paper also contains analytical studies for calibration of shear wall panels with and without openings.

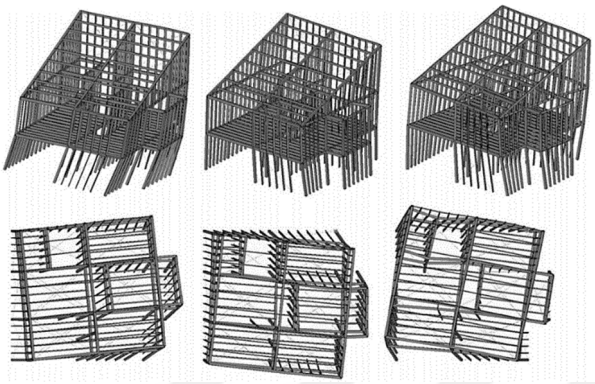

Figure 1.4. Modal shapes for the first three structural modes of the full-scale building, obtained through FE modelling [15].

Finally, the calibrated structural properties are utilized through a numerical simulation of a full-scale building for which an ambient vibration test is also performed, and the obtained results are compared. Images in Figure 1.4 illustrate the modal shapes of the first three natural modes, whereas Table 1.3 summarizes the modal parameters obtained from finite element modelling and from the ambient vibration tests, respectively.

Table 1.3. Modal parameters of the full-scale building, (a) obtained by FE modelling, and (b) obtained by ambient vibration tests [15].

Stage	T_1 (s)	Type[a]	T_2 (s)	Type[a]	T_3 (s)	Type[a]
1	0.44	Tr	0.39	To	0.35	Lo
2	0.19	Lo	0.18	Tr	0.13	To
3[b]	0.33	Lo	0.31	Tr	0.23	To

[a] Note[1]: Tr — transversal, Lo — longitudinal, To — Torsional.
[b] Note[2]: Only the masses changed from Stage 2 to Stage 3.

(a)

S	Mode 1			Mode 2			Mode 3		
	T_1 (s)	ξ_1 (%)	Type	T_2 (s)	ξ_2 (%)	Type	T_3 (s)	ξ_3 (%)	Type
1	.546	1.2	Lo	.437	1.1	Tr	.456	1.3	To
2	.103	3.4	Tr	.096	3.7	Lo	–	–	–
3	.101	4.1	Tr	.096	3.8	Lo	.072	4.1	To

Note: Vibration shapes: Tr — transversal, Lo — longitudinal, To — Torsional

(b)

Velchev *et al.* [16] evaluated typical strap braced wall configurations with respect to their strength and inelastic behavior. For such an evaluation, 44 strap braced stud wall specimens were put to test. The testing protocols include both monotonic loading and reversed cyclic loading. The monotonic loading procedure involved a relatively low and steady rate of displacement. The reversed cyclic test frequency was 0.5 Hz, except that 0.25 Hz was used towards the end of the protocol. There is very detailed information about the results of all tests, categorized with respect to the type of loading and the type of connections. Post-test calculations include various parameters such as elastic stiffness and ductility of the specimens, absorbed energy, and the estimated force modification factors (both ductility-related and overstrength-related). The conclusions of this study can be summarized as:

- The findings of this study showed the potential of walls with an aspect ratio of less than or equal to 2:1 to obtain and sustain their yield resistance in the inelastic deformation range, provided that capacity design principles were applied and the material requirements were fulfilled.
- Therefore, it is advised that using strap-braced walls with higher aspect ratios (usually greater than 2:1) is avoided unless the capacity design of the chord studs also incorporates the moments associated with flexure of these studs.
- Inelastic deformations generally originated from brace yielding in the walls with the aspect ratio of 1:1 (2440 mm) and 2:1 (1220 mm), while the 4:1 (610 mm) walls experienced combined flexure and axial compression of the chord studs with only limited brace yielding.
- The seismic force modification factors R_d = 2.0 and R_o = 1.3 provided in AISI S213 are suitable for walls of 1220 and 2440 mm length, but not for the 610 mm long walls, which were not observed to have adequate ductility or overstrength.

Nithyadharan and Kalyanaraman [17] reported the findings of an experimental analysis on the behavior and strength of cold-formed steel shear wall panels which were subjected to monotonic and reversed cyclic loading. The authors also formulated a simplified design method for the ultimate shear strength of CFSSWP, using the data obtained from a sub-assemblage shear strength test conducted for evaluating the strength of the screw connections. This method defines the in-plane shear strength of the CFSSWP as

the minimum of the strength calculated by the cumulative strength of the screws within either the board-to-track or board-to-stud connections. Only the assemblages of the end chord studs are considered, and the contribution of interior stud and blocking connections are ignored. Thus, the simplified method gives the shear strength of the CFSSWP as in Equation 1.2,

$$F_{u-simplified} = Minimum\ of\left[(n_t \times F_{u-screw}), \left(n_s \times F_{u-screw} \times \frac{w}{h}\right)\right] \tag{1.2}$$

whereas the shear strength tested by Easley method is given by Equation 1.3.

$$\begin{aligned} &\text{for monotonic loading} \\ &F_{u-Easley} = 11.28 \times F_{u-screw} \\ &\text{for cyclic loading} \\ &F_{u-Easley} = 9.83 \times F_{u-screw} \end{aligned} \tag{1.3}$$

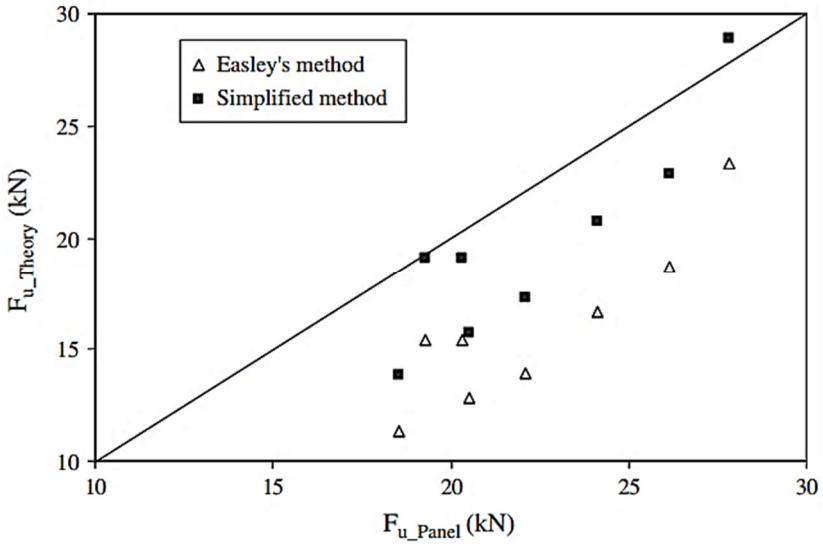

Figure 1.5. The comparison between the results of the Simplified Method and Easley's Method [17].

Shamim and Rogers [18] described the numerical design of shear walls constructed of CFS framing and flat steel sheathing, by utilizing OpenSees modelling software. The first step of the process consisted of non-linear models calibrated using available reversed cyclic test results. The second step included more complex models optimized by using the

results from dynamic shake table tests of single-story and double-story shear walls, supported with ancillary component testing.

Figure 1.6 illustrates the OpenSees dynamic modelling options for double-storey walls, which respectively correspond to a predictive model prior to the shake table tests (a), a modified model based on the test data (b), and a developed model with the brace net system (c). Idealizations have also been made for connections in the specimens, analytically factored in as rotational springs.

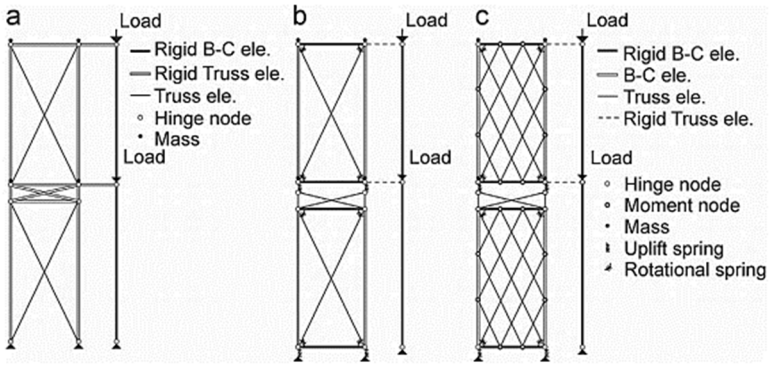

Figure 1.6. FE modelling options for double-story walls [18].

In order to calibrate the analytical models of the specimens, they are subjected to enhanced ground motions. The projected behavior obtained from the first numerical models was not in line with the shake table test results. Hence, the analytical model with the brace net system (identified previously) was developed to eliminate discrepancies and capture a more realistic response to lateral dynamic loading. The OpenSees analyses involving the second phase models also revealed that the accuracy of the numerical results can be affected by the Rayleigh damping ratio, particularly for the double-story walls.

As a concluding example, a building with similar structural properties to a two-story office building examined previously was modelled numerically and analyzed in OpenSees. The building was designed in accordance with the seismic hazard level in Vancouver Canada. The recommended seismic force reduction factors of R_d = 2.0 and R_o = 1.3 were applied, as described in the 2010 NBCC and AISI S213. The components of the model such as CFS frames, shear walls and the P-delta apparatus were identical to those utilized in the second phase numerical models of the tested shear walls.

Sato and Uang [19] used the FEMA P695 methodology to verify the suitability of the proposed seismic performance factors in the AISI S110 Seismic Standard for the newly developed Cold-Formed Steel Special Bolted Moment Frames. A total of 13 model prototypes, representing two seismicity and two gravity load levels were developed and evaluated for this purpose. The design set was arranged into four performance categories as per P695 to represent the range of design ground motion intensity and gravity loading (i.e. minimum/maximum seismic loading, low/high gravity loading). The said prototypes were designed for a Site Class D condition (soft soil) in line with seismic parameters $S_{DS} = 1.0g$ and $S_{D1} = 0.6g$ for seismic design category D_{max} , whereas $S_{DS} = 0.5g$ and $S_{D1} = 0.2g$ were applied for seismic design category D_{min}.

There was also a sensitivity study conducted for evaluating the effect of bolt over-tightening or under-tightening on the seismic response of SBMF, which included the story drift ratio and the maximum moment in the bolted connection. Three models were considered for each of the 13 archetypes. The standard (ST) model assumes that the bolts were correctly adjusted to the snug-tight position, so that the tension of the bolt is the same as presumed. The over-tightened (OT) model assumes that all the bolts were over-tightened such that the bolt tension is 50% larger, and the under-tightened (UT) model assumes that the bolt tension is 30% smaller. Conclusions can be summarized as follows:

- The proposed seismic performance factors $R = 3.5$ and $C_d = 3.0$ were reasonable and had an acceptable margin against collapse under the maximum earthquake ground motions considered.
- Over-tightening the bolts reduced the story drift by up to 3.4%, whereas the maximum moment in the connection increased by 4.4%. Under-tightening the bolts, however, increased the story drift by 3.3%, and the maximum moment in the connection decreased by up to 5.7%. The impact of bolt tension was insignificant in evaluating the collapse margin, and the acceptance criteria were satisfied. Thus, over-tightening or under-tightening of the bolts was not a major concern.
- Even though the study proved that a lower value of C_d (= 3.0) was sufficient due to the significant bearing hardening effect in the bolt groups, the Code still opted to set C_d equal to R (= 3.5), as seen in the relevant Table 12.2-1 of ASCE 7-10.

- In addition, since S110 includes a design method for computing the ultimate strength of the structural system, and thus the usage of Ω_0 would be redundant, the code committee agreed to assign a value of 3.0 to Ω_0 in order to be consistent with the format for other systems. However, a reference is given in such a way that the designer can still use S110 to directly calculate the amplified seismic effects for capacity design instead of utilizing the empirical Ω_0 factor.

Within the scope of an Italian research project called RELUIS-DPC 2010-2013, undertaken at the University of Naples, Iuorio *et al.* [20] investigated the seismic behavior of strap-braced stud walls. This research primarily concentrated on 'all-steel design' solutions, and incorporated three typical wall configurations which were governed by elastic and dissipative design requirements for three specific seismic scenarios.

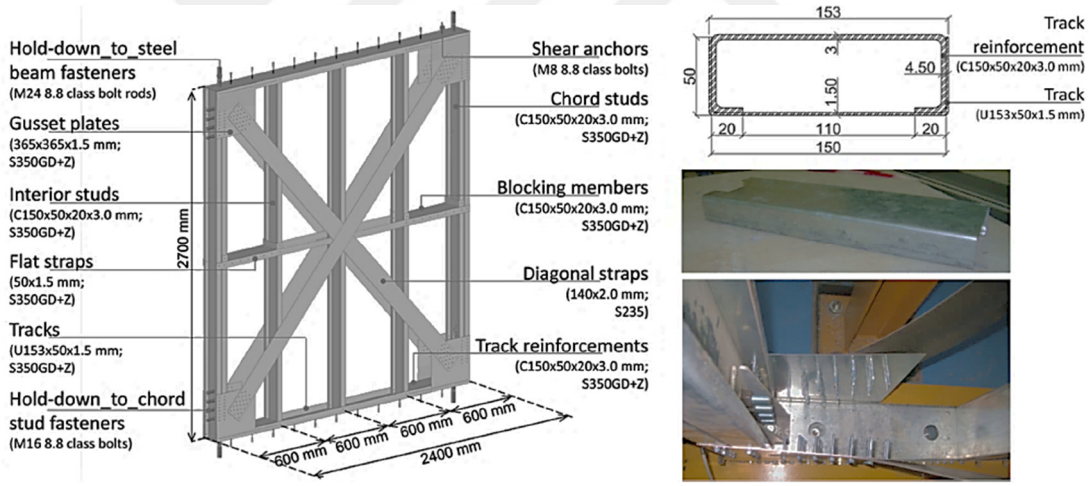

Figure 1.7. The general view of a representative wall specimen, and typical connection details including track reinforcement [20].

These configurations were basically altered by introducing three different bracing types, which are illustrated in Figures 1.7 – 1.10: elastic light bracing (WLE), dissipative light bracing (WLD) and dissipative heavy bracing (WHD). The nuance between light and heavy simply manifests itself with thicker and/or wider straps. On the other hand, the difference between elastic and dissipative bracing comes from their fastener configuration: the smaller and/or less congested they are, the more the connection is likely to fail before the design plastic resistance is attained in the connected straps and/or other dissipative members. In elastic connections, it is either the bracing plate or the fasteners that fail first.



Figure 1.8. The general view and the corner detail of the wall specimen with elastic light (WLE) bracing configuration [20].



Figure 1.9. The general view and the corner detail of the wall specimen with dissipative light (WLD) bracing configuration [20].

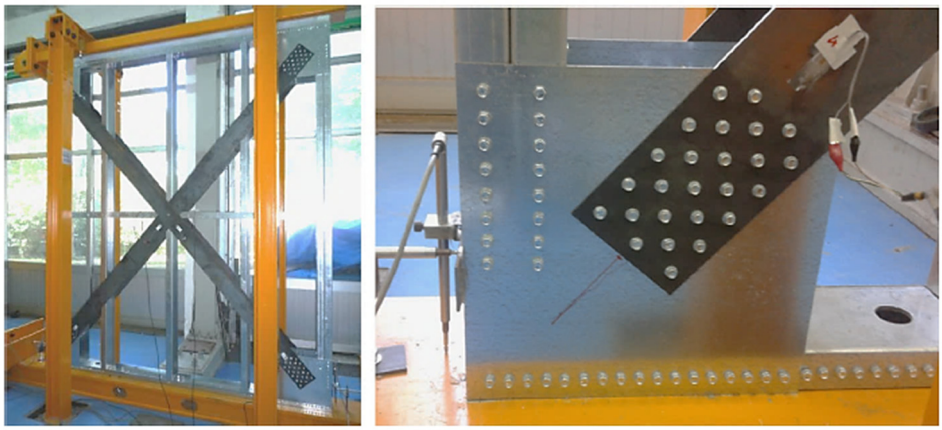

Figure 1.10. The general view and the corner detail of the wall specimen with dissipative heavy (WHD) bracing configuration [20].

Two monotonic and two cyclic tests were performed on each type of configuration. Figure 1.11 displays the failure mechanisms of each type of specimen after the monotonic tests, and their failure mechanisms after the cyclic tests are provided in Figure 1.12.



(a) (b) (c) (d)

Figure 1.11. (a) Net section failure for WLE specimen, (b) brace yielding mechanism for WLD specimen, (c) and (d) brace yielding mechanism for WHD specimen [20].

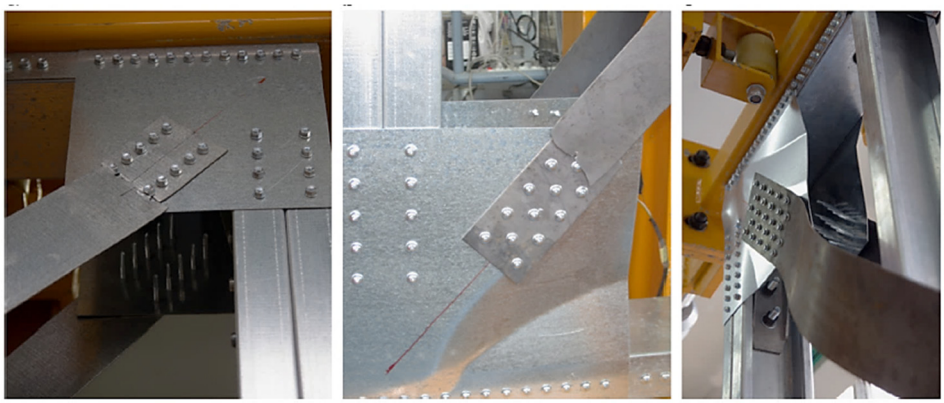

(a) (b) (c)

Figure 1.12. (a) Net cross-section fracture for WLE specimen, (b) net cross-section fracture for WLD specimen, and (c) strap yielding mechanism for WHD specimen [20].

Additional shear tests were performed on elementary (single) connections, and are illustrated in Figure 1.13. Finally, shear tests were also performed on frame-to-strap connections, and are presented in Figure 1.14. All of these experimental evidence was later used for validation of the design criteria, i.e. national codes and other design specifications.

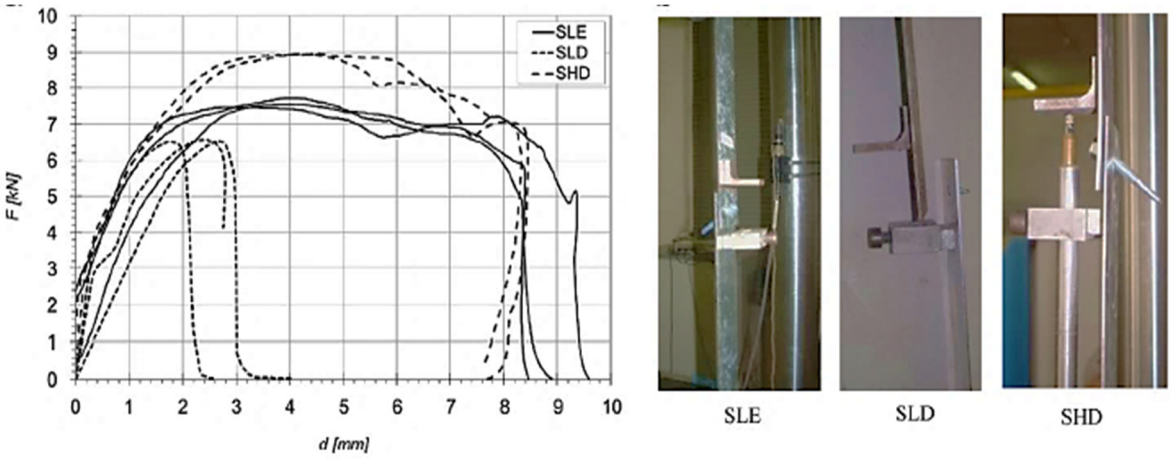

Figure 1.13. Test results for single connections: (a) force-deformation curves, and (b) failure modes for SLE, SLD and SHD specimens [20].

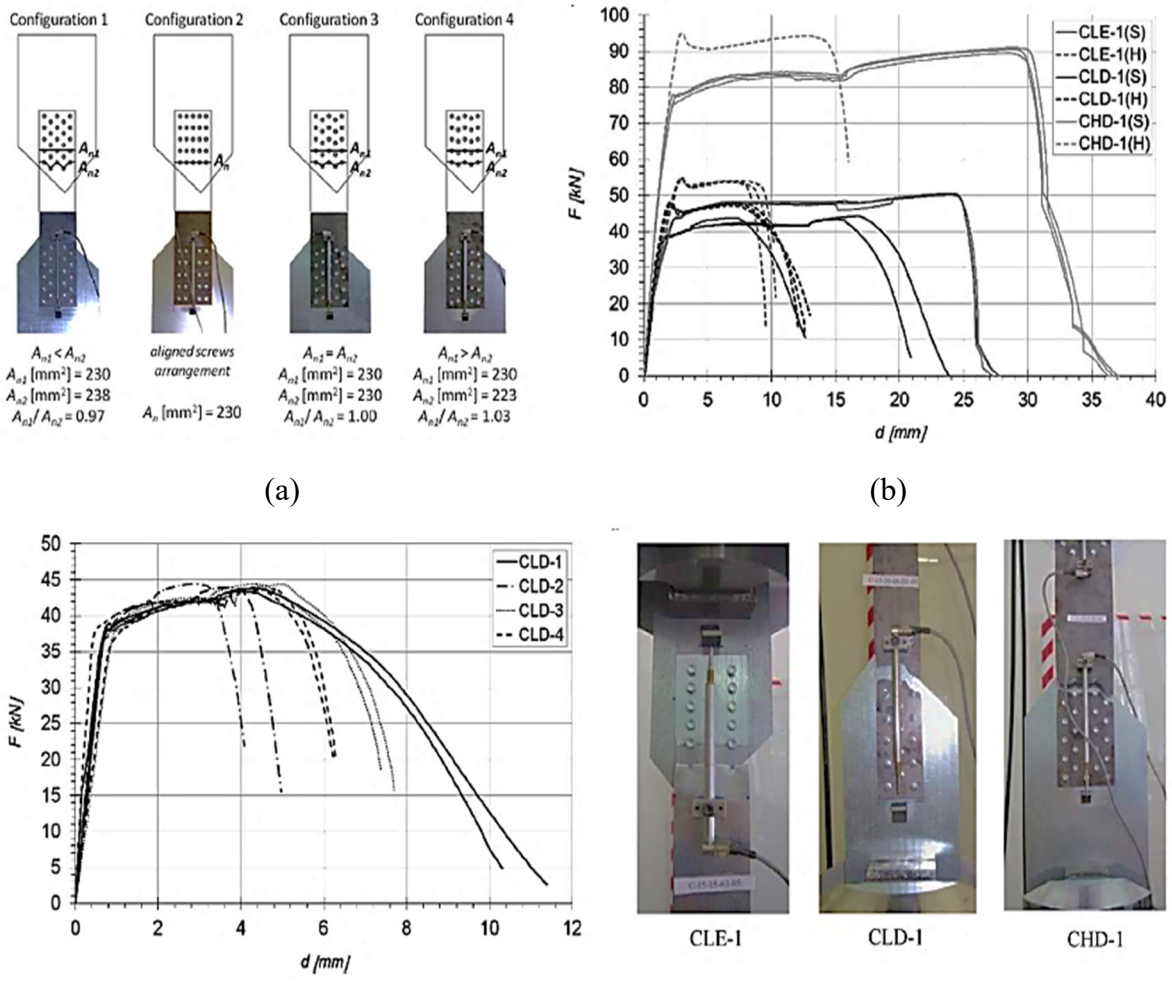

Figure 1.14. (a) Specimen configurations, (b) and (c) test results, and (d) failure modes for CLE, CLD and CHD frame-to-strap connection specimens [20].

Both ductility-related and overstrength-related modification factors are evaluated, where Table 1.4 summarizes the calculated values. It was observed that the behavior factor values defined in AISI S213 for either *Conventional Construction* category (WLE wall type) or *Limited Ductility Braced Wall* category (WLD and WHD wall types) were always smaller than experimental results, i.e. the code values representing the lower limits.

Table 1.4. Structural behavior factors for WLE, WLD and WHD wall configurations [20].

Test	R_d	R_o	q
WLE-M1	1.74	1.15	2.00
WLE-M2	1.74	1.17	2.04
WLE-C1	1.80	1.21	2.19
WLE-C2	1.73	1.20	2.08

Test	1.5% *Interstorey drift*			2% *Interstorey drift*			7% *Interstorey drift*		
	R_d	R_o	q	R_d	R_o	q	R_d	R_o	q
WLD-M1	2.18	1.42	3.09	2.58	1.43	3.68	5.08	1.53	7.76
WLD-M2	2.28	1.40	3.20	2.70	1.43	3.87	5.29	1.56	8.24
WLD-C1	2.18	1.51	3.29	2.58	1.50	3.88	5.08	1.53	7.75
WLD-C2	2.39	1.53	3.65	2.82	1.51	4.26	4.77	1.64	7.83
WHD-M1	1.89	1.38	2.60	2.26	1.38	3.11	[a]		
WHD-M2	1.83	1.37	2.51	2.19	1.41	3.08	4.40	1.46	6.40
WHD-C1	1.96	1.45	2.84	2.33	1.46	3.41	4.64	1.51	7.02
WHD-C2 (Pull)	2.12	1.41	2.99	2.52	1.44	3.63	[b]		
WHD-C2 (Push)	1.98	1.41	2.80	2.36	1.44	3.39	4.69	1.41	6.64

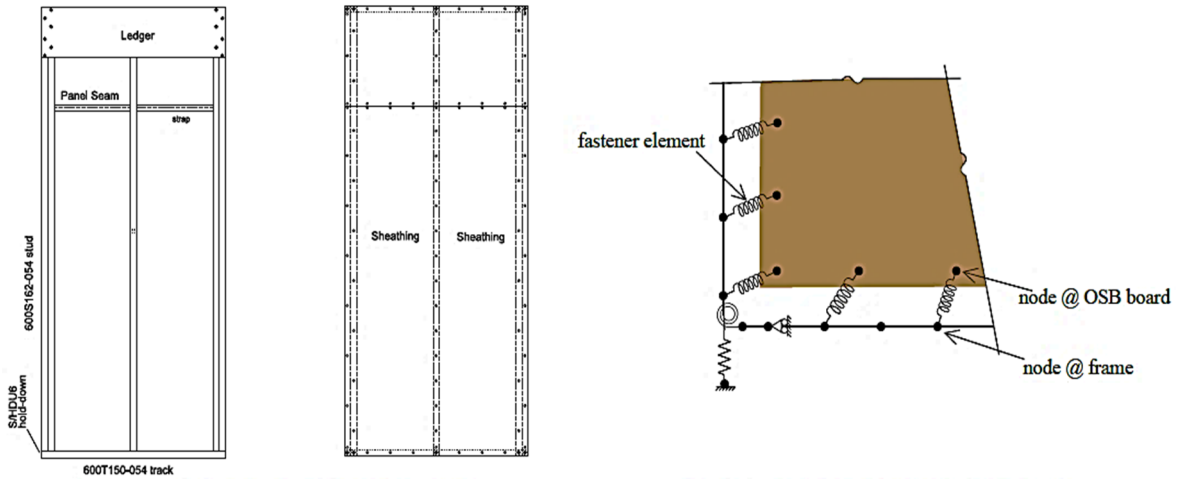

(a) benchmark CFS-framed shear wall (b) corner modeling detail in OpenSees

Figure 1.15. The reference model used for element idealization [21].

Bian *et al.* [21] have merged two types of analytical modelling techniques to provide a proficient shear wall model useful in capturing fastener-based and member-based limit

states in the shear wall. The same group of authors previously showed that OpenSees models which incorporated nonlinear stud-to-sheathing fasteners and were calibrated only to fastener-level tests, were still capable of predicting the full hysteretic performance of the shear wall, provided that chord stud buckling or other failures are avoided. In another work, the authors also experimentally characterized the hysteretic behavior of chord studs and introduced phenomenological models suitable for the frame-element in OpenSees.

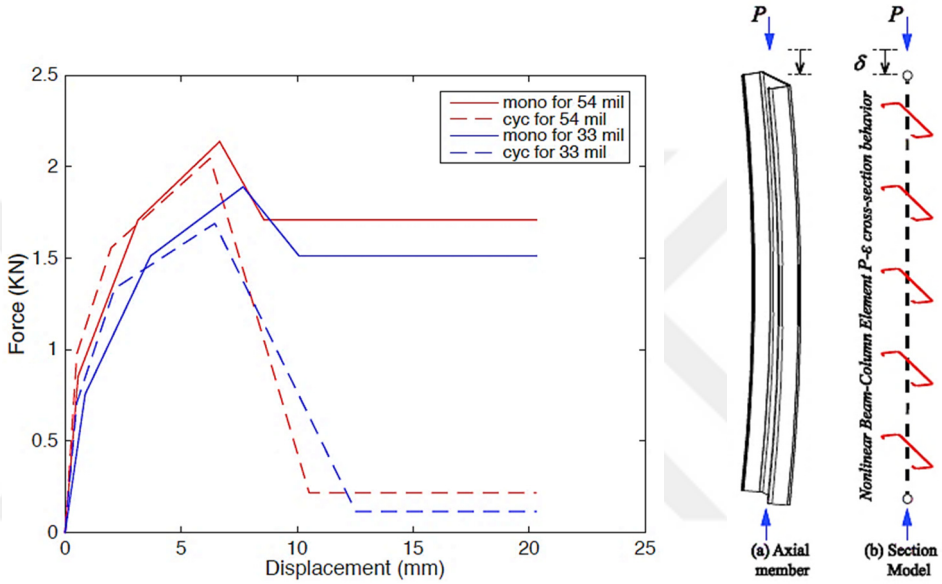

Figure 1.16. The development of chord stud model in OpenSees [21].

Monotonic loading response of the developed OpenSees model mostly agreed with experimental results to some extent. As can be seen in Figure 1.17(a), there is quite a difference between the lateral force capacities obtain from the analytical and experimental data. Analyses were also reiterated with varying levels of gravity loads (Figure 1.17 (b)), where P_{nl} corresponds to the critical (buckling) load of a single stud. Fastener response was also included (Figure 1.17(c)), for which the fastener with the largest deformations is selected as reference.

For comparison purposes, an additional shear wall model was developed using ABAQUS software, where the CFS framing members and sheathing were modeled as four-node shell finite elements (S4R), and the steel-to-sheathing connections were modeled as Spring-A elements with the same backbone curve as used in OpenSees. According to the analyses, OpenSees and ABAQUS results agreed reasonably well.

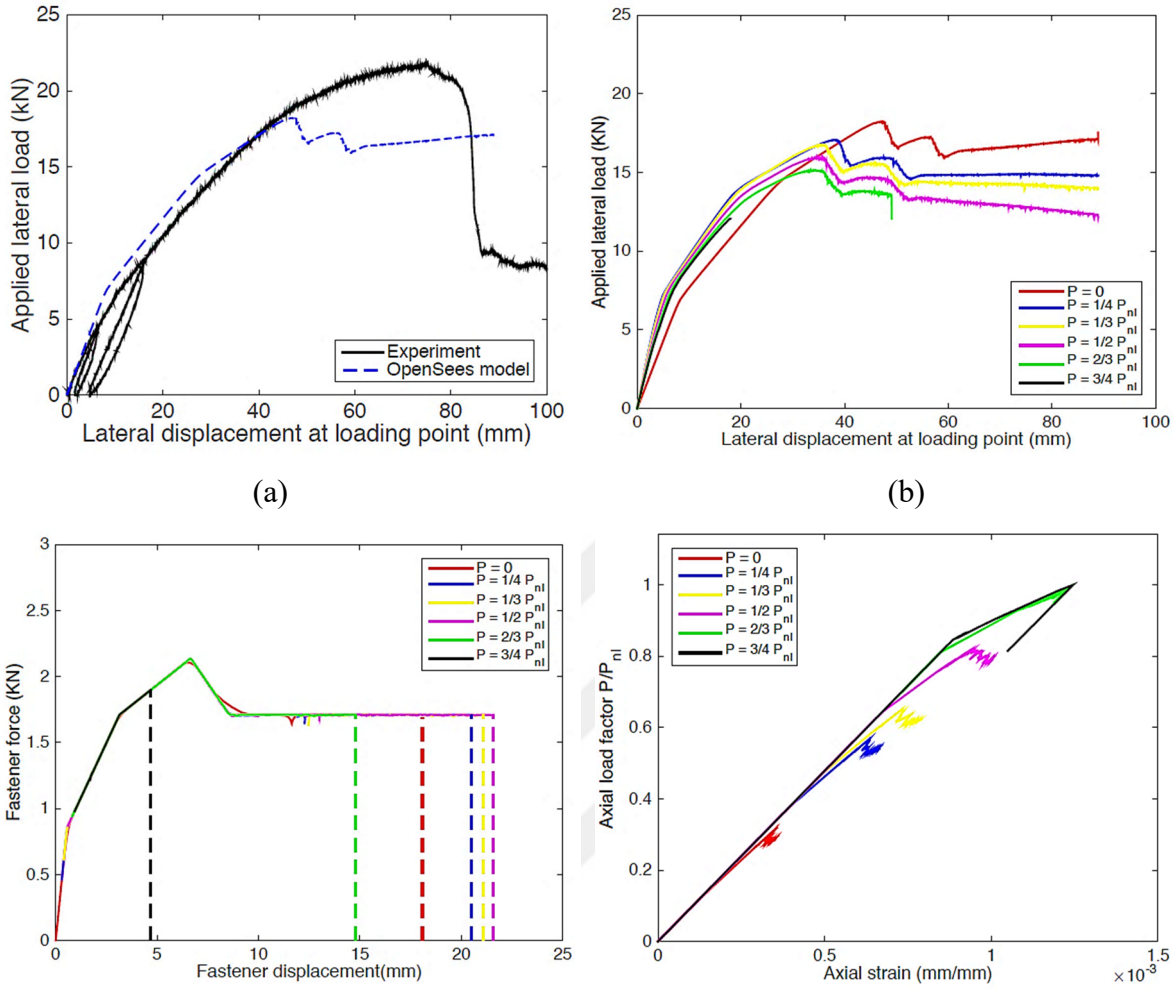

Figure 1.17. Extensive results and comparisons obtained from the analytical studies [21].

Karabulut [22] performed cyclic tests on a number of specimens using various configurations, which were aimed at determining the influence of board type, steel thickness, screw spacing and axial loads on structural performance of CFS shear panels. Out of three available loading protocols proposed by ASTM E2126-11, CUREE Basic Loading Protocol was used during the experiments. The loading speed was chosen in such a way that the load is applied in a static fashion, thus allowing for potential observations of damage.

The force-displacement hysteretic curves obtained from the experiments were then converted to a bilinear force-displacement relationship by using the envelope curve from hysteretic data. In each experiment, the values of the shear strength and strength reduction factors were determined using the average force-displacement envelope curve (Table 1.5).

Table 1.5. The ultimate shear strength and the relevant strength reduction factor of each specimen [22].

Experiment	Shear Strength (kN)	Strength Reduction Factor (R)
1. Type 1 Specimens	3.2	5.1
2. Type 2 Specimens	6.0	4.1
3. Type 3 Specimens	7.4	4.2
4. Type 4 Specimens	4.1	3.7
5. Type 5 Specimens	4.7	4.0
6. Type 6 Specimens	4.9	3.5
7. Type 7 Specimens	5.1	3.6
8. Type 8 Specimens	4.9	3.8

The paper also contains analytical study and calibration of the test specimens. Calibration process included a specimen without sheathing, a specimen with one-sided gypsum sheathing, and a specimen with one-sided (gypsum) sheathing subjected to an axial load on top. Analyses contained both an analytical screw model and a Richard-Abbott screw model. The numerical study concluded that the analytical results of the Richard-Abbott model did not match the experimental results. The model was then updated on the basis of a trial and error approach until a good convergence between analytical and experimental results was obtained. In the final step, where the effect of the axial load on panel behavior was observed, using this modified analytical screw model (Figure 1.18) proved successful, and the analytical results converged to the actual experimental results.

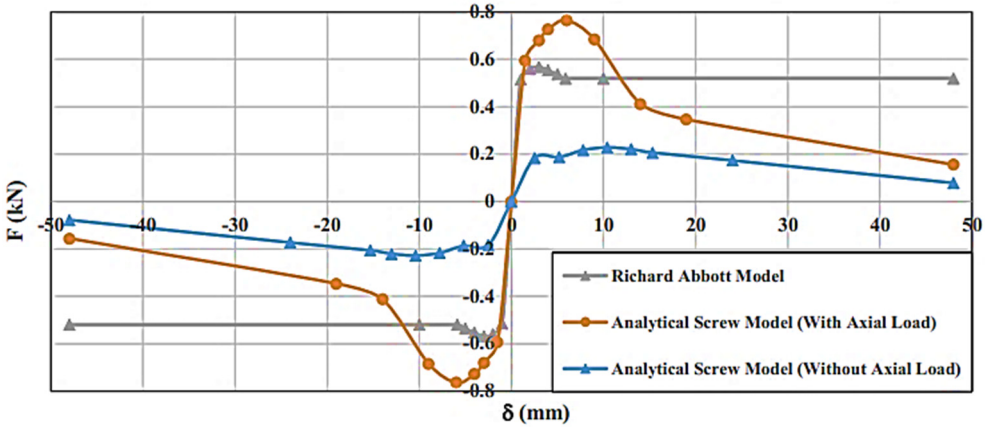

Figure 1.18. Screw models used in the analytical studies [22].

Due to this consistency between analytical and experimental results of CFS shear panels under the effect of axial loads, a one-story representative CFS structure was also analytically modelled and assessed for seismic performance (Figure 1.19).

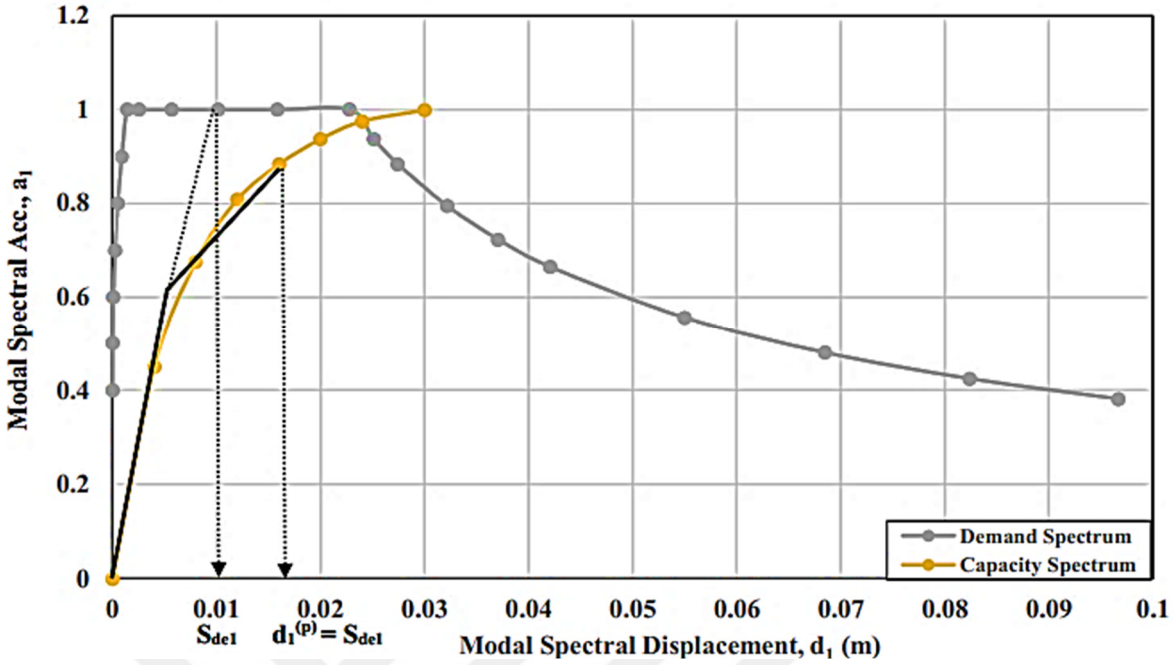

Figure 1.19. The pushover curve of the one-story representative model with performance point assessment [22].

Following observations and conclusions can be listed according to the experimental results presented in the paper:

- The primary contribution to the specimen performance is derived from high ductility and energy absorption capacity.
- The screw connections between the board and CFS frame system are the key elements that provide high ductility to all of the specimens. Generally, the demand from lateral loading is compensated through the energy absorption capacity within the slots opened by the screws alongside the board.
- Thus, the connection between the board and CFS frame remained intact under relatively high lateral forces by the help of the previously mentioned movement of the screws along these slots. This activity may be viewed as a further addition to the energy absorption capacity of the specimens.
- After comparing relevant types of shear panels, it was observed that using the board type 2 (which was a reinforced type of GWB), decreasing the screw spacing and increasing the axial loads had a positive impact on the lateral load resisting capacity. This stiffer behavior, however, usually resulted in lower values of strength reduction factors, indicating a lower ductility.

Following conclusions can be drawn from the analytical studies carried out on the CFS bare frame, shear panel and one-story structure:

- Satisfactory consistency between analytical and experimental results allowed for a good basis to be developed for 3-D structural analysis of CFS structures and performance evaluation of such structures with respect to seismic regulations.
- Following the pushover analysis of a one-story structure, the performance point obtained from the comparison between capacity and demand spectra clearly demonstrated that CFS structures can be safely constructed in seismic-prone regions such as Turkey, provided that adequate engineering supervision and application is adhered to. These satisfactory results may promote the use of such structures more widely in Turkey, where one- or two-story residential building quota is dominantly populated by masonry or reinforced concrete structures.



Figure 1.20. Visuals of the specimens and the actuator [23].

Şenkardeşler *et al.* [23] presented the results of dynamic and cyclic experiments performed on two specific 3-D and 2-storey models, which were two CFS structures with and without infill materials. The modal frequencies of the models at different damage levels were obtained through ambient vibration tests, while forced vibration tests were also carried out to determine modal damping ratios at high vibration levels. The hysteretic behavior of the model was attained by cyclic tests, which incorporated a mass shaker attached at the top of the full-scale specimen (Figure 1.20). According to the test results, the following conclusions were made:

- The experiments proved that the ambient vibration test may be a practical tool for detecting damage in a structure. There was a noticeable reduction in the first natural frequency of the system due to imposed damage, which can be related to the corresponding damage level of the structure. The decrease in the squares of natural frequencies was associated with a decline in the effective stiffness. As long as damage levels can be written in terms of effective stiffness, ambient vibration tests may also be utilized as a performance assessment tool.
- Dynamic tests allowed for the evaluation of the modal damping ratio of structures. Based on forced vibration tests, the modal damping ratios for the CFS bare-frame model and the CFS frame model with infill material were calculated to be 6.7% and 9.0%, respectively.
- Introduction of the infill material increased the lateral load carrying capacity of the specimen by approximately 3.5 times. The lateral load carrying capacity values of each specimen correspond to base shear coefficients of 1.25 and 1.60 respectively.
- Ductility related strength reduction factors were computed as 2.58 for CFS bare-frame system, and 3.96 for CFS frame with infill material, according to the cyclic test results. These values agree with similar results reported in various papers on cold-formed steel panels.
- Yield displacements were 45 mm for CFS bare-frame system, and 10 mm for CFS frame with infill material. These values refer to drift ratios of 0.0188 and 0.0042.
- It was concluded that the CFS frame with infill material absorbs more energy and is apparently more ductile than the CFS bare-frame.

Borzoo *et al.* [24] investigated the stiffness, strength and failure modes of CFS shear panels under monotonic loading. The authors favored analytical studies over full-scale testing, thus two finite element models were constructed based on two experiments with steel sheathing and nonlinear connections. This study mainly consists of analytical studies carried out to investigate the effect of varying stud sheathing thickness, the effect of varying fastener spacing, the effect of sheathing type (one- or two-sided), and the effect of height-to-width ratio of the wall on the lateral force capacity. The said analyses were done with ABAQUS software, integrating both the nonlinearity of the steel material and also P-delta effects into the analytical models. After calibrating these models with their respective test specimens, studies were focused on changing as many parameters as possible. Figures

1.21 and 1.22 provide some representative results from the investigation. Conclusions of the study can be summarized as follows:

- Greater thickness values (stud or sheathing) increase both the wall lateral strength and stiffness. For example, by doubling the thickness of the frame, the ultimate strength of the wall can be increased by as much as 94%. It was also observed that the structural elements were less prone to buckling, either local or global.
- The obtained results indicate that an important amount of the ultimate lateral strength comes from fastener spacing. The lateral load capacity of the wall usually increases with decreasing spacing between the screws. It was observed that there might be certain screw patterns or spacing values that cause diagonal stretching in the wall, which was desirable since the lateral load capacity increased in such cases. Other than that, it was concluded that screw spacing did not affect the lateral strength by much.
- Two-sided steel sheathing almost doubles the lateral stiffness of the wall. On the other hand, the lateral load capacity only increases by about 60%.
- It was observed that a height-to-width ratio of 2 had better response characteristics than any other cases.

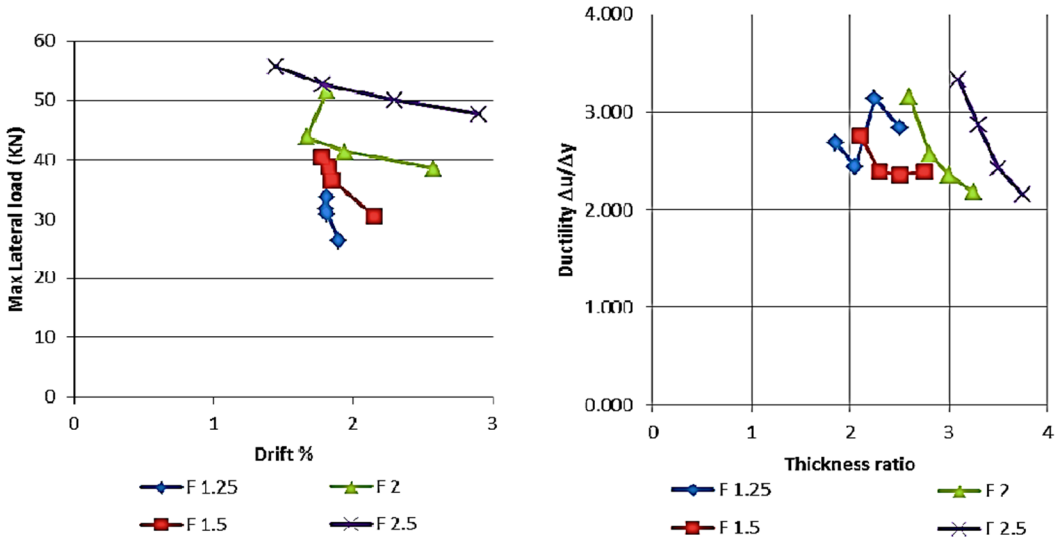

(a) (b)

Figure 1.21. The effect of varying stud and/or steel sheathing thickness (a) on lateral load capacity, and (b) on ductility [24].

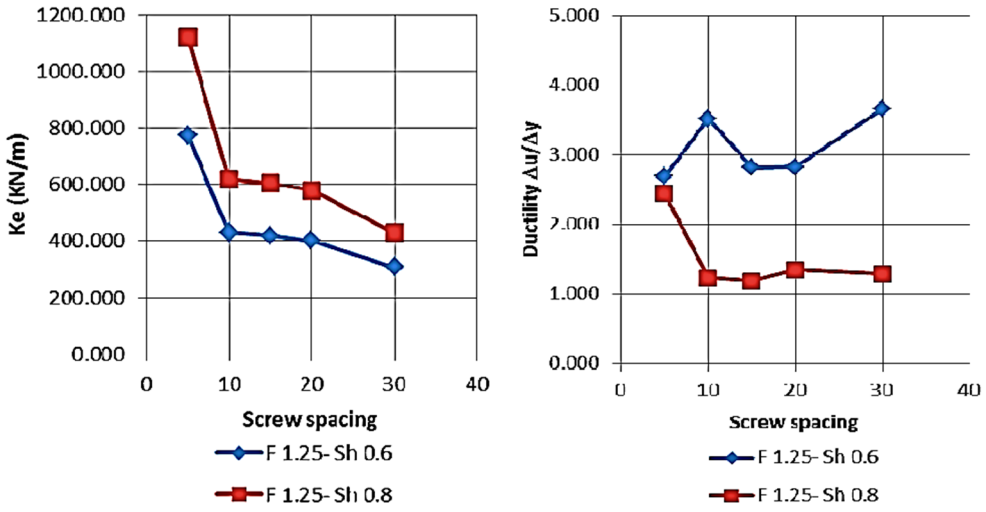

(a) (b)

Figure 1.22. The effect of fastener spacing (a) on lateral stiffness, and (b) on ductility [24].

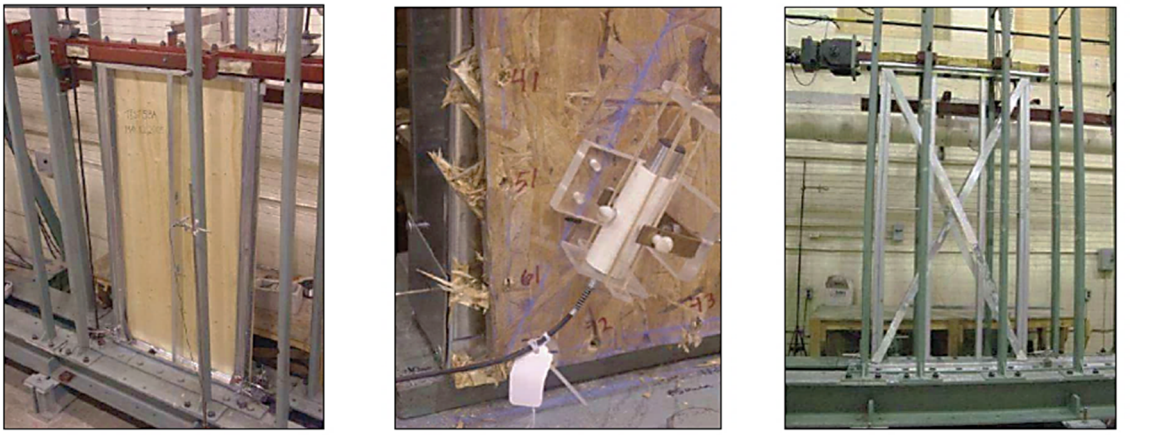

(a) Typical one-sided specimen in test rig (adapted from Hikita 2006 Figure 4-11)

(b) Example of pull-through and edge tear-out at end of test (adapted from Hikita 2006 Figure 4-24)

(c) Typical strap-braced wall specimen in test rig (adapted from Comeau 2008 Figure 2.21)



(d) Strap-braced wall after testing, showing yielding in strap (adapted from Comeau 2008 Figure 2.23)

(e) Typical one-sided steel sheet sheathed specimen in test rig (adapted from Balh and Rogers 2010 Figure 2.17)

(f) Steel sheet shear wall exhibiting shear buckling during testing (adapted from and Rogers 2010 Figure 2.18)

Figure 1.23. Typical testing rigs and subsequent test results for various CFS SFRS [25].

Madsen *et al.* [25] provided guidelines for *NEHRP Seismic Design Technical Brief No.12*, which is an extensive document specialized for cold-formed steel structures, including basic construction outlines as well as seismic design guidelines and experimental literature. In Chapter 6 of the guidelines, for instance, cyclic performance of 3 types of CFS seismic force-resisting systems is evaluated: wood structural panels, strap-braced wall panels and steel sheet sheathed panels. Figure 1.23 provides some images of the relevant test rigs and resulting panel deformations of each type.

Leng *et al.* [26] performed shake table tests on a two-story CFS framed building with OSB sheathed shear walls. Finite element models of the prototype building during its various phases of testing were developed in OpenSees software, which were also thoroughly discussed within the paper. In order to calibrate the modeling parameters of the structural system, an isolated shear wall test was conducted, and two separate modeling approaches were utilized: the conventional state-of-the-practice (P-) and a more detailed state-of-the-art (A-). Test response of the shear wall was compared to the force-displacement behavior of the usually preferred 'Pinching4 truss model' in OpenSees, and to that of the state-of-the-art idealization. In conclusion, both comparisons were deemed satisfactory.

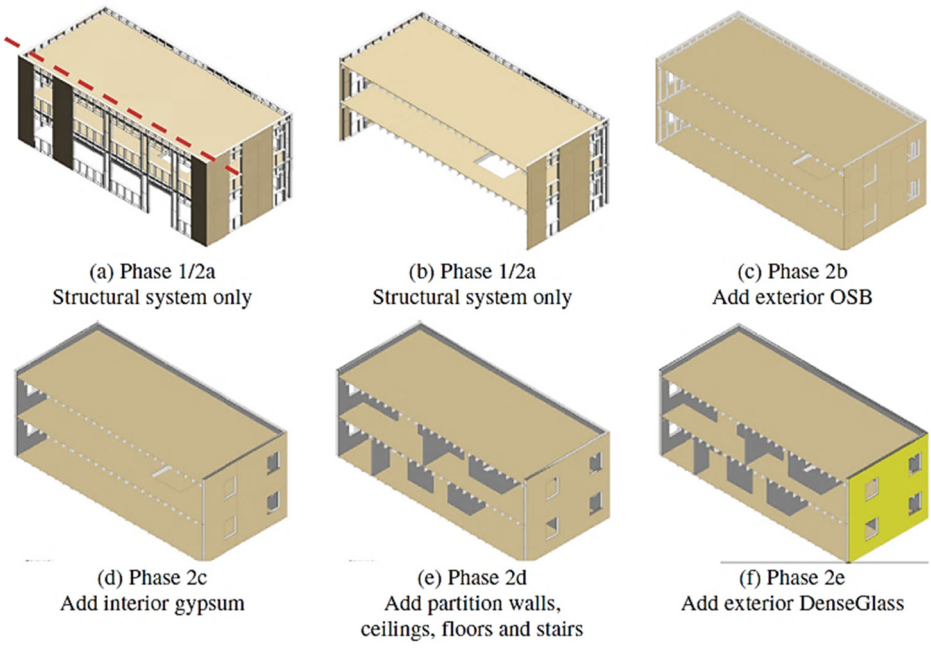

(A)

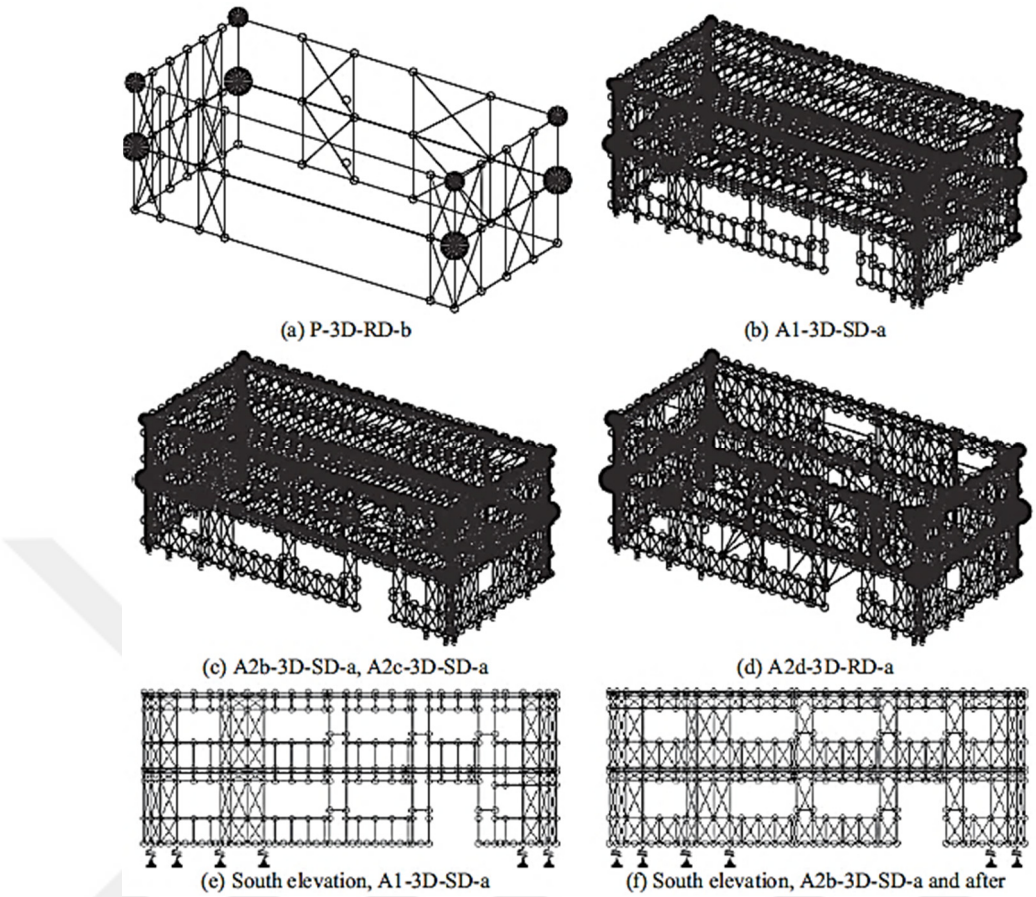

(B)

Figure 1.24. (A) Construction phases of the test building, for which shake table tests are conducted, and (B) relevant analysis models with varying levels of detail [26].

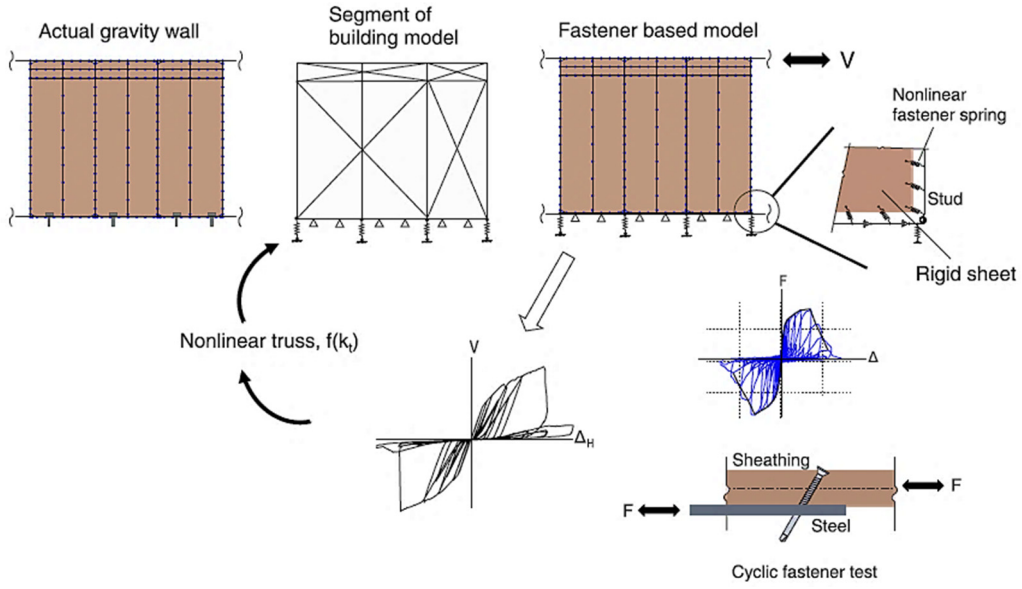

Figure 1.25. Development of the force-displacement relationship from surrogate fastener-based models [26].

There is also a ‘fastener-based model’ implemented for improving the reliability of the Pinching4 truss model. Figure 1.25 illustrates the development of the model and the idealizations made in the process. A comparison between the backbone curves of a sheathed shear wall using the fastener-based and the characteristic Pinching4 models yielded close results up to lateral deflections of 8–10 cm. It is remarked that the parameters for pinching are kept the same with the tested walls, because of limited test data.

Analysis models are finally validated and compared with full-scale shake table test results. Figure 1.26 provides a simple sketch for comparing natural periods, where the leftmost column corresponds to the state-of-the-practice model and the others are state-of-the-art models. Pushover curves of the building model at various phases are also given (Figure 1.27), where the blue curves correspond to the long dimension of the building and the red ones to the short dimension. As can be easily observed, state-of-the-art models appear to be stiffer than the state-of-the practice model. It may be assumed that P- models are suitable for design idealization purposes and eventually result in a building with reasonable performance (with respect to existing design methodologies), but are not consistent with the results observed. Another noteworthy aspect is that A- models are a good example of how stiffness and strength improve during construction.

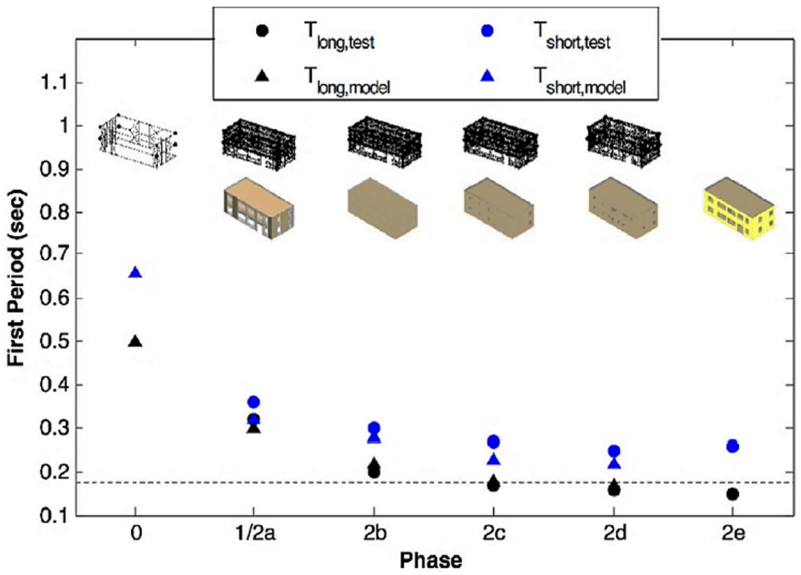

Figure 1.26. Natural periods of the test building at various construction phases, obtained by shake table tests [26].

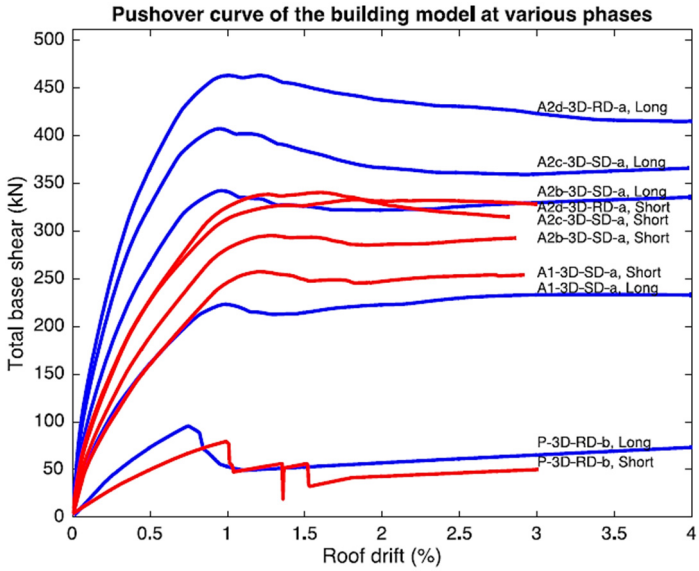

Figure 1.27. Pushover analysis results of the test building, performed for various construction phases [26].

Shake table tests were then repeated using a simulation data of the Canoga Park earthquake. Story drifts for some specific construction phases and the corresponding FE models, as well as time history plots of the selected load cells (the hold-down anchors and such) are recorded and evaluated.

1.4. Scope and Objective of the Thesis

Cold-formed steel construction is widely used all over the world, with North and South America, Great Britain and Germany as the leading regions where it is popular. There are already numerous projects in Turkey, too, in which cold-formed steel is utilized. Considering that our country frequently falls prone to earthquakes with mild to severe intensities, this growing construction sector has recently seen an increasing interest. Whilst having various advantages, cold-formed steel structures also have some downsides: instability problems, vulnerability to global, local and distortional buckling, and isolation capability are some to mention.

Thus, the newest Turkish Seismic Code (TSC 2018) provides some very helpful and elaborate design methodologies on cold-formed steel structures. Some information is based on various experimental studies performed with different panel sheathings in Boğaziçi

University. Yet some engineers and/or academics are not entirely content with some of the rules and recommendations given in TSC 2018. Some even criticize that the force modification factors defined in the Code are a little too conservative, and thus should be negotiated.

The primary objective of this thesis is to seek for evidence on whether the force modification factors defined in structural design codes for cold-formed steel structures (especially those in the TSC 2018) are reliable. These codes have only come into existence in the last decade, so it may still require further study in order to finalize the relevant articles. Therefore, necessary investigation is carried out to verify the reliability of the code-specified values for force modification factors. There are already many useful data on the design of cold-formed steel structures, where research activity involves the design of both members and other components (connections, boards etc.). Some latest studies include seismic design and non-linear analysis of such structures. In order to achieve the afore-mentioned goals, available research data conducted for the same purpose is thoroughly utilized.

In order to have a reliable basis for verification of the strength reduction factors, ambient vibration tests are performed on a real-life CFS structure, and a faithful representation of the structure is generated through an analytical model. Then the model is used for performance assessment and other required studies related to the thesis objective. Also, cyclic tests are performed on typical specimens to obtain various structural parameters. Available research data conducted for the same purpose is thoroughly utilized, where necessary and applicable.

1.5. Thesis Overview

General information on cold-formed steel structures is provided hitherto in Chapter 1. It also contains some literature survey and the thesis statement. In Chapter 2, an ambient vibration test performed on a real-life structure is extensively studied. Analytical verification and the calibration process of the tested building is also included in this chapter. Chapter 3 contains information on additional experiments, performed in the Structures Laboratory of Boğaziçi University. Test specimens are braced and sheathed CFS

frames, aimed at providing supplementary parameters later to be used in analytical studies. Chapter 4 deals with the analytical performance assessment of the tested building, utilizing the important data obtained during the lab tests. Chapter 5 provides some additional analyses, based on various alternating structural parameters. Finally, in Chapter 6 conclusions are drawn, and some ideas for likely future works are also suggested.

2. AMBIENT VIBRATION TEST AND ANALYTICAL CALIBRATION OF A REAL-LIFE STRUCTURE

2.1. Introduction

The main objective of this thesis is to verify that the force modification factors defined in the design codes for cold-formed steel structures are convenient. Therefore, it is essential to have at least one real-life structure analyzed in order to check for modification factors. For this purpose, a two-story CFS building was provided by courtesy of Akşan Yapı A.Ş. and has been monitored through ambient vibration tests. The equipment used in this test is manufactured by Kinemetrics, which is a 12-channel substation with a sampling rate of 200 Hz, and is provided by the Structures Laboratory of Boğaziçi University.

2.2. General Information about the Building and Experiment

The building is situated in one of the resorts close to the Enez Harbour in Trapez district of Enez/Edirne. This resort consists of monotype two-story mirror-villas and is one of the many similarly constructed groups of villas that can be seen around in the district. The housing estate covers roughly 7300 m^2 of land in which there is a small swimming pool. Each house has approximately 12.0 m by 6.7 m dimensions on plan. At the time of the visit there were no or very few inhabitants in the estate. Some sample drawings regarding the CFS walls and the slabs of the tested building are given in Appendix A.



Figure 2.1. The location of the tested building.



Figure 2.2. Some images of the typical mirror-villa used for AVT.

The sensors of the monitoring device were all placed on the second floor (slab or ceiling) in the left-half of the building. The following images represent the location planning and the on-site placement of the sensors, respectively from Channel-1 to Channel-10. The only sensors that are placed on the wall close to the ceiling are Channel-9 and Channel-10, the rest of the sensors are all placed on the second story floor. There was no need to use any sensors on the ground level.

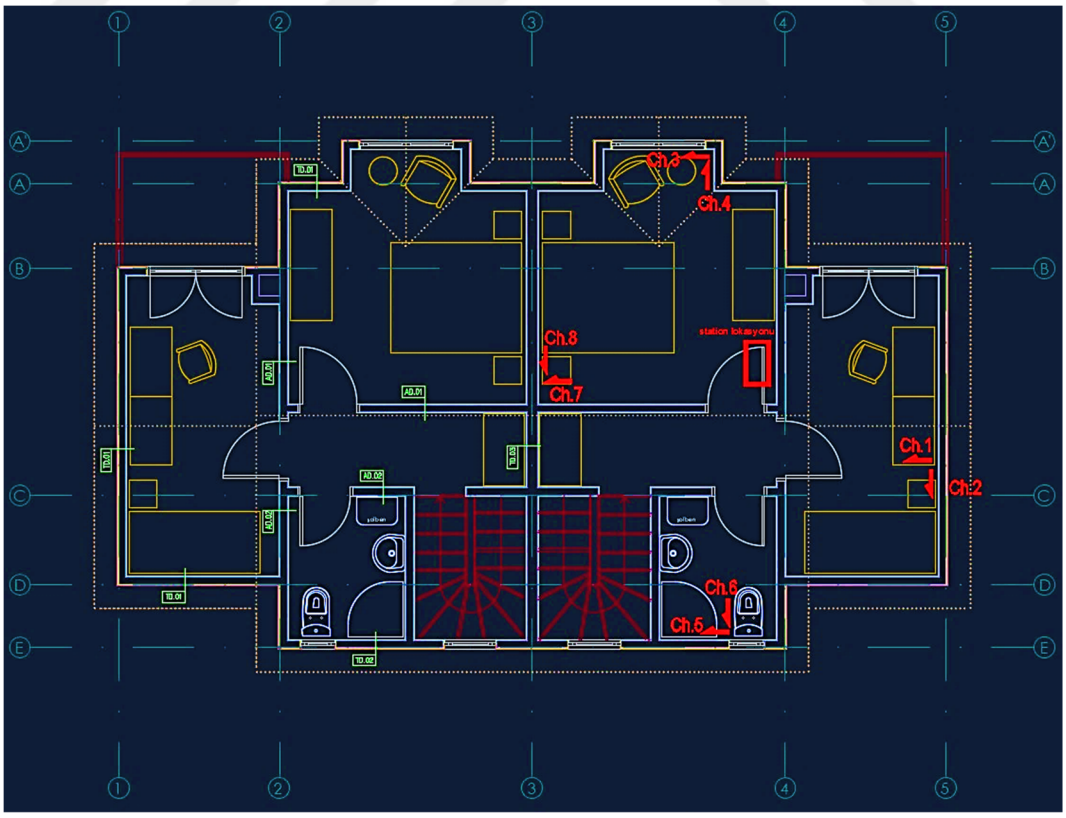

Figure 2.3. Sensor layout on the upper floor slab.



Figure 2.4. Sensor placement on the upper floor slab.

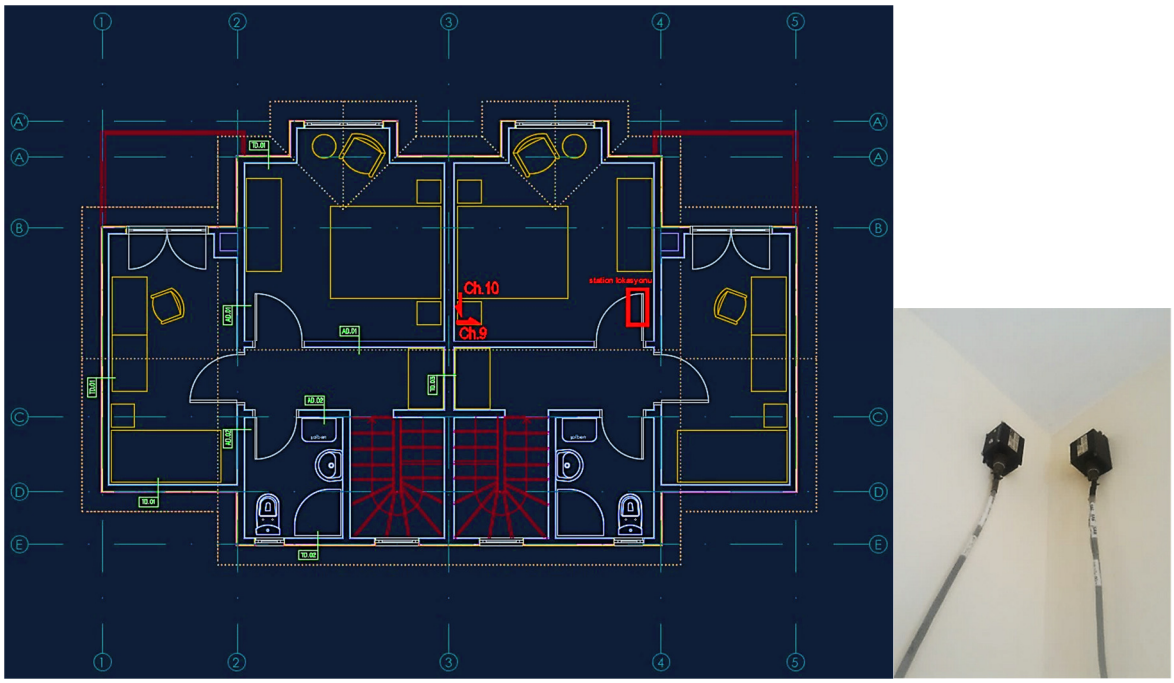

Figure 2.5. Sensor layout and placement on the upper floor ceiling.

2.3. Evaluation of the Experimental Data

After the experiment, the monitored data for each channel was computed for natural frequencies using Discrete Fourier Transform via a MATLAB code. Power Spectral Density was obtained by 'windowing' the total length data, for which the length was assumed as 2048 data-points. The sampling rate of the data was 200 Hz, the same as obtained from the test. Cut-off frequency of 50 Hz and an overlap (averaging rate) of 50% was used in the analysis. Also a high-pass filter (0.15 – 0.50 Hz) was applied to all acceleration records. The detailed output data of the channels are provided in Appendix B.

As can be traced from these FFT decompositions, the first natural frequency of the building appears to be 8.9 Hz (T_1 = 0.112 sec) in X-direction (along the longer dimension of the building), and the second natural frequency is 9.8 Hz (T_2 = 0.102 sec) in Y-direction (along the shorter dimension – Figure 2.6). While the first two modes are easier to point out, the third mode doesn't seem so obvious. There is a slight contribution from some of the sensors in X-direction as well as Y-direction, but not much can be said about the proper value and/or orientation of the third mode. It can arguably be concluded that it is about 12 Hz ($T_3 \approx$ 0.08 sec) either in X- or Y-direction (or both). Test results are also provided in Appendix B in more detail.

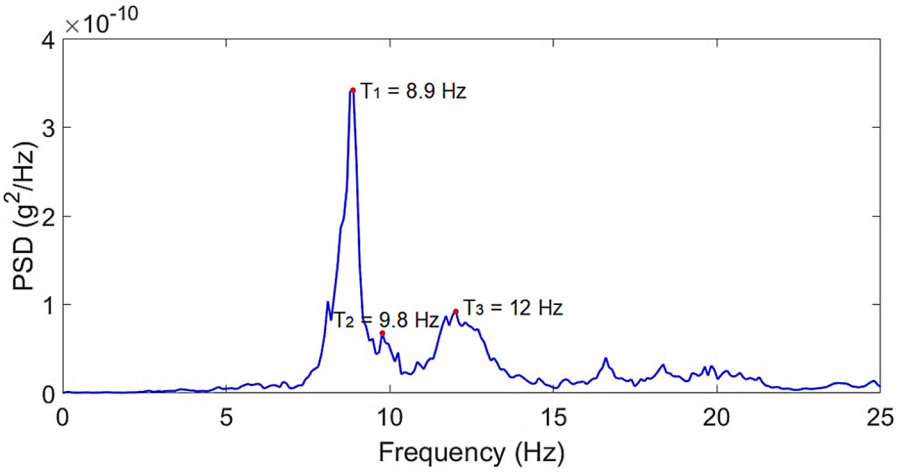

Figure 2.6. Windowed and filtered results of the Fast Fourier Transformation.

2.4. Analytical Verification and Calibration

In order to carry on with the performance assessment phase, a 3-dimensional analysis model was prepared in line with the information provided by Akkon Çelik Yapı Sistemleri A.Ş. (Figure 2.7). The walls of the structure incorporate double layers of OSB panels, with a thickness of 12.5 mm each. The dimensions of the panels are 1220 mm (width) by 2440 mm (height), with a stud spacing of 610 mm on average. The screw distance is reported to be 150 mm on the exterior studs (of each panel) and 300 mm on the interior studs. The same panel and screw configuration is also used for the slabs. Suspended ceiling is not included in the model.

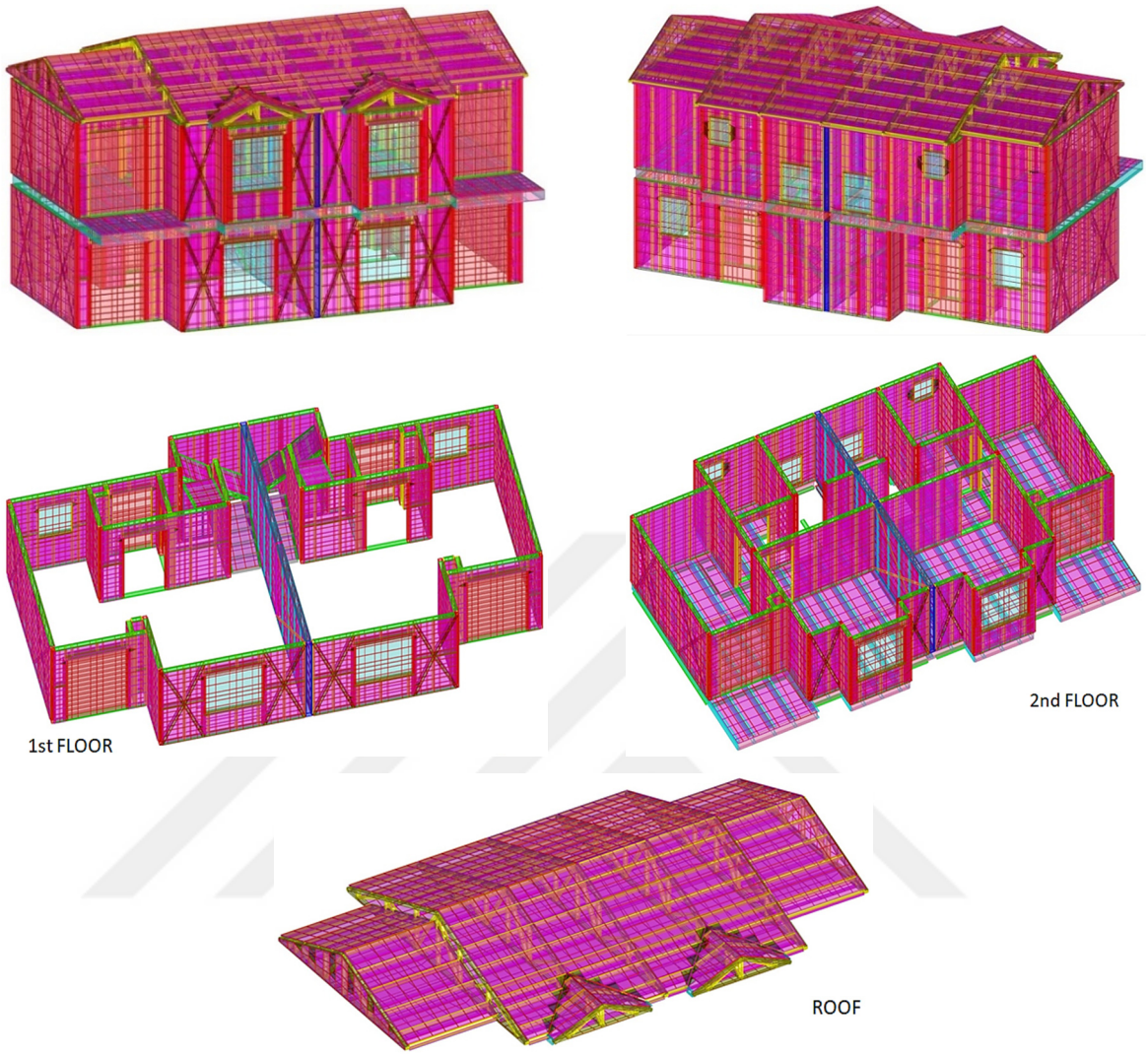

Figure 2.7. Some images from the analytical model of the building.

Apart from the project drawings, the mechanical properties of the panels and screws are defined similar to those provided by Karabulut [22]. The only apparent difference is that the screw distance is 200/300 mm in Karabulut's study, whereas it is 150/300 mm in this one. The behavior of the screws (under the influence of gravity and lateral loads) is not expected to differ largely. Figures 2.8 and 2.9 briefly illustrate some of the link parameters used for connections between frames and OSB panels. We are given to understand that panels are generic OSB, thus the related parameters in the model are defined accordingly. Other than that, minor differences between the real-life structure and the analytical model are ignored.

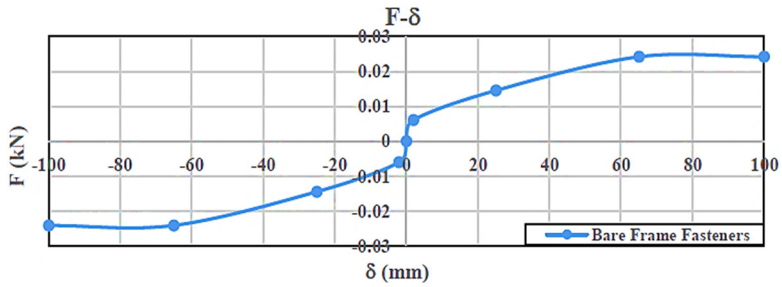

Figure 2.8. A sample force-deformation curve of the link elements used for the connections in between frame elements (studs, girders and braces) [22].

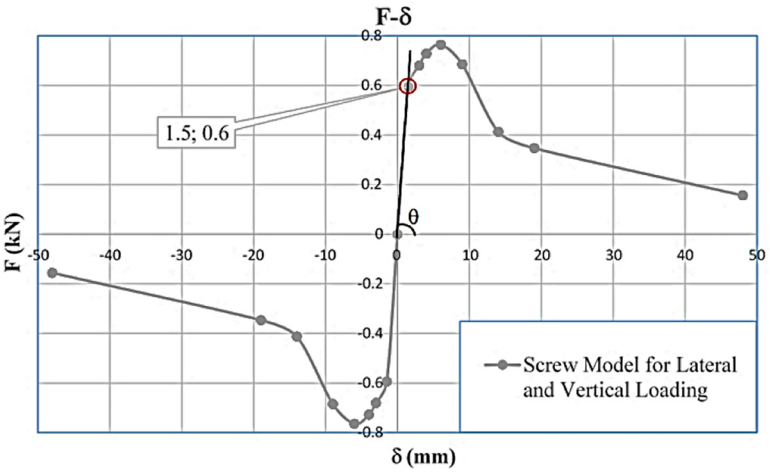

Figure 2.9. A sample force-deformation curve of the link elements used for the connections between frames and shell elements (OSB panels) [22].

One aspect that inevitably affects the modal characteristics of such a lightweight structure is obviously the loading conditions. Considering that the site was mostly uninhabited at the time of the visit, and that the present layout of the household consisted of limited furniture, a cautious approach was adopted for load definitions (Figure 2.10).

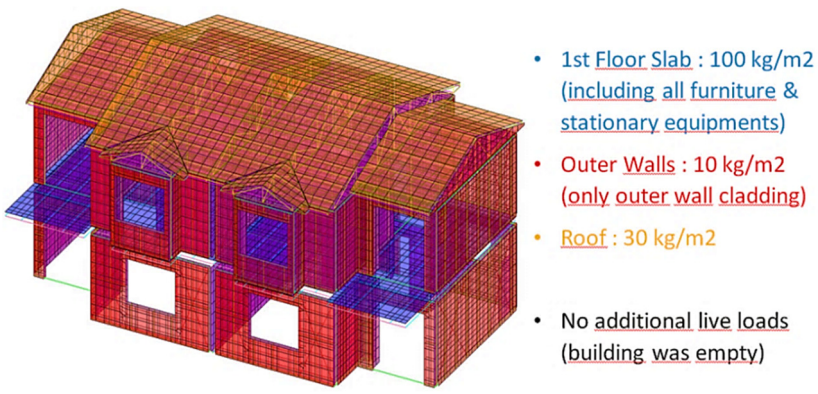

Figure 2.10. Graphical representation of the loads applied on the structure.

The calibration of the analytical model is done by modal analysis. It is carried out and interpreted through a few steps. Firstly, the link elements between all structural elements are assumed to be completely rigid. This allows for checking on any possible connection errors between structural elements. The resulting modal periods are lower than those obtained by the experiment, as expected. After re-defining the link elements as given in Figures 2.8 and 2.9, it is observed that the structure attains some flexibility: the structural modal periods are slightly higher than the experimental results, yet still acceptable. Finally, to improve realism, exterior doors and windows are also inserted as shell elements composed of structural materials timber and glass, respectively. The modal results for this modelling option are obtained as closest to the experimental data.

Table 2.1. Structural modal periods obtained for various modelling options.

COMPARISON OF NATURAL VIBRATION MODES	1st Natural Vibration Mode	Dir.	Modal Participating Mass Ratio	2nd Natural Vibration Mode	Dir.	Modal Participating Mass Ratio	3rd Natural Vibration Mode	Dir.	Modal Participating Mass Ratio
EXPERIMENTAL RESULTS	0.115 sec	X	-	0.107 sec	Y	-	0.08 sec	X/Y	-
ANALYTICAL RESULTS									
W/O LINKS - RIGID CONNECTIONS	0.072 sec	X	% 44	0.06 sec	Y	% 66.6	0.043 sec	X	% 20
W/LINKS (ELASTIC STIFFNESS), NO DOORS/WINDOWS	0.13 sec	X	% 37.7	0.117 sec	Y	% 32.3	0.079 sec	Y	% 27.5
W/LINKS (ELASTIC STIFFNESS), EXT.DOORS&WINDOWS	0.116 sec	X	% 36.5	0.115 sec	Y	% 39.9	0.074 sec	Y	% 19.2

2.5. Corrections and Improvements to the Analytical Model

Due to numerical difficulties and unreliable results encountered during the initial analyses, a couple of refinements had to be made to the analytical model, some of which are outlined here.

So far it has been discovered that the nonlinear response of a sheathed CFS shear wall is generally dominated by the local behavior at each steel-fastener-sheathing connection. Thus it is of critical importance to define these elements as correctly as possible. The ‘completely-rigid link’ assumption initially made for interstory screw connections led to the upper floor toppling over the other, since the analysis software apparently tried to redistribute the internal forces to the nearby (weaker) link elements in

order to comply with the displacement request set in the analysis parameters. Thus they were replaced with a more flexible link definition. This editing necessitated for a stiffer force-displacement behavior for frame-to-frame connections in order to attain the same values for natural vibration periods. The updated force-displacement properties for some of the frame-to-frame and frame-to-panel connections are illustrated in Figure 2.11.

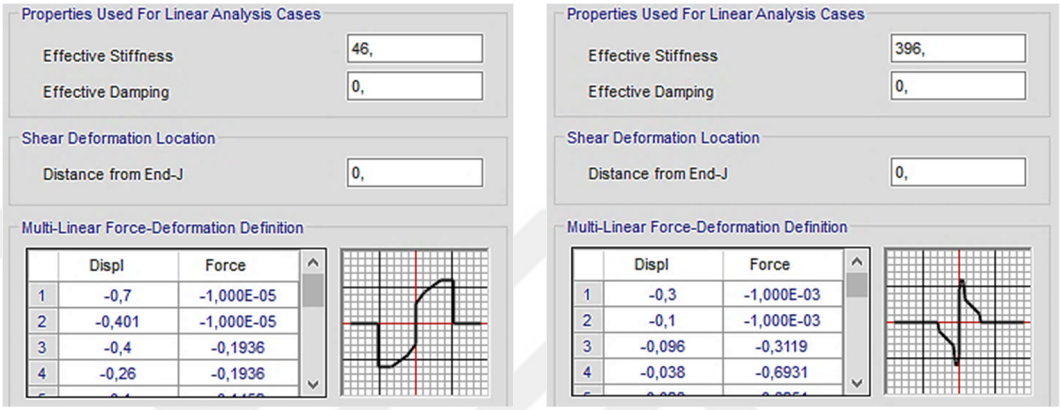

Figure 2.11. Sample force-displacement curves for some of the updated frame-to-frame and frame-to-panel connections (link elements).

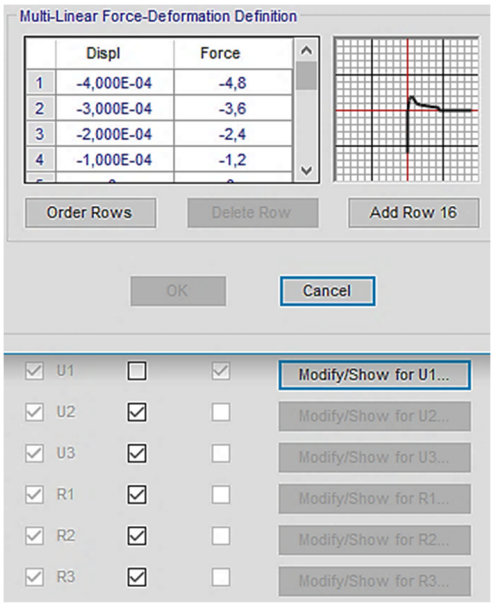

Figure 2.12. Force-deformation definition for the link elements to be used at locations where the second floor studs meet the first floor studs.

Other numerical difficulties with the analysis model materialized in the form of some of the first floor walls almost independently displacing as the analysis progressed. These

deformations appeared to wholly depend on the connection types between adjacent walls, which were later rectified by defining additional link elements. The said links are used for simulating a stiffened connection to improve the structural connectivity of the lower and upper floor studs. Therefore, at certain points where lower and upper floor studs meet and connect to the floor beams at inner and/or outer walls, link properties needed to be redefined. It was assumed that the link simulating the stiffening elements at these locations is fully restrained against all rotations and transverse displacements, and is only allowed to elongate (axially) in the manner illustrated in Figure 2.12.

After modifying the said link elements as demonstrated above, the relevant modal results are highlighted in Table 2.2. The positive effect of the modifications can be immediately captured in the difference between the modal participating mass ratios.

Table 2.2. Structural modal periods after updated link properties.

COMPARISON OF NATURAL VIBRATION MODES	1st Natural Vibration Mode	Dir.	Modal Participating Mass Ratio	2nd Natural Vibration Mode	Dir.	Modal Participating Mass Ratio	3rd Natural Vibration Mode	Dir.	Modal Participating Mass Ratio
EXPERIMENTAL RESULTS	0.115 sec	X	-	0.107 sec	Y	-	0.08 sec	X/Y	-
ANALYTICAL RESULTS									
W/O LINKS - RIGID CONNECTIONS	0.072 sec	X	% 44	0.06 sec	Y	% 66.6	0.043 sec	X	% 20
W/LINKS (ELASTIC STIFFNESS), NO DOORS/WINDOWS	0.13 sec	X	% 37.7	0.117 sec	Y	% 32.3	0.079 sec	Y	% 27.5
W/LINKS (ELASTIC STIFFNESS), EXT.DOORS&WINDOWS	0.116 sec	X	% 36.5	0.115 sec	Y	% 39.9	0.074 sec	Y	% 19.2
W/LINKS (UPDATED STIFFNESS), EXT.DOORS&WINDOWS	0.121 sec	X	% 75.2	0.114 sec	Y	% 82.7	0.094 sec	X	% 8.7

These findings obtained from the analyses so far did not yield satisfactory results, and only necessitated for a supplementary experimental investigation. In order to verify and improve the link properties (if and where required) used in the model, two laboratory experiments were made, which will be covered in Chapter 3.

Additional nonlinearity is considered in the analysis that includes plastic hinges in the studs, girders and braces. Hinges are assumed to be of semi-ductile character: the force-displacement relationship was similar to that of hot-rolled steel for tensile forces, yet they tend to lose their load-carrying capacity when a certain compressive load is reached. Plastic hinges are covered in more detail in Chapter 4.

The structure is also examined against panel failure, by taking into account the following tension/compression strengths, which have been provided by Efe and Kasal [27]. Average strength values for OSB are considered only.

Malzeme çeşidi	Çekme direnci (N/mm^2)			
	X_{min}	X_{max}	X_{ort}	v (%)
Doğu Kayını	73,55	167,41	128,5	22,26
Sarıçam	65,84	87,56	73,01	8,95
OKP	33,73	44,05	39,76	10,44
MDF	14,37	17,69	15,62	6,10
OSB	7,74	13,82	10,93	18,84

X_{min} , X_{max} , X_{ort} : Sırasıyla en düşük, en yüksek ve ortalama değer v : Varyasyon katsayısı

Malzeme çeşidi	Basınç direnci (N/mm^2)			
	X_{min}	X_{max}	X_{ort}	v (%)
Doğu Kayını	77,79	80,51	79,15	1,05
Sarıçam	43,58	54,18	49,70	5,85
OKP	36,01	41,16	37,83	4,62
MDF	17,85	19,37	18,73	3,01
OSB	13,01	21,49	16,61	25,11

Figure 2.13. Allowable tensile and compressive stress limits defined for timber types [27].

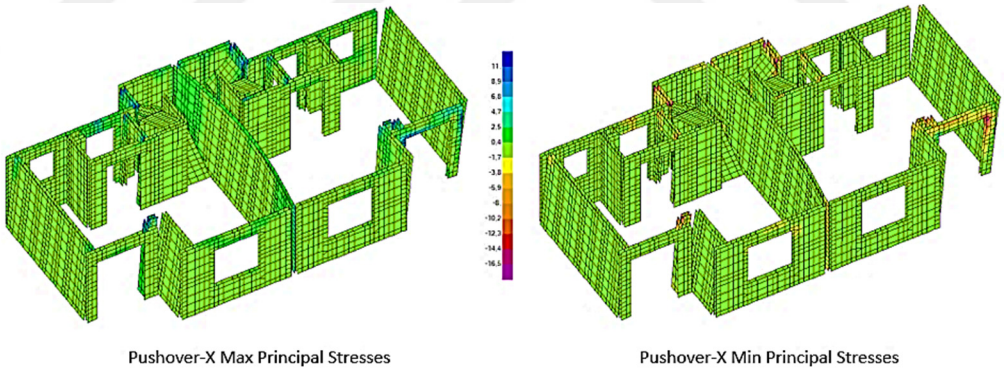

(a)

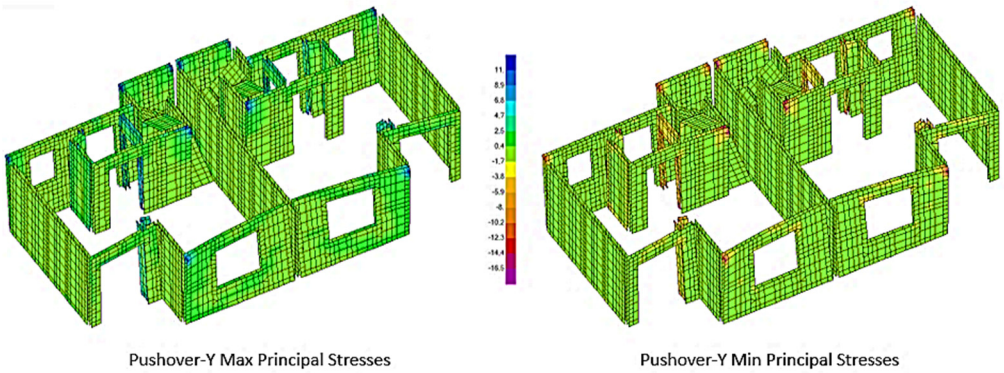

(b)

Figure 2.14. The principal stress levels in the OSB panel elements after pushover analyses in (a) X-direction, (b) in Y-direction.

As can be traced from the images in Figure 2.14, only local failures occur in the panels, and they appear to be mostly concentrated around the staircase, where the shear panels are densely located and the slightest deformation could mean significant stress changes. All in all, none of these failures seem to be of any certain cause for structural collapse, and they tend to be only local, both in studs and/or panels. It can be concluded that the structure remains within safety limits and no apparent collapse mechanism can form before the displacement levels obtained from the pushover analysis are reached. Thus, any possibility of a shear failure mechanism in the panels will not be considered henceforth.

3. CYCLIC TESTS AND NONLINEAR MODELLING OF PANELS

The main purpose of these additional tests was to improvise the link properties of the brace-frame connections, since it was shown in Chapter 2 that the structural behavior was rather far from intended. It also provided a valuable opportunity to learn to calibrate any numerical model (at first hand) with the help of experimental results. In this regard, two experiments were carried out in the Structures Laboratory of Boğaziçi University. The available test specimens at the laboratory did not necessarily bear similarities to the walls of the Enez building, which was no real cause for concern.

3.1. General Information about the Experiments

The test specimens were prepared by combining two 1200×2400 mm^2 CFS frames, since the testing rig could not accommodate for a larger one. In Figure 3.1 a photo of the bare frame test specimen assembled with 70×1.5 mm^2 strips as braces on both sides is given. Bracing strips are provided by Akşan Yapı A.Ş., as with the ambient vibration test. Brace connections to the bare frame consist of 4 screws on the corners and the mid-point (which were increased to 6 for the second experiment), and 2 screws on each of the interior studs. Due to inherent geometric imperfections on the material brought to the lab, minor difficulties were experienced during the assembly of the braces. They ended up being slightly loose and wavy, yet apparently posed no threat to the accuracy of the test since they were fully straight after pushing the specimen by only 5 mm.

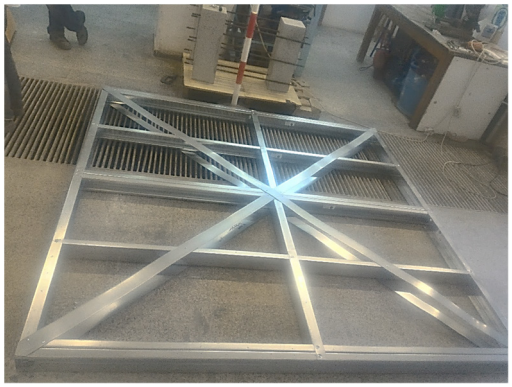

Figure 3.1. CFS frame with braces on both sides, during the assembly of the specimens.

The first specimen was equipped with 11 mm gypsum, and the second was equipped with 11 mm OSB boards on both sides. Screw spacing is 150 mm on the outer studs and girders, including the middle stud. The spacing on the interior studs and girders is 300 mm. The screws used for both frame connections and panel connections are generic 'smart-screws' (Figure 3.2).



(a) (b)

Figure 3.2. The test specimens with (a) gypsum boards, and (b) OSB boards.

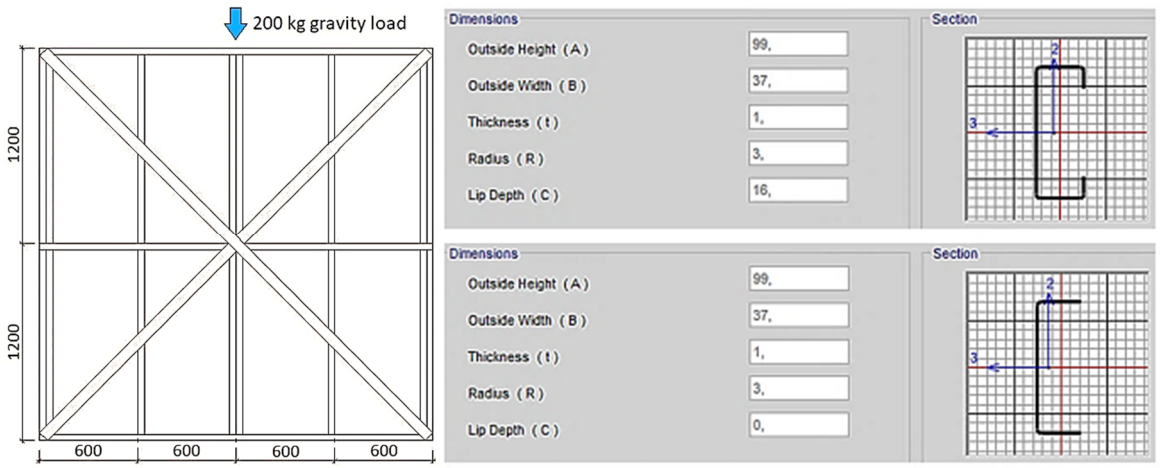

(a) (b)

Figure 3.3. (a) Specimen dimensions, and (b) stud/girder sections.

Dimensions of the specimens and the geometric properties of their studs and girders are outlined in Figure 3.3. It should also be noted here is that an additional 200 kg mass available at the lab (in the form of steel plates and other junk) was secured on the top girder of the specimen to act as gravity loading, which corresponds to approximately 80

kg/m uniform load. The panel is fixed at the bottom through stud anchors, and restrained against out-of-plane displacements at the top via fixing pins.

For measurement purposes there are 3 sensors and 5 strain gauges installed on the specimen: 2 sensors for reading the uplift in the outer studs, 1 sensor for reading the top panel displacement, 2 gauges for reading the strains at the bottom end of the outer studs, 2 gauges for reading the strains at the bottom end of the braces, and 1 gauge for reading the strains at the top end of the free-side brace (i.e. the upper brace opposite to the actuator). From the three loading protocols proposed by ASTM E2126-11, Test Method C (CUREE Basic Loading Protocol) was used (Figure 3.5).

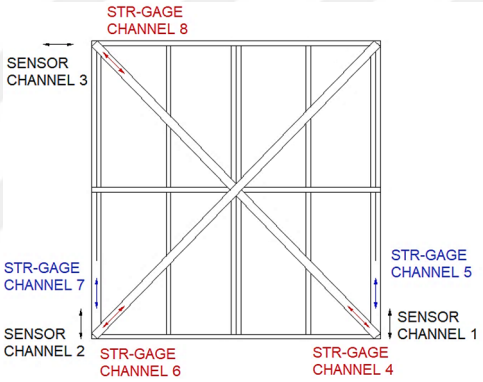

Figure 3.4. Sensor and strain gauge orientations.

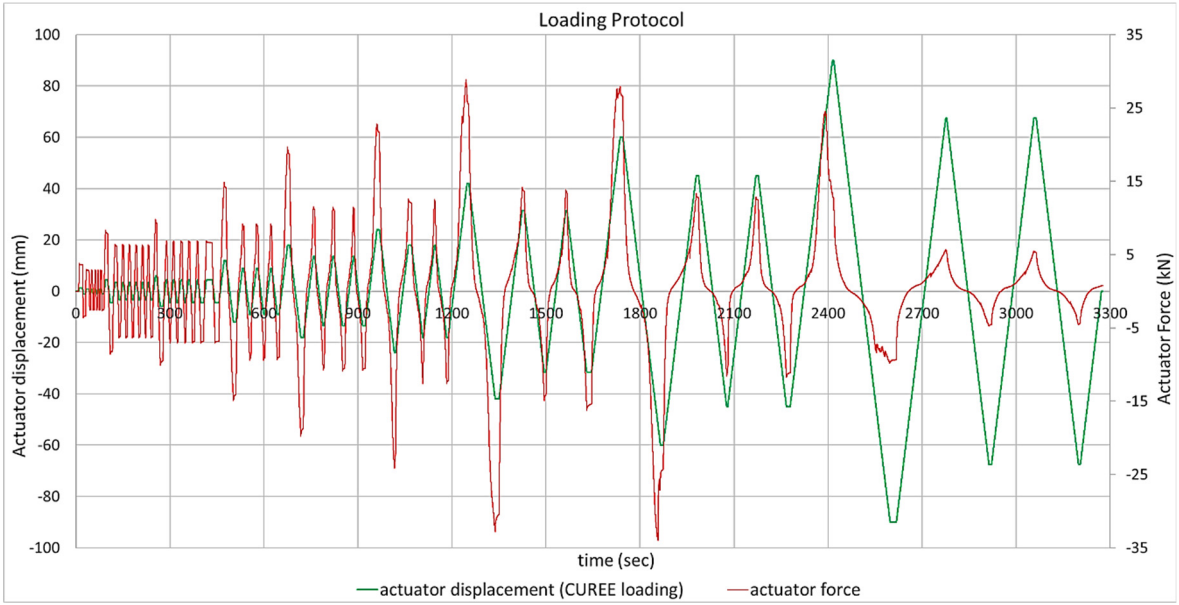

Figure 3.5. Test Method C: CUREE Basic Loading Protocol (applied actuator displacements).

3.2. Test Results for the Specimen with Gypsum Boards

A brief test progress could be depicted in such manner: by the time the specimen was pushed around 2 cm, noise of the displacing screws and other components could be easily heard. Around 4 cm displacements, visible cracking on the gypsum panel surface could be observed. When the displacements reached around 6 cm, huge noises were coming from within the specimen, hinting that some screws and/or other components broke. Also, visible slots (of varying breadth) began to occur on the gypsum panel surface where the screws were bolted. Finally, around 9 cm displacements, the said slots became so big that the gypsum was torn up and the screws detached from the panel (Figure 3.6).



(a) (b)

Figure 3.6. The local damage in (a) the upper portion, and (b) the lower portion of the panels.

Removing the gypsum panels revealed more damage on the inside of the specimen. The most notable one was that all the braces were separated from the frame at the upper joints. Apparently their 4-screw connection failed to keep the frame intact at those points (hence the 6 screws in the second experiment). Literature study of similar tests suggest that brace connections should be heavily reinforced with screws so that the failure only occurs in the form of ruptured braces. For these tests, it was not possible to reinforce the bracing strips further.

Other than that, the increased waviness of the braces was also noticeable, which hints to a severe (and repetitive) buckling mechanism taking place. The other visible damage on the frame elements are limited to local buckling at several points (Figure 3.7). More detailed images and numerical results from the experiment are provided in Appendix C.



(a)



(b)

Figure 3.7. The local damage in (a) general, and (b) specific parts on the CFS frame.

The graphical representation of the test and the specimen behavior can be summarized by the hysteresis curve given in Figure 3.8. Consider the positive values of displacement as actuator pushing the specimen, and the negative values as actuator pulling the specimen.

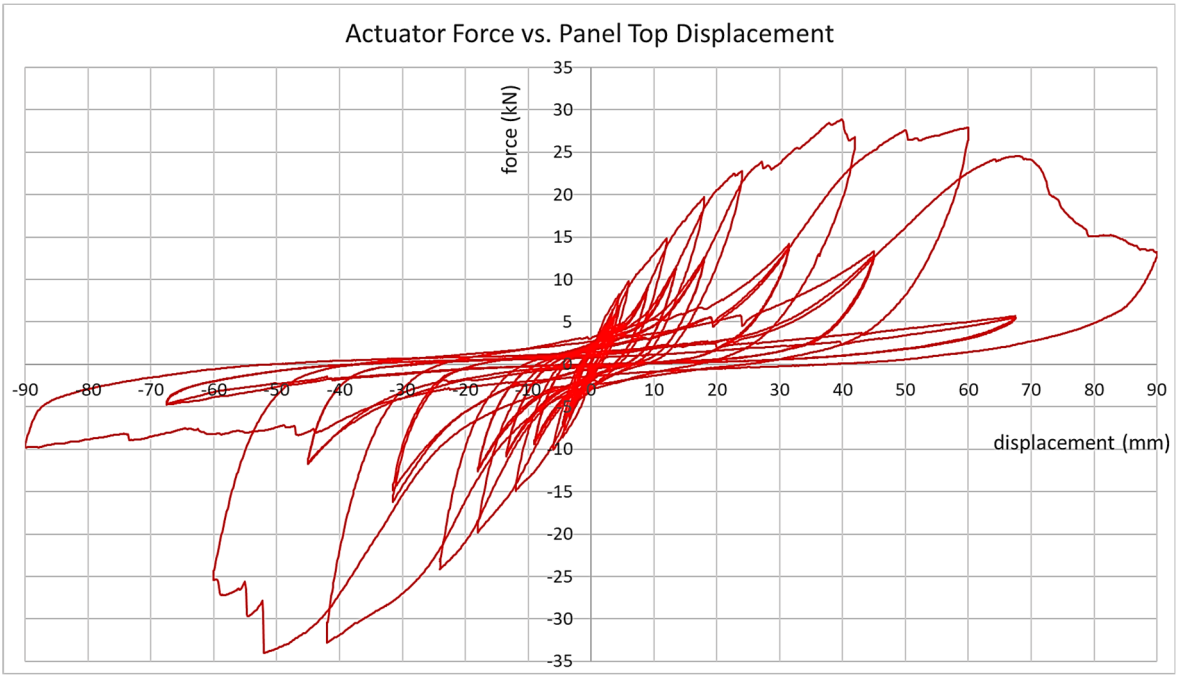

Figure 3.8. Hysteretic force-displacement curve of the test specimen.

It is interesting to examine some of the sensor and gauge readings (Figure 3.9). Consider the uplift of the studs for example (the blue colored sketch on the graph). As expected, the stud closer to the actuator deforms in line with the actuator moves: the stud moves upwards (positive deformations) when the actuator pushes the panel (positive displacements), and moves downwards when the panel is pulled back. The displacements of the stud on the opposite side are the other way around, again as expected: it moves downwards when the panel is pushed and moves upwards when pulled. This trend persists until at some stage uplift begins to pile up towards positive values, as if the sensor is stuck and can no longer read into negative displacements. An explanation for this may be that the bottom girder begins to bend from the mid-point (when pushed against the base) and interferes with stud deformations, preventing the stud to get back into equilibrium position. It also curious that after some certain limit, each stud seems to sustain compressive forces where it is expected to be the other way around (the green colored sketch on the graph).

This is possibly due to the stud being pressed against the top girder, which is fixed to a much stiffer upper base connected to the actuator (i.e. rigidly constrained at the top).



(a)

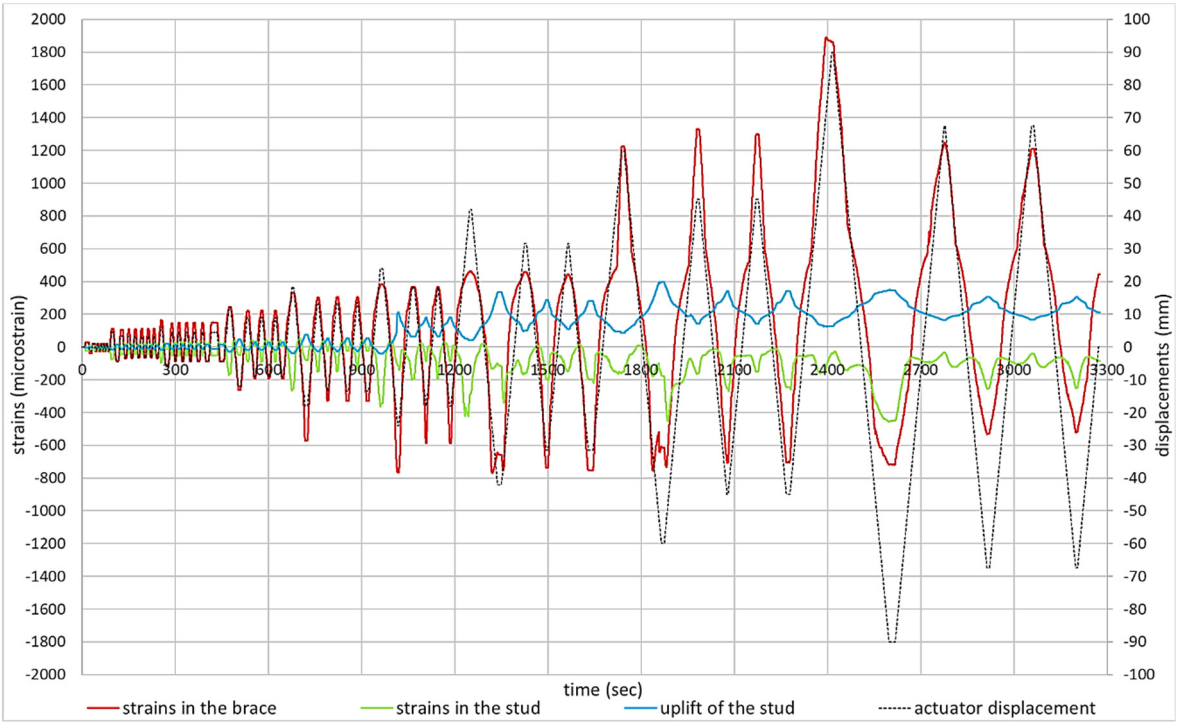

(b)

Figure 3.9. Time-history of the sensors and strain gauges (a) on the actuator side of the specimen, and (b) on the opposite (outer) side of the specimen.

Brace strains appear to be mostly in line with what is expected of them (the red colored sketch on the graph): they generally sustain tensile forces. However, here at some stage they tend to bear compressive strain levels of almost 30% of the tensile strains. It is possibly due to the opposite braces touching each other (inside the specimen) after buckling, and gaining some compressive capacity before they reach a higher order buckling state. This could be an interesting phenomenon to pursue.

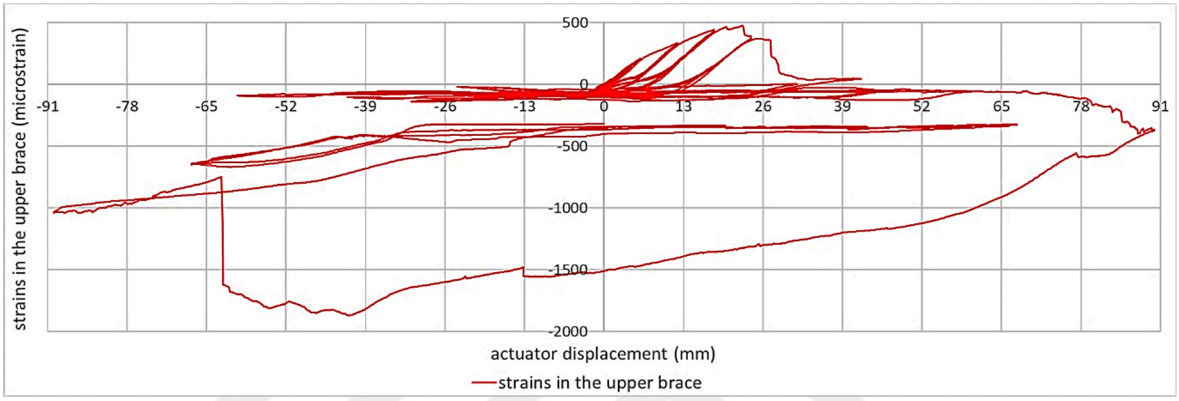

Figure 3.10. Time-history of the strain gauge attached to the upper brace.

Figure 3.10 illustrates the brace strains (in the only gauge used at the upper end) against actuator displacement. The sketch starts with expected behavior characteristics: positive increments in the strains correlated with positive actuator displacements. Then, at some stage around 40 mm displacement limit, it abruptly goes to zero: at this stage it is estimated that the brace connection fails. The weird-looking measurements recorded from then on are possibly just repercussions of the loose brace getting stuck somewhere inside the panel. More recorded data from the experiment are provided in Appendix C.

3.3. Analytic Verification for the Specimen with Gypsum Boards

As previously stated, the main purpose of these additional tests is to learn to calibrate any numerical model with the help of experimental results. Thus at this stage, a representative numerical model of the test specimen has been created. The model is intended to be as realistic as possible, and to display all mechanical characteristics of the specimen (including the constraints generated by the testing equipment). Figure 3.11 displays a visual of the analytical model with gravity loads applied and a graphical representation of the finite element model, respectively.

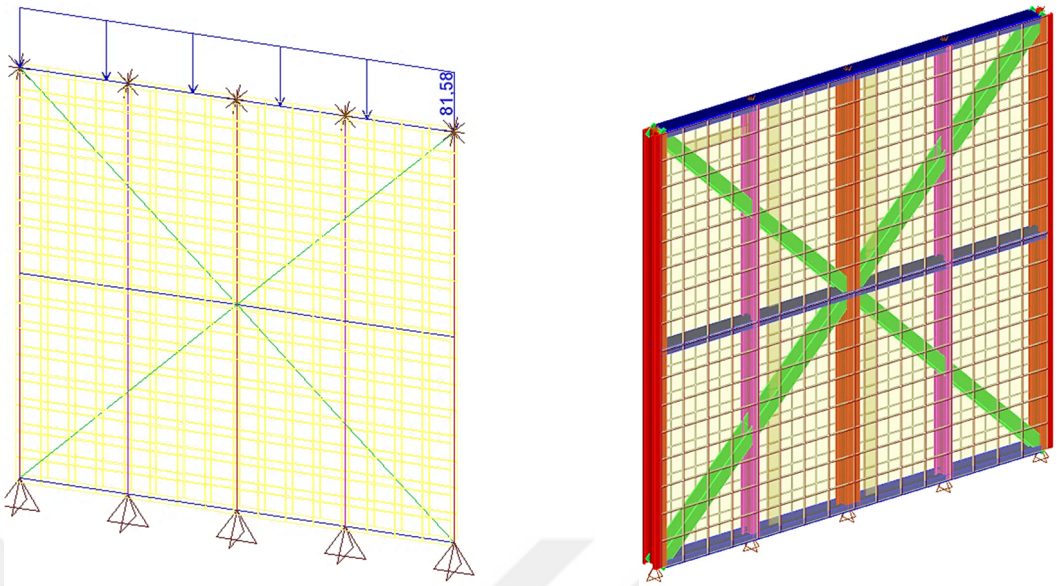

Figure 3.11. The graphical representation of the analytical model for the test specimen.

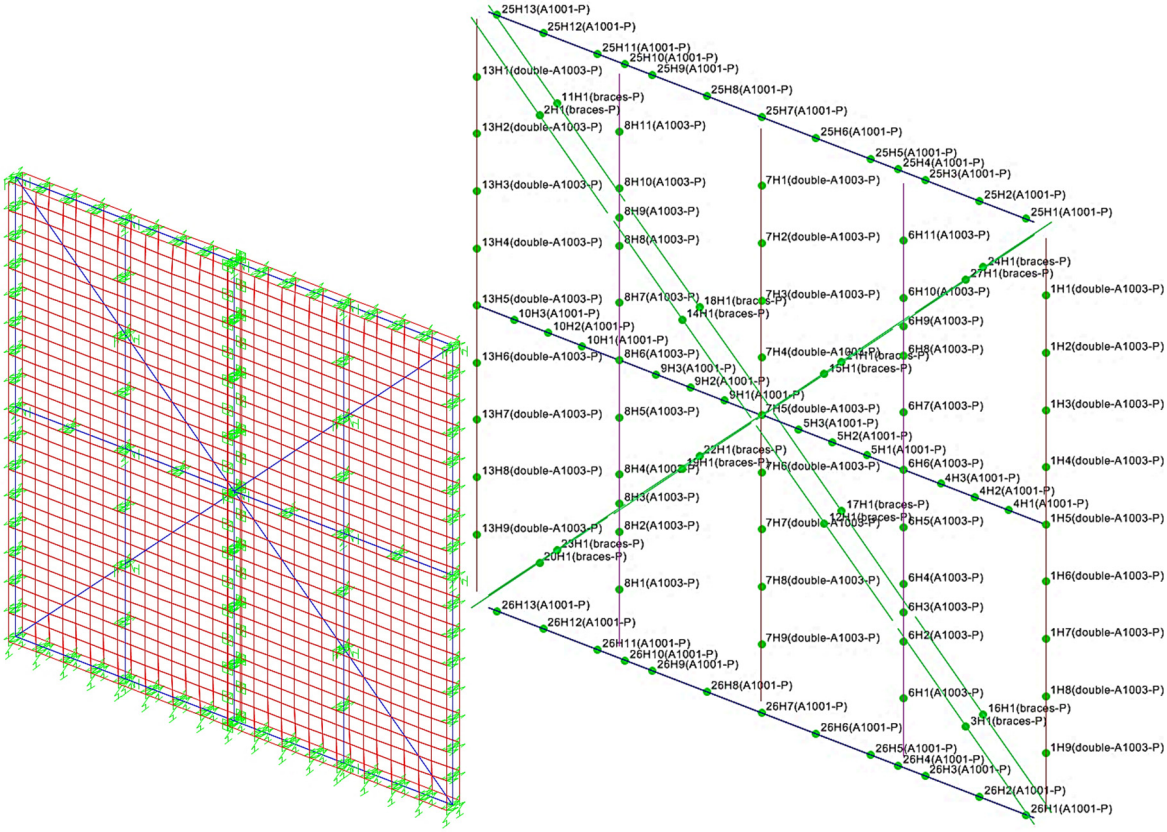

(a) (b)

Figure 3.12. A detailed representation of the analysis model with (a) link elements, and (b) plastic hinge assignments.

More detailed versions of the numerical model, including the link assignments of the connections and all plastic hinges assigned in the CFS elements, are illustrated in Figure 3.12. Analytical verification was again done by pushover analysis. The resultant pushover curve is then superimposed into the force-displacement curve of the test specimen, as provided in Figure 3.13. As can be observed, the results of the analytical evaluation do not match the experimental results. Some possible explanations can be outlined as follows:

- Mechanical properties of the gypsum panel are incorrect: assigned properties may be too rigid since the base shear capacity differs almost threefold.
- Assigned parameters for the links in between gypsum panel meshing are incorrect: the displayed model does not incorporate these, but an alternative model that includes additional links between each panel meshing is also created with the purpose of capturing the panel failure mechanisms. Yet the outcome was not satisfactory, so it was omitted here.
- Assigned parameters for the links between panel meshing and CFS frames are incorrect: this error is apparently the main cause of the difference between the dominant curve trends, the analytical model does not behave as intended.
- Assigned parameters for the links in between CFS frame elements are incorrect: this is probably of the least importance, compared to the other reasons.
- Difference between loading procedures: the loading procedure used in the test is a cyclic loading, whereas it is a multi-step static loading in the analytical evaluation. Again, this is presumed to be less effective on the results, compared to the others.

A few trials were made in the scope of a sensitivity analysis, in order to see how the force-displacement curve would be affected by changing some of the aspects listed above. Figure 3.13 also includes the results of the following cases when:

- the elasticity modulus of the gypsum panel was decreased tenfold,
- all the values of the force-displacement curve for the link elements between the frame and the gypsum panel were decreased by half and,
- these two modification methods were applied simultaneously.

As can be seen, none of these modifications helped improve the nonlinear response.

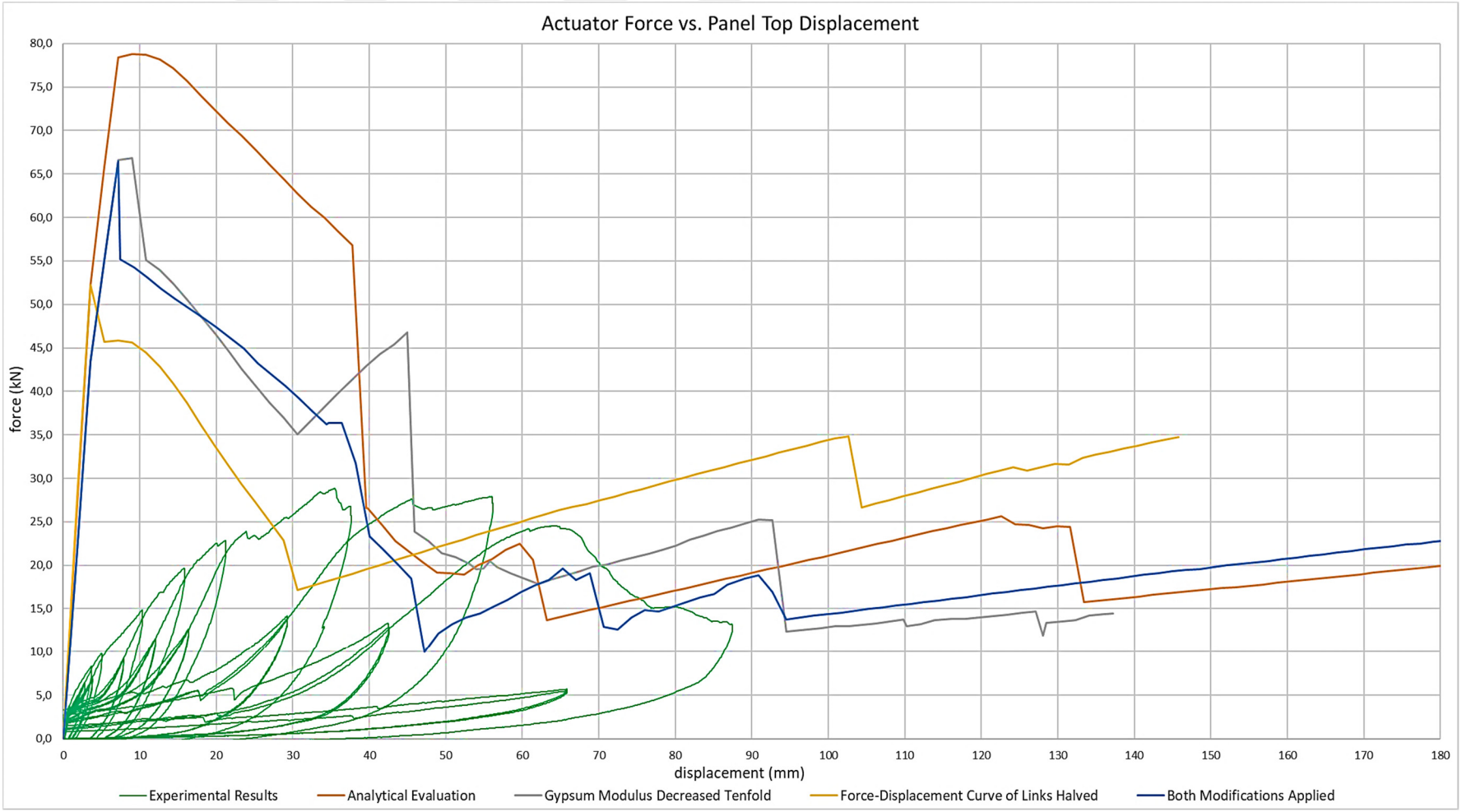

Figure 3.13. Sensitivity analysis for the numerical model of the test specimen.

3.3.1. Updated Definition for Brace-to-Frame Links

Further investigation hinted that the analytical representation of the braces was inaccurate. So at this stage, a thorough verification and re-calibration process was needed.

Previously the braces were defined as a single frame element consisting of two-piece steel strips, facing each other at a certain distance. They were then connected to the CFS frame via single-joint links at relevant intersections. Thus, it was very difficult (and impractical) to define the characteristics of the said single-joint links, which were expected to simulate the behavior of the conjoint connection, as well as simulating the breakage of the connection (which was observed during the experiment).

Therefore, as an alternative, the braces have been redefined as two separate frame elements, connected to the CFS frame via additional two-joint links. The modified link definitions and force-deformation characteristics for the brace connections are proposed in Figure 3.14.

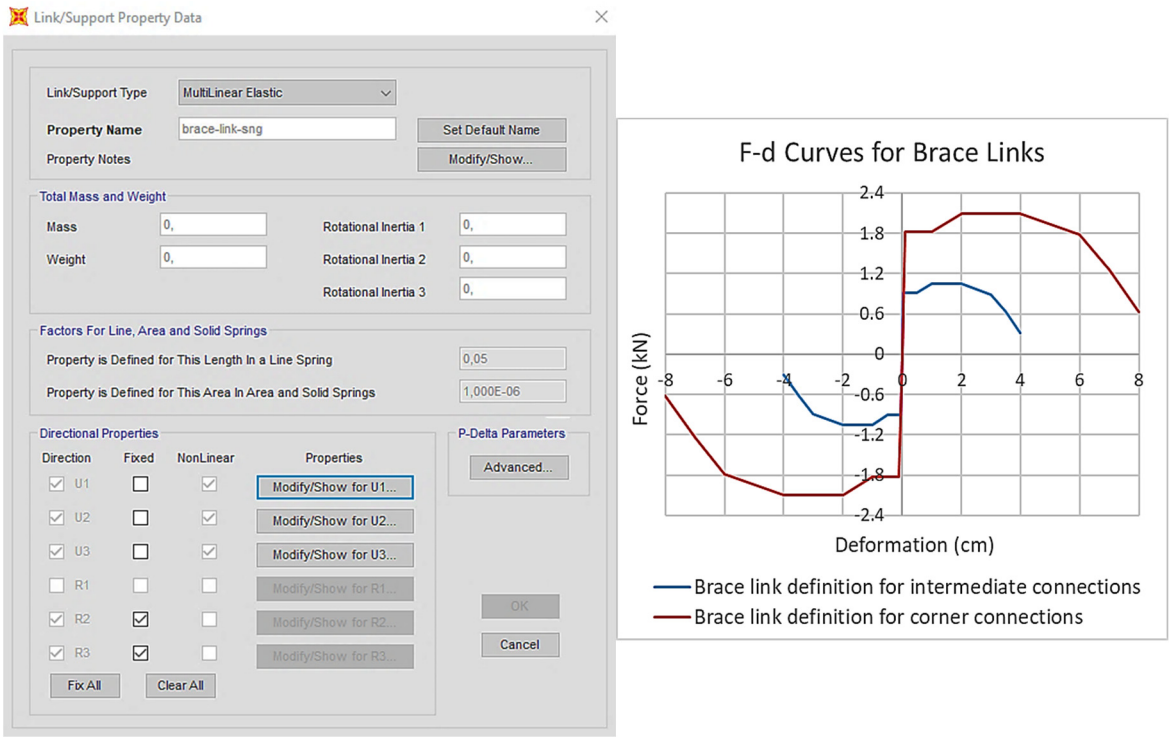

Figure 3.14. The proposed force-deformation curves for the brace connections.

3.3.2. Updated Definition for Plastic Hinges

At this point, it is useful to provide some information regarding the plastic hinge definitions and assignments in the analytical model. In studs for example, deformation controlled axial hinges are assigned along every one-tenth of the stud length. Similarly for girders, deformation controlled axial hinges are defined along every one-fifth, one-fourth, one-third or half length of the girder (depending on the girder length). And for braces, deformation controlled axial hinges are considered and assigned at the midspan of the braces, for which a small compression limit is defined to account for buckling.

The buckling loads for each type of member are calculated using either CUFSM, CUTWP or GBTUL, which are all specifically designed software for evaluating the buckling modes of CFS sections. Their respective results are compared and also verified through the Buckling Analysis Module available in SAP2000. Then the lowest value is assigned as the buckling load of the member to be on the safe side. Figures 3.15 – 3.18 illustrate a representative buckling mode evaluation for the stud members, computed by GBTUL 2.06 software as an example. It is presented here for having a sophisticated, yet simple and easy-to-follow user interface.

In general, both the generalized beam theory (GBT) and the constrained finite strip method (cFSM) lead to very similar solutions. Their main difference is that GBT is a generalization of *classical beam theories* that includes additional degrees of freedom to allow for cross-section deformation, and that cFSM is a specialization of the *classical plate theory* which selects constraints in order to force the member to deform in accordance with pre-defined configurations. Adany *et al*. [28] performed an in-depth comparison between the fundamentals of these approaches. They provided numerical examples to show the effectiveness of both methods in separating general stability problems into pure solutions related to the buckling mode types, and demonstrated that these two distinct methods essentially delivered the same extended capabilities for examining and understanding thin-walled member stability. Nonetheless, there are minor, yet fully explainable discrepancies between the results yielded by these methods. Presentation of GBTUL here is only a matter of personal preference, derived from the simple usage of the software.

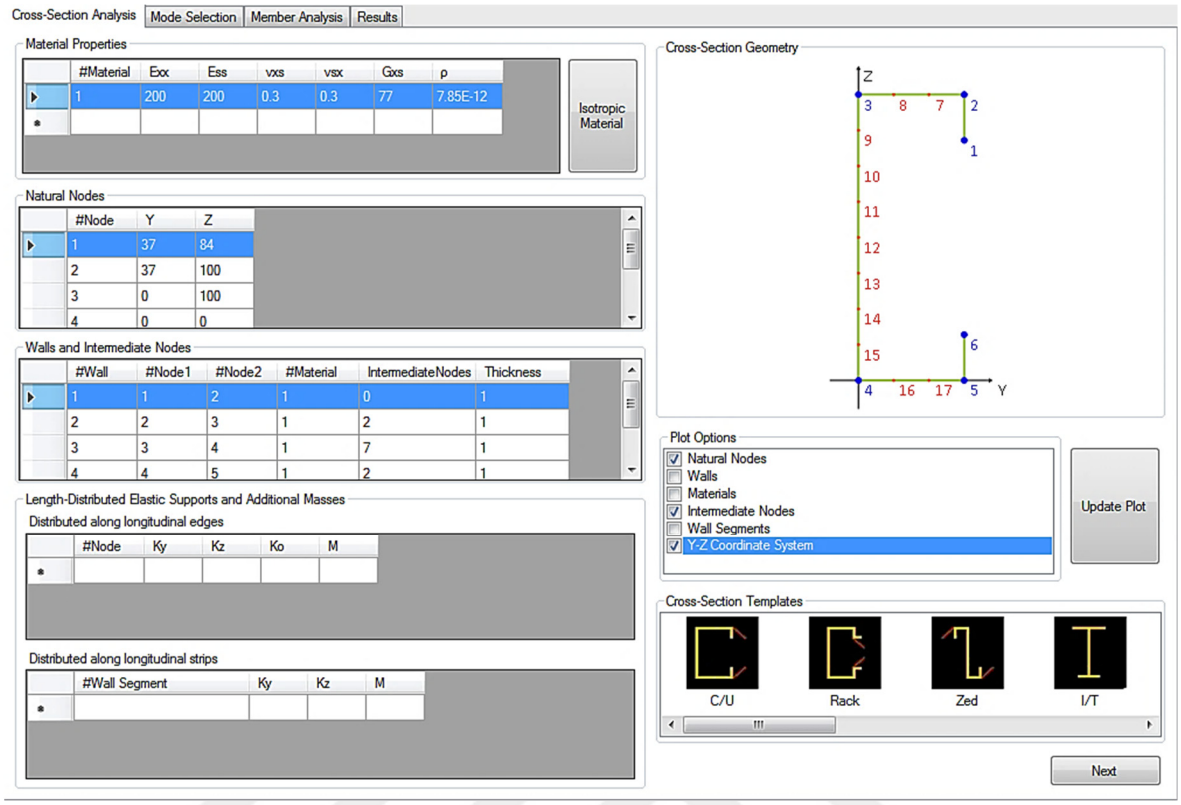

Figure 3.15. Cross-section definition in GBTUL software.

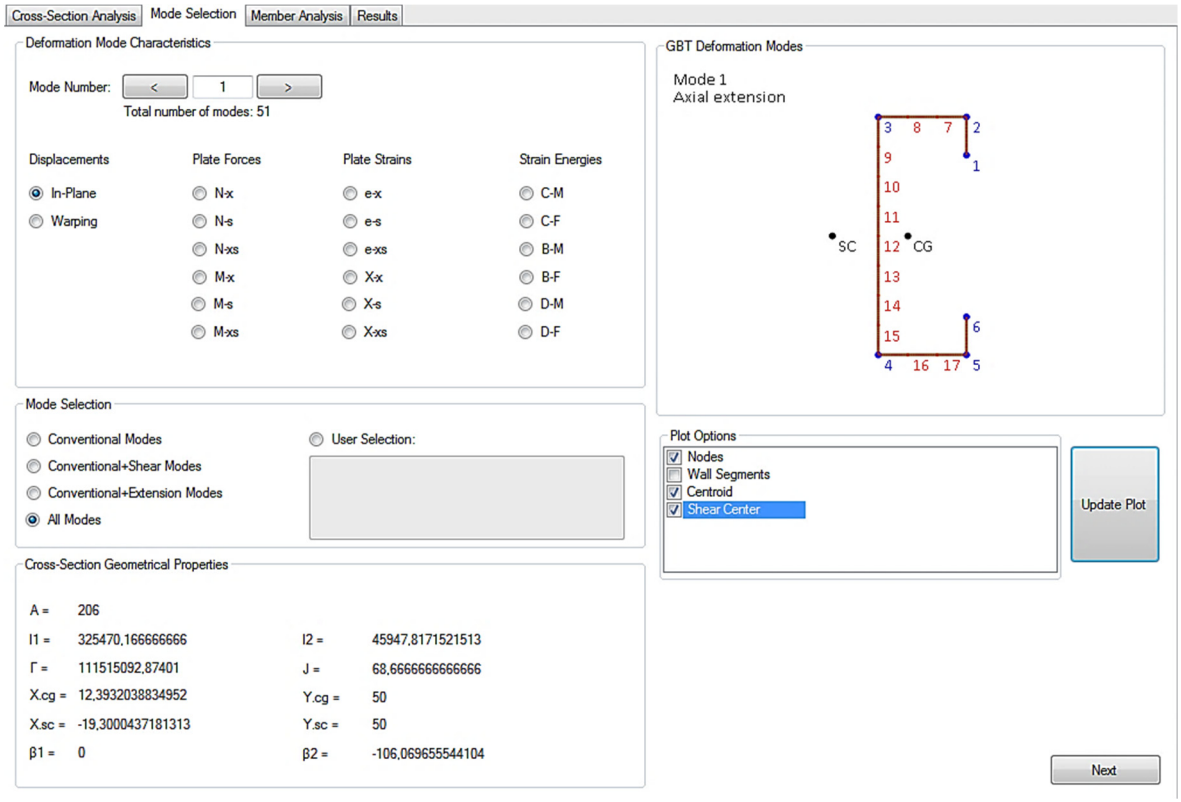

Figure 3.16. Selection of the available buckling mode types in GBTUL software.

The primary units used in the software are ‘kN’ for force quantities and ‘mm’ for dimensional quantities. There are a wide range of section templates the user can choose from when defining section properties (Figure 3.15). Depending on the specified number of intermediate nodes, GBTUL automatically calculates the available mode shapes, which the user can choose to include or ignore in the stability computations (Figure 3.16).

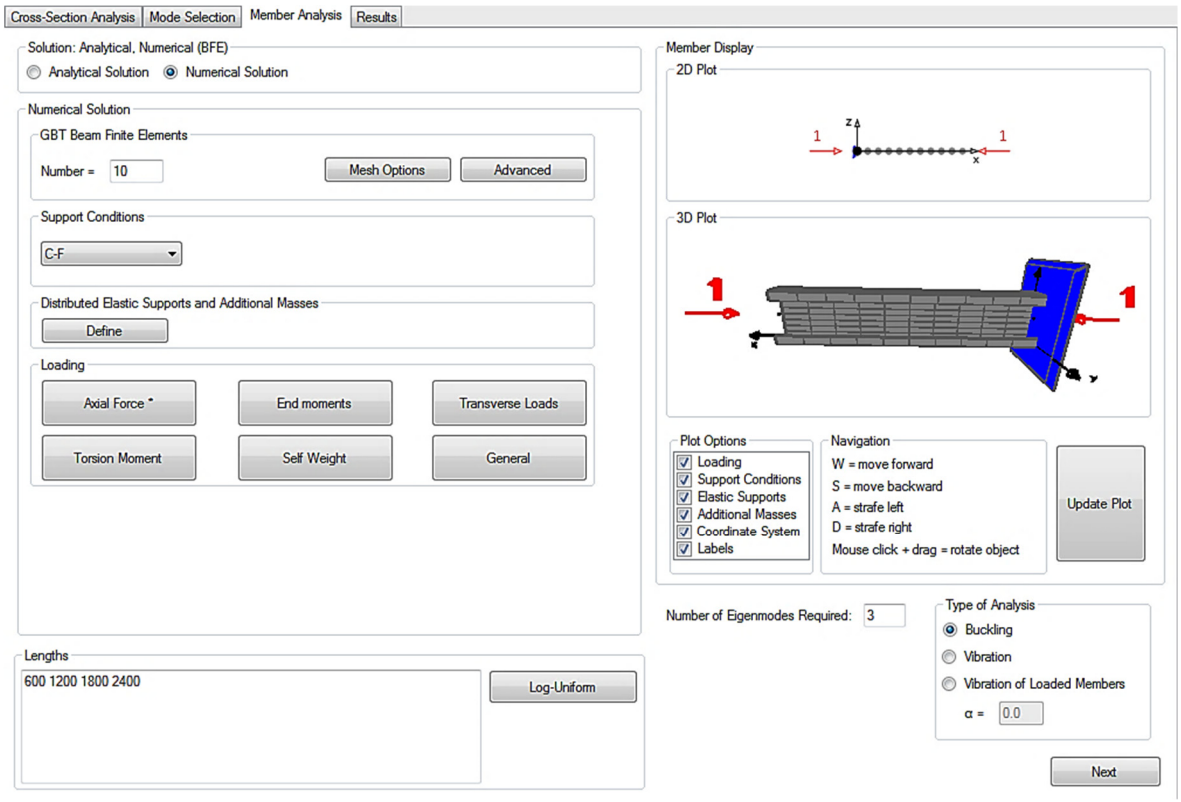

Figure 3.17. The definition of the other analysis parameters: solution type, support conditions, loading, member length etc.

For most purposes, it is advisable to use the numerical solution method (Figure 3.17) since it offers a broad practicality with regards to support conditions and external loads alike, whereas the analytical solution only considers simply supported frames (a typical Eigenvalue problem). The analysis results can be reviewed through different member lengths and Eigenmodes, by picking the suitable values for the design conditions. The buckling load is calculated as a factor of the specified axial load. In this example it is approximately 11, which means that the buckling load limit of the given stud member is about 11.0 kN (Figure 3.18).

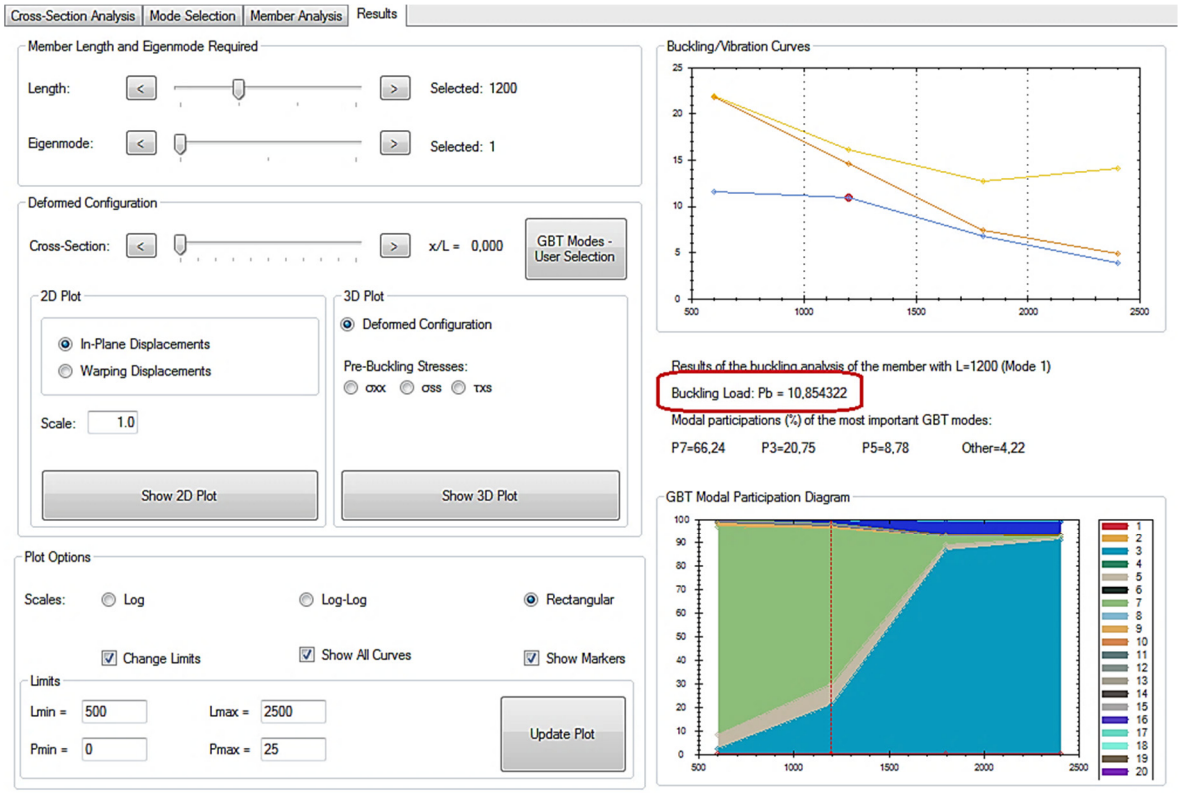

Figure 3.18. Analysis results page of GBTUL software.

During buckling mode calculations, braces are assumed to be clamped at both ends, considering that adjacent portions of the brace would both have to buckle towards the inside of a shear wall, and the rotations where they are fixed to the frame would then be practically zero. Studs are assumed to be free at one end and clamped at the other. Also only half-length of the member is considered since it was observed during laboratory tests (Chapter 3) that specimens showed almost no deformations around the mid-height of the studs, hence the clamped-end assumption. Girders are again assumed to be free at one end and clamped at the other. Member length is taken as the unrestrained distance between each stud, which is approximately 600 – 610 mm.

Through similar calculations, the buckling load limits are finalized as 11.0 kN for studs, 6.0 kN for girders, and 0.22 kN for braces. Then these load values are converted to (negative) stresses in order to define a stress-strain relationship for plastic hinges. Positive stress limit is taken as the yield stress, and the corresponding strain limit is obtained by simply dividing the yield stress by the elasticity modulus of steel. Negative (yield) strain limit is calculated by proportioning to the positive values. Effective area calculation is

neglected for the sake of simplicity. Figure 3.19 provides a sample hinge definition for studs. The negative threshold value here corresponds to the stress level at the calculated buckling load limit of the stud member. It is assumed that the section almost completely loses its load carrying capacity with the slightest (compressive) deformation. It is then verified that the deformed shape of the analytical model is compatible with that of the test specimen, i.e. it is checked whether the same failures (plastic hinges) occur at the same locations of the experimental and analytical models.

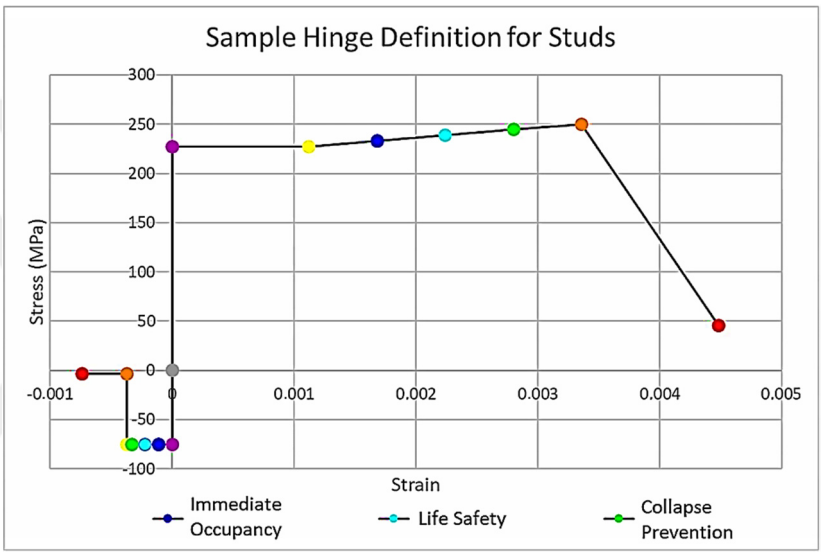

Figure 3.19. A sample stress-strain relationship defined for stud members.

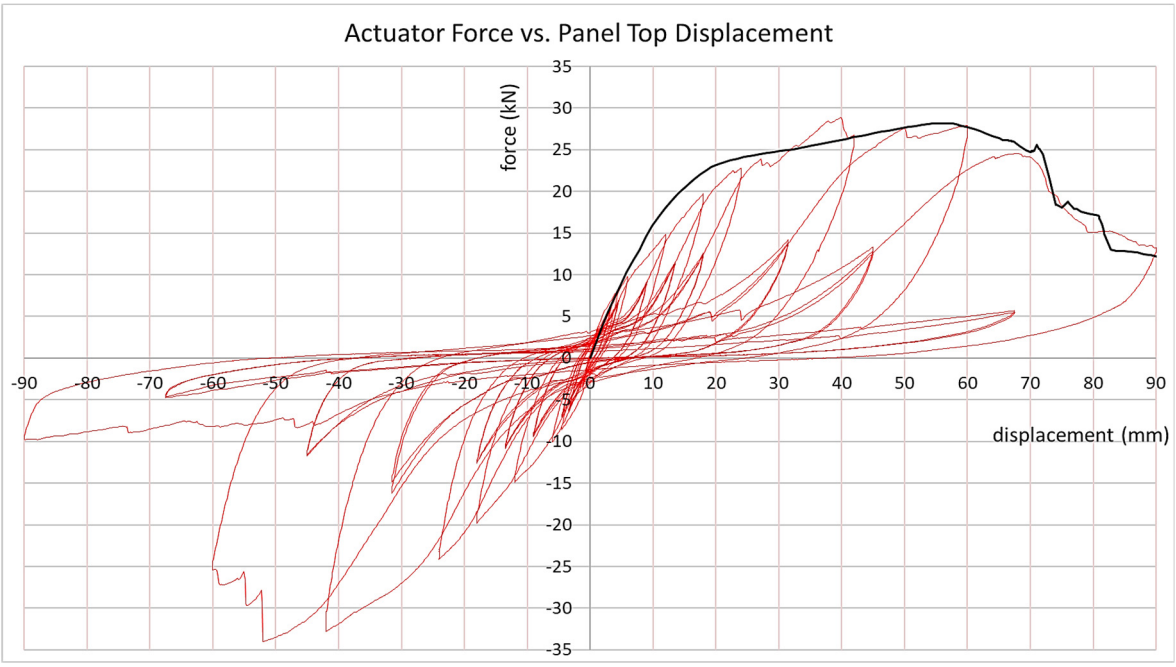

Figure 3.20. Resultant pushover curve compared with the experimental data.

By using the proposed *F-d* curve given in Figure 3.14 and incorporating the knowledge from relevant literature, after lots of trial-and-errors the analytical (pushover) response of the specimen has been obtained as close to the experimental results as possible (the best approximation so far – Figure 3.20). It is important to note that these modified link properties are the finalized versions adapted to the performance assessment studies of the Enez building (see Chapter 5).

3.4. Test Results for the Specimen with OSB Boards

In order to validate the results of the previous experiment and the subsequent analytical studies, conducting a second experiment would have been helpful. Thus, a new experiment incorporating OSB panels was conducted. As can be seen from the resulting hysteresis curves, the OSB panels already appear to be stronger by almost 50% than their GWB counterparts (Figure 3.21).

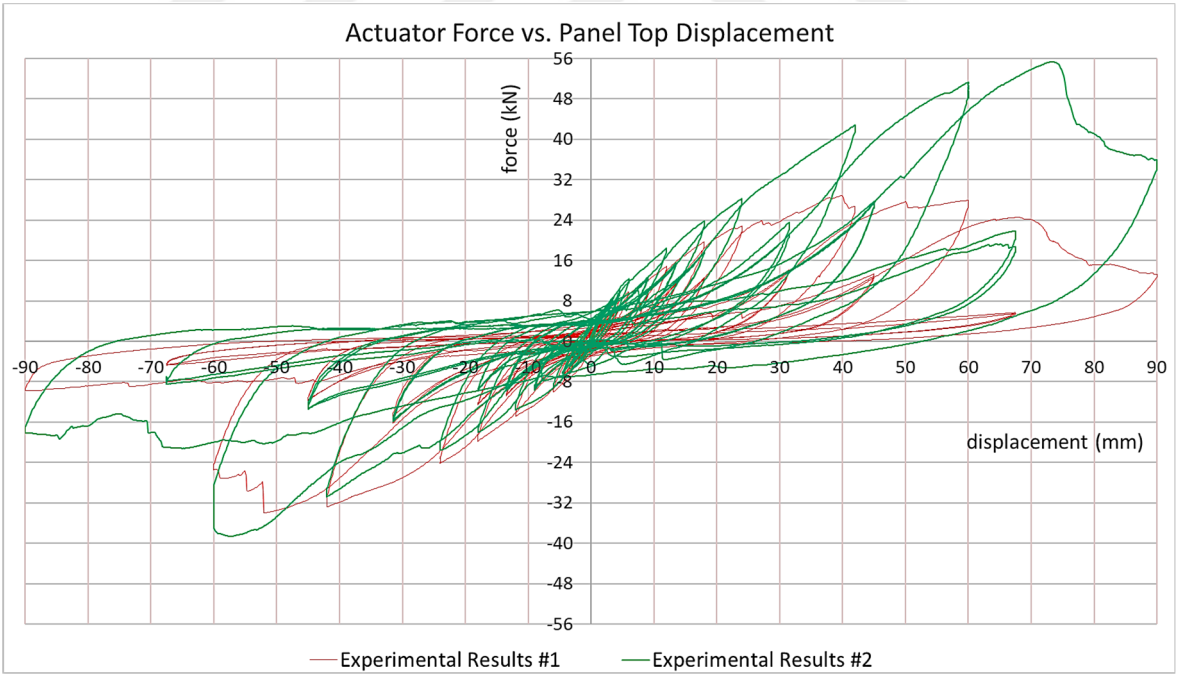

Figure 3.21. Superimposed hysteresis curves for both experiments.

Damage to the specimen is observed to be concentrated more on the CFS braced-frame. Upper corners of the OSB panels begin to fail and rupture at around 4 – 6 cm displacement (exterior damage – Figure 3.22). From then on, applied load is progressively transferred to the frame elements.



Figure 3.22. The local damage in OSB panels.

Brace connections consist of 6 screws each for this experiment (whereas it was 4 screws previously), and this detailing proves to be effective on the structural behavior. As can be followed from the post-experiment images below, all brace connections remain intact and the interior damage is heavily concentrated on the upper girder and surrounding components.



Figure 3.23. General view of the local damage in CFS frame elements.

Close-up photos to the proximity of the upper girder reveal that damage has occurred in various forms of local buckling, local tearing, breaking and even splitting of the back-to-back studs (Figures 3.23 – 3.25). Figure 3.26 shows a tiny piece of steel that was break-thrown from inside the specimen during the later stages of the experiment.

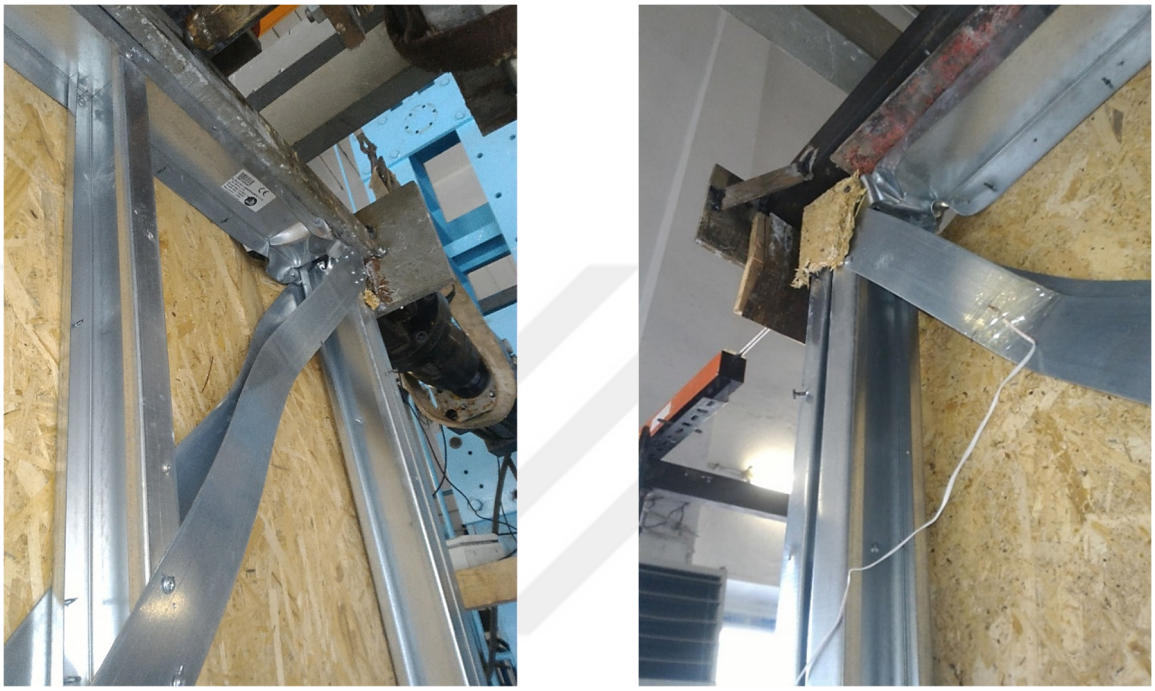

Figure 3.24. The local damage in the upper girder and the nearby braces.



Figure 3.25. The local damage in the middle portion of the upper girder.



Figure 3.26. A broken piece of steel, most probably from the heavily damaged mid-point of the upper girder.

Having completed the test at the prescribed displacement limit, and without any unlooked-for failures, the resulting time-history records are as expected. There are no obstrusive undulations and/or kinks, which were the case in the first experiment with the gypsum board panels. Figure 3.27 illustrates some of the recorded data during the test. More data from the experiment is available in Appendix D.

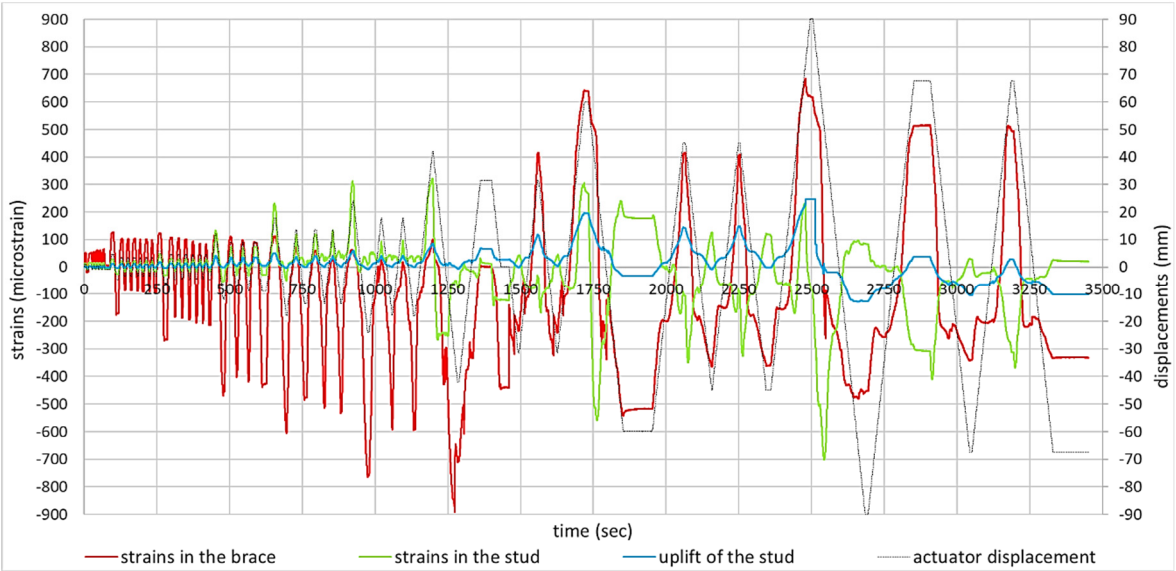

(a)

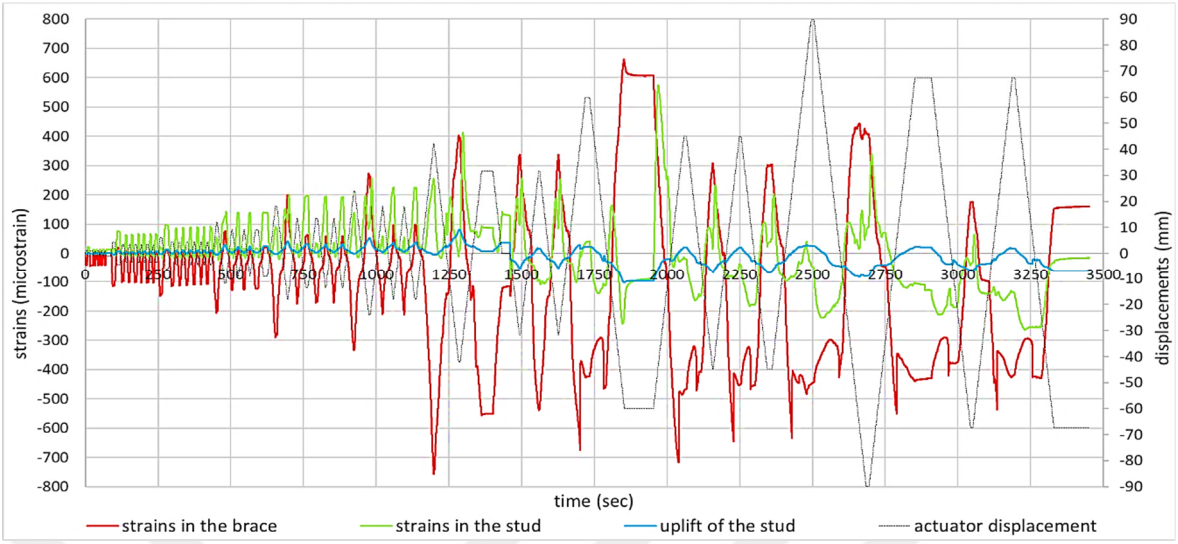

(b)

Figure 3.27. Time-history of the sensors and strain gauges (a) on the actuator side of the specimen, and (b) on the opposite (outer) side of the specimen.

3.5. Analytic Verification for the Specimen with OSB Boards

Again, an analytical model for the OSB-sheathed specimen is prepared and verified against the test observations. For brace-to-frame connections, the proposed force-deformation curves (Figure 3.14) are utilized, and are only altered slightly if needed. After further tryouts and comparisons, finalized pushover curves are illustrated in Figure 3.28.

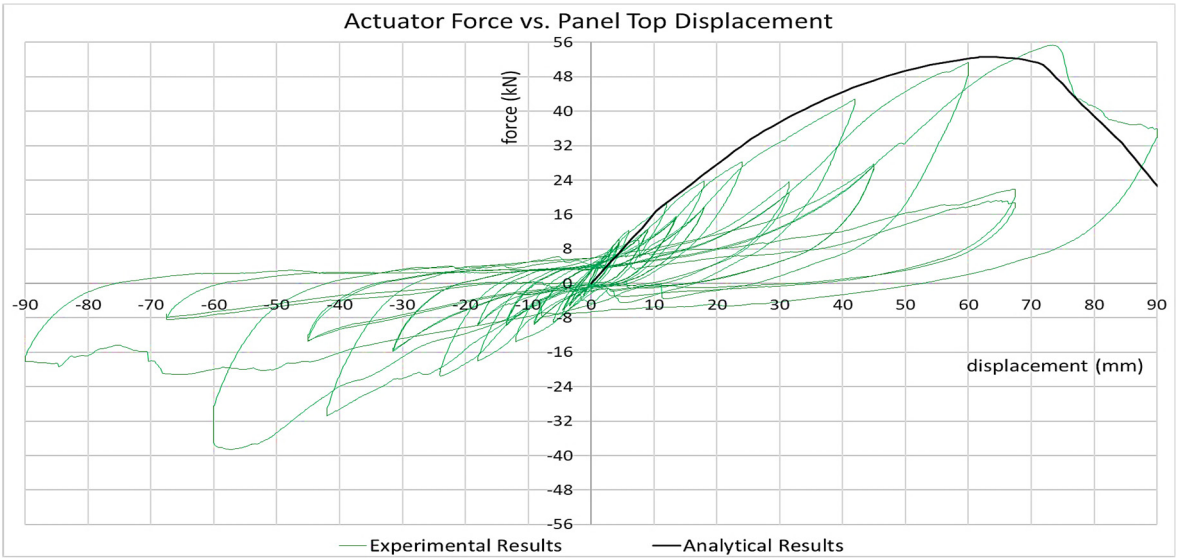

Figure 3.28. Resultant pushover curve tryouts for the modified model of the specimen, compared with the experimental data.

4. PERFORMANCE ASSESSMENT OF THE FINALIZED FE MODEL

4.1. Introduction

In line with the assumptions and revisions made during experimental analyses, all braces in the analytical model of the Enez building have been similarly redefined as two separate frame elements, connected to the CFS frame via additional two-joint links. Force-displacement behavior of the said links has been demonstrated in Figure 3.15 of Chapter 3.

The first thing to check after these modifications is the structural vibration periods. As can be observed in Table 4.1, the structural modes remain unchanged. It is known that the structure will stiffen, and the natural vibration periods will decrease when doors and windows are included, as shown previously in Chapter 2.

Table 4.1. Modal periods after updating the link properties of the brace connections.

COMPARISON OF NATURAL VIBRATION MODES	1st Natural Vibration Mode	Dir.	Modal Participating Mass Ratio	2nd Natural Vibration Mode	Dir.	Modal Participating Mass Ratio	3rd Natural Vibration Mode	Dir.	Modal Participating Mass Ratio
EXPERIMENTAL RESULTS	0.115 sec	X	-	0.107 sec	Y	-	0.08 sec	X/Y	-
ANALYTICAL RESULTS									
W/O LINKS - RIGID CONNECTIONS	0.072 sec	X	% 44	0.06 sec	Y	% 66.6	0.043 sec	X	% 20
W/LINKS (ELASTIC STIFFNESS), NO DOORS/WINDOWS	0.13 sec	X	% 37.7	0.117 sec	Y	% 32.3	0.079 sec	Y	% 27.5
W/LINKS (ELASTIC STIFFNESS), EXT.DOORS&WINDOWS	0.116 sec	X	% 36.5	0.115 sec	Y	% 39.9	0.074 sec	Y	% 19.2
W/LINKS (UPDATED STIFFNESS), EXT.DOORS&WINDOWS	0.121 sec	X	% 75.2	0.114 sec	Y	% 82.7	0.094 sec	X	% 8.7
W/LINKS (UPDATED BRACE LINKS), NO DOORS&WINDOWS	0.12 sec	Y	% 43	0.117 sec	X	% 54.1	0.099 sec	Y	% 32.9

4.2. Performance-Based Analyses: Introduction

Regarding the pushover analyses, hinge definitions and assignments have also been modified. In studs for example, deformation controlled axial hinges are assigned along every one-tenth of the stud length.

Similarly for girders around the door and window openings, deformation controlled axial hinges are defined along every one-fifth, one-fourth, one-third or half length of the girder (depending on the total girder length). After thoroughly examining the initial (pushover) analysis results, and observing that some of the upper girders of the first floor walls experience high compressive forces at the later stages of the analysis, it is acknowledged that these members, too, might be undergoing some significant nonlinear deformations. Thus, additional hinge definitions are made for girders at story levels in a similar manner. Formation of any shear-induced plastic hinges are ignored since there is no evident and reliable data in recent literature regarding this concept.

For braces, deformation controlled axial hinges are considered and assigned at the midspan of the braces, for which a small compression limit is defined to account for buckling. Hinges in all elements at rooftop level are also ignored.

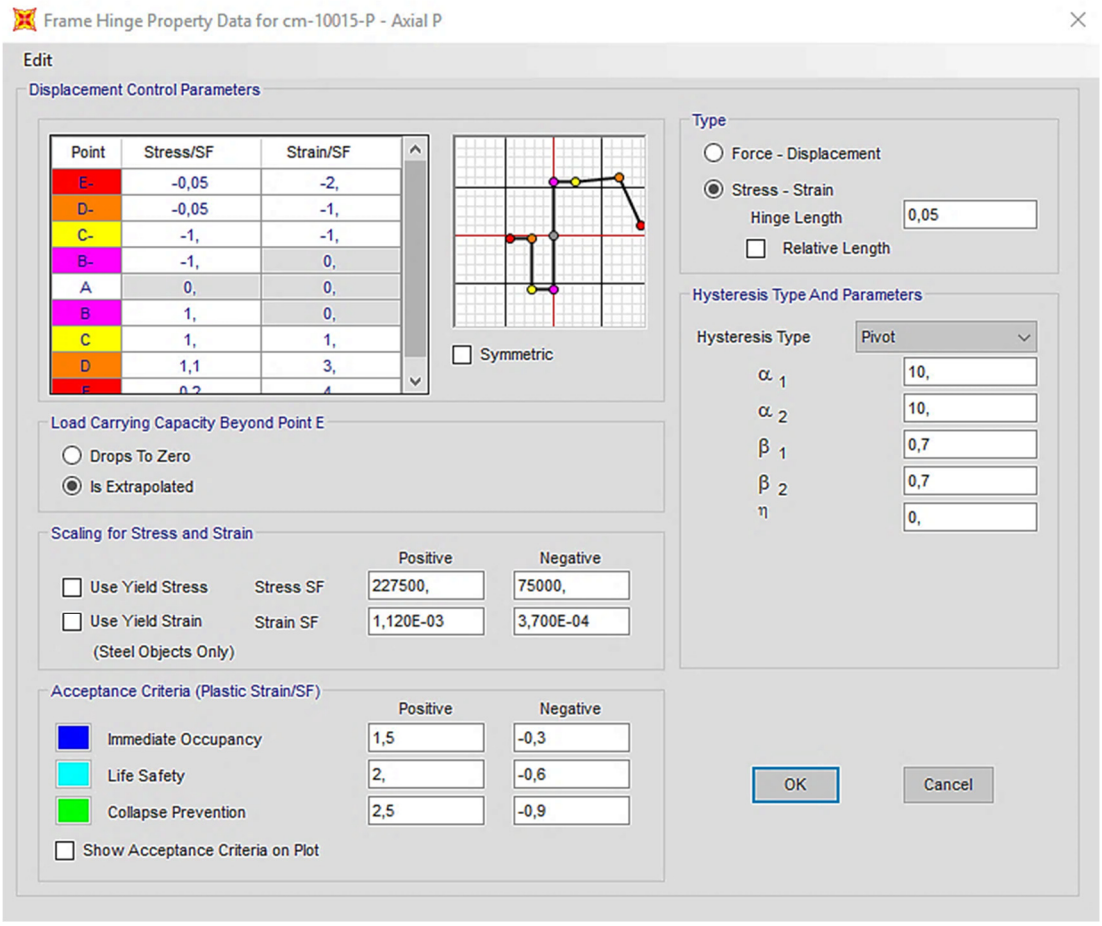

Figure 4.1. Sample hinge definition for studs.

A sample definition for stud hinges is given in Figure 4.1. As can be noticed, the value of applicable compressive stress immediately drops to 5% of the assumed buckling stress level, just after the yield strain is attained (point C & D). A typical stress-strain relationship is utilized to define controlling parameters, which is only a personal preference with regards to the simplicity of the calculations. Hinge length is taken as approximately the half-depth of the section.

Positive stress limit is taken as the yield stress, and the corresponding strain limit is obtained by simply dividing the yield stress by the modulus of elasticity (of steel). Negative stress and strain limits are calculated using the software CUFSM, CUTWP and GBTUL, which are all specifically designed for evaluating the buckling modes of CFS sections. Then the lowest value is assigned as the buckling load of the member to be on the safe side, and divided by the cross-section area to obtain the relevant stress values. The corresponding (negative) strain limit is calculated by proportioning to the positive values. Effective area calculation is neglected for the sake of simplicity.

During buckling mode calculations, braces are assumed to be clamped at both ends, considering that adjacent portions of the brace would both have to buckle towards the inside of a shear wall, and the rotations where they are fixed to the frame would then be practically zero. Studs are assumed to be free at one end and clamped at the other. Also only half-length of the member is considered since it was observed during laboratory tests (Chapter 3) that specimens showed almost no deformations around the mid-height of the studs, hence the clamped-end assumption. Girders are again assumed to be free at one end and clamped at the other. Member length is taken as the unrestrained distance between each stud, which is approximately 600 – 610 mm.

Post-buckling response of the elements (if there could be any) is neglected, since their reliability is not verified for this specific model and/or requires extensive and time-consuming research. Instead, plastic hinges in compressive members are defined such that their load carrying capacity is diminished as soon as the buckling load limit is reached. A detailed interpretation for the post-buckling option is provided in Chapter 4.4, and it is eventually concluded that post-buckling need not be taken into consideration.

4.3. Performance-Based Analyses: Results

The resultant pushover curves are illustrated in Figures 4.2 and 4.3. There is a notable kink at the beginning of each curve, corresponding to the majority of the braces buckling at the initial stages of the analysis, which will be covered in detail in the following chapters. It is also worth mentioning that pushover curves are only plotted up to the point where the analysis results are found to be reliable.

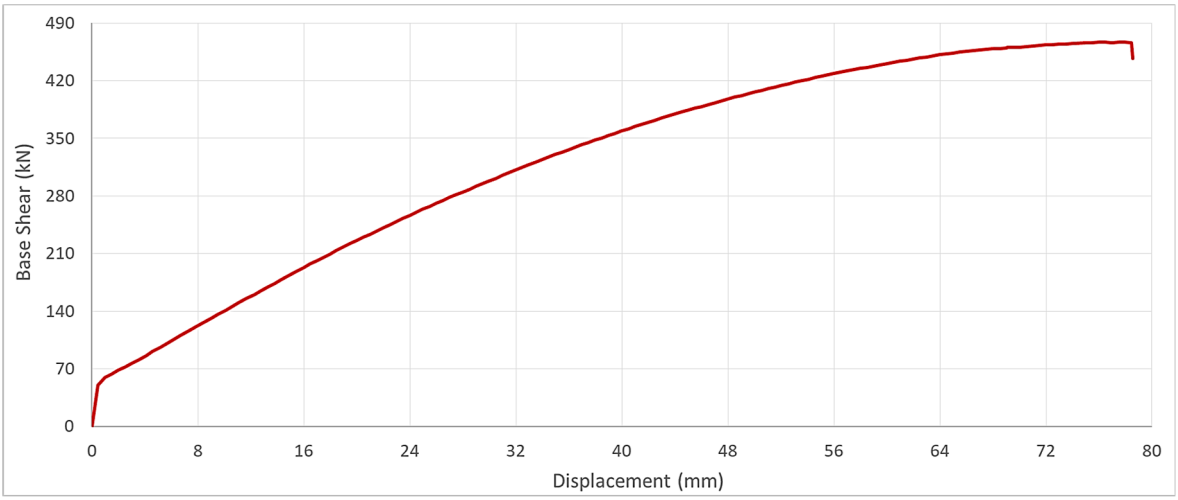

Figure 4.2. The resultant pushover curve in X-direction.

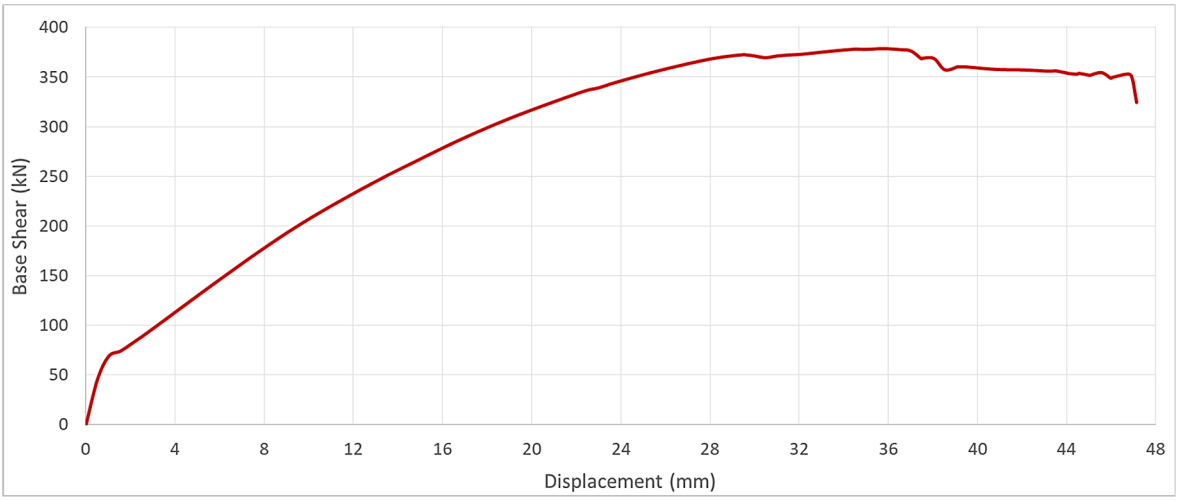

Figure 4.3. The resultant pushover curve in Y-direction.

A general representation for the resultant deformed shape of the building after the pushover analysis in X-direction is given in Figure 4.4. Note the damage concentration in

the structural elements around the stairs and back doors. There is also a slight damage propagation around the first floor windows. Likewise, a general representation for the resultant deformed shape of the building after the pushover analysis in Y-direction is provided in Figure 4.5. This time, the damage appears to be concentrated in the structural elements on the central walls and around the first floor windows.

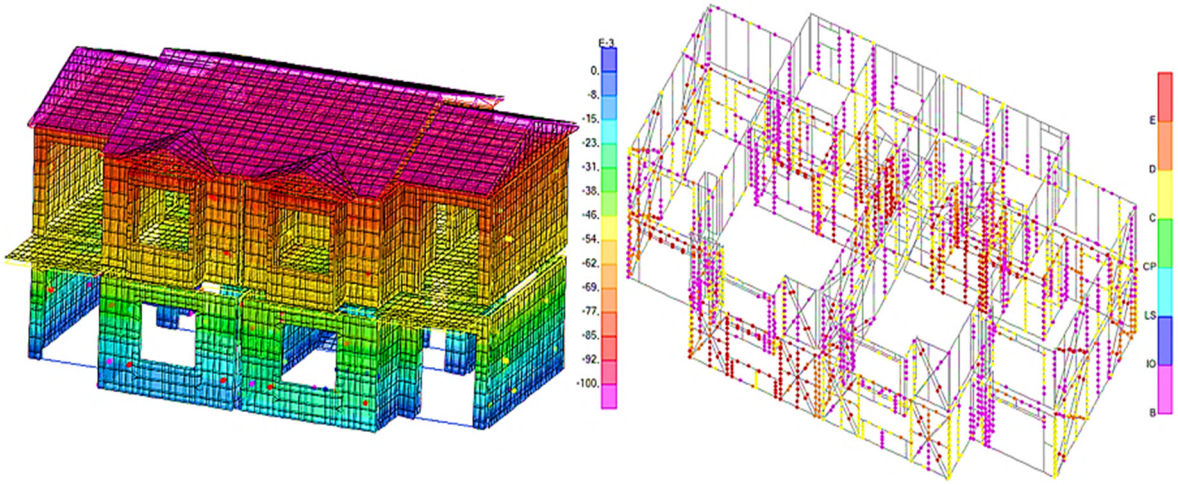

Figure 4.4. Deformed shape after pushover analysis in X-direction.

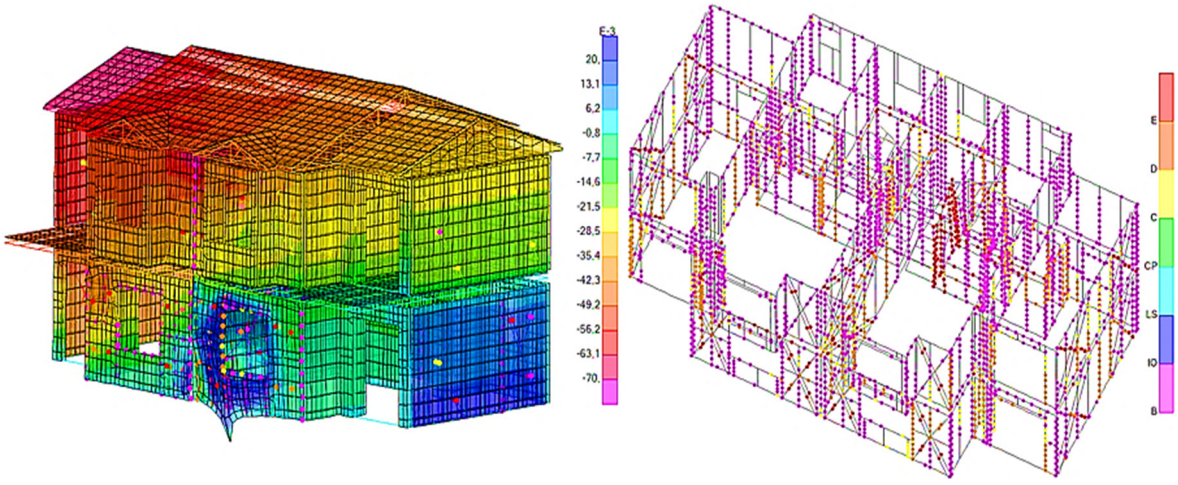

Figure 4.5. Deformed shape after pushover analysis in Y-direction.

It may also be interesting to observe the damage progress through the structure. Important events during the pushover analysis in Y-direction are outlined here as an example. It is observed that, in as early as the fourth step of the analysis (where the structural sway is just about 1.5 mm) almost half of the first floor braces are already past their buckling load limit. And when the sway is about 11 mm, some of the upper floor

braces (again half of them, to be precise) join them. The first hinge in a stud is visible at a structural sway of about 13 mm (Figure 4.6). According to the pushover analysis results in Y-direction of the building, it can be said that failure progression generally takes place in the braces and the staircase studs.

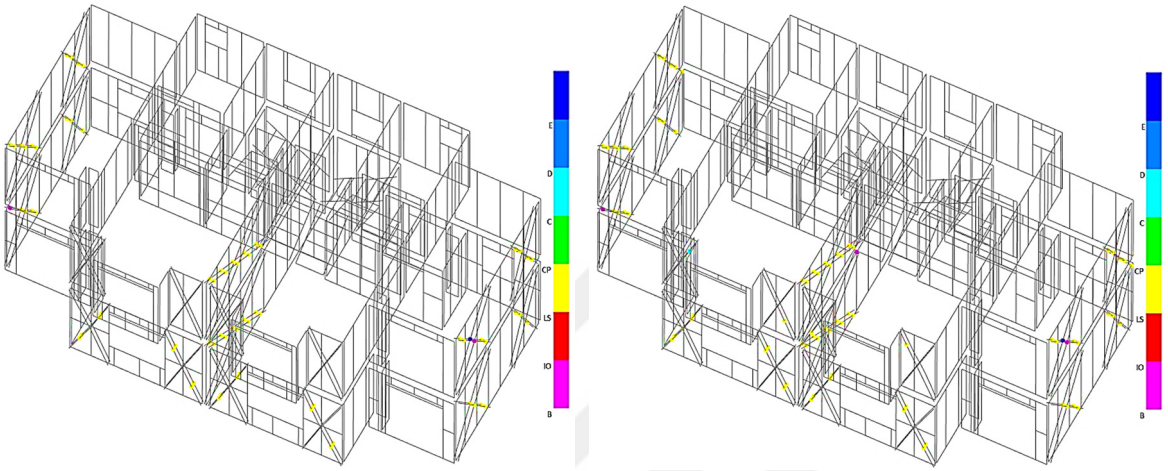

Figure 4.6. Representative hinge progression at analysis steps 23 and 27, respectively.

After the structural sway levels reach about 45 mm and onwards, progression of failing elements around the stairs begin to escalate quickly, before the structure attains an ultimate deformation level of about 52 mm. More detailed information regarding the hinge progress within the structure is provided in Appendix E.

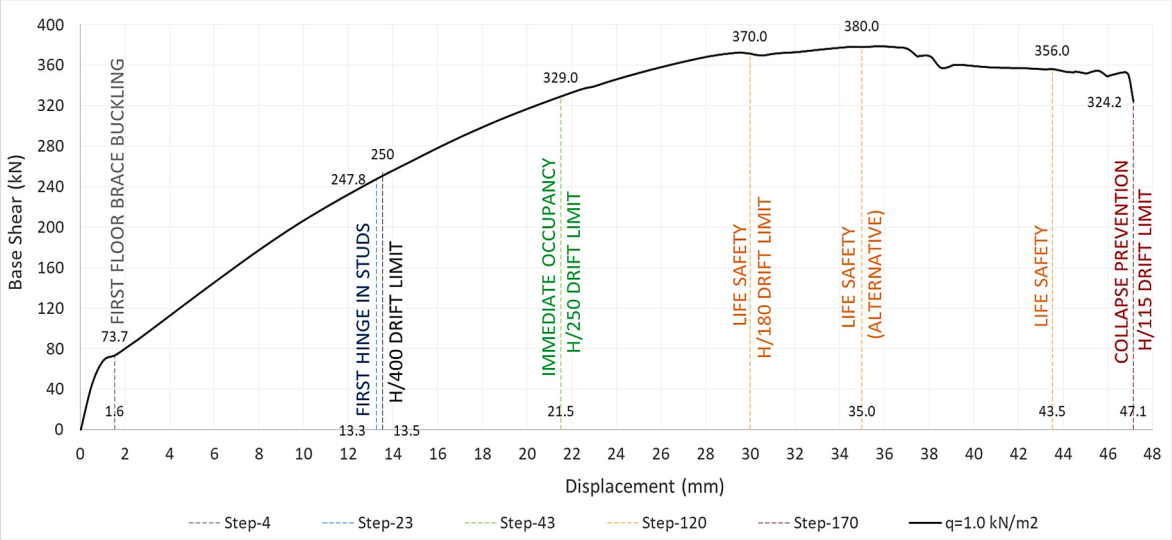

Figure 4.7. Significant event progression and the proposed structural damage levels.

Event progression is also illustrated on the pushover curve in Figure 4.7, and it can easily be seen that the structure attains its base shear capacity at about 35 mm structural sway, when the structure nears to its unstable state where the number of failing elements increases unpredictably.

Considering these results, *Immediate Occupancy* damage level has been selected as the stage where the first buckling members occur back at the staircase, and not the stage where the first hinge in a stud is observed. This is just a personal preference, prioritizing the importance of the stairwell rather than just any studs. It may be argued that prioritizing the staircase above all other structural components sounds more like a *life safety* condition. However, it should be noted that the proposed IO damage level only corresponds to the *first* plastic hinge in the staircase, which occurs at a reasonable displacement level of about 2.0 cm. Defining the same displacement as a life safety limit could as well be considered as over-design.

Life Safety damage level, on the other hand, has been selected as the penultimate stage just before a multiple failure progression starts in any member. And understandably, *Collapse Prevention* damage level has been selected as the final point on the curve. Obviously LS and CP damage levels appear too close for comfort, thus it is fair to say that LS damage level could as well be taken as the reference point in the design process.

It may also be logical to shift LS damage level to the stage where the ultimate base shear is attained, which in this case corresponds to approximately 30 – 35 mm structural sway. While it is doable according to the curve, it should be mentioned that this displacement level does not appear to physically represent a milestone in the performance history of the building. There are on-going hinge formations here and there, yet it is difficult to ascertain which of the failing elements at this stage should define the ‘life safety’ limits.

Now let’s consider a structural drift limit of $H/400$, where H is the height of the building. Excluding the rooftop, the effective height of this building is 5.40 m, and thus the allowable drift limit corresponds to approximately 13.5 mm of structural sway. It has been demonstrated that this sway level corresponds to the very first plastic hinge occurring in a

stud. Thinking that way, it can be said that the proposed IO damage level corresponds to a structural drift limit of *H*/250. Similarly, CP damage level is attained at a structural drift of about *H*/115. Therefore, it can be suggested that LS damage level should be in-between, such as *H*/180. This translates to a 30 mm displacement, which in this case (coincidence or not) roughly corresponds to the stage where the base shear capacity is reached.

It is important to note that the use of *H*/400 limit here can be considered as a second method for determining the conventional elastic limit of the pushover curve. It is known that there are two available methods in literature for determining the elastic limit of force-displacement relationships. One of them considers that the initial stiffness can be taken as the secant stiffness to the load level of $0.4\times F_{max}$. In the other method, the initial stiffness is considered as the secant stiffness to the drift level of *H*/400. A detailed interpretation for both methods is provided in the following chapter.

4.4. Evaluation of the Force Modification Factors

An additional analysis option was examined which also considered post-buckling in the structural elements. Thus, depending on the section properties, a post-buckling strength of 5–10% higher, for example, was defined for CFS members and their respective hinge behavior characteristics were adjusted. This method was only trialed out to check if the analysis results could be any different. In the end, it was observed that the results yielded only minor discrepancies.

In all honesty, these results must have been expected, because it was shown that buckling in studs appear very late, yet very rapidly. The nonlinear behavior of the structure remained indifferent, due that the only elements in the structure that would be in their 'post-buckling' state (before any of the studs reached their buckling load limit) would have been braces. In contrast, their failures appear earlier, and since their load carrying capacity is relatively very low, any post-buckling strength they would acquire would *not* change the overall nonlinear behavior of the structure. In other words, the post-buckling strength of the braces is very low (due to inherent small capacity) and therefore could be neglected. The post-buckling strength of the studs could also be neglected, since any hinge formation in the studs begin much later, so it does not have a considerable effect on the structural

behavior before the state of collapse. Thus the analysis results obtained without post-buckling option were retained, there was no significant need to take post-buckling into account.

Other than that, it may be sensible to say a few words regarding the structural stiffness abruptly decreasing in the initial stages of the analysis. Obviously this breaking point on the capacity curve does not predominantly represent the general structural behavior. This portion of the curve may always be approximated to a smoother transition. However, it is a fact that the structure does behave in a linear fashion at the very beginning of the analysis. It should be fair to consider that if all structural elements (links, frames, etc.) could retain their elasticity, the structural response would have remained completely linear. And that is exactly how the pushover curve would look like: just like the very steep initial portion of the curve. Thus, it is concluded that this initial portion *must* remain as it is in the related figures.

Evaluation of the seismic force modification factors is described in Appendix 4A of the latest Turkish Seismic Code. After converting the pushover curves for both X- and Y-directions into ADRS format (Acceleration-Displacement Response Spectra), performance assessment of the building can be done as follows. The first step of the process requires that a bilinear EEEP approximation of the pushover curve is generated. Generally, it is acknowledged that the first portion of any capacity curve up to the force level of $0.4\times P_{peak}$ more or less behaves linearly (the conventional elastic limit). Thus this point is located, and a linear relationship is continued until the yield force level. By equating the areas below the capacity curve and the provisional bilinear curve, yield point is computed. Figure 4.8 illustrates the determination of the bilinear EEEP curve for the pushover analysis in X-direction. The displacement at yield is calculated to be about $\Delta_y = 27.7$ mm, and the ultimate displacement is $\Delta_u = 65.2$ mm, which denotes the collapse point.

With regards to Table 1.2, this specific building can be categorized as a structural system with limited ductility, for which the Structural Behavior Factor is defined as $R = 3$ and the Overstrength Factor is given as $D = 2$. These values correspond to a ductility ratio of $\mu_k = 1.5$, as given in Equation 4.1, which is provided by the code in Appendix 4A.3.1.

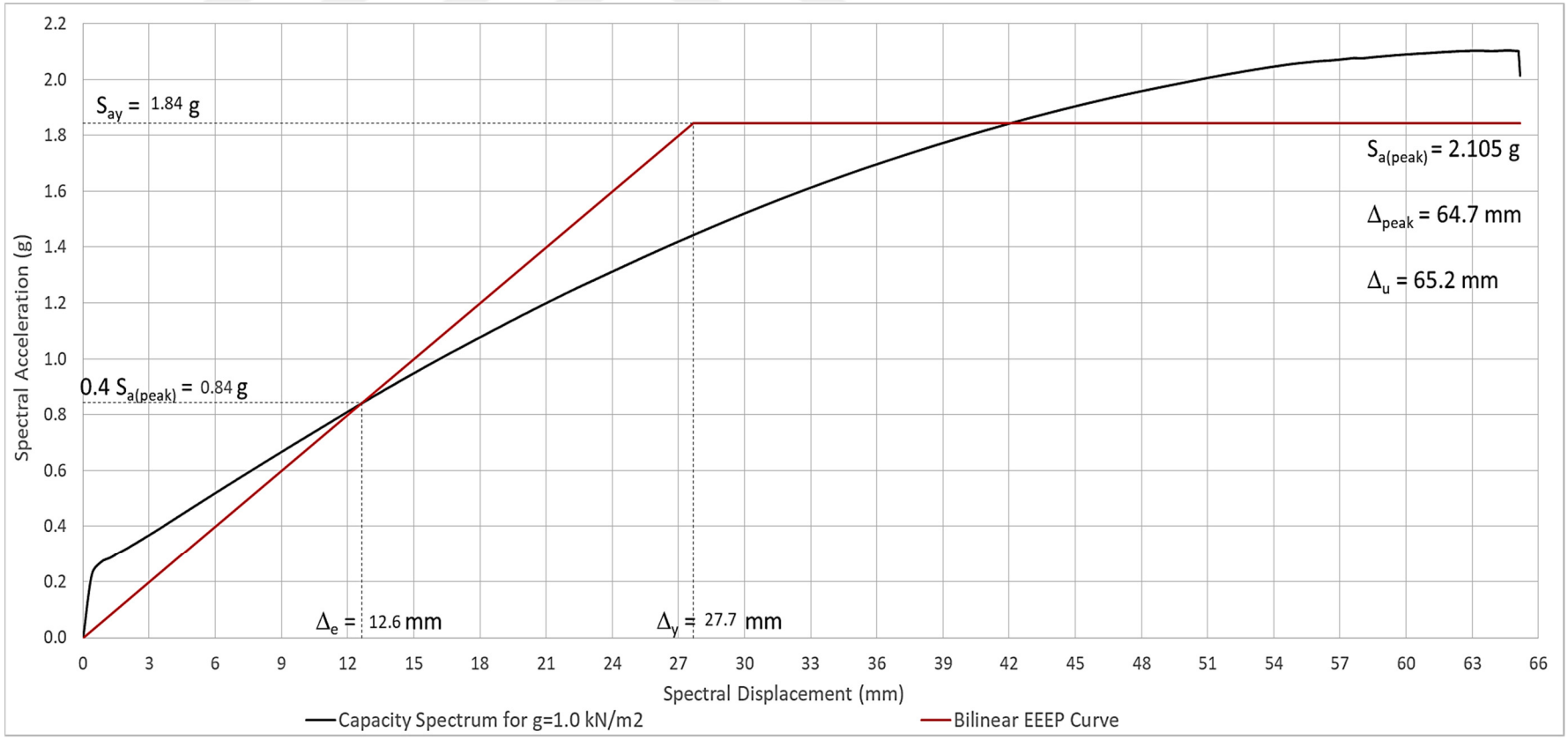

Figure 4.8. Performance assessment in X-direction.

$$\frac{R}{I} = \mu_k * D \quad \rightarrow \quad \mu_k = \frac{R}{I*D} = \frac{3}{1*2} = 1.5 \tag{4.1}$$

However, the bilinear EEEP curve indicates that the real ductility ratio must be,

$$\mu_k = \frac{\Delta_u}{\Delta_y} = \frac{65.2}{27.7} = 2.35 \tag{4.2}$$

Replacing this value back in Equation 4.1, the Structural Behavior Factor can be computed as in Equation 4.3,

$$R = I * \mu_k * D = 1 * 2.35 * 2 = 4.7 \tag{4.3}$$

which is about 57% greater than that defined in the code. For comparison, R_a values computed by using the default values in the code and by using the ductility ratio obtained from the pushover analysis are given in Equations 4.4 and 4.5.

$$R_a = D + \left(\frac{R}{I} - D\right)\frac{T}{T_B} = 2 + (3-2)\frac{0.11}{0.52} = 2.21 \qquad (\textit{TSC 2018}) \tag{4.4}$$

$$R_a = D + \left(\frac{R}{I} - D\right)\frac{T}{T_B} = 2 + (4.7-2)\frac{0.11}{0.52} = 2.57 \qquad (\textit{Pushover Analysis}) \tag{4.5}$$

Ductility- and overstrength-related modification factors can also be calculated in accordance with AISI S213, intended for informative purposes only. Equations 4.6 – 4.8 provide the relevant computations in this regard.

$$R_d = \sqrt{2\mu - 1} = \sqrt{2 * 2.35 - 1} = 1.92 \tag{4.6}$$

$$R_\mathrm{o} = \frac{P_{peak}}{P_{yield}} = \frac{2.11}{1.84} = 1.15 \tag{4.7}$$

$$R = R_d * R_\mathrm{o} = 1.92 * 1.15 = 2.21 \tag{4.8}$$

Much can also be said about the Overstrength Factor. The value in TSC 2018 is intentionally preserved for above calculations, since the computation of the factor varies from code to code. In TSC 2018 it is defined as the yield force value obtained from the EEEP approximation by the force value at which the first yielding in the structure takes place. Since there are very slender members such as braces in the structure, it can easily be claimed that buckling occurs at very early stages, which is testified by the analysis results. However, this may not always be considered as 'yielding', and it may be feasible to investigate for other structural members which undergo higher levels of deformations: positive elongations, for example. Identifying such members may not always be an easy task, and the obtained results may always be debatable, which may lead to incoherently low or high overstrength values. Hence, the default value provided in the code is utilized in order to eliminate any invalid reasoning.

Similar computations can also be done for the pushover analysis in Y-direction. The determination of the bilinear EEEP curve is illustrated in Figure 4.9. The ductility ratio and subsequently the Structural Behavior Factor are calculated in Equations 4.9 and 4.10.

$$\mu_k = \frac{\Delta_u}{\Delta_y} = \frac{39.1}{12} = 3.26 \tag{4.9}$$

$$R = I * \mu_k * D = 1 * 3.26 * 2 = 6.5 \tag{4.10}$$

which is more than twice of the code value. The comparison of the code-computed and analysis-obtained R_a values is provided in Equations 4.11 and 4.12. It can easily be observed that the difference between the values is even greater.

$$R_a = D + \left(\frac{R}{I} - D\right)\frac{T}{T_B} = 2 + (3-2)\frac{0.1}{0.52} = 2.19 \qquad (\textit{TSC 2018}) \tag{4.11}$$

$$R_a = D + \left(\frac{R}{I} - D\right)\frac{T}{T_B} = 2 + (6.5-2)\frac{0.1}{0.52} = 2.86 \qquad (\textit{Pushover analysis}) \tag{4.12}$$

Again, for informative purposes, the seismic force reduction factors obtained by AISI S213 regulations are provided in Equations 4.13 – 4.15.

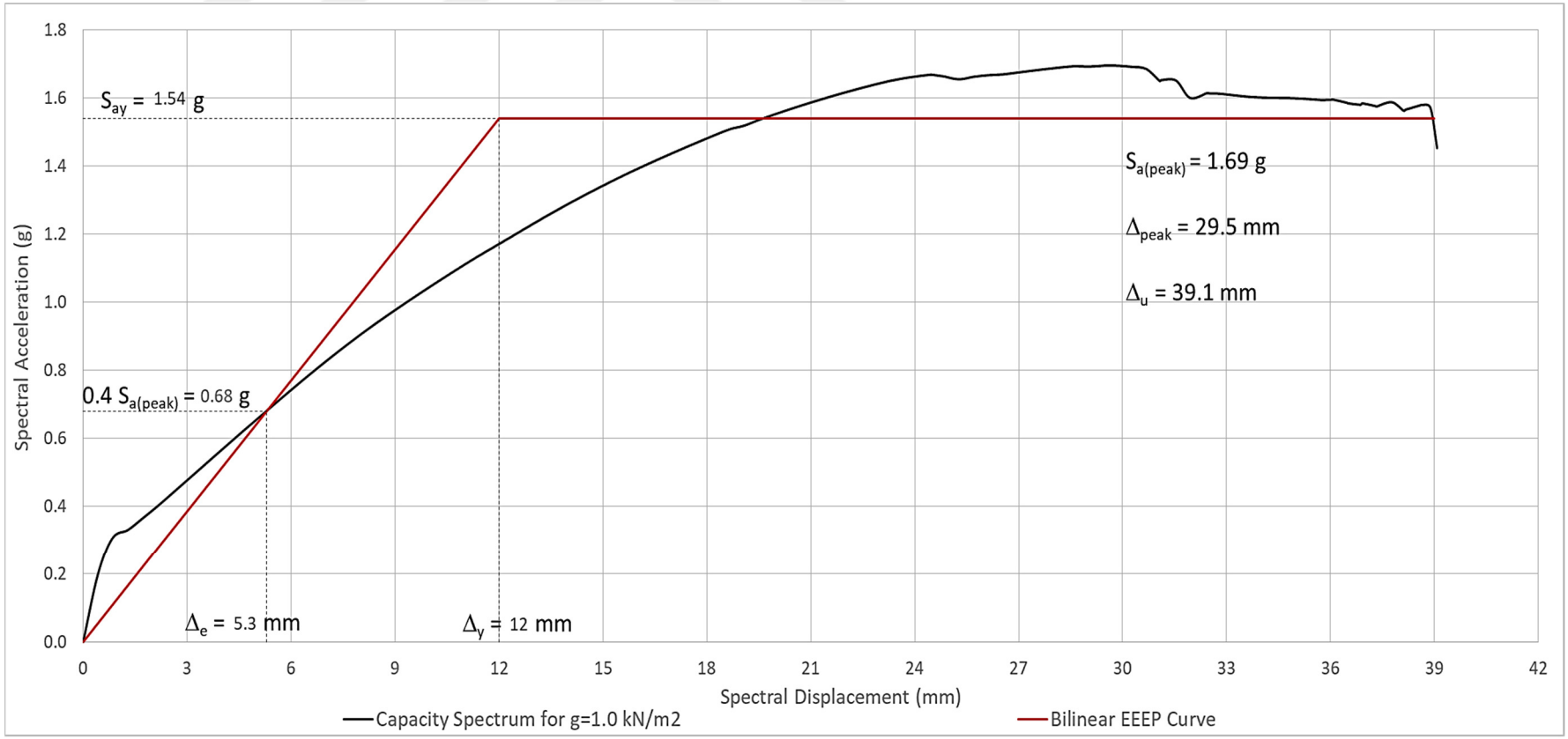

Figure 4.9. Performance assessment in Y-direction.

$$R_d = \sqrt{2\mu - 1} = \sqrt{2 * 3.26 - 1} = 2.35 \quad (4.13)$$

$$R_o = \frac{P_{peak}}{P_{yield}} = \frac{1.69}{1.54} = 1.1 \quad (4.14)$$

$$R = R_d * R_o = 2.35 * 1.1 = 2.59 \quad (4.15)$$

By looking at these results, it may be concluded that the seismic force reduction factors tend to increase compared to those calculated with the default code values. In other words, seismic forces could have been decreased by more.

It is interesting to note that using the drift limit *H*/400 here for determining the elastic limit is almost impractical, since the drift value of 13.5 mm corresponds to a spectral displacement of about 11.0 mm. This value is already quite close to the elastic limit assumption for the capacity curve in X-direction, and can as well be considered. However, it is just too large to be the elastic limit for the capacity curve in Y-direction, and using this drift limit can only yield to unreliable calculations. It can only be applicable for structures whose nonlinear behavior is similar in both directions.

There is also another curious aspect that needs to be pointed out at this stage. An elaborate observation of the hysteresis curves obtained from laboratory experiments (see Figures 3.8 and/or 3.22) hints that the envelopes of the curves appear to break slightly at a load level of about $0.3\times F_{max}$. This point may also be considered as the yielding point since a significant decrease in stiffness takes place. However, the same trend does not persist in the force-displacement curves of the building model, apart from the obvious breaking in the initial portion. This may be attributed to the fact that component-based behavior may not always represent the full-scale structural response. In this specific case, for example, taking the $0.3\times P_{peak}$ value as the conventional elastic limit results in a smaller yield displacement, and consecutively a larger ductility ratio, which then only exaggerates the already higher force modification factors. Thus, it can be concluded that the existing assumption of $0.4\times P_{peak}$ for the elastic limit is valid.

5. ADDITIONAL ANALYSES WITH VARIABLE PROPERTIES

5.1. Introduction

In order to investigate the variation of *R* values with regards to changeable design parameters, additional numerical studies have also been performed. The scope of these additional analyses are summarized below. They are provided as supplementary data, and only the capacity spectra in Y-direction are considered for the sake of simplicity. Again it should be noted that the pushover curves are only plotted up to the point where the analysis results are considered to be reliable.

- Gravity Loading Variations
  - (i) Case-1: g=1.0 kN/m^2 & q=1.0 kN/m^2
  - (ii) Case-2: g=1.5 kN/m^2 & q=2.0 kN/m^2
  - (iii) Case-3: g=2.0 kN/m^2 & q=3.0 kN/m^2
  - (iv) Case-4: g=2.5 kN/m^2 & q=4.0 kN/m^2
  - (v) Case-5: g=3.0 kN/m^2 & q=5.0 kN/m^2

- OSB Shear Panel Variations
  - (i) 9 mm OSB Panels
  - (ii) 11 mm OSB Panels
  - (iii) 12.5 mm OSB Panels

- Gypsum Shear Panel Variations
  - (i) 9 mm Gypsum Panels
  - (ii) 11 mm Gypsum Panels
  - (iii) 12.5 mm Gypsum Panels

- Connection Rigidity Variations
  - (i) Mild Connection Type
  - (ii) Original Connection Type
  - (iii) Stiff Connection Type

5.2. Gravity Loading Variations

As can be observed from the results, it can be concluded that both base shear capacity and deformation capacity of the structure tend to decrease with higher gravity loads (as expected) (Figure 5.1). Moreover, it was observed that the applied gravity loads and their distribution along the building greatly effects the structural capacity spectrum (Figure 5.2). Load distribution mainly dominates the first mode shape, thus resulting in different capacity spectra with increasing gravity loads. In conclusion, it can be said that capacity spectra varies with respect to the magnitude and distribution of the gravity loads.

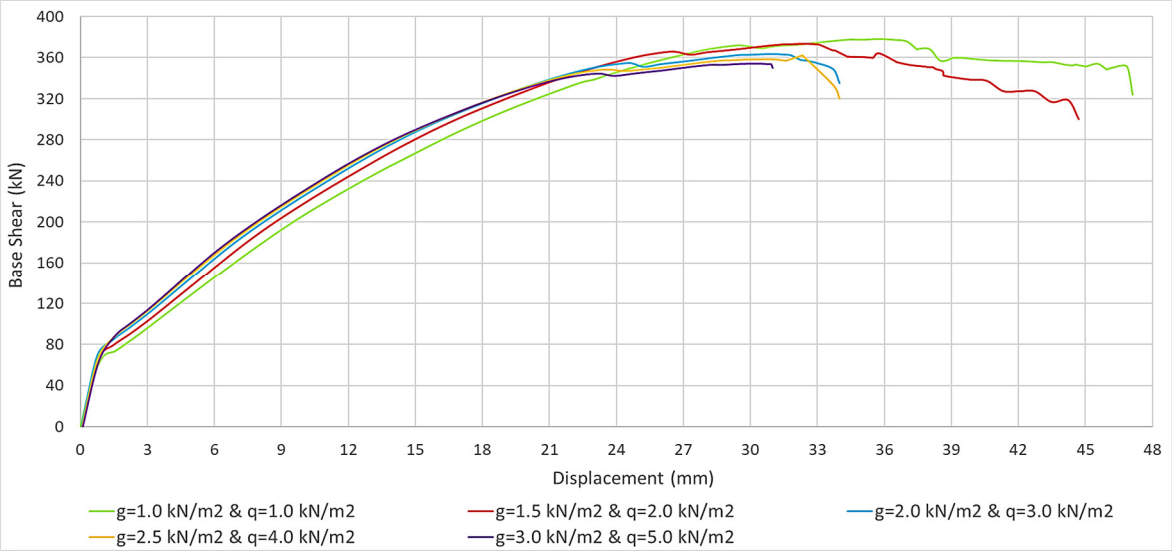

Figure 5.1. Pushover curves of analysis models with varying gravity loads.

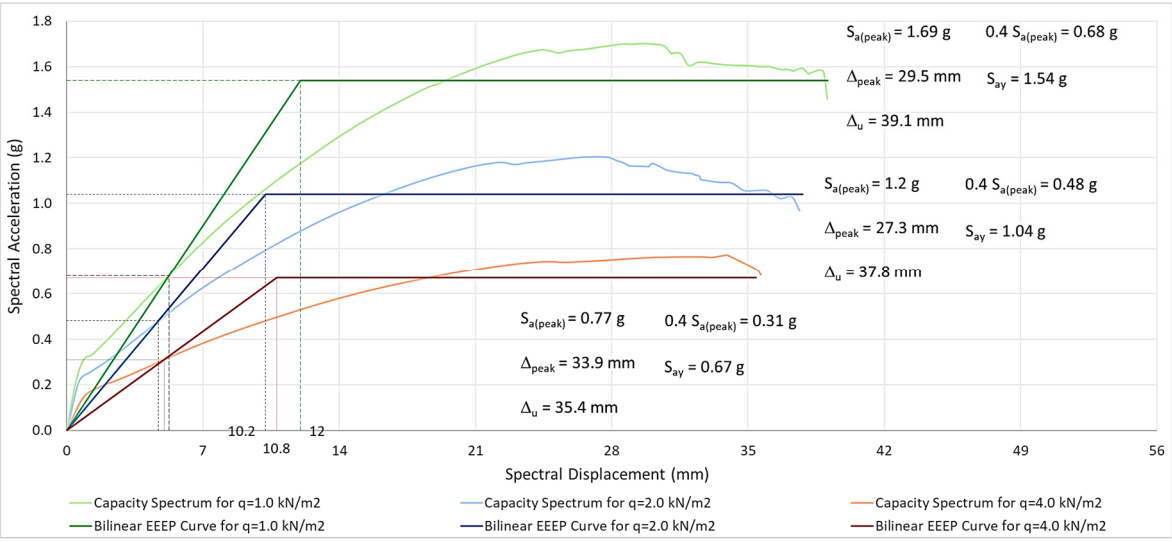

Figure 5.2. Bilinear EEEP Curve evaluation for varying gravity loads.

Determination of the Structural Behavior Factor and the Seismic Force Reduction Factor is demonstrated in Equations 5.1 – 5.15 for each gravity load level. In Figure 5.2, only three of the cases are presented for the sake of simplicity. It should be noted that the natural vibration period of the building also changes with increasing load levels. Larger scale versions of the figures are provided in Appendix F.

Calculations for Case-1: g=1.0 kN/m² & q=1.0 kN/m²

$$\mu_k = \frac{\Delta_u}{\Delta_y} = \frac{39.1}{12} = 3.26 \tag{5.1}$$

$$R = I * \mu_k * D = 1 * 3.26 * 2 = 6.5 \tag{5.2}$$

$$R_a = D + \left(\frac{R}{I} - D\right)\frac{T}{T_B} = 2 + (6.5 - 2)\frac{0.1}{0.52} = 2.86 \tag{5.3}$$

Calculations for Case-2: g=1.5 kN/m² & q=2.0 kN/m²

$$\mu_k = \frac{\Delta_u}{\Delta_y} = \frac{37.8}{10.2} = 3.7 \tag{5.4}$$

$$R = I * \mu_k * D = 1 * 3.7 * 2 = 7.4 \tag{5.5}$$

$$R_a = D + \left(\frac{R}{I} - D\right)\frac{T}{T_B} = 2 + (7.4 - 2)\frac{0.13}{0.52} = 3.35 \tag{5.6}$$

Calculations for Case-3: g=2.0 kN/m² & q=3.0 kN/m²

$$\mu_k = \frac{\Delta_u}{\Delta_y} = \frac{31.7}{10.3} = 3.08 \tag{5.7}$$

$$R = I * \mu_k * D = 1 * 3.08 * 2 = 6.16 \tag{5.8}$$

$$R_a = D + \left(\frac{R}{I} - D\right)\frac{T}{T_B} = 2 + (6.16 - 2)\frac{0.15}{0.52} = 3.2 \tag{5.9}$$

Calculations for Case-4: g=2.5 kN/m² & q=4.0 kN/m²

$$\mu_k = \frac{\Delta_u}{\Delta_y} = \frac{35.4}{10.8} = 3.28 \tag{5.10}$$

$$R = I * \mu_k * D = 1 * 3.28 * 2 = 6.56 \tag{5.11}$$

$$R_a = D + \left(\frac{R}{I} - D\right)\frac{T}{T_B} = 2 + (6.56 - 2)\frac{0.16}{0.52} = 3.4 \tag{5.12}$$

Calculations for Case-5: g=3.0 kN/m² & q=5.0 kN/m²

$$\mu_k = \frac{\Delta_u}{\Delta_y} = \frac{36.3}{11} = 3.3 \tag{5.13}$$

$$R = I * \mu_k * D = 1 * 3.3 * 2 = 6.6 \tag{5.14}$$

$$R_a = D + \left(\frac{R}{I} - D\right)\frac{T}{T_B} = 2 + (6.6 - 2)\frac{0.17}{0.52} = 3.5 \tag{5.15}$$

5.3. OSB Shear Panel Variations

For this investigation, gravity load levels are taken as 1.0 kN/m^2 live loads in addition to 1.0 kN/m^2 superimposed dead loads. It was observed that the natural vibration period of the building did not change by much, thus the original value is used in the calculations.

By looking at the results (Figure 5.3), it can be concluded that both base shear and structural deformation capacities do not change by much with respect to panel thickness, there are only small alterations. Determination of the Structural Behavior Factor and the Seismic Force Reduction Factor is demonstrated in Equations 5.16 – 5.24 for each thickness value, taking the data provided in Figure 5.4 into account. It can be easily observed that *R* values are larger than those defined in TSC 2018, for the same panel type. Larger scale versions of the figures are provided in Appendix F.

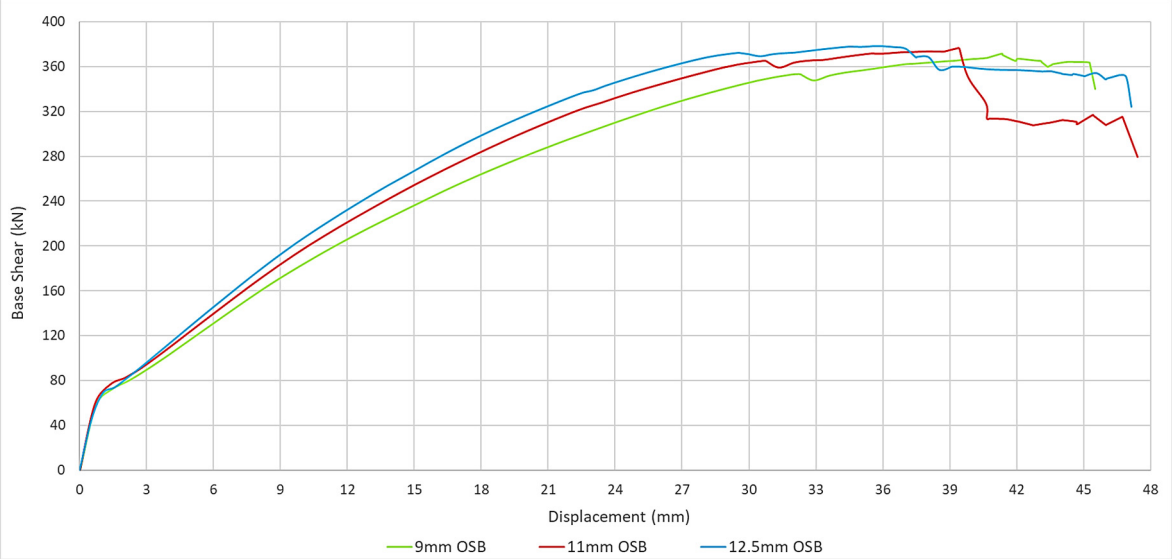

Figure 5.3. Pushover curves of analysis models with varying OSB panel thickness.

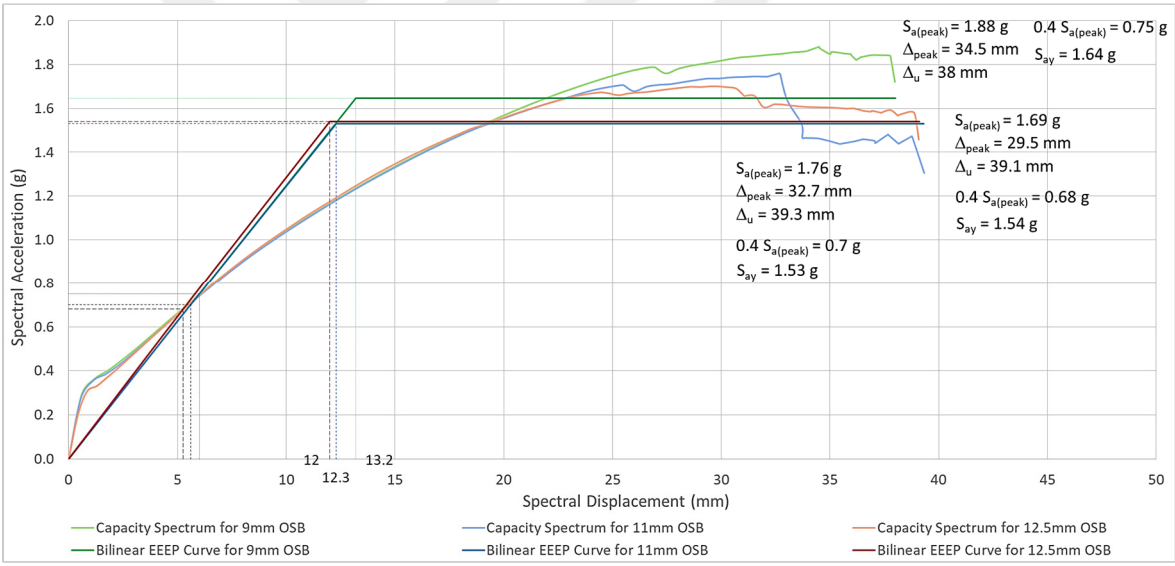

Figure 5.4. Bilinear EEEP Curve evaluation for varying OSB panel thickness.

Calculations for 9.0 mm OSB thickness

$$\mu_k = \frac{\Delta_u}{\Delta_y} = \frac{38}{13.2} = 2.9 \tag{5.16}$$

$$R = I * \mu_k * D = 1 * 2.9 * 2 = 5.8 \tag{5.17}$$

$$R_a = D + \left(\frac{R}{I} - D\right)\frac{T}{T_B} = 2 + (5.8 - 2)\frac{0.1}{0.52} = 2.73 \tag{5.18}$$

Calculations for 11.0 mm OSB thickness

$$\mu_k = \frac{\Delta_u}{\Delta_y} = \frac{39.3}{12.3} = 3.2 \tag{5.19}$$

$$R = I * \mu_k * D = 1 * 3.2 * 2 = 6.4 \tag{5.20}$$

$$R_a = D + \left(\frac{R}{I} - D\right)\frac{T}{T_B} = 2 + (6.4 - 2)\frac{0.1}{0.52} = 2.85 \tag{5.21}$$

Calculations for 12.5 mm OSB thickness

$$\mu_k = \frac{\Delta_u}{\Delta_y} = \frac{39.1}{12} = 3.26 \tag{5.22}$$

$$R = I * \mu_k * D = 1 * 3.26 * 2 = 6.5 \tag{5.23}$$

$$R_a = D + \left(\frac{R}{I} - D\right)\frac{T}{T_B} = 2 + (6.5 - 2)\frac{0.1}{0.52} = 2.86 \tag{5.24}$$

5.4. Gypsum Shear Panel Variations

Similar to the previous investigation, a live load level of 1.0 kN/m^2 in addition to 1.0 kN/m^2 superimposed dead loads is taken as gravity loads. Again, it was observed that the natural vibration period of the building did not change by much, thus the original value is used in the calculations.

By looking at the results (Figure 5.5), it can be concluded that both base shear and structural deformation capacities do not change by much with respect to panel thickness, in fact they look almost identical. Determination of the Structural Behavior Factor and the Seismic Force Reduction Factor is demonstrated in Equations 5.25 – 5.33 for each thickness value, taking the data provided in Figure 5.6 into account. It can be easily observed that *R* values are much larger than those defined in TSC 2018, for the same panel type. Larger scale versions of the figures are provided in Appendix F.

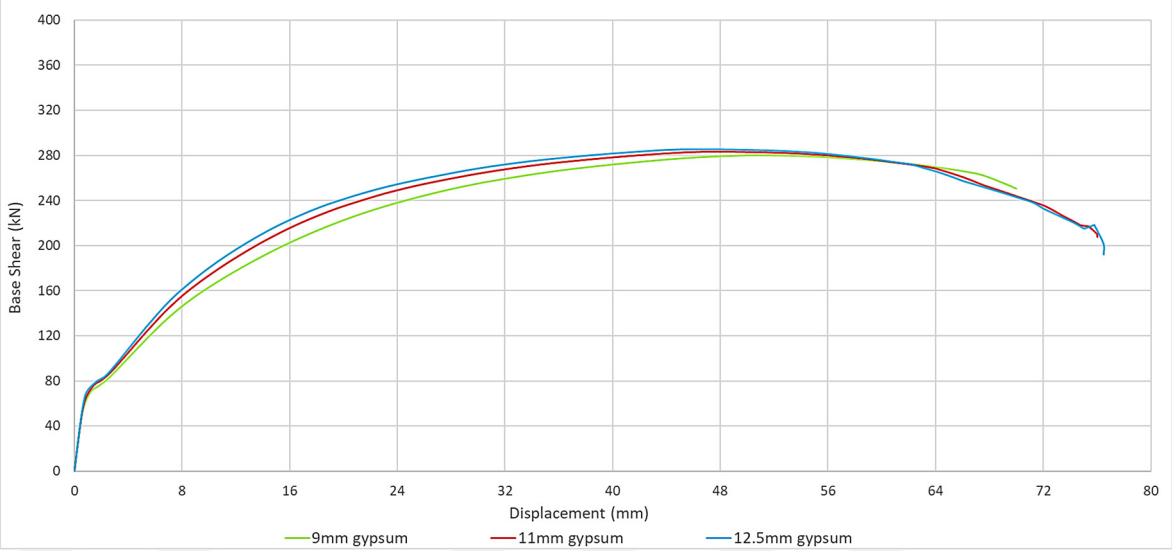

Figure 5.5. Pushover curves of analysis models with varying gypsum panel thickness.

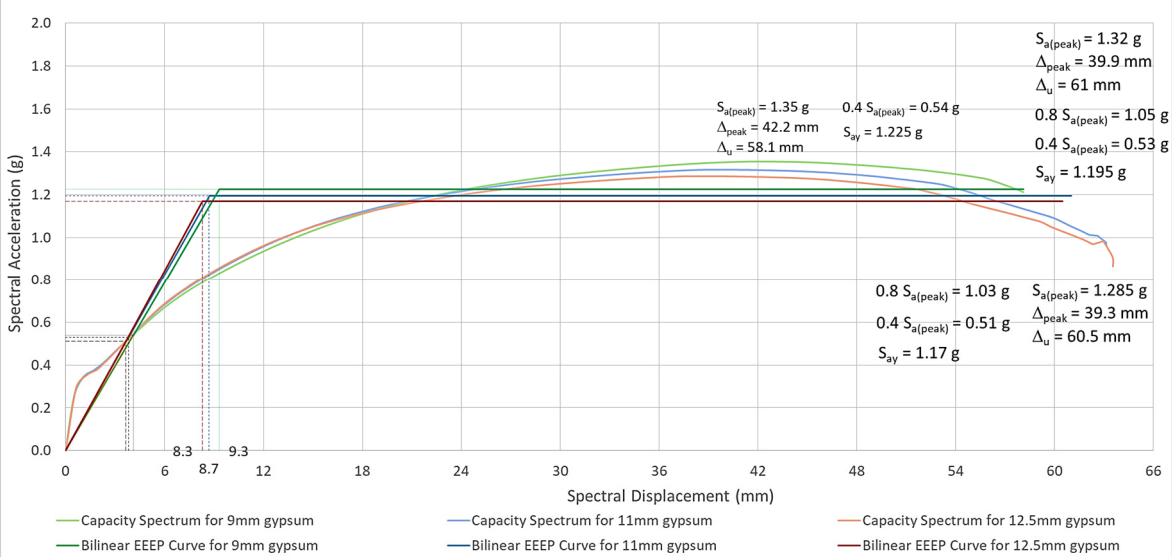

Figure 5.6. Bilinear EEEP Curve evaluation for varying gypsum panel thickness.

Calculations for 9.0 mm gypsum thickness

$$\mu_k = \frac{\Delta_u}{\Delta_y} = \frac{58.1}{9.3} = 6.25 \tag{5.25}$$

$$R = I * \mu_k * D = 1 * 6.25 * 2 = 12.5 \tag{5.26}$$

$$R_a = D + \left(\frac{R}{I} - D\right)\frac{T}{T_B} = 2 + (12.5 - 2)\frac{0.1}{0.52} = 4.02 \tag{5.27}$$

Calculations for 11.0 mm gypsum thickness

$$\mu_k = \frac{\Delta_u}{\Delta_y} = \frac{61}{8.71} = 7.0 \tag{5.28}$$

$$R = I * \mu_k * D = 1 * 7.0 * 2 = 14.0 \tag{5.29}$$

$$R_a = D + \left(\frac{R}{I} - D\right)\frac{T}{T_B} = 2 + (14.0 - 2)\frac{0.1}{0.52} = 4.31 \tag{5.30}$$

Calculations for 12.5 mm gypsum thickness

$$\mu_k = \frac{\Delta_u}{\Delta_y} = \frac{60.5}{8.3} = 7.3 \tag{5.31}$$

$$R = I * \mu_k * D = 1 * 7.3 * 2 = 14.6 \tag{5.32}$$

$$R_a = D + \left(\frac{R}{I} - D\right)\frac{T}{T_B} = 2 + (14.6 - 2)\frac{0.1}{0.52} = 4.42 \tag{5.33}$$

5.5. Connection Rigidity Variations

In fact, the original screw spacing is kept unaltered for all analyses for the sake of simplicity. Instead, varying levels of robustness is taken into consideration for singular connections. 'Mild connection' corresponds to half as much *F-d* values, and 'stiff connection' means twice as much *F-d* values than those given for the original set of singular connections. Here again, it was observed that the natural vibration period of the building did not change by much, thus the original value is used in the calculations.

It can be observed from the results that, using a stiffer connection type greatly increases both the base shear capacity and the structural deformation capacity (Figure 5.7). Determination of the Structural Behavior Factor and the Seismic Force Reduction Factor is demonstrated in Equations 5.34 – 5.39 for each robustness level, taking the data provided in Figure 5.8 into account. Larger scale versions of the figures are provided in Appendix F.

Again, it should be noted that the gravity loads are taken as 1.0 kN/m^2 live loads in addition to 1.0 kN/m^2 superimposed dead loads. It should also be remembered that the calculations for the original connection type exactly correspond to the those given for 12.5 mm OSB thickness (provided with Equations 5.22 – 5.24), thus they are not given herein.

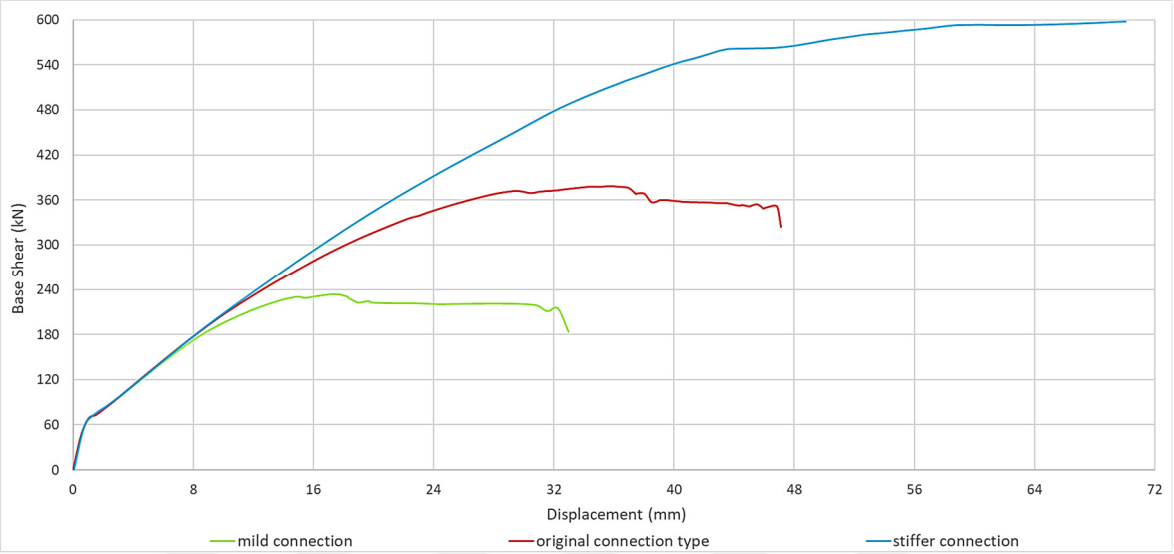

Figure 5.7. Pushover curves of analysis models with varying connection stiffness.

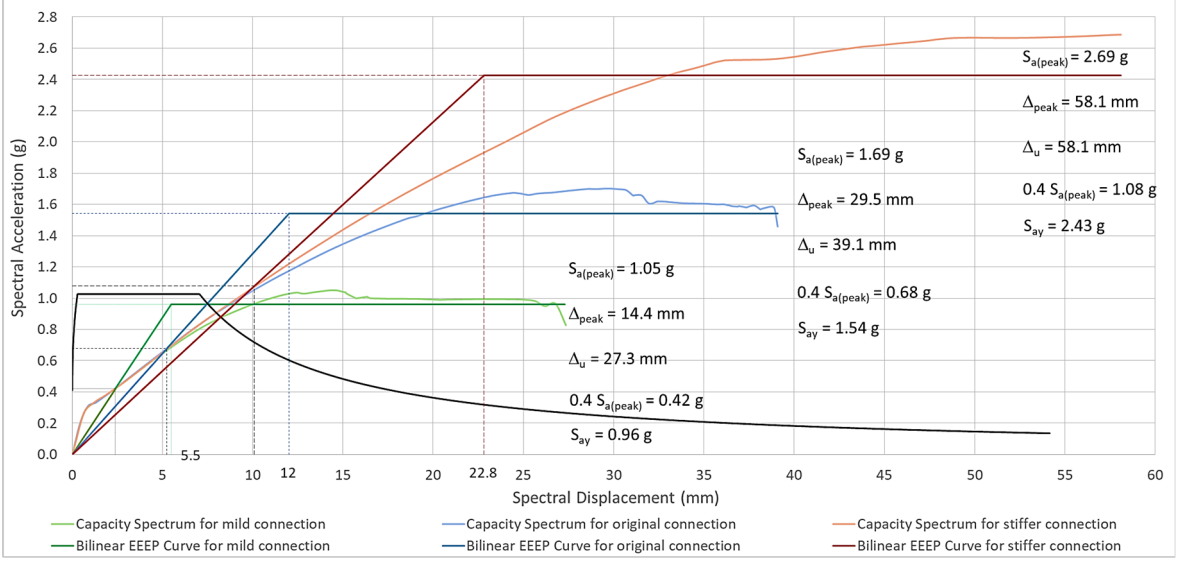

Figure 5.8. Bilinear EEEP Curve evaluation for varying connection stiffness.

Calculations for mild connection type

$$\mu_k = \frac{\Delta_u}{\Delta_y} = \frac{27.3}{5.5} = 5.0 \qquad (5.34)$$

$$R = I * \mu_k * D = 1 * 5.0 * 2 = 10.0 \quad (5.35)$$

$$R_a = D + \left(\frac{R}{I} - D\right)\frac{T}{T_B} = 2 + (10.0 - 2)\frac{0.1}{0.52} = 3.54 \quad (5.36)$$

Calculations for stiff connection type

$$\mu_k = \frac{\Delta_u}{\Delta_y} = \frac{58.1}{22.8} = 2.55 \quad (5.37)$$

$$R = I * \mu_k * D = 1 * 2.55 * 2 = 5.1 \quad (5.38)$$

$$R_a = D + \left(\frac{R}{I} - D\right)\frac{T}{T_B} = 2 + (5.1 - 2)\frac{0.1}{0.52} = 2.6 \quad (5.39)$$

6. CONCLUSIONS AND FUTURE WORKS

In this chapter, the main conclusions which can be drawn according to the study completed so far in the content of this thesis are outlined. Some of the conclusions regarding the chapters have more or less been drawn in the sections of concern, yet a broader adjustment to the conclusions is carried out herein to illustrate the main picture in an efficient way. Provisional trendlines are derived from the limited data presented in the previous chapter, and are illustrated in the following items. In order to validate or improvise the said trendlines, some prospective future works are also suggested, which may come as a result of this research.

6.1. List of Conclusions

- The experimental and analytical studies carried out within the scope of this thesis should be expanded and supported by more of similar studies on the subject. It is certain that results obtained from only one building are not sufficient to draw a precise picture.

- Yet, the objective of this thesis is to get a reasonable idea whether the proposed factors in TSC 2018 are practical. In this specific study, it was shown that the Structural Behavior Factors calculated from the pushover analysis results were generally higher than those defined in TSC 2018. In some cases, calculated values appeared to go up by as much as two or three times, which is in fact higher than they normally should be. There is always an inevitable possibility of numerical errors in such sensitive analyses, therefore it is essential that these results are backed by further studies. The Structural Behavior Factor definition of the code could as well be interpreted as having a decent margin for safety.

- Both base shear capacity and deformation capacity of the structure tend to decrease with higher gravity loads.

- The applied gravity loads and their distribution along the building greatly effects the structural capacity spectrum. Load distribution mainly dominates the first mode shape, i.e. the natural vibration period(s) of the building changes with increasing load levels. In conclusion, capacity spectrum varies with respect to the magnitude and distribution of the gravity loads.

Although not perfectly-fit, the proposed approximate trendline (Figure 6.1) suggests that the ductility ratio (hence the Structural Behavior Factor) should slightly decrease with increasing amount of dead and live loads, which sounds meaningful to some degree. The notation 'seismic weight ratio' in the figure corresponds to the total seismic weight computed in compliance with the Code, divided by the dead weight of the building (rooftop and sidewall claddings included). For example, the self-weight of the building is 165 kN according to analysis results, while the seismic weight of the building is calculated as 267.1 kN for the gravity loading case where dead loads are 1.0 kN/m^2 and live loads are 1.0 kN/m^2. So this gives us the ratio 1.62, which is the lowest value on the figure. For higher levels of the gravity loading, higher seismic weight ratios are obtained, which are subsequently indicated on the figure.

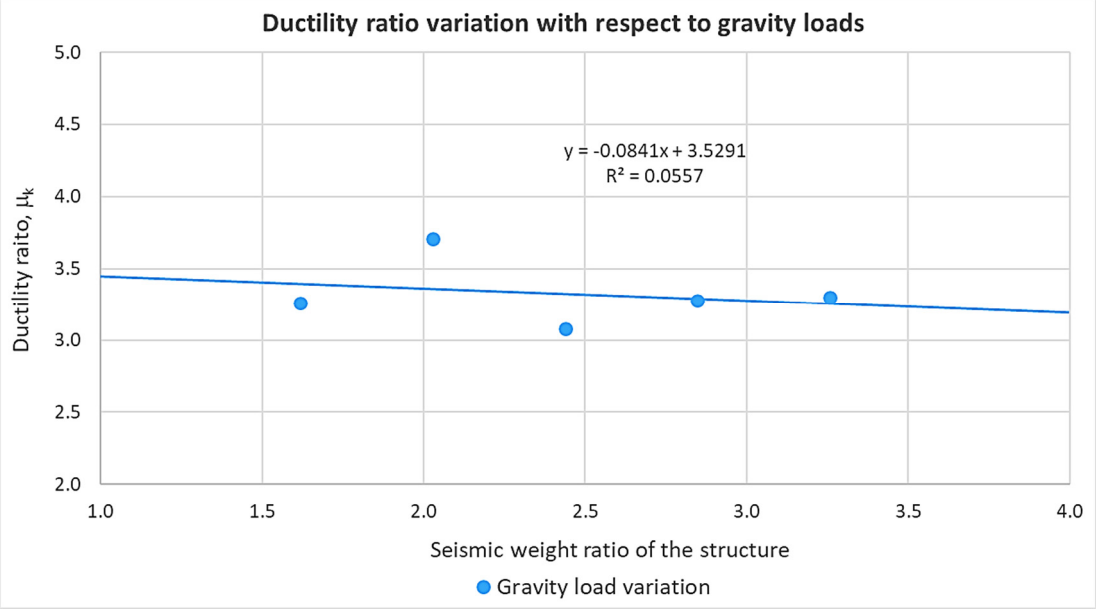

Figure 6.1. The variation of ductility with respect to varying seismic weight ratios.

When there are absolutely no loads acting on the structure, i.e. the very initial case where the structure has just been constructed, the seismic weight ratio of the structure is 1.0, according to the above definition. In such a case, trendline suggests that the ductility ratio could be just about 3.5. Needless to say that further studies are required to validate and support this trend. An approximate formula for the relationship between the seismic weight of the structure and the ductility ratio is also provided on the figure.

- For a predefined level of the gravity loads, OSB or gypsum thickness is nearly ineffectual on either the resultant base shear capacity or the resultant structural deformation capacity. The calculated values of the ductility ratio for both panel types are tabulated in Figure 6.2, along with their respective trendlines. It should be noted that the respective Structural Behavior Factors are simply twice the given ductility values, according to the assumptions $D = 2.0$ and $I = 1.0$.

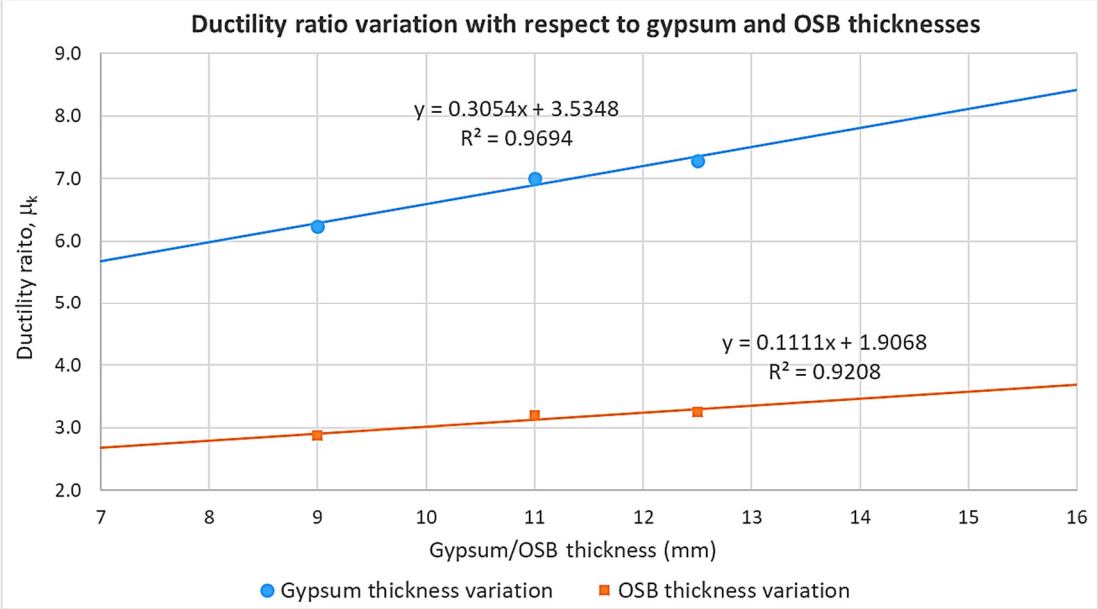

Figure 6.2. The variation of ductility with respect to gypsum or OSB thickness.

Approximate formulations of the ductility ratio variation with respect to OSB or gypsum thickness is provided on the figure. It is evident that the ductility appears to be higher in buildings with gypsum-sheathed CFS shear walls. Also, the variation of the ductility ratio with respect to panel thickness is greater with gypsum panels. The proposed trendlines suggest that, while an average value could

be applied for the Structural Behavior Factor in buildings with OSB-sheathed CFS shear walls, *R* values should be increased along with greater values of board thickness in buildings with gypsum-sheathed CFS shear walls. It is fair to say that TSC 2018 lacks necessary guidelines in this aspect, and should be improvised.

- Regarding the rigidity level of a single frame-to-frame or frame-to-panel connection, it was shown that using a stiffer connection type greatly increases both the base shear capacity and the structural deformation capacity. However, the proposed trendline (Figure 6.3) suggests that the stiffer they are, the smaller the Structural Behavior Factor is. While this is somewhat addressed in TSC 2018 by defining a lower *R* value for structural systems with limited ductility, there is no exact definition of a structural system with limited ductility, other than the referral to utilizing braces and/or gypsum panels within the structure. There is no example of what ductility level should be considered for buildings where OSB panels *and* braces are used together, for example. In this specific study, it was shown that in such systems the ductility ratio could be as much as 5.0 or even greater.

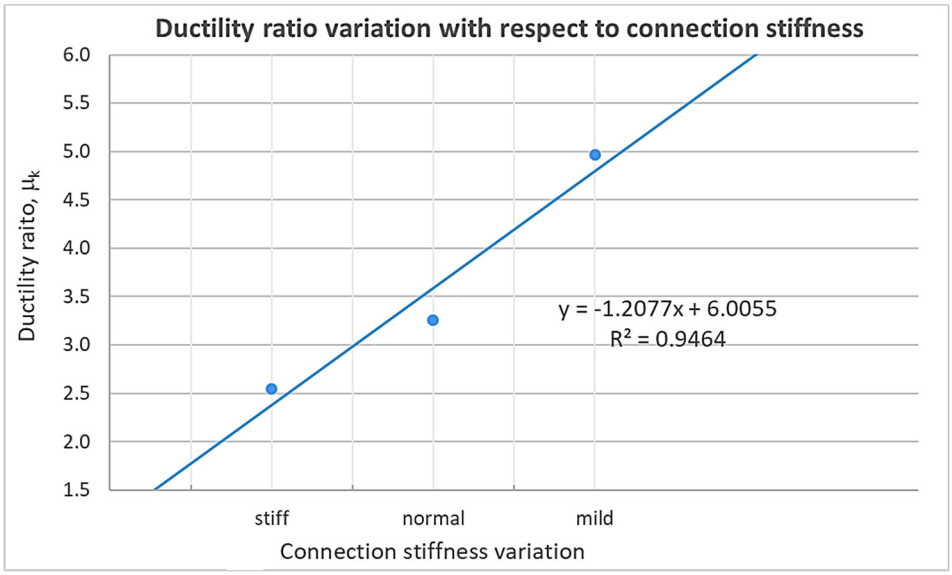

Figure 6.3. The variation of the ductility ratio with respect to connection stiffness.

- Inevitably, all these propositions should be taken with a pinch of salt. Although this construction material can be regarded as one of the most reliable, it may still contain imperfections. Moreover, a cold-formed steel section is arguably more

sensitive to faulty workmanship during construction phase: even the slightest tilting or bending of the member may cause significant second-order stress concentrations within the cross-section. Thus, it may be helpful to introduce a safety factor just in case. Taking this into account, the formulations given previously can be rewritten as below. According to the formulae, the effect of gravity loads appears to be of less importance compared to the panel thickness.

for considering the effect of gravity loading:

$$R = \frac{I*D}{\gamma_m}(3.5 - \frac{W_E}{12W}) \tag{6.1}$$

(where W_E is the total seismic weight, and W is the dead weight of the structure)

for OSB-sheathed CFS buildings with double-X strap braces:

$$R = \frac{I*D}{\gamma_m}\left(\frac{t}{9} + 1.9\right) \qquad \text{(where } t \text{ is panel thickness)} \tag{6.2}$$

for gypsum-sheathed CFS buildings with double-X strap braces:

$$R = \frac{I*D}{\gamma_m}(\frac{t}{3.3} + 3.5) \qquad \text{(where } t \text{ is panel thickness)} \tag{6.3}$$

- While it is obvious that stiffer connections are less ductile, it is difficult to formulate this relationship. As already stated, many factors contribute to the connection rigidity, and should be separately analyzed. Here for this case study, only the screw cross-section may be considered for the sake of simplicity. Thus, a formula can be written as:

$$R = \frac{I*D}{\gamma_m}(6 - \frac{1.2A}{A_{ref}}) \tag{6.4}$$

where A is the area of the screw cross-section, and A_{ref} is a reference screw section. Instead of area proportioning, the term d/d_{ref} may also be preferred, since the

diameter of the screw can be more of a meaningful criterion in design. Here it is important to determine a reference screw section (d_{ref} or A_{ref}), and a benchmark experiment may be required to define a standard ductility level. The screws used in this experiment may be accepted as A_{ref} or d_{ref} for example, and the effect of different screw sections on the structural behavior factor can be put into numbers with the above formula.

6.2. List of Future Works

- The remark in the very first clause of the conclusions can be repeated here: more similar studies on the matter should be carried out, whenever possible, for more understanding of the subject.

- It was shown in this specific example that the ductility ratio, hence the Structural Behavior Factor generally decreases with increasing gravity loads. The reason for this was based on the load distribution within the building, thus affecting the structural mode shapes. Load distributions may not always be similar in different types of buildings. However, if additional studies on the same subject support this trend, i.e. R values decrease with gravity loads, it may be convenient to associate the values in the code with the project loads of a structure. In practice, this could mean that the Structural Behavior Factors of a CFS-framed residential building and a CFS-framed school or hospital, for example, would not be the same.

- The analytical studies within this thesis only included the investigation of the structural performance with respect to the rigidity level of a singular connection, for the sake of simplicity. The rigidity of a single connection may as well originate from the thickness of the screws, the thickness of the frame cross-section, the thickness of the panels, or a combination of all. It was shown that the increasing connection stiffness yields a higher base shear capacity and a higher deformational capacity. Yet, the exact manner by which the connection stiffness is doubled or tripled is open to discussion. Thus, it may also be interesting to see if structural performance is anyhow affected by varying screw spacing, which is a more meaningful interpretation of connection rigidity.

- Another aspect that could be fruitful if investigated is the damping ratio. In fact, there are several studies available in the literature which refer to the determination of damping ratio in such structures, yet they are mostly limited to the research conducted for smaller scale specimens or individual structural components. Damping plays an important role in the seismic design of CFS structures, and could consecutively have an impact on the results obtained within the scope of this thesis. Thus, any addition to the existing data regarding this aspect would always be welcome.

- Analytical models utilized within the scope of this thesis, although being very detailed and realistic, are rather cumbersome, and it is fair to say that they are not preferable in design stage. Therefore, many fellow engineers requested that a simpler modelling method is sought for. Alternative modelling methods could as well be the subject of another study in this regard.

REFERENCES

1. Yu, W.W., "*Cold-Formed Steel Structures*", CRC Press LLC, Rolla, Missouri, 1999.

2. American Iron and Steel Institute -S213-07, "North American Standard for Cold-Formed Steel Framing-Lateral Provisions", *American Iron and Steel Institute*-S213-07, Washington, D.C., 2007.

3. American Society for Testing and Materials E2126, "Standard Test Methods for Cyclic (Reversed) Load Test for Shear Resistance of Vertical Elements of the Lateral Force Resisting Systems for Buildings", *American Society for Testing and Materials International,* West Conshohocken, Pennsylvania, 2011.

4. FEMA 440, "Improvement of Nonlinear Static Seismic Analysis Procedures", *Applied Technology Council (ATC-55 Project)*, Redwood City, California, 2005.

5. Turkish Seismic Code, "Principles For The Design Of Buildings Subjected To Earthquake Effects", *The Ministry of Public Works and Settlement*, Ankara, 2018.

6. CUFSM 5.01, "Constrained and Unconstrained Finite Strip Method", *Thin-Walled Structures Group*, Department of Civil and Systems Engineering, Johns Hopkins University, Baltimore, 2019.

7. CUTWP, "Cornell University Thin-Walled (Section) Properties", *Cold-Formed Steel Structures Research Group (Andrew Sarawit, and Prof. Teoman Peköz)*, School of Civil and Environmental Engineering, Cornell University, Ithaca, New York, 2003.

8. GBTUL 2.06, "Generalized Beam Theory at the University of Lisbon", *Generalised Beam Theory Research Group at Lisbon*, Instituto Superior Técnico, University of Lisbon, 2016.

9. MATLAB Runtime v91 (R2016b), *The MathWorks Incorporated*, Apple Hill Campus, Natick, Massachusets, 2016.

10. CSI SAP2000 v20.2.0, "Integrated Finite Element Analysis and Design of Structures", *Computers and Structures Incorporated*, Berkeley, California, 2019.

11. Serrette, R., K. Ogunfunmi, "Shear Resistance of Gypsum-Sheathed Light- Gauge Steel Stud Walls", *Journal of Structural Engineering*, Vol. 122, No. 4, pp. 383-389, 1996.

12. Tian, Y.S., J. Wang, and T.J. Lu, "Racking Strength and Stiffness of Cold-Formed Steel Wall Frames", *Journal of Constructional Steel Research*, Vol. 60, pp. 1069-1093, 2004.

13. Della Corte, G., L. Fiorino, and R. Landolfo, "Seismic Behavior of Sheathed Cold-Formed Structures: Numerical Study", *Journal of Structural Engineering*, Vol. 132, No: 4, pp. 558-569, 2006.

14. Landolfo, R., L. Fiorino, and G. Della Corte, "Seismic Behavior of Sheathed Cold-Formed Structures:Physical Tests", *Journal of Structural Engineering*, Vol. 132, No: 4, pp. 570-581, 2006.

15. Dubina, D., "Behavior and Performance of Cold-Formed Steel-Framed Houses Under Seismic Action", *Journal of Constructional Steel Research*, Vol. 64, pp. 896-913, 2008.

16. Velchev, K., G. Comeau, N. Balh, and C.A. Rogers, "Evaluation of the AISI S213 Seismic Design Procedures Through Testing of Strap Braced Cold-Formed Steel Walls", *Thin-Walled Structures*, Vol. 48, pp. 846-856, 2010.

17. Nithyadharan, M., V. Kalyanaraman, "Behavior of Cold-Formed Steel Shear Wall Panels Under Monotonic and Reversed Cyclic Loading", *Thin-Walled Structures*, Vol. 60, pp. 12-23, 2012.

18. Shamim, I., C.A. Rogers, “Steel Sheathed/CFS Framed Shear Walls Under Dynamic Loading: Numerical Modelling and Calibration”, *Thin-Walled Structures*, Vol. 71, pp. 57-71, 2013.

19. Sato, A., C.M. Uang, “A FEMA P695 Study for the Proposed Seismic Performance Factors for Cold-Formed Steel Special Bolted Moment Frames”, *Earthquake Spectra*, Vol. 29, No: 1, pp. 259-282, 2013.

20. Iuorio, O., V. Macillo, M.T. Terracciano, T. Pali, L. Fiorino, and R. Landolfo, “Seismic Response of CFS Strap-Braced Stud Walls: Experimental Investigation”, *Thin-Walled Structures*, Vol. 85, pp. 466-480, 2014.

21. Bian, G., D.A. Padilla-Llano, S.G. Buonopane, C.D. Moen, and B.W. Schafer, “OpenSees Modeling of a Wood-Sheathed Cold-Formed Steel-Framed Shear Walls”, *Proceedings of the Annual Stability Conference*, Structural Stability Research Council, Nashville, Tennessee, 2015.

22. Karabulut, B., *Analytical and Experimental Studies of Cold-Formed Steel Shear Panels*, Master Thesis, Bogazici University, 2015.

23. Senkardesler, O., G. Goler, and S. Soyoz, “Dynamic and Cyclic Response of a Full-Scale 2-Story Cold-Formed Steel Structure with and without Infill Materials”, *Bulletin of Earthquake Engineering*, Vol. 15, No: 8, pp. 3207-3326, 2016.

24. Borzoo, S., S.R. Mir Ghaderi, S. Mohebi, and A. Rahimzadeh, “Nonlinear Finite Element Modeling of Steel-Sheathed Cold-Formed Steel Shear Walls”, *Steel and Composite Structures*, Vol. 22, No: 1, pp. 79-89, 2016.

25. Madsen, R.L., T.A. Castle, and B.W. Schafer, “Seismic Design of Cold-Formed Steel Lateral Load-Resisting Systems: A Guide for Practicing Engineers”, *NEHRP Seismic Design Technical Brief No.12*, National Institute of Standards and Technology, Engineering Laboratory, Gaithersburg, 2016.

26. Leng, J., K.D. Peterman, G. Bian, S.G. Buonopane, and B.W. Schafer, “Modeling Seismic Response of a Full-Scale Cold-Formed Steel-Framed Building”, *Engineering Structures*, Vol. 153, pp. 146-165, 2017.

27. Efe, H., A. Kasal, “Determination of Some Physical and Mechanical Properties of Various Wood and Wood Composite Materials”, *Journal of Polytechnic*, Vol. 10, No: 3, pp. 303-311, 2007.

28. Adany, S., N. Silverstre, B.W. Schafer, and D. Camotim, “GBT and cFSM: Two Modal Approaches to the Buckling Analysis of Unbranched Thin-Walled Members”, *Advanced Steel Construction*, Vol. 5, No: 2, pp. 195-223, 2009.

APPENDIX A: TECHNICAL DOCUMENTATION (REPRESENTATIVE DRAWINGS) OF THE PROJECT BUILDING

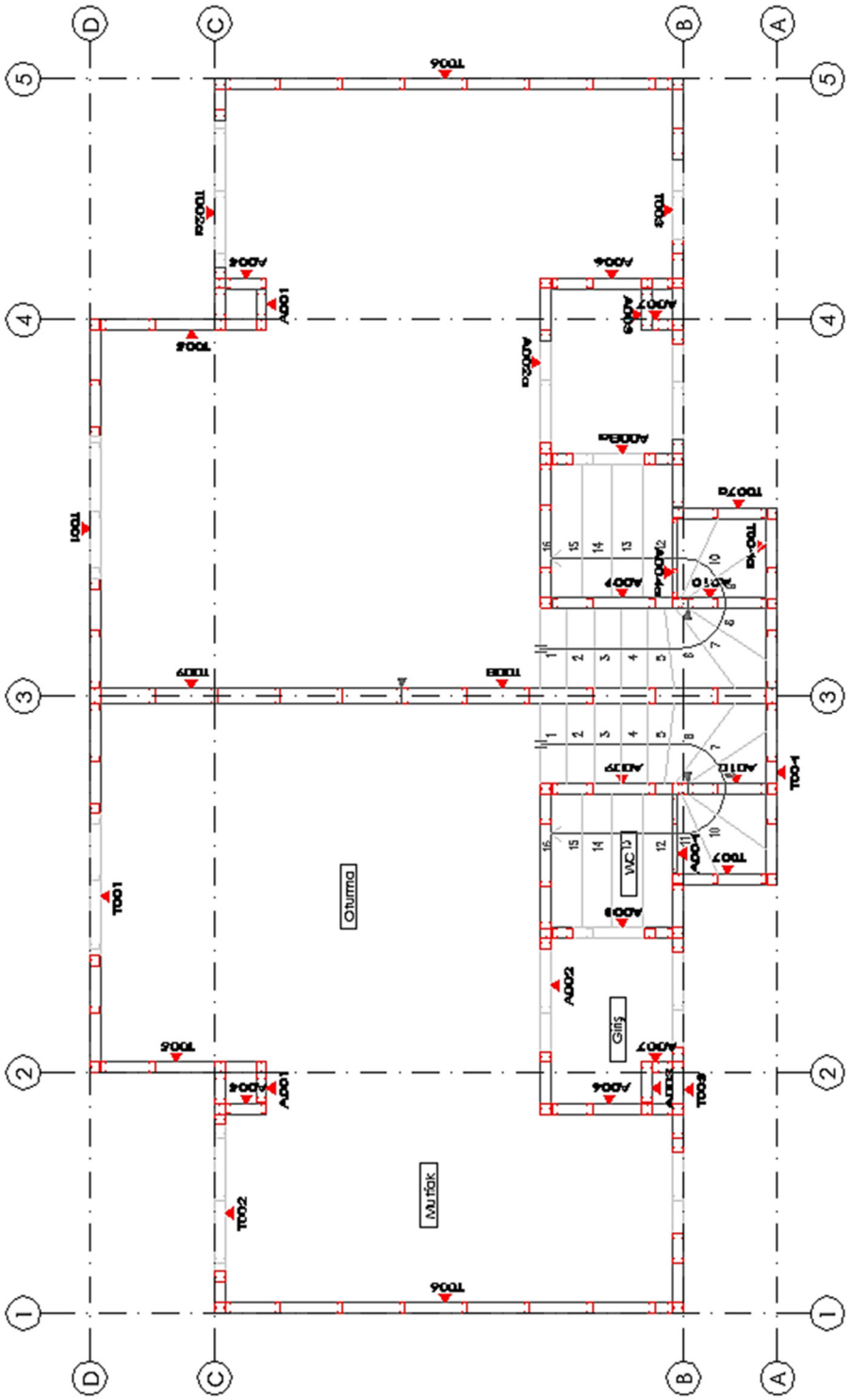

Figure A.1. First floor plan (wall numbering) of Enez villa (provided by the manufacturer company for educational purposes).

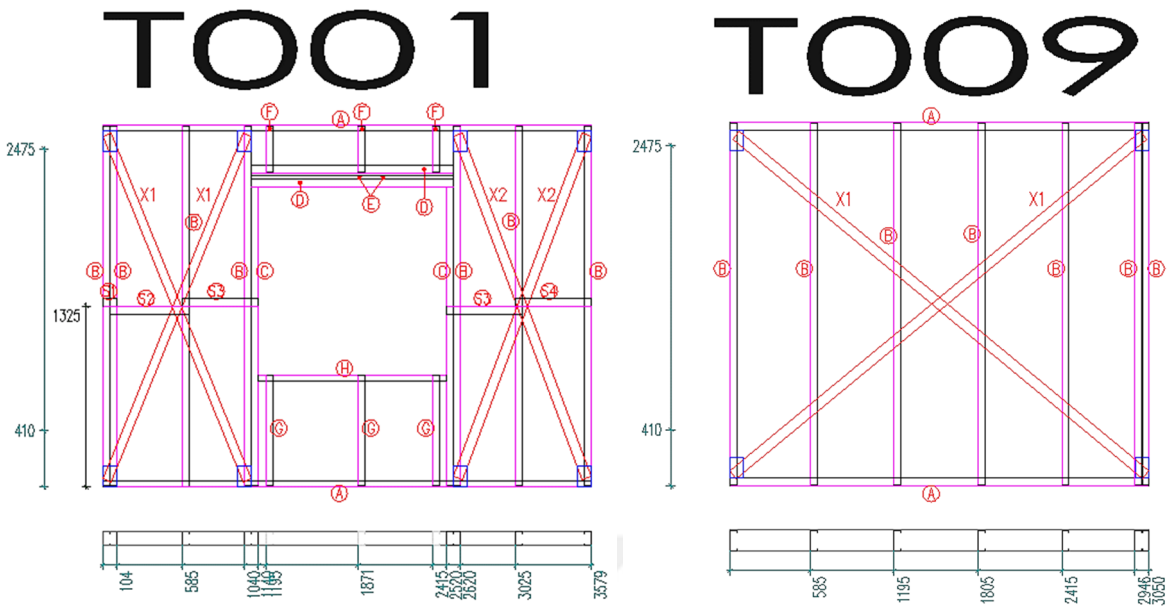

Figure A.2. T001 and T009 wall configurations for representative purposes (provided by the manufacturer company for educational purposes).

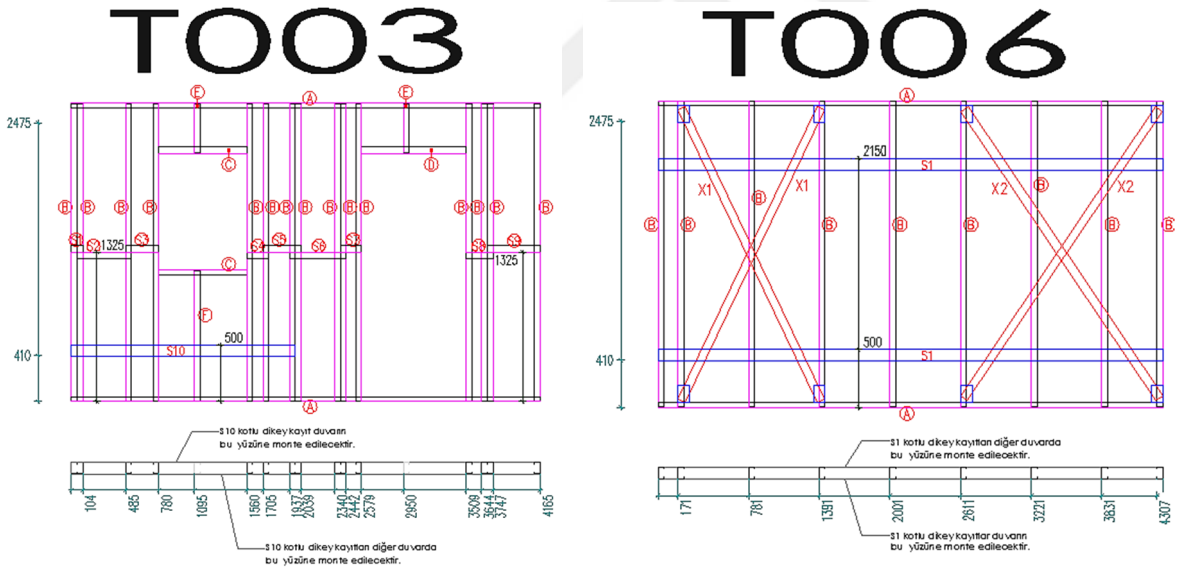

Figure A.3. T003 and T006 wall configurations for representative purposes (provided by the manufacturer company for educational purposes).

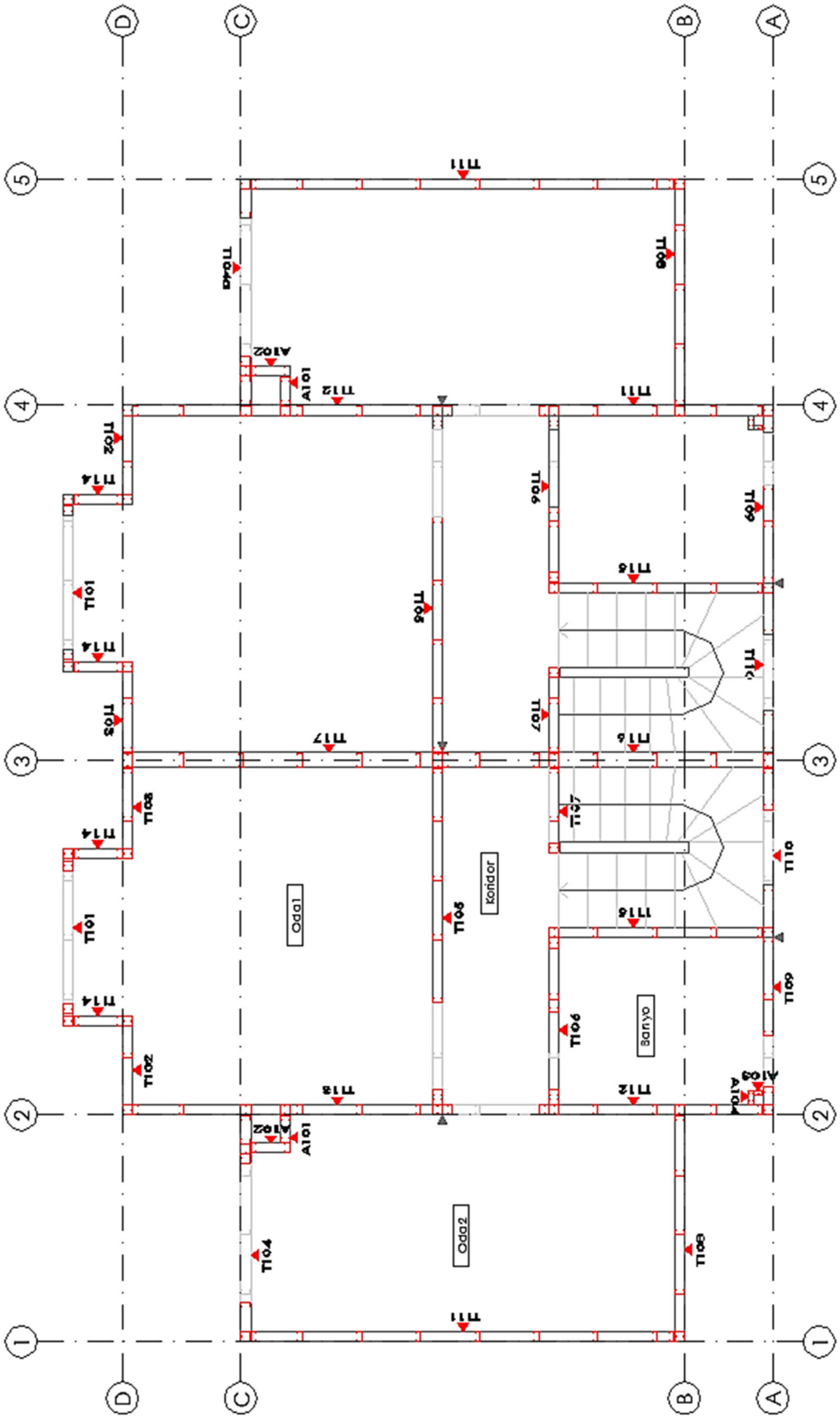

Figure A.4. Second floor plan (wall numbering) of Enez villa (provided by the manufacturer company for educational purposes).

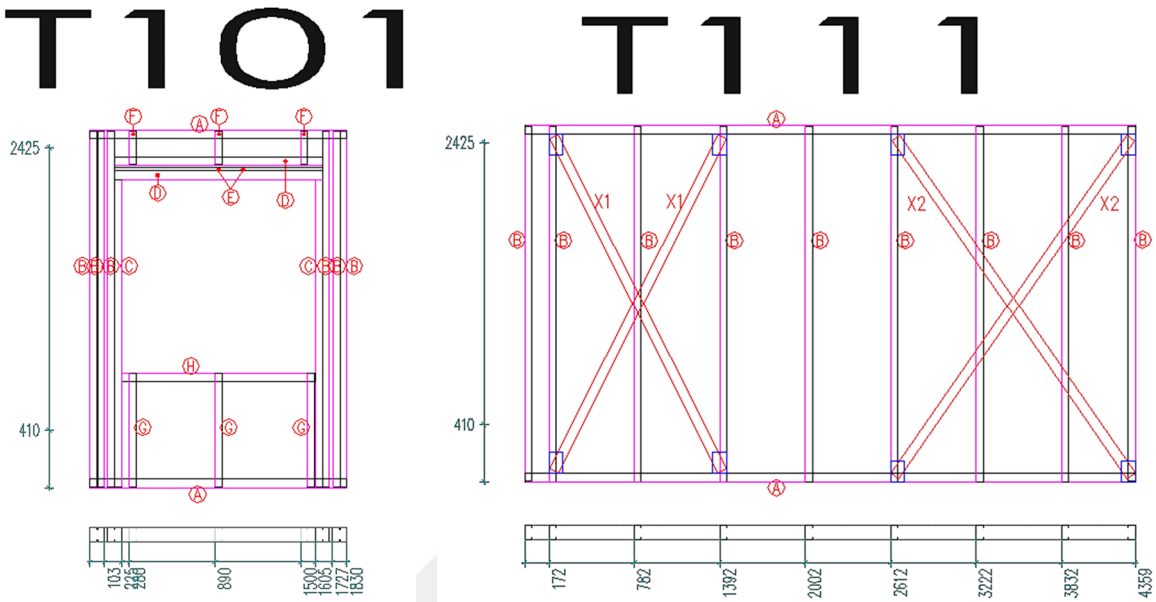

Figure A.5. T101 and T111 wall configurations for representative purposes (provided by the manufacturer company for educational purposes).

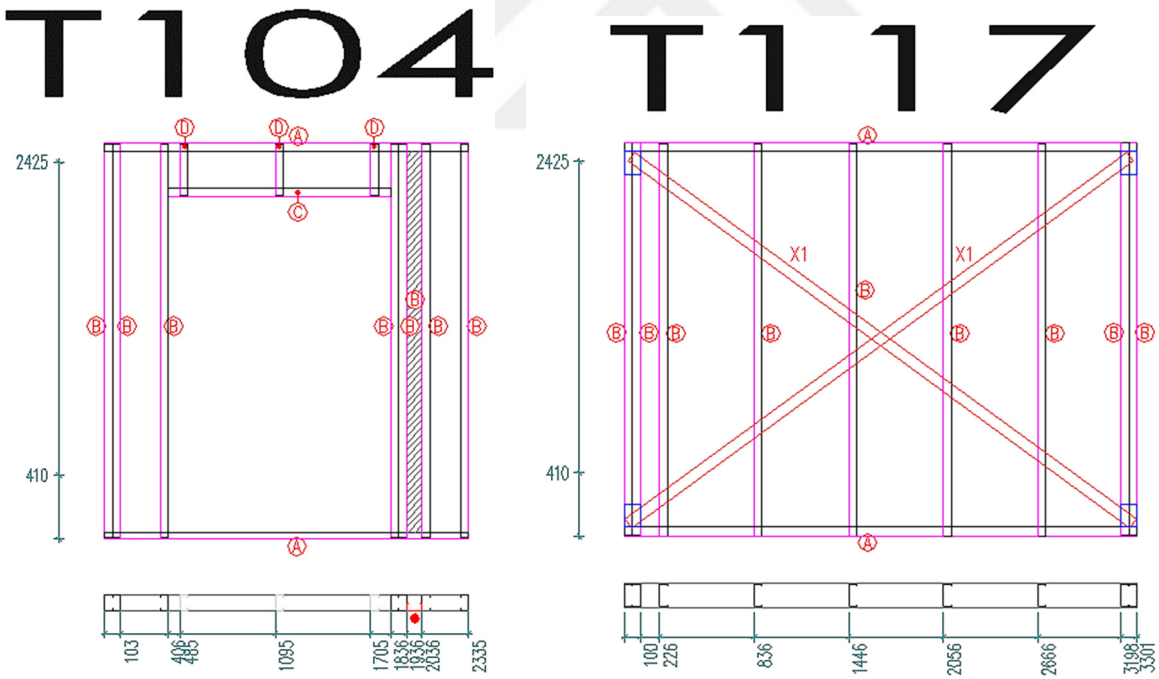

Figure A.6. T104 and T117 wall configurations for representative purposes (provided by the manufacturer company for educational purposes).

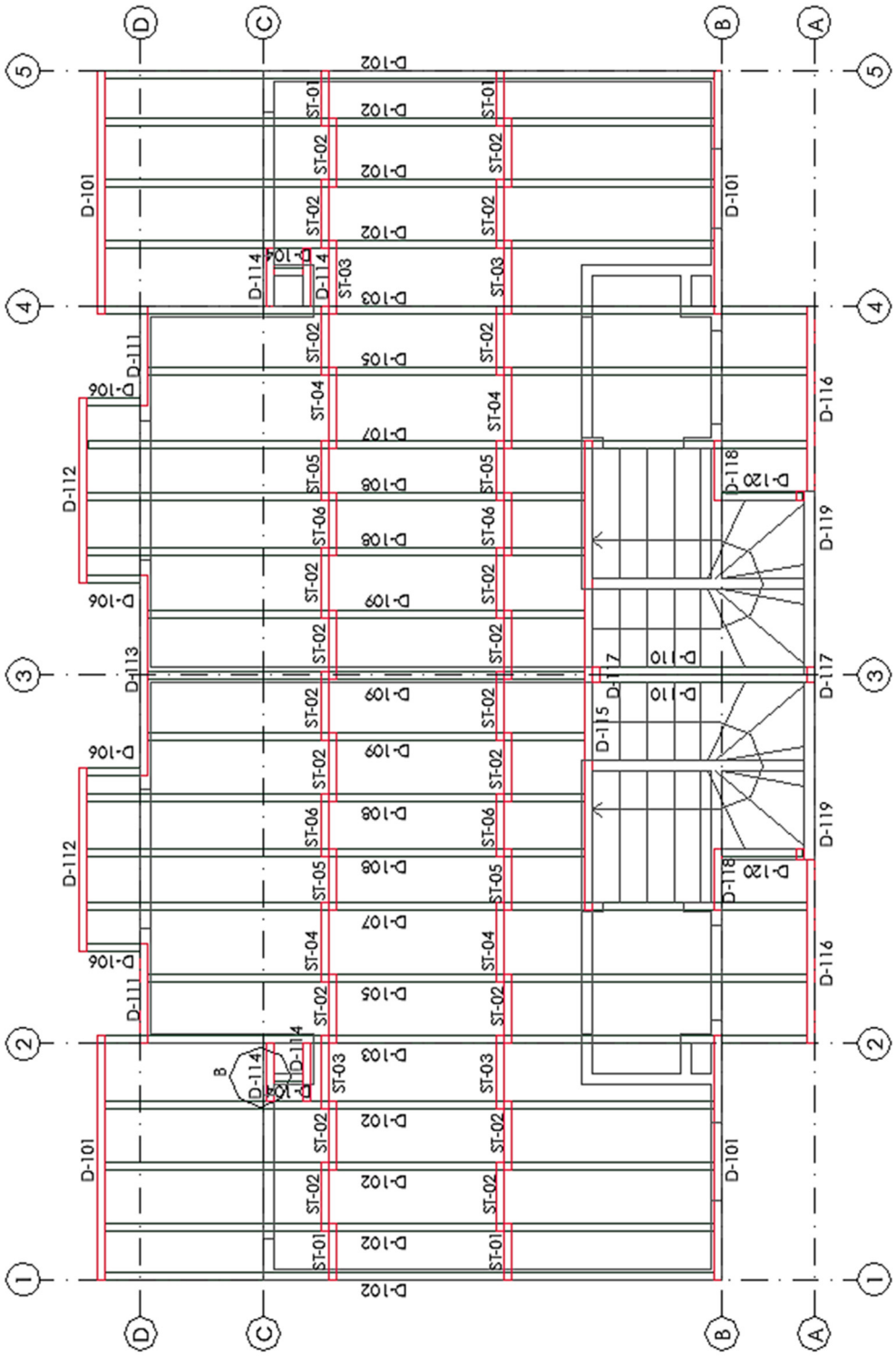

Figure A.7. First floor girder plan of Enez villa (provided by the manufacturer company for educational purposes).

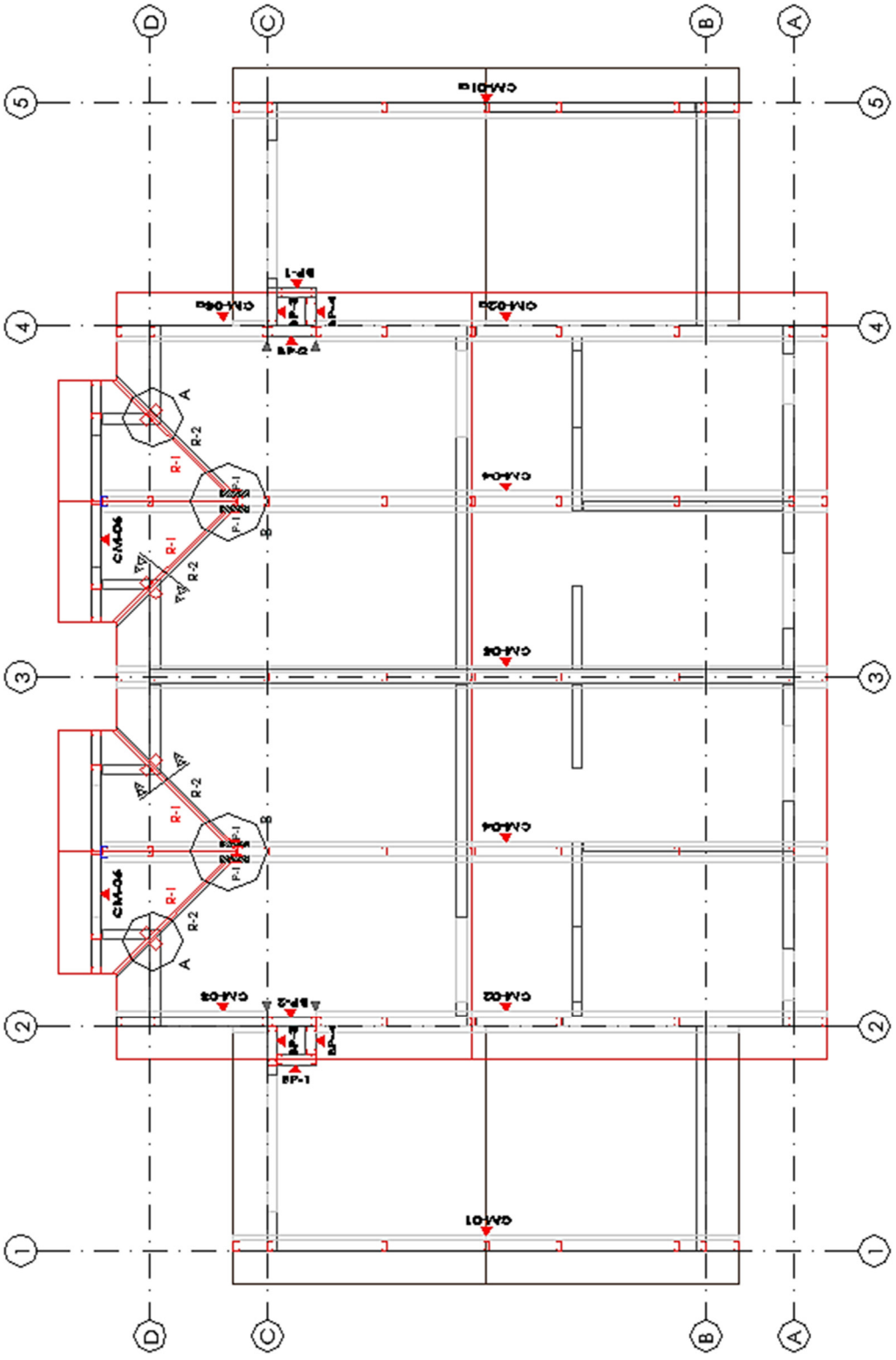

Figure A.8. Roof level truss plan of Enez villa (provided by the manufacturer company for educational purposes).

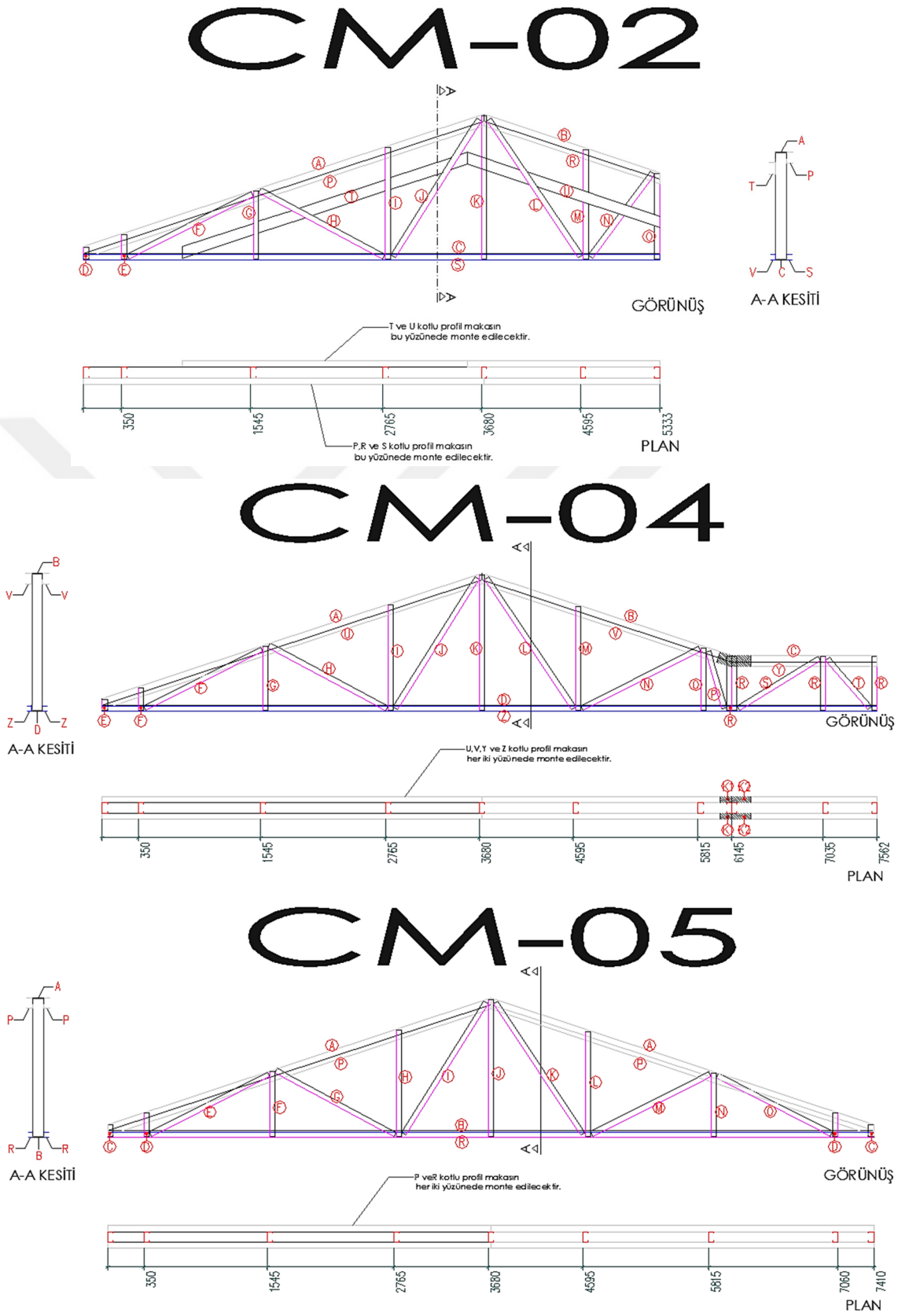

Figure A.9. CM-02, CM-04 and CM-05 truss configurations for representative purposes (provided by the manufacturer company for educational purposes).

APPENDIX B: AMBIENT VIBRATON TEST RESULTS OF THE PROJECT BUILDING

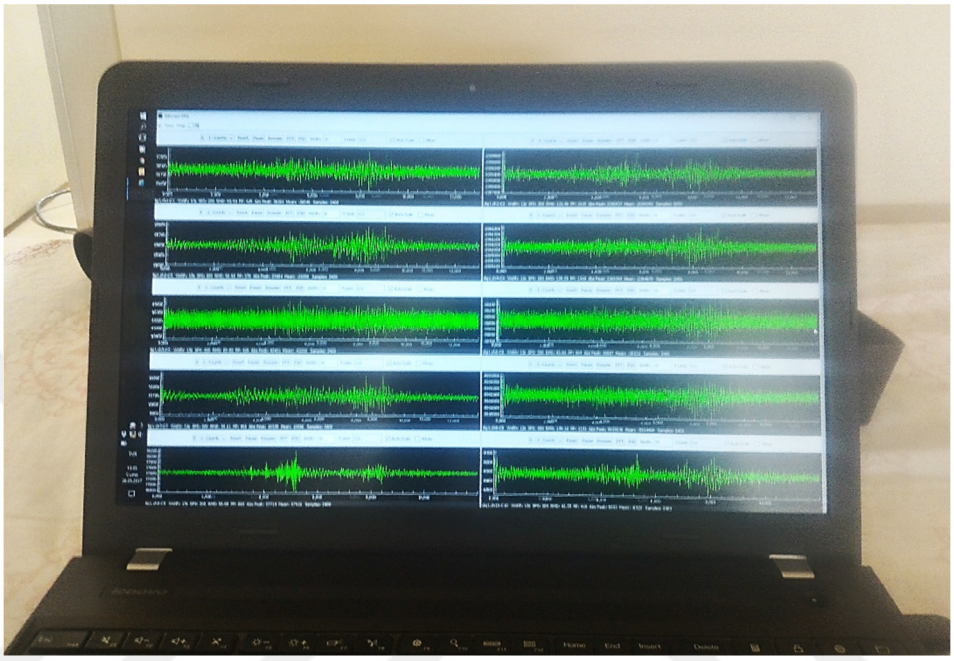

Figure B.1. Live on-site monitoring of the ambient vibration test at Enez villa.

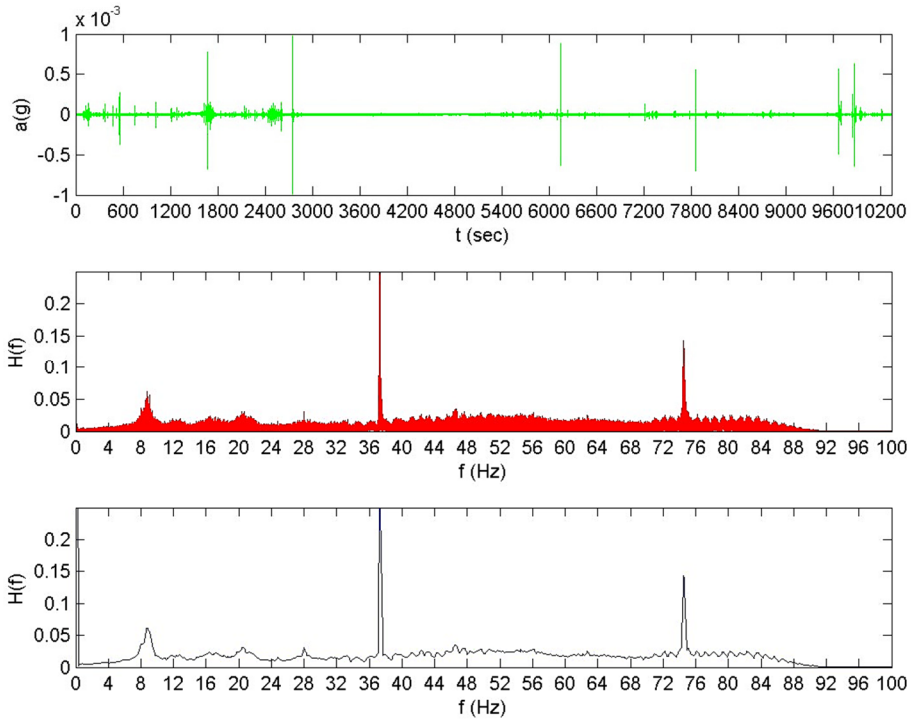

Figure B.2. Full AVT records and consequent FFT decompositions of Channel-1 readings.

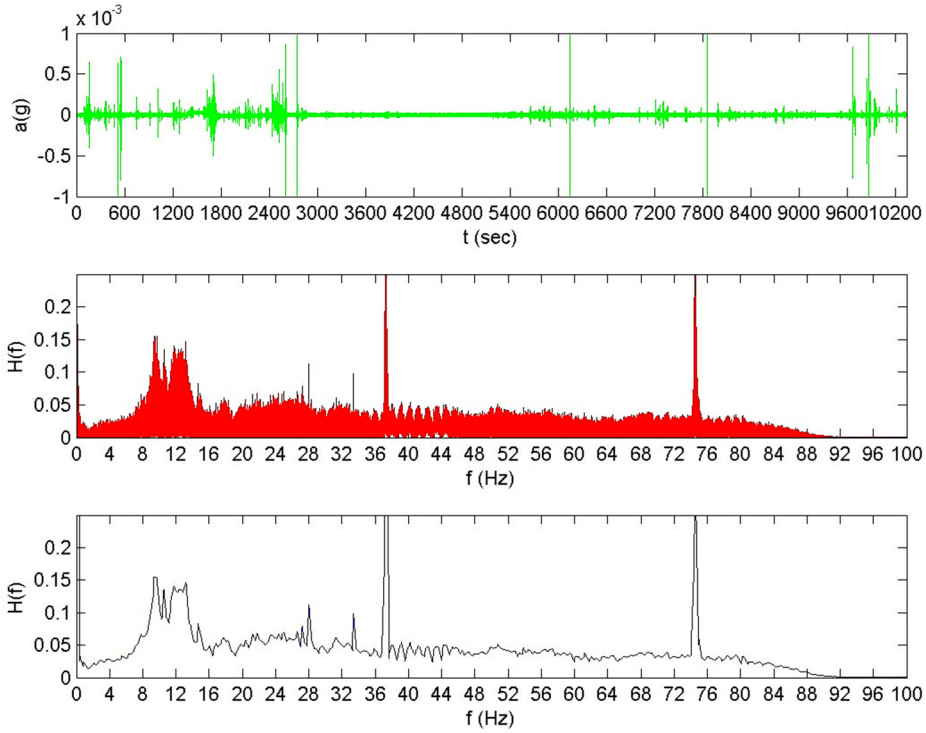

Figure B.3. Full AVT records and consequent FFT decompositions of Channel-2 readings.

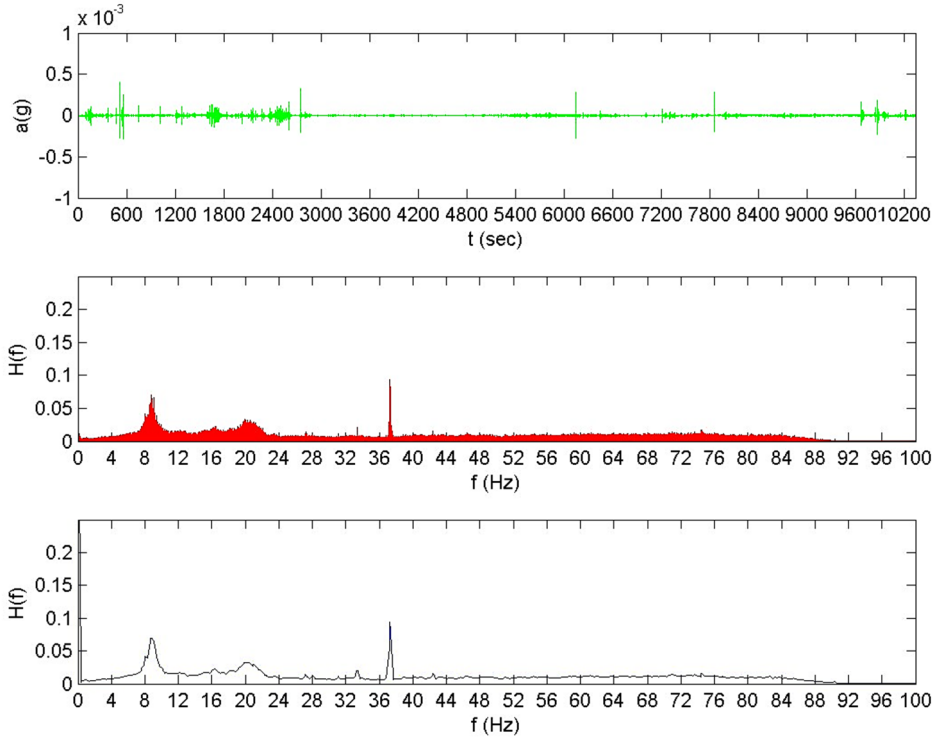

Figure B.4. Full AVT records and consequent FFT decompositions of Channel-3 readings.

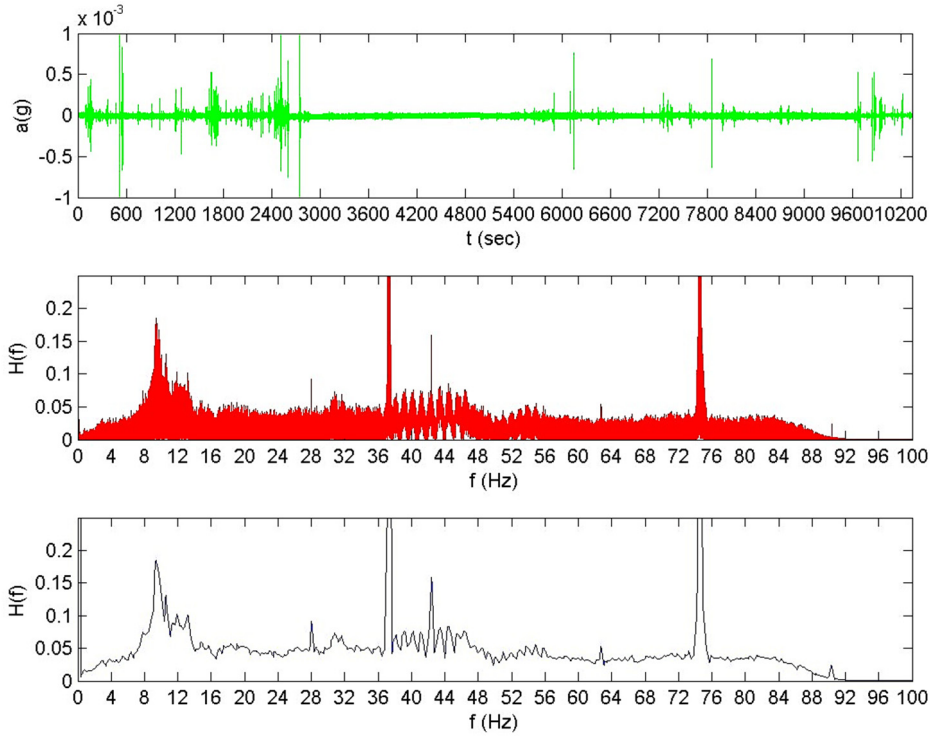

Figure B.5. Full AVT records and consequent FFT decompositions of Channel-4 readings.

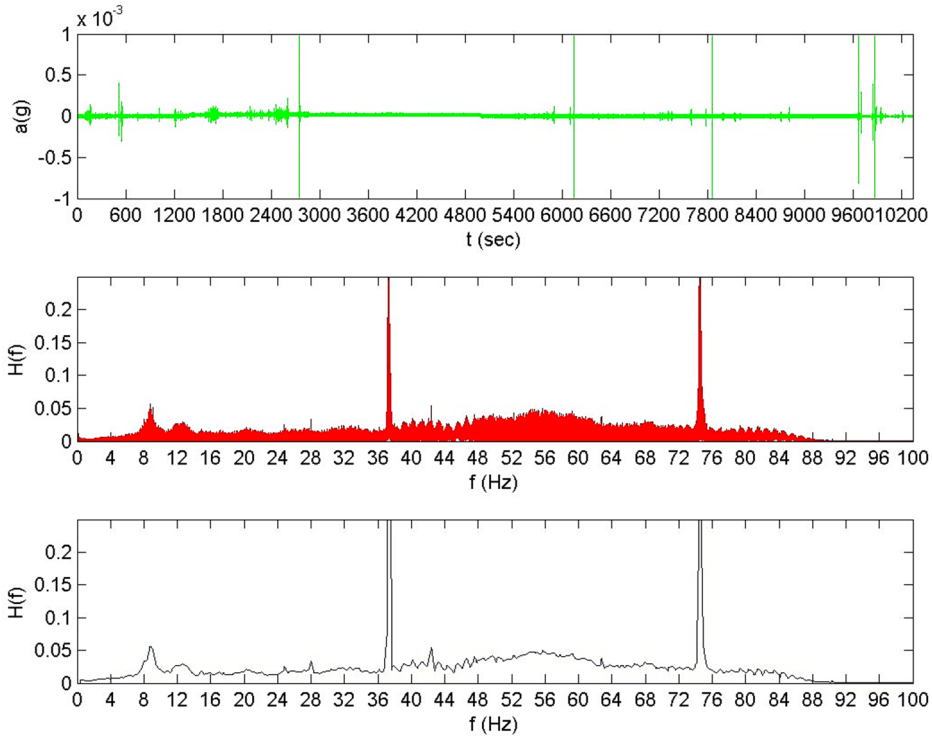

Figure B.6. Full AVT records and consequent FFT decompositions of Channel-5 readings.

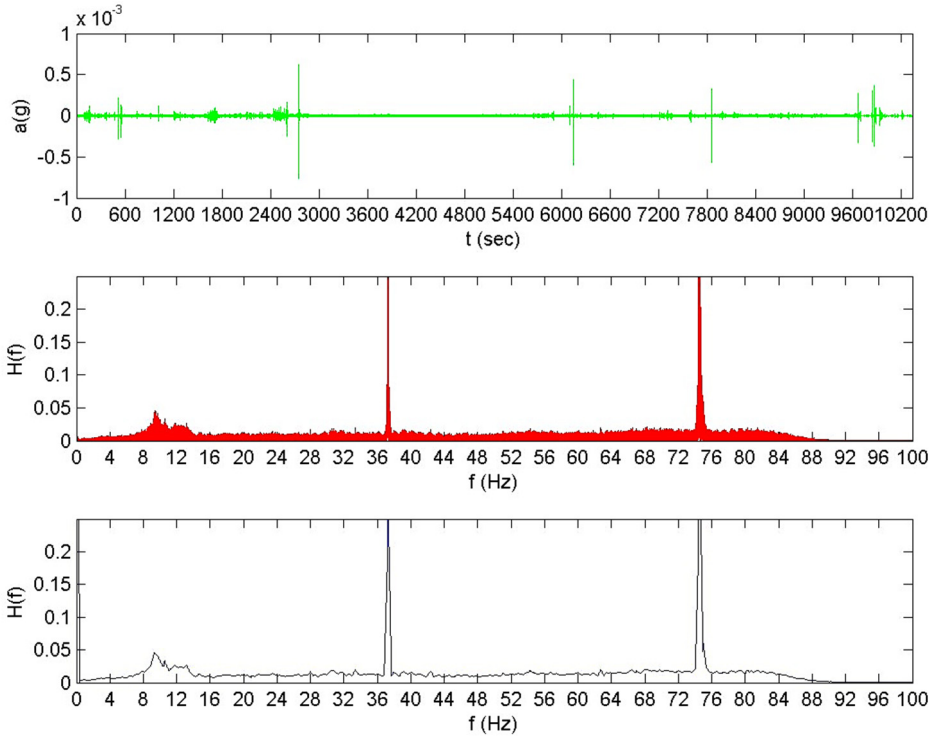

Figure B.7. Full AVT records and consequent FFT decompositions of Channel-6 readings.

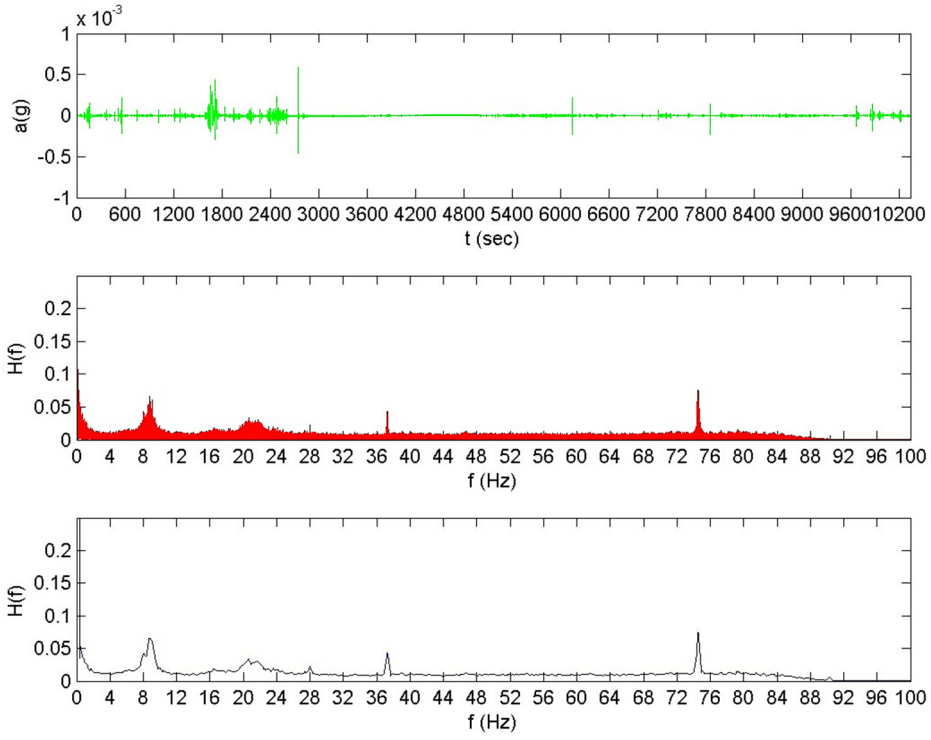

Figure B.8. Full AVT records and consequent FFT decompositions of Channel-7 readings.

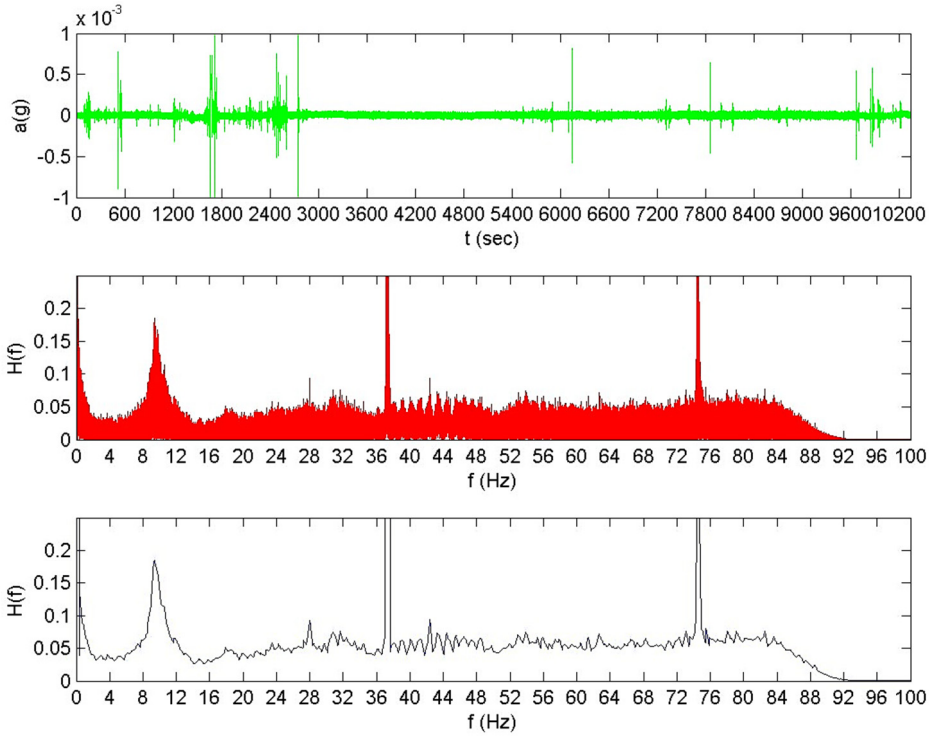

Figure B.9. Full AVT records and consequent FFT decompositions of Channel-8 readings.

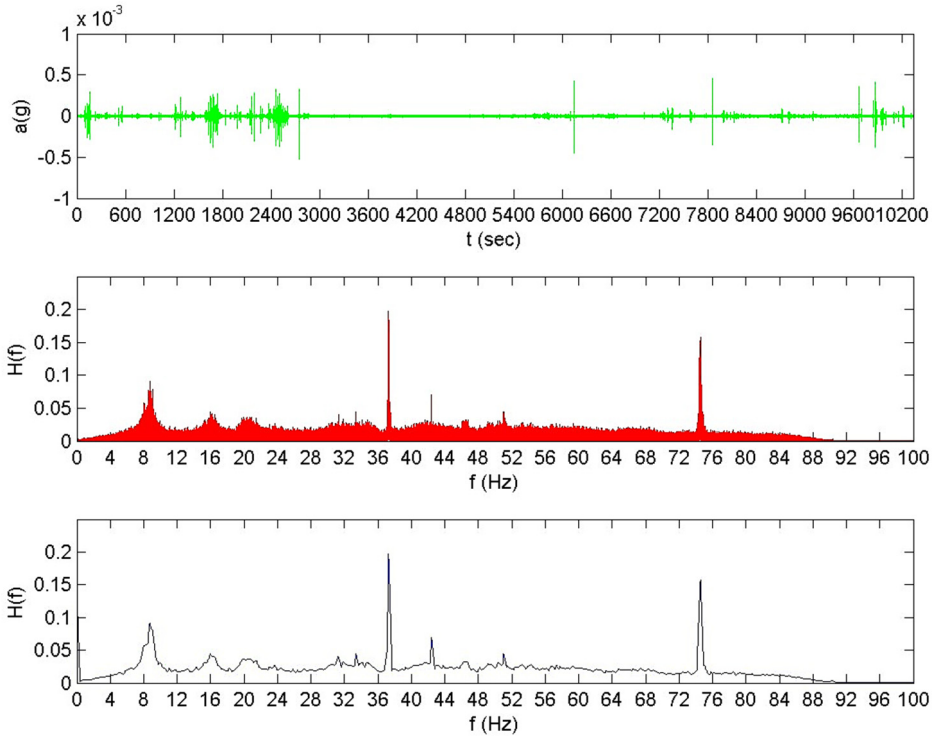

Figure B.10. Full AVT records and consequent FFT decompositions of Channel-9 readings.

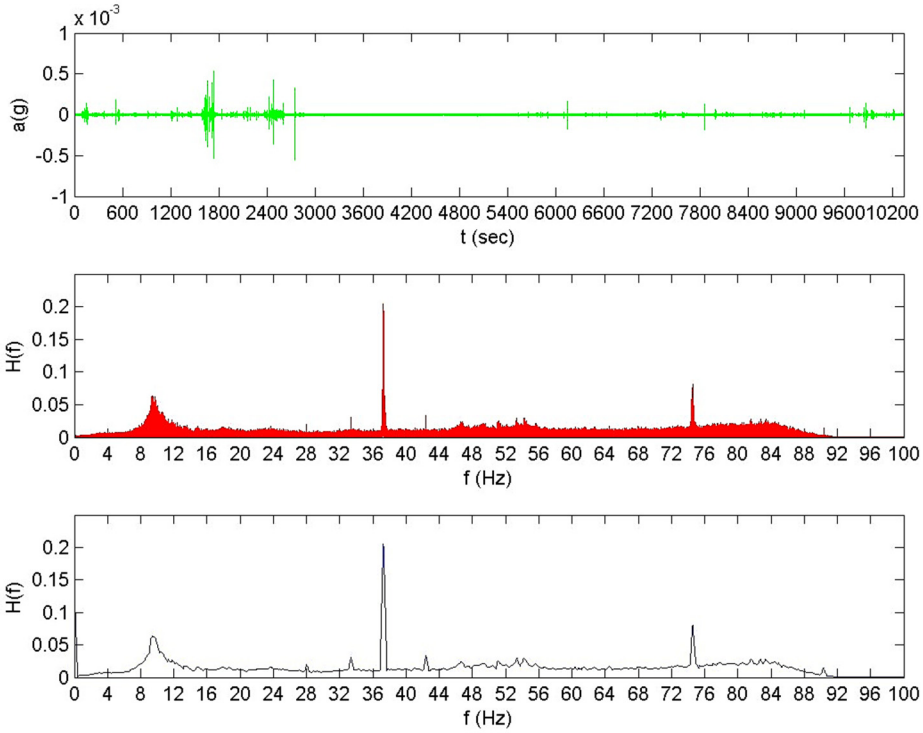

Figure B.11. Full AVT records and consequent FFT decompositions of Channel-10 readings.

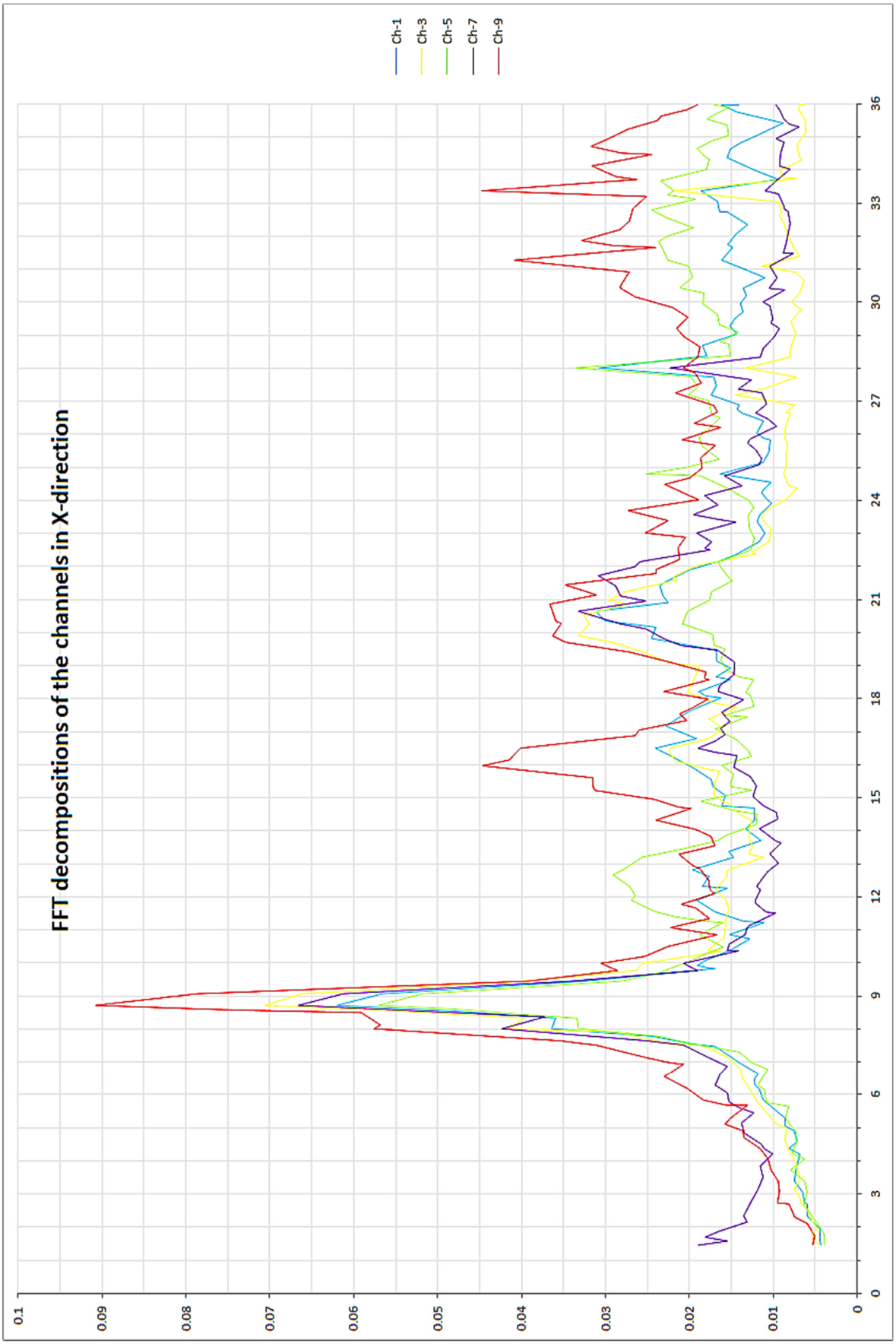

Figure B.12. The resultant FFT decompositions of all the channels in X-direction.

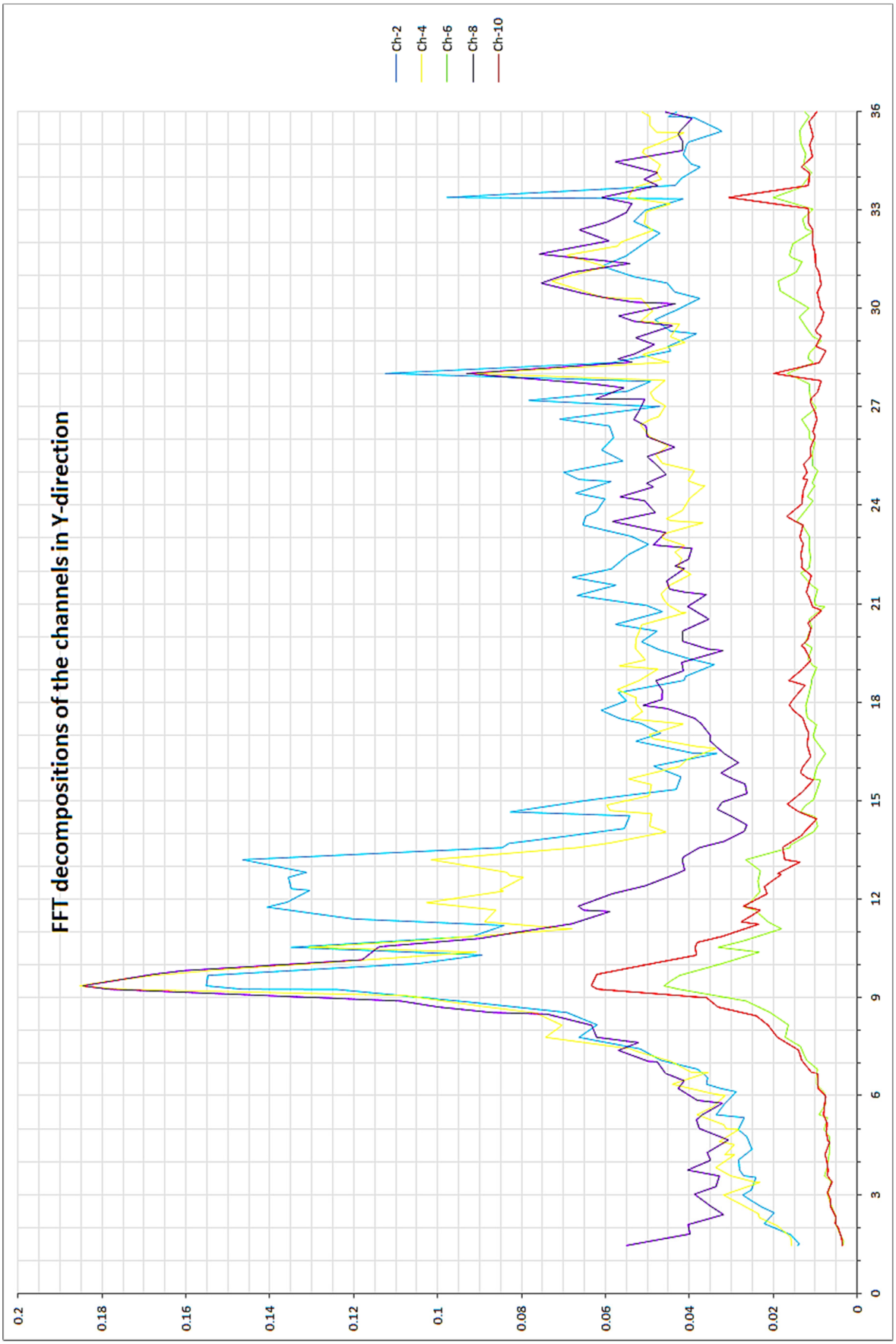

Figure B.13. The resultant FFT decompositions of all the channels in Y-direction.

APPENDIX C: IMAGES & RESULTS FROM THE LAB EXPERIMENT #1



Figure C.1. General view of the test pad in the Structures Laboratory of Boğaziçi University.

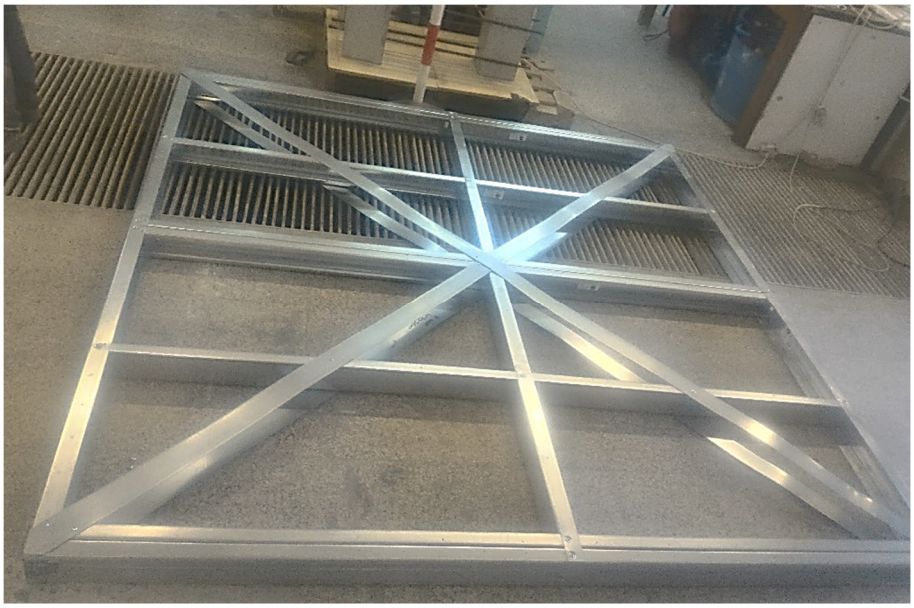

Figure C.2. General view of the assembled CFS frame with bracings.



Figure C.3. General view of the completed test specimen being attached to the testing rig.





Figure C.4. Local damage observed on each side of the upper corners of the gypsum panels after the test.



Figure C.5. Local damage observed on the lower corners of the gypsum panels after the test.



Figure C.6. General view of the damage observed in the frame elements after the test.

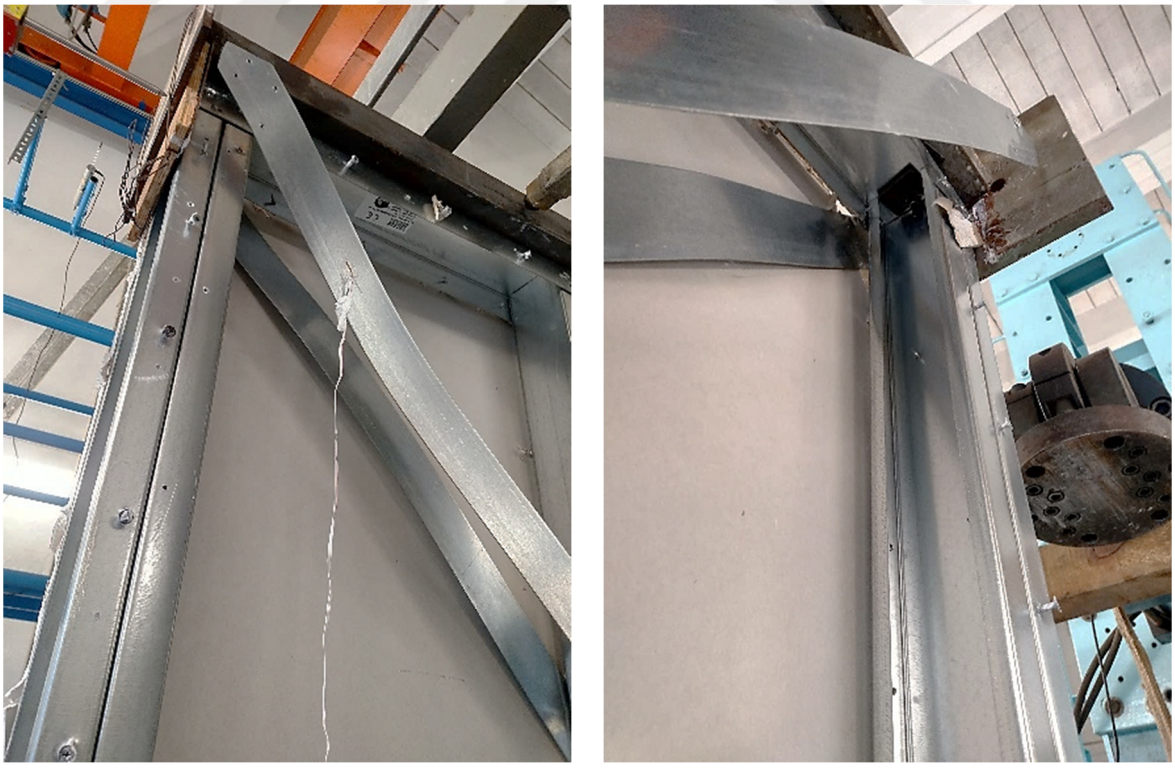

Figure C.7. Local damage observed in upper corner brace connections.



Figure C.8. Local damage observed in the lower corner brace connections.

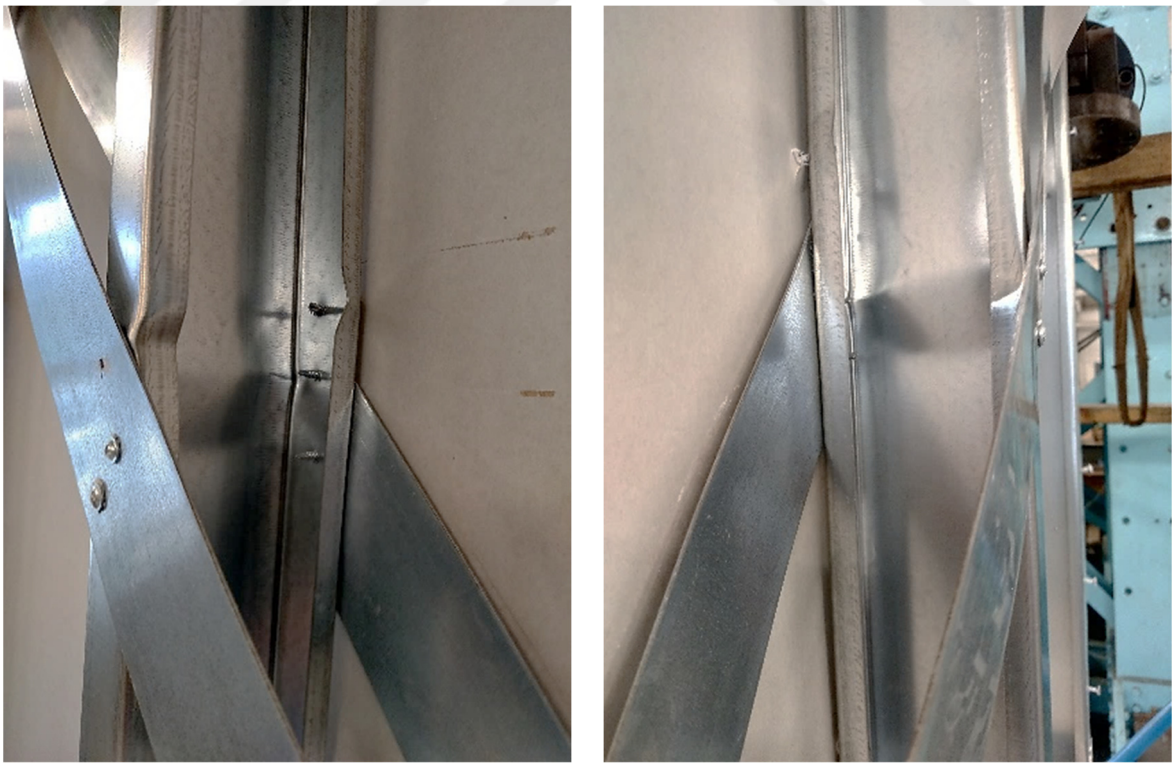

Figure C.9. Local damage observed on the intermediate studs.



Figure C.10. Local damage observed on the exterior girders.

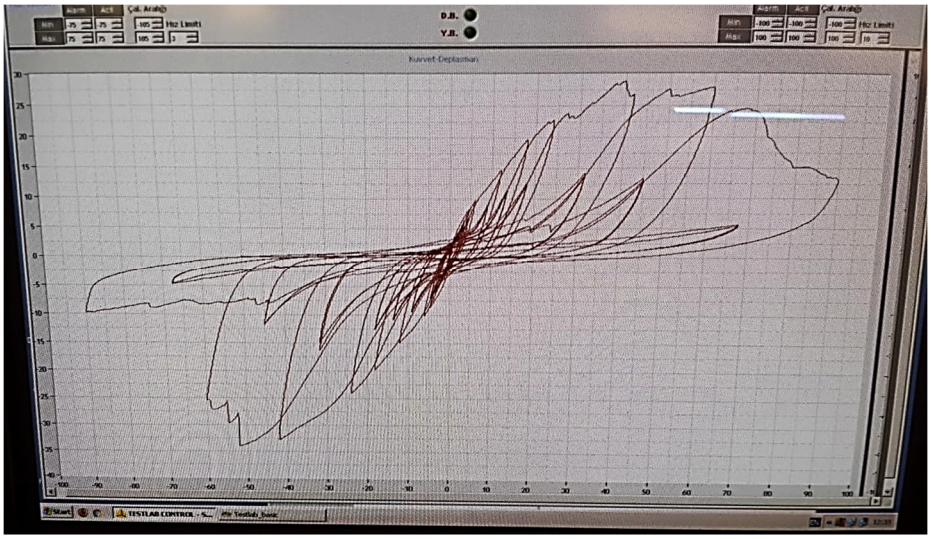

Figure C.11. General view of the resultant hysteresis curve obtained after the test.

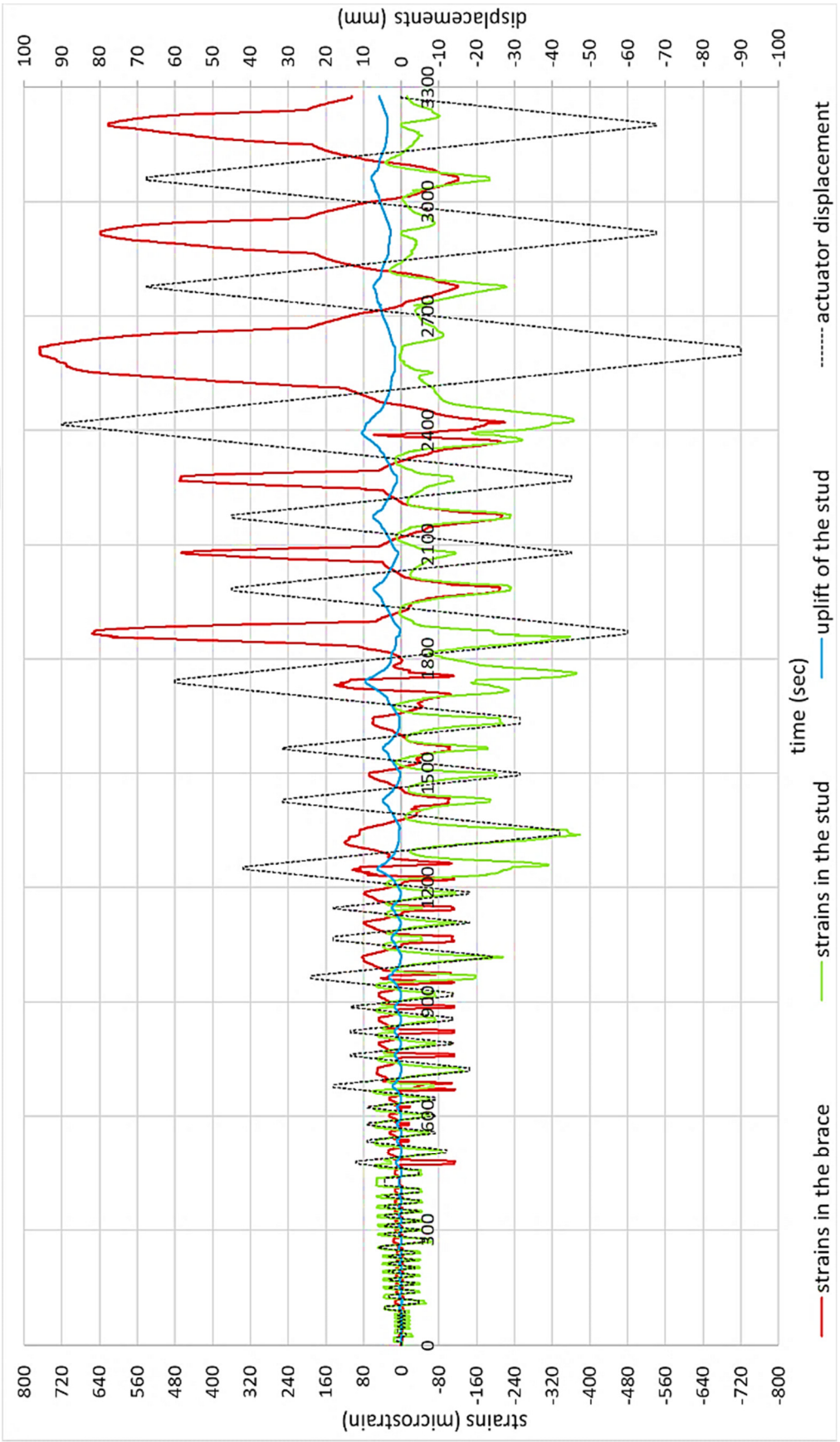

Figure C.12. Time-history sketches of the sensors and gauges on the actuator-side of the test specimen.

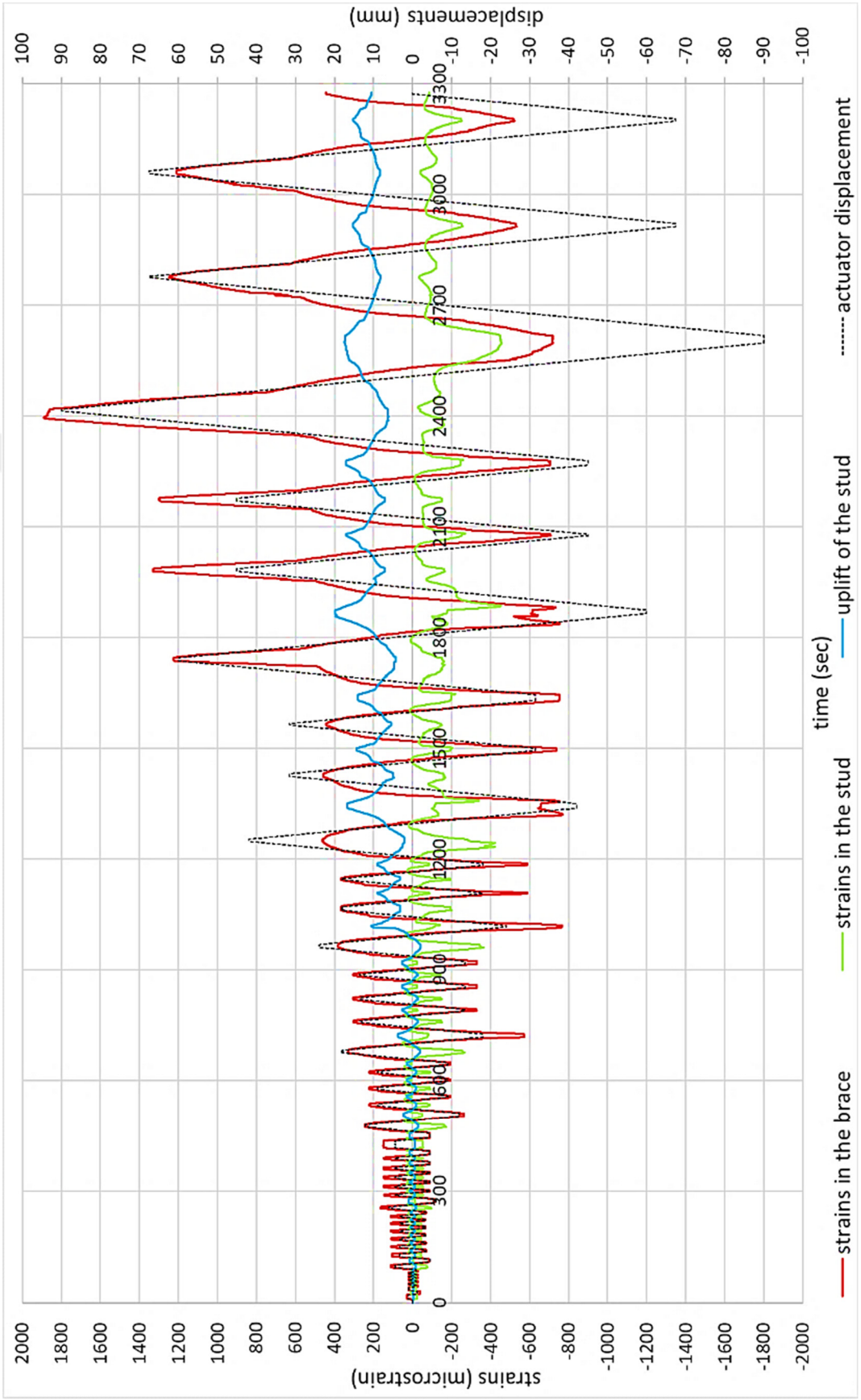

Figure C.13. Time-history sketches of the sensors and gauges on the free-side of the test specimen.

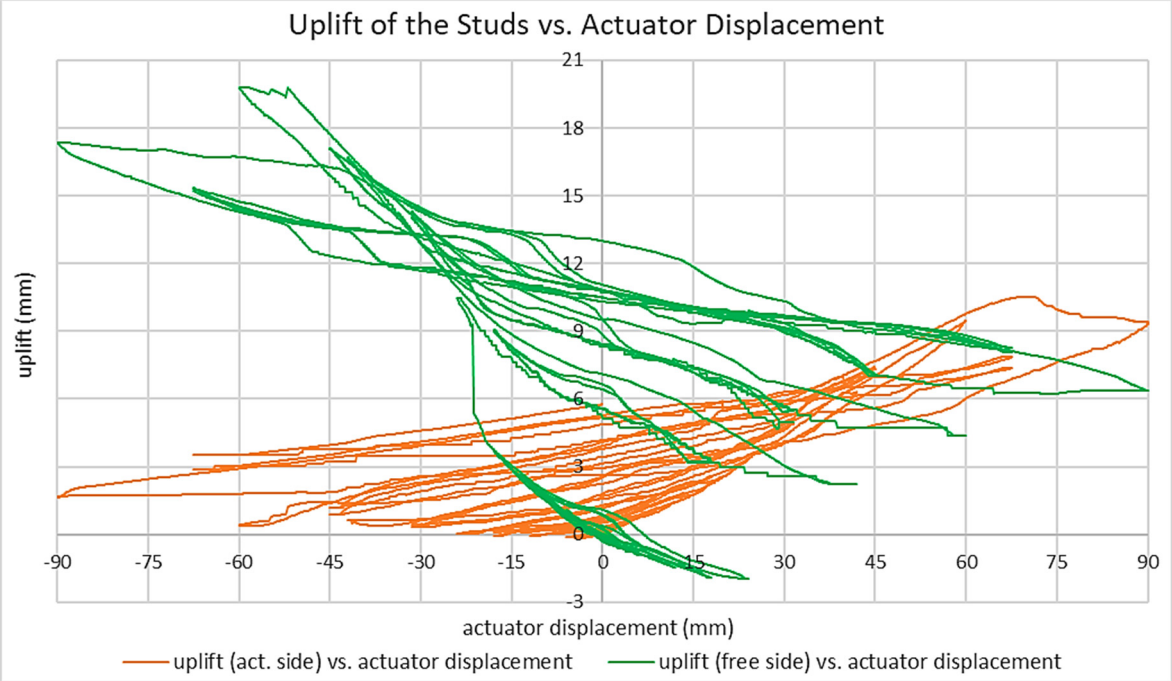

Figure C.14. Uplift of the studs vs. actuator displacement.

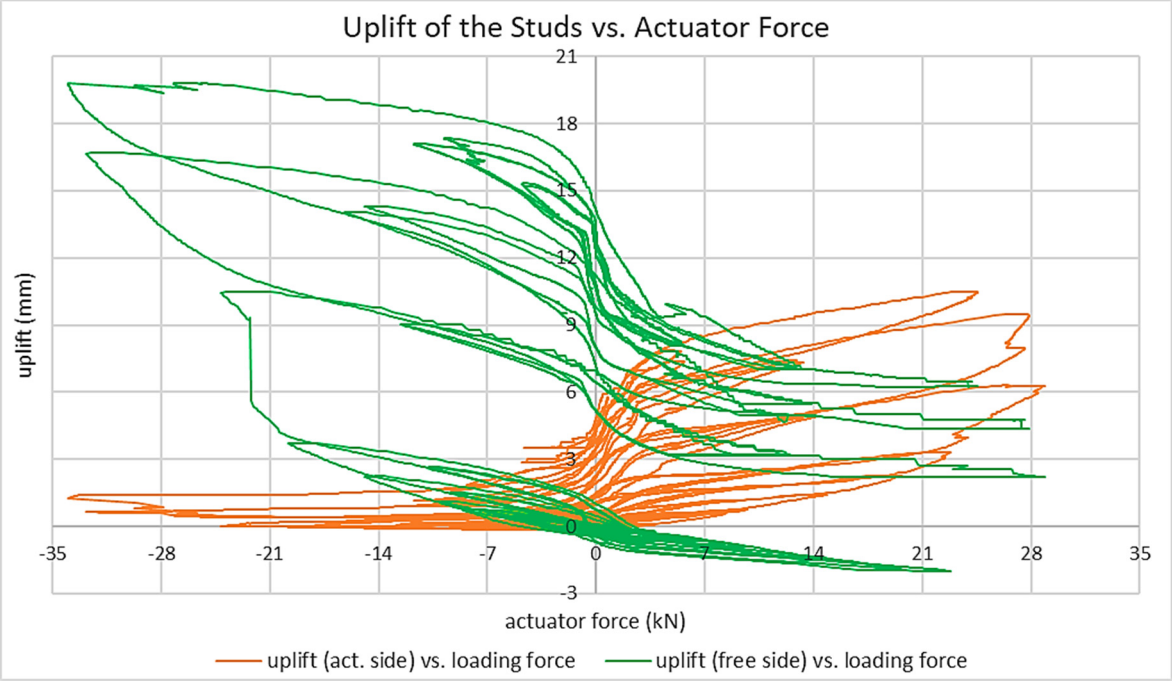

Figure C.15. Uplift of the studs vs. actuator force.

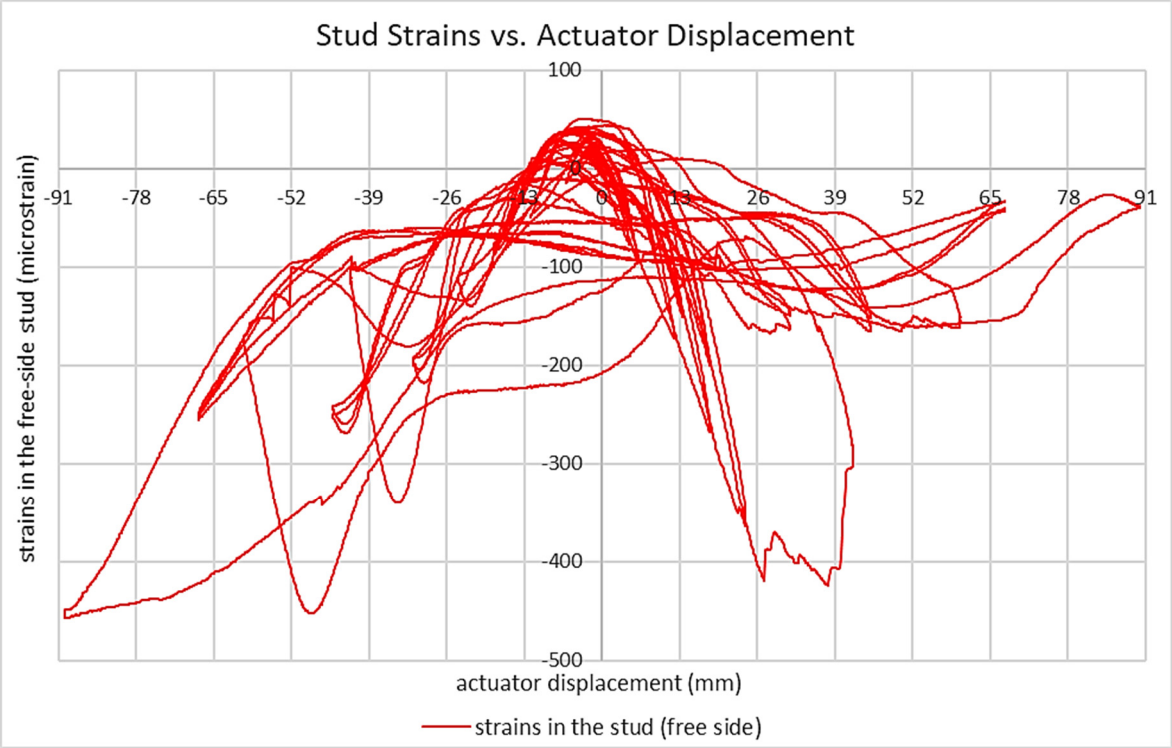

Figure C.16. Strains in the stud on the free-side of the test specimen vs. actuator displacement.

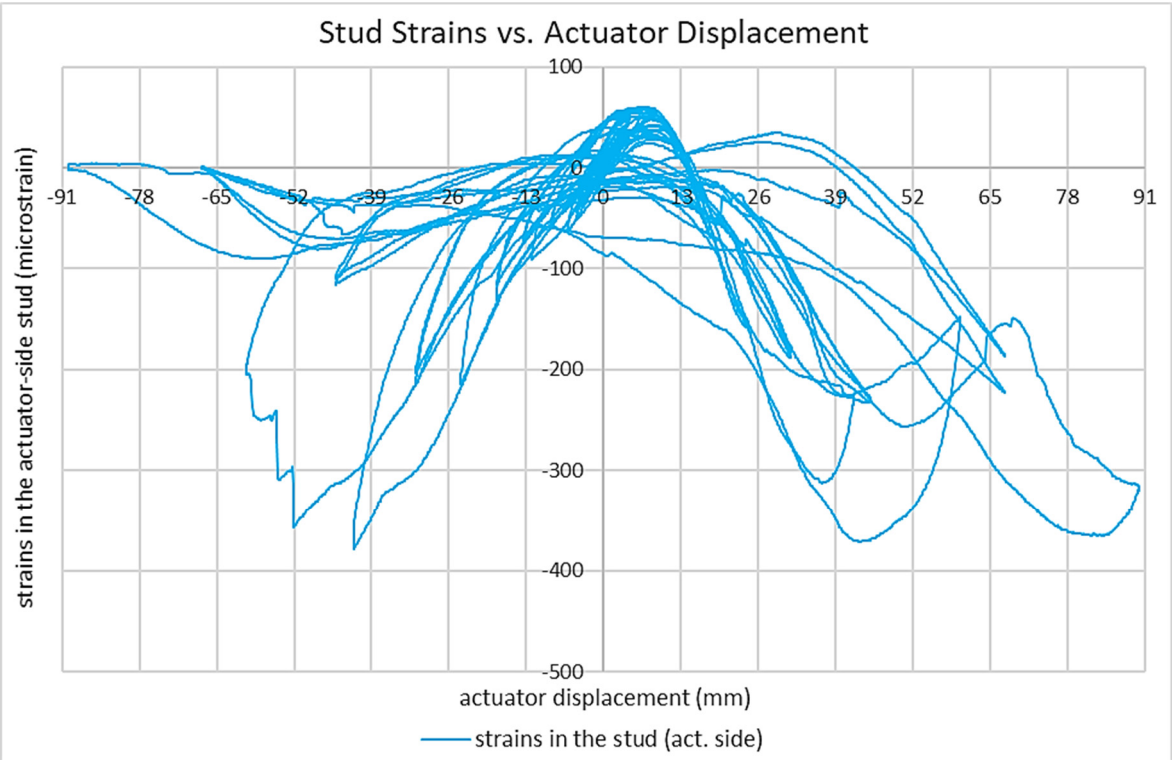

Figure C.17. Strains in the stud on the actuator-side of the test specimen vs. actuator displacement.

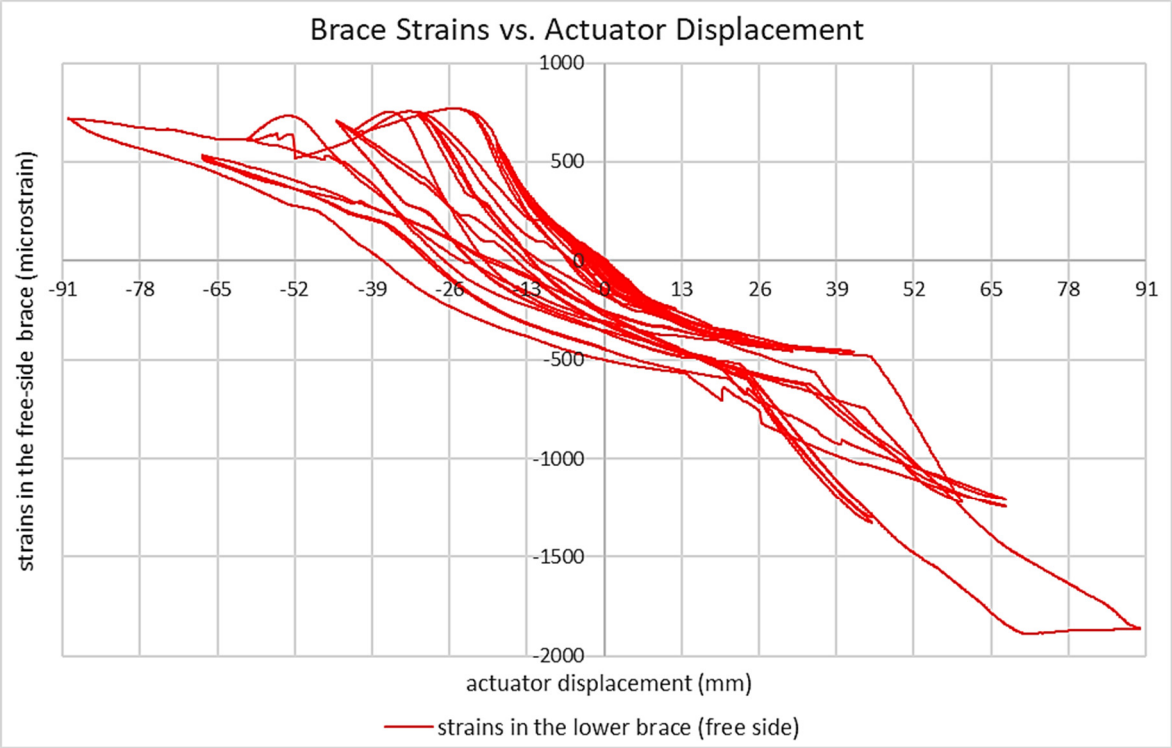

Figure C.18. Strains in the brace on the free-side of the specimen (lower corner) vs. actuator displacement.

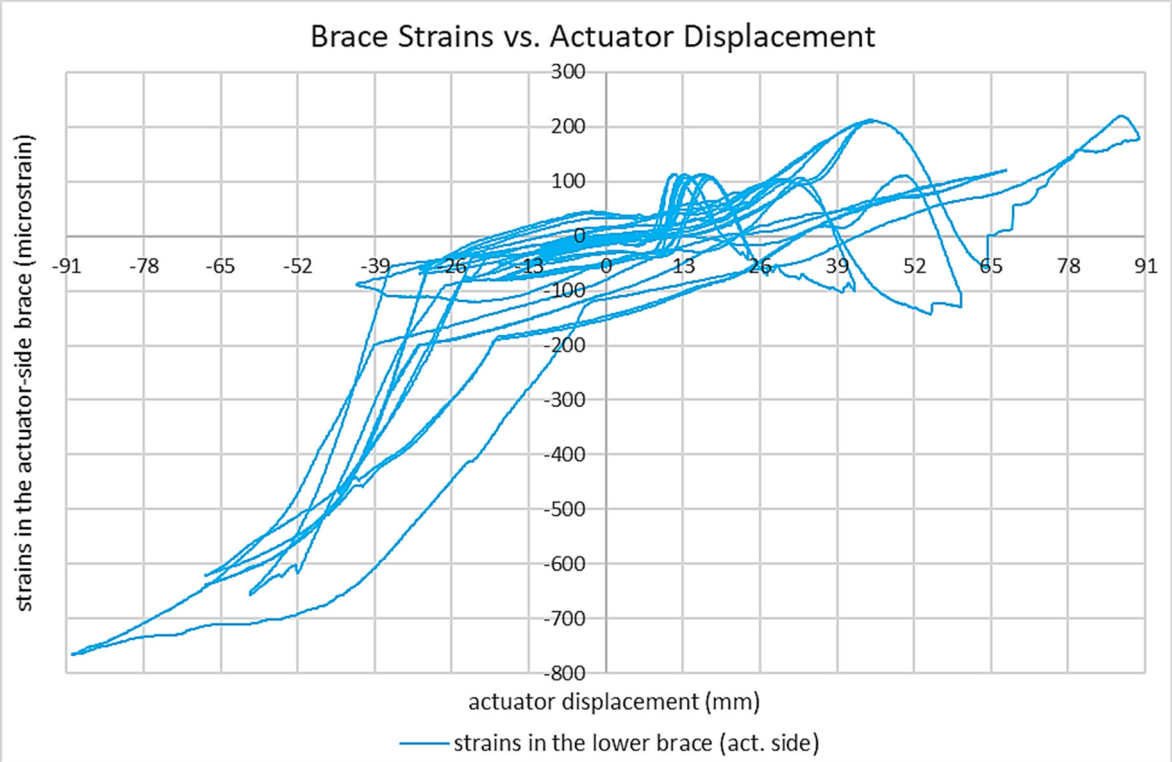

Figure C.19. Strains in the brace on the actuator-side of the specimen (lower corner) vs. actuator displacement.

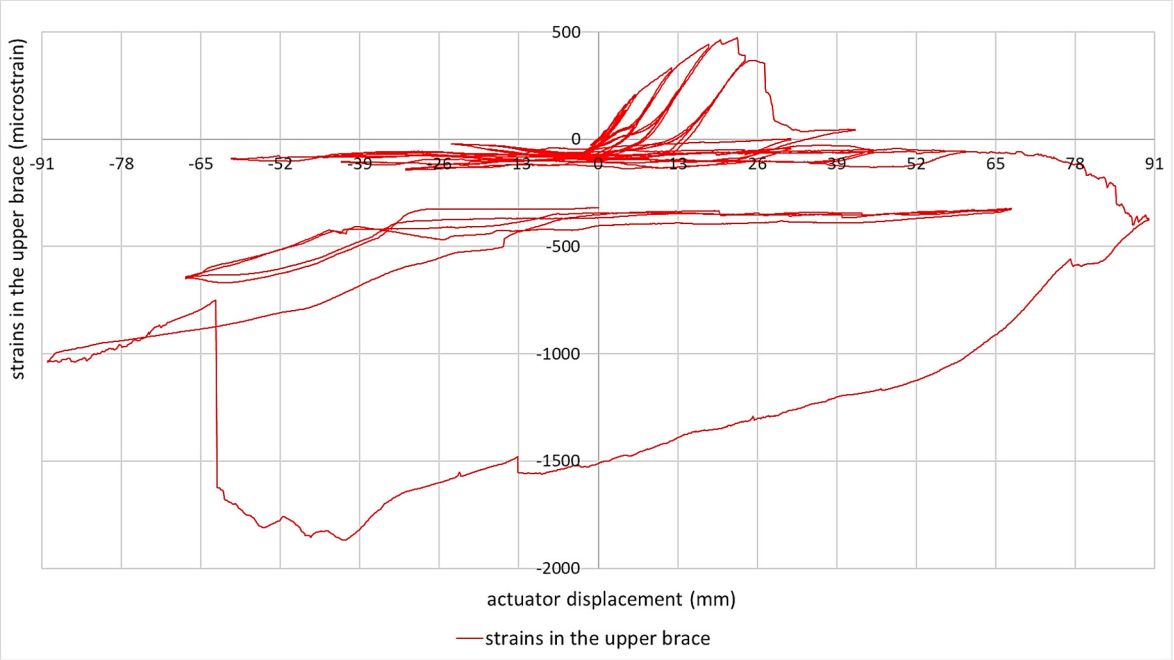

Figure C.20. Strains in the brace on the free-side of the specimen (upper corner) vs. actuator displacement.

APPENDIX D: IMAGES & RESULTS FROM THE LAB EXPERIMENT #2



Figure D.1. General view of the test specimen (with OSB panels mounted).



Figure D.2. Local damage observed on each side of the upper corners of the OSB panels after the test.



Figure D.3. Local damage observed on each side of the upper corners of the OSB panels (continued).



Figure D.4. General view of the damage observed in the frame elements after the test.



Figure D.5. Local damage observed in the upper corner elements.



Figure D.6. Local tearing observed in the upper girder, along with the broken piece.



Figure D.7. Local damage observed in the lower corner elements.

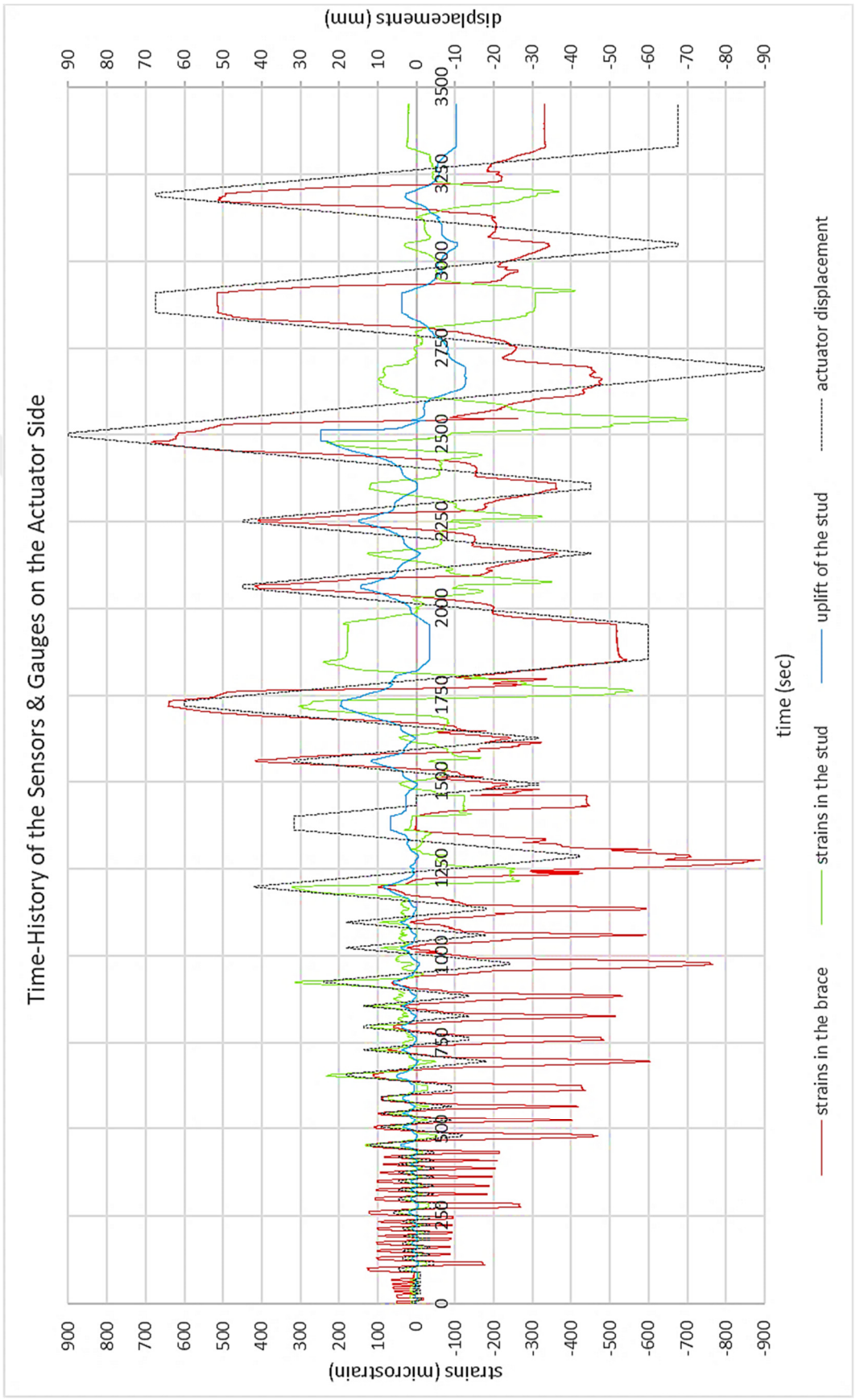

Figure D.8. Time-history sketches of the sensors and gauges on the actuator-side of the test specimen.

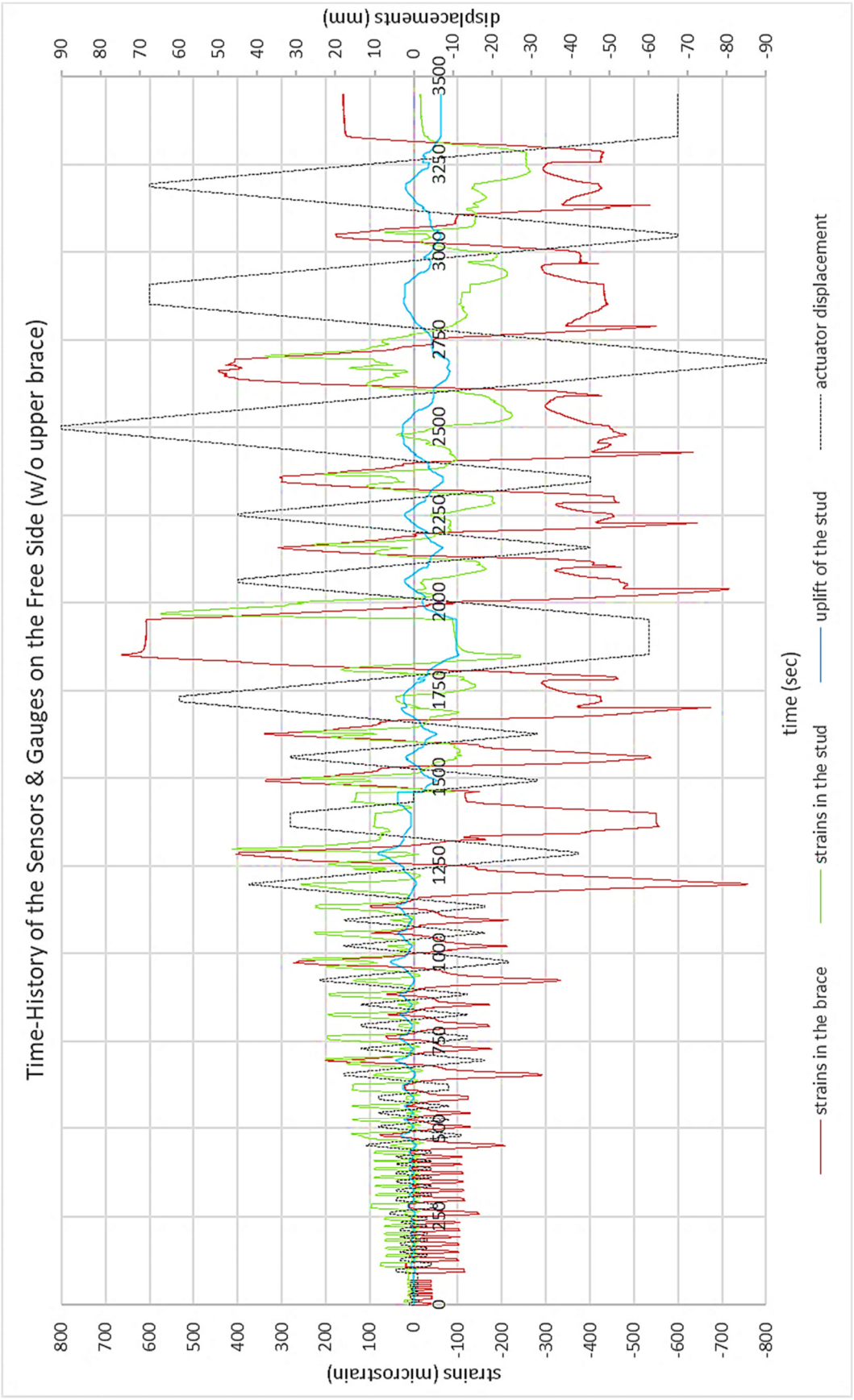

Figure D.9. Time-history sketches of the sensors and gauges on the free-side of the test specimen.

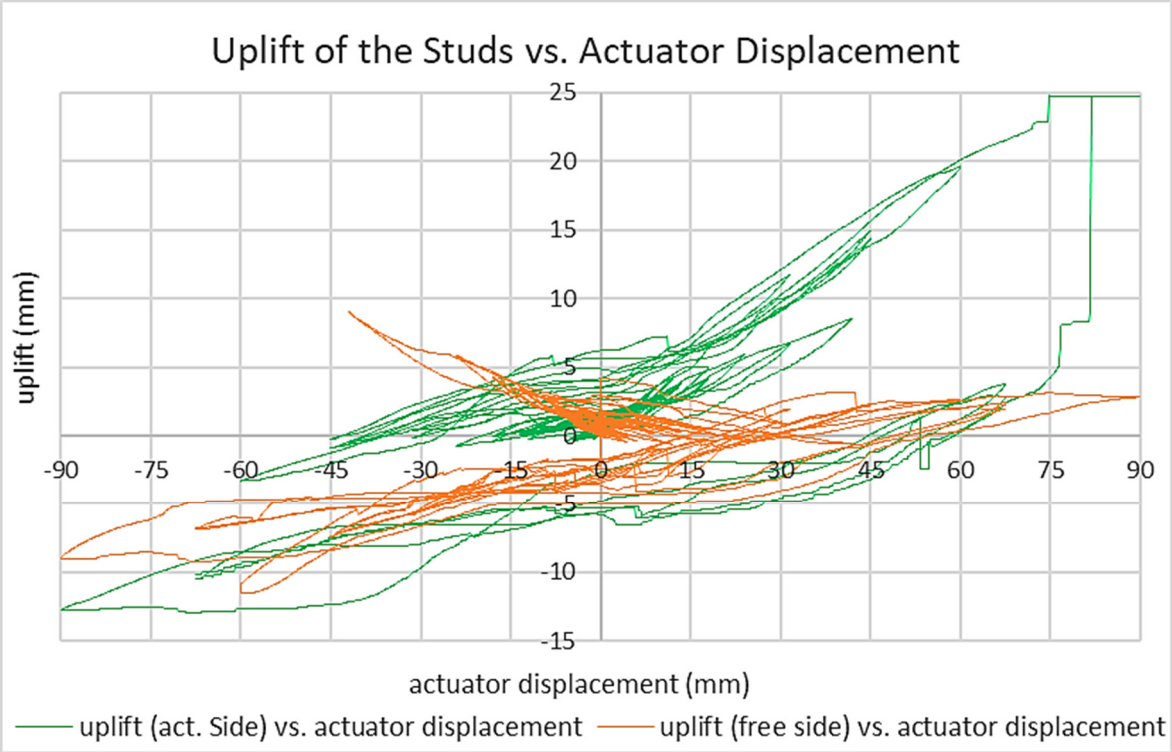

Figure D.10. Uplift of the studs vs. actuator displacement.

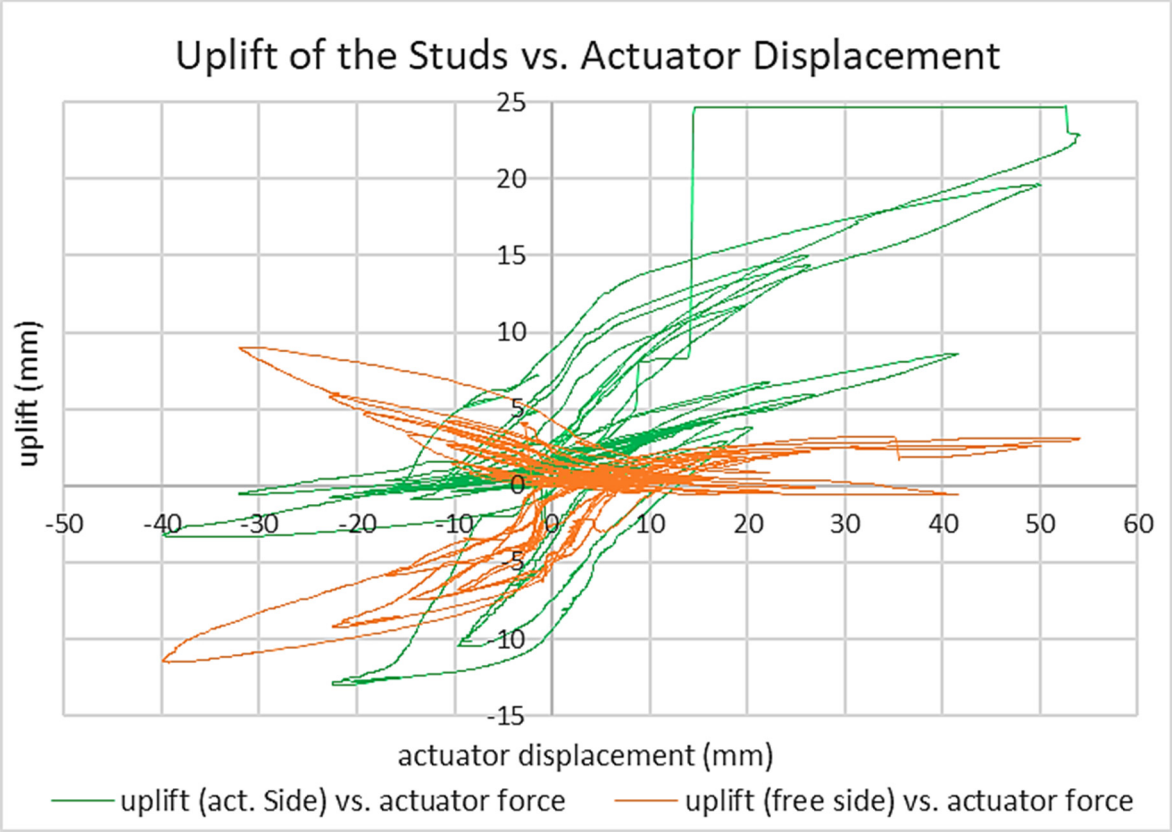

Figure D.11. Uplift of the studs vs. actuator force.

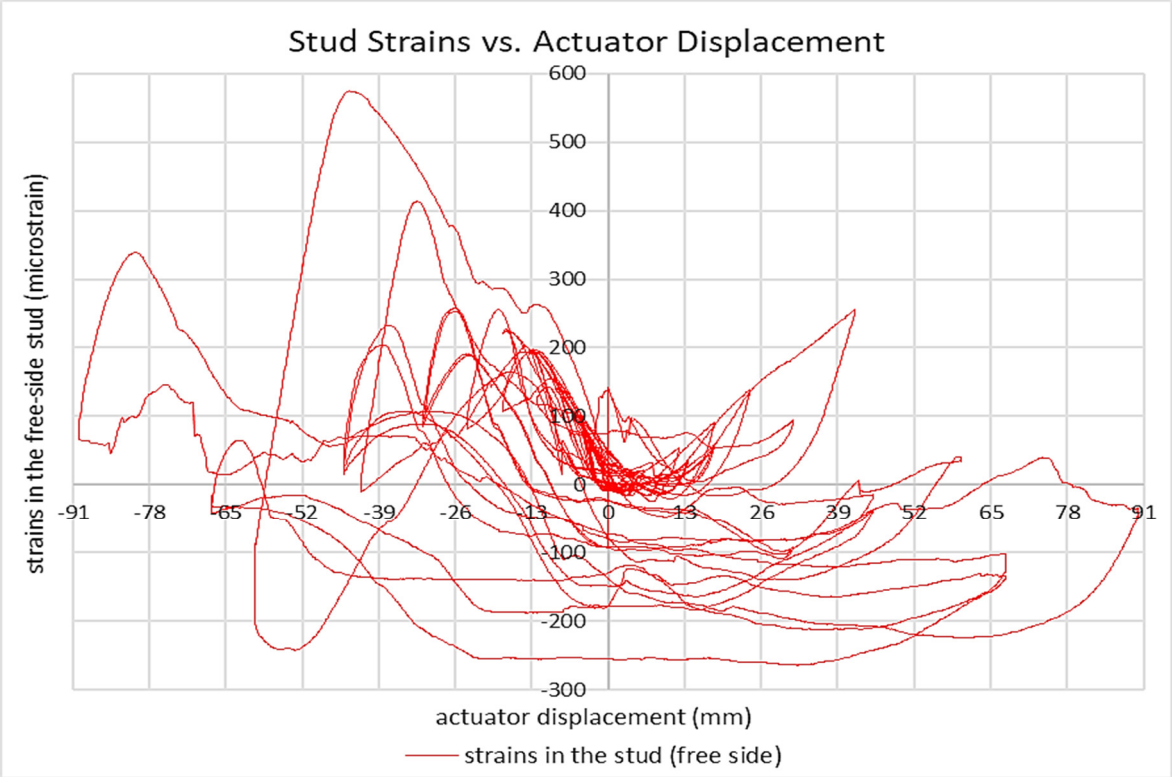

Figure D.12. Strains in the stud on the free-side of the test specimen vs. actuator displacement.

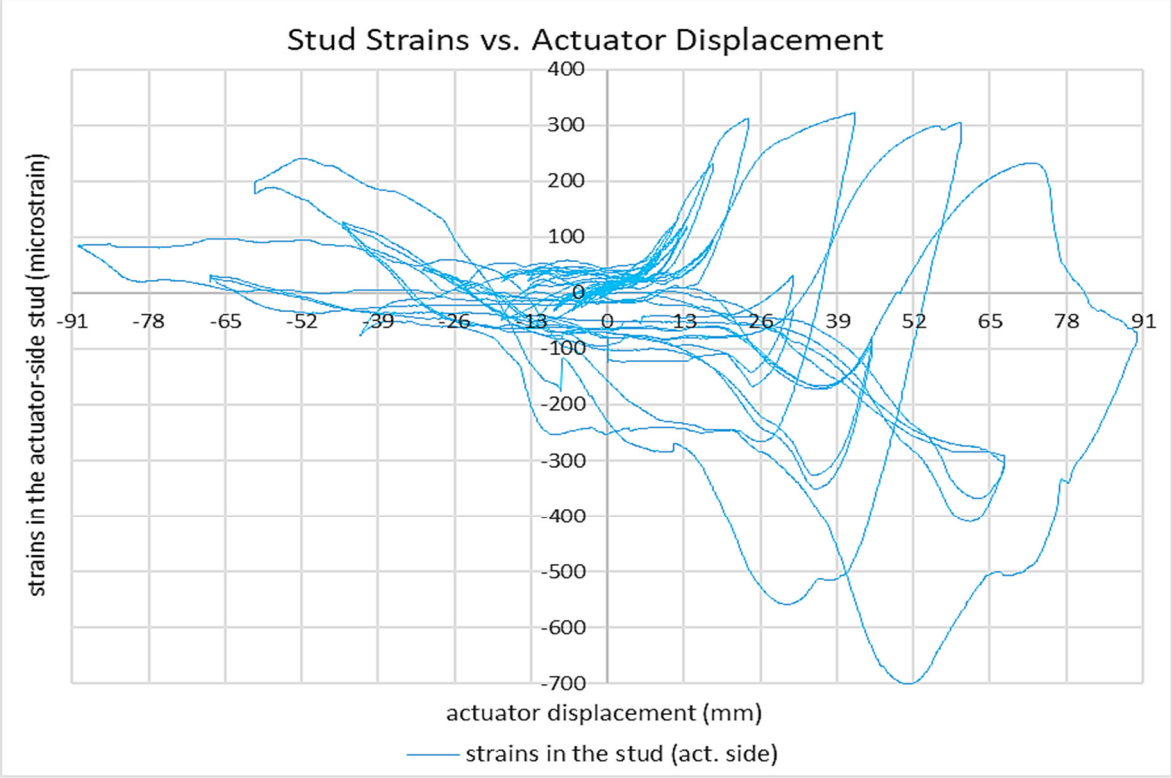

Figure D.13. Strains in the stud on the actuator-side of the test specimen vs. actuator displacement.

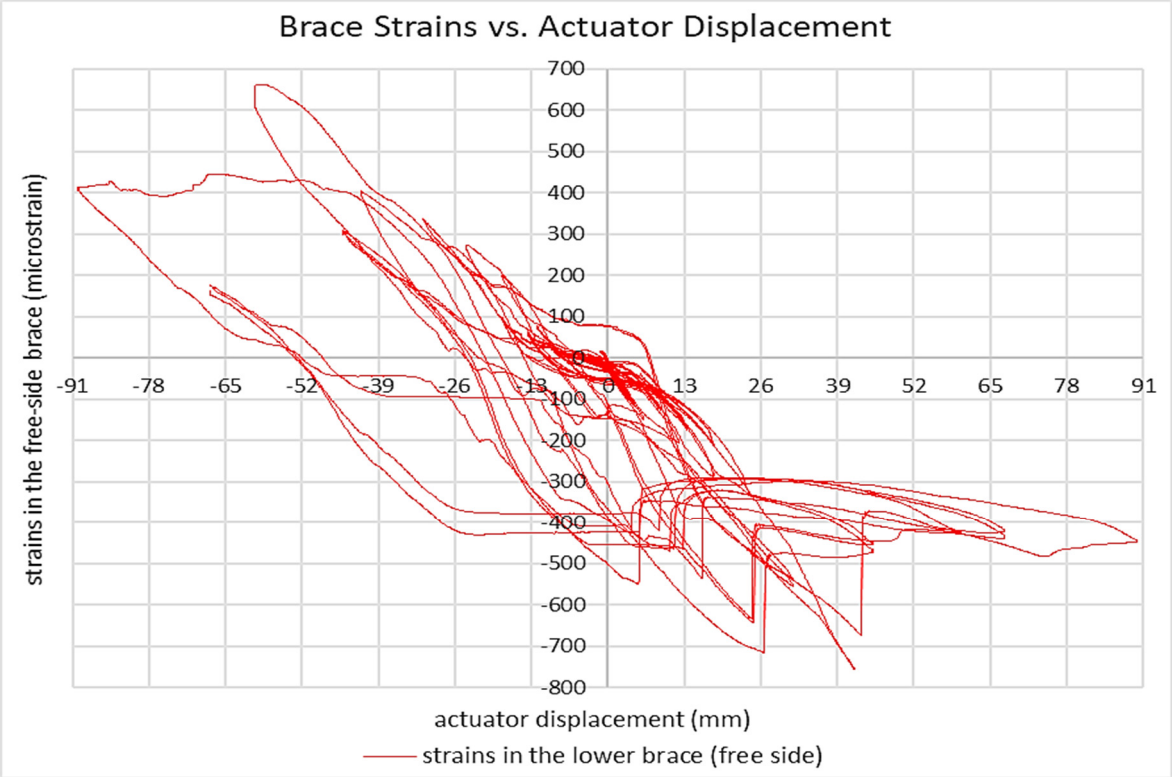

Figure D.14. Strains in the brace on the free-side of the specimen (lower corner) vs. actuator displacement.

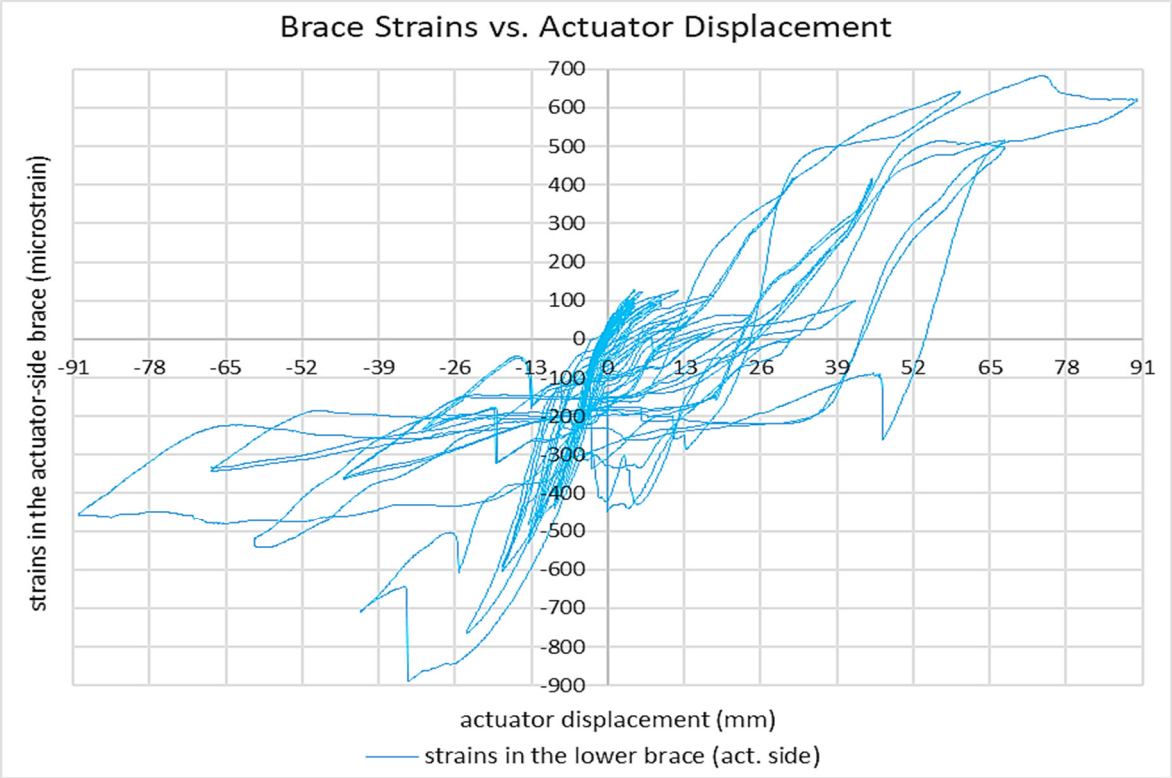

Figure D.15. Strains in the brace on the actuator-side of the specimen (lower corner) vs. actuator displacement.

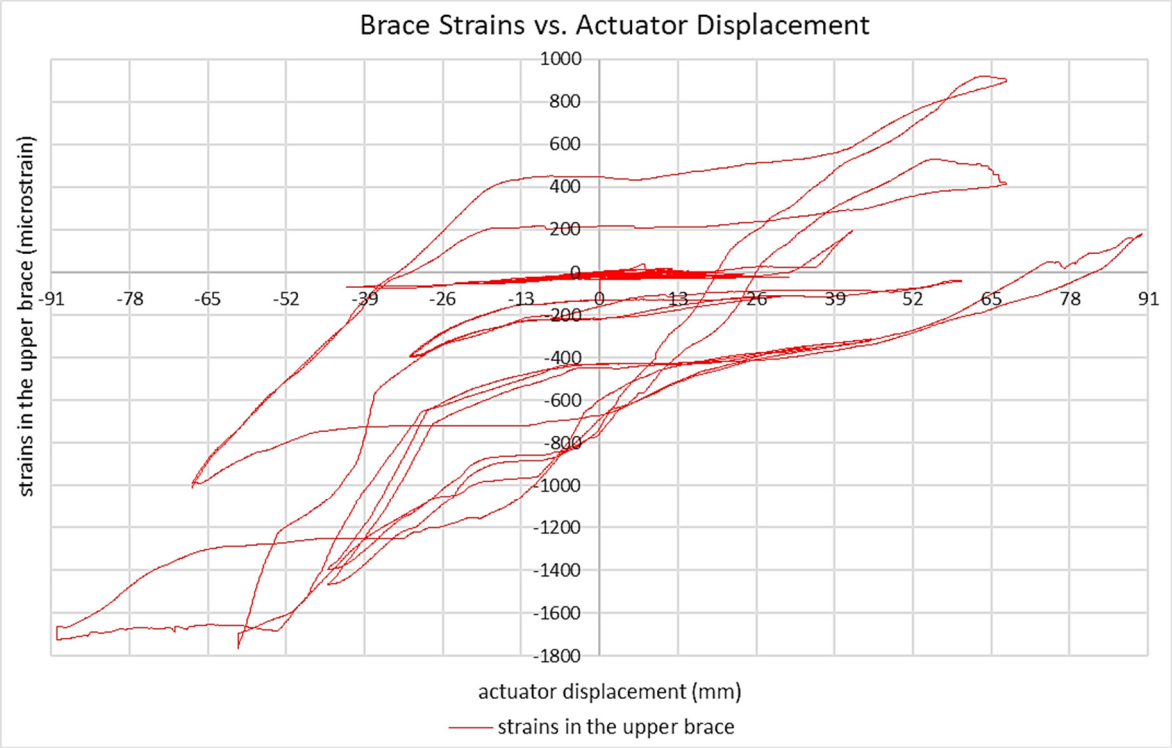

Figure D.16. Strains in the brace on the free-side of the specimen (upper corner) vs. actuator displacement.

APPENDIX E: PLASTIC HINGE PROPAGATION WITHIN THE STRUCTURAL MODEL

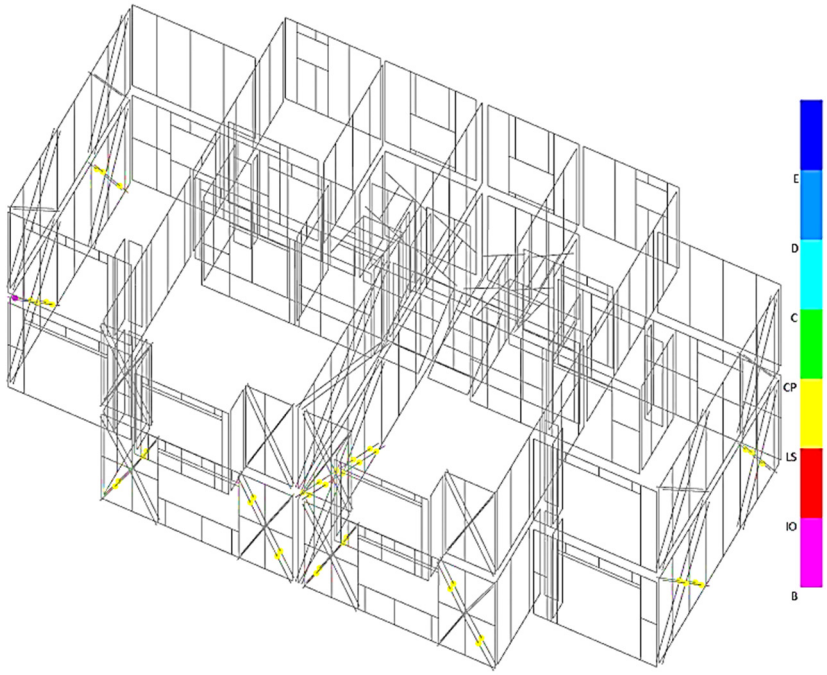

Figure E.1. Plastic hinge progression at the 4th step of the pushover analysis in Y-direction.

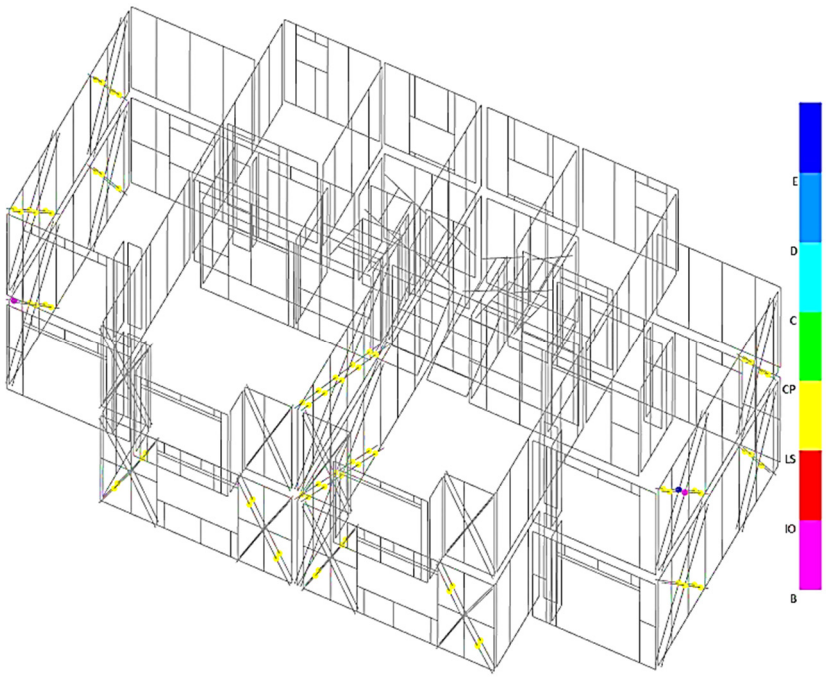

Figure E.2. Plastic hinge progression at the 23rd step of the pushover analysis in Y-direction.

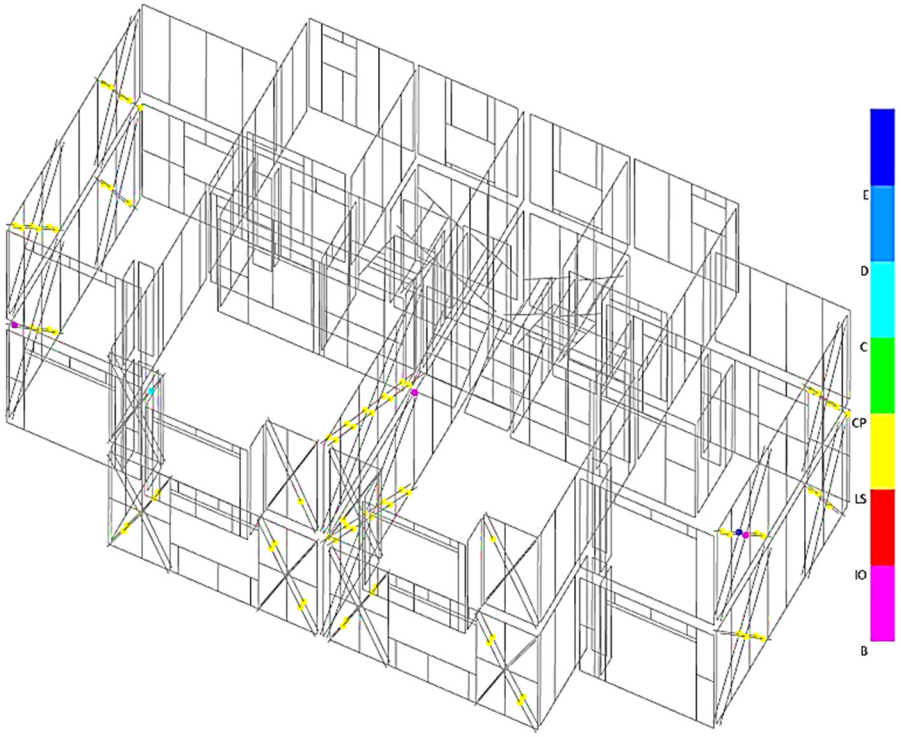

Figure E.3. Plastic hinge progression at the 27th step of the pushover analysis in Y-direction.

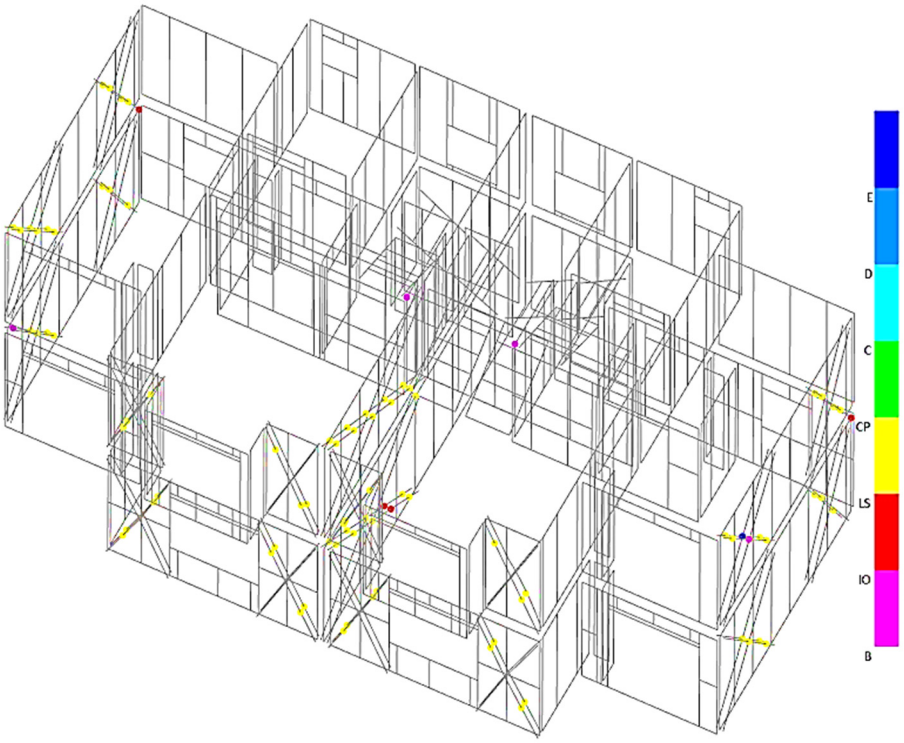

Figure E.4. Plastic hinge progression at the 43rd step of the pushover analysis in Y-direction.

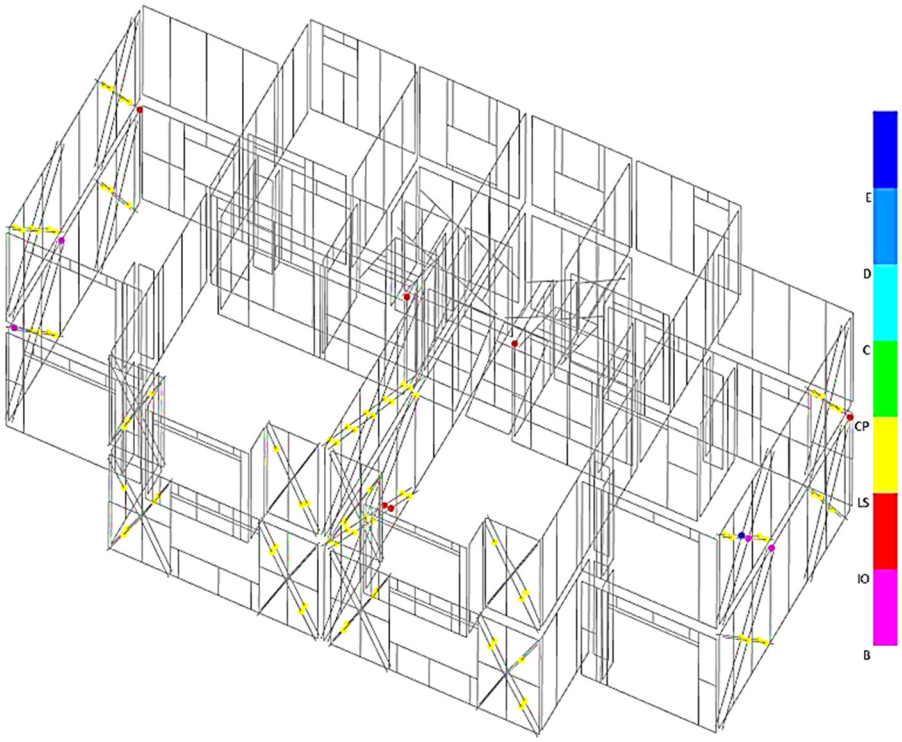

Figure E.5. Plastic hinge progression at the 47th step of the pushover analysis in Y-direction.

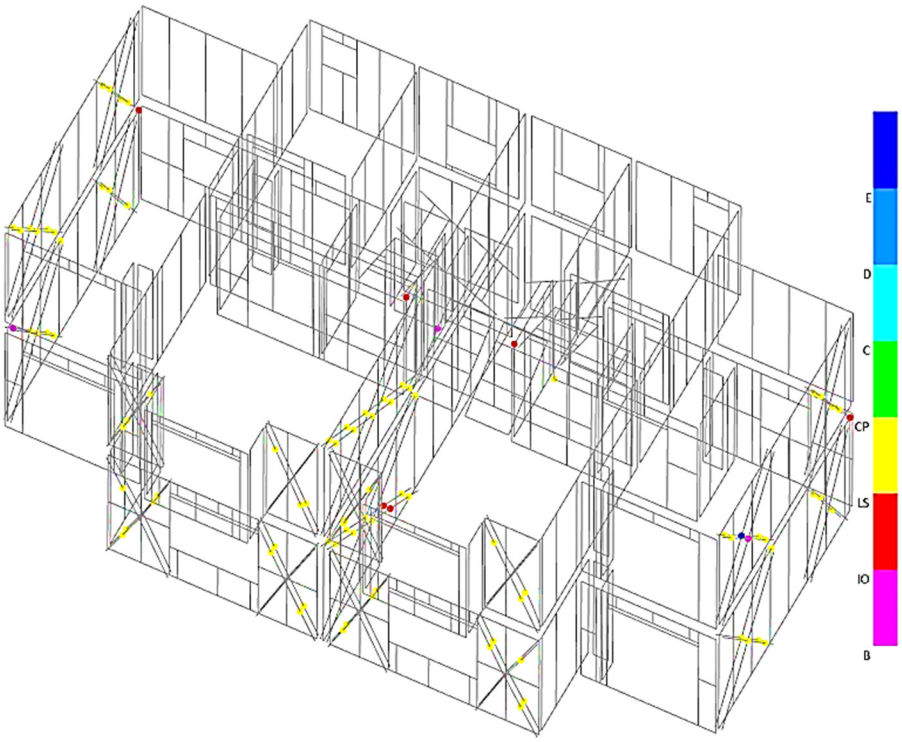

Figure E.6. Plastic hinge progression at the 50th step of the pushover analysis in Y-direction.

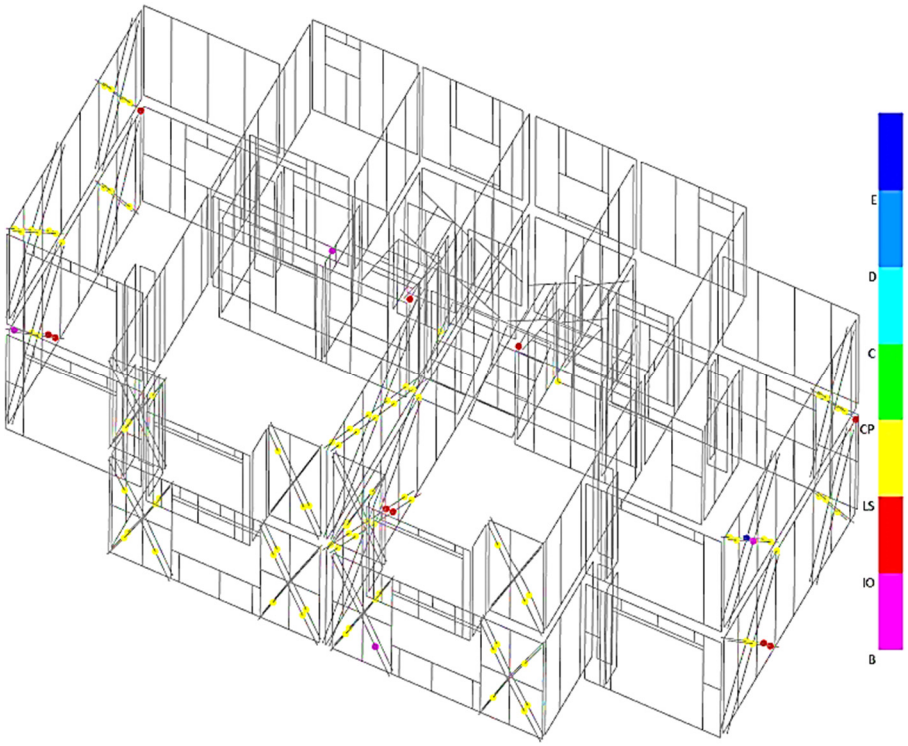

Figure E.7. Plastic hinge progression at the 120th step of the pushover analysis in Y-direction.

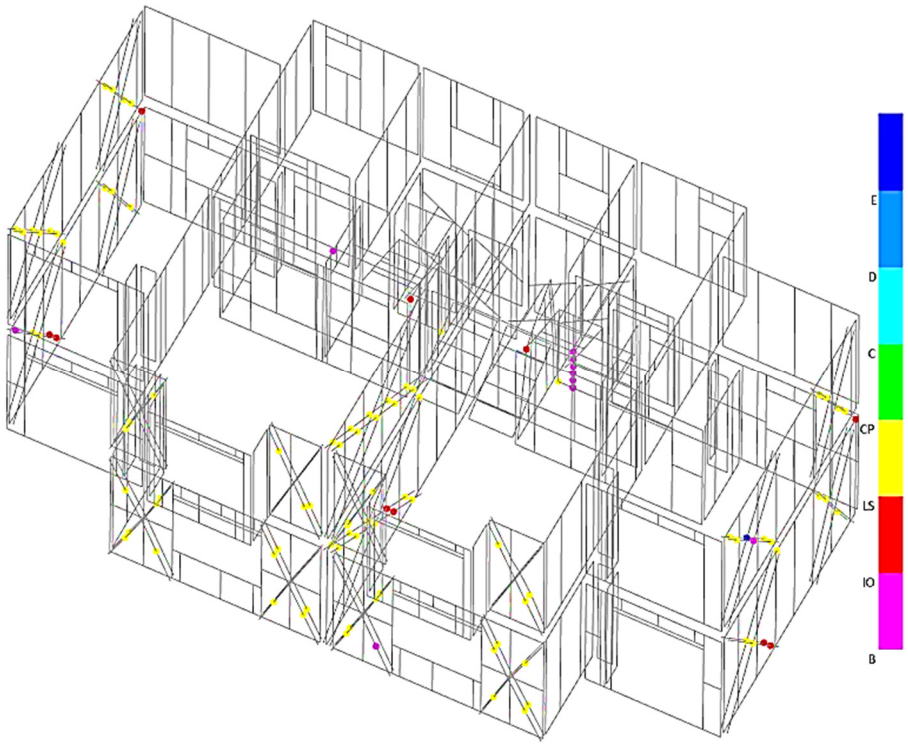

Figure E.8. Plastic hinge progression at the 121st step of the pushover analysis in Y-direction.

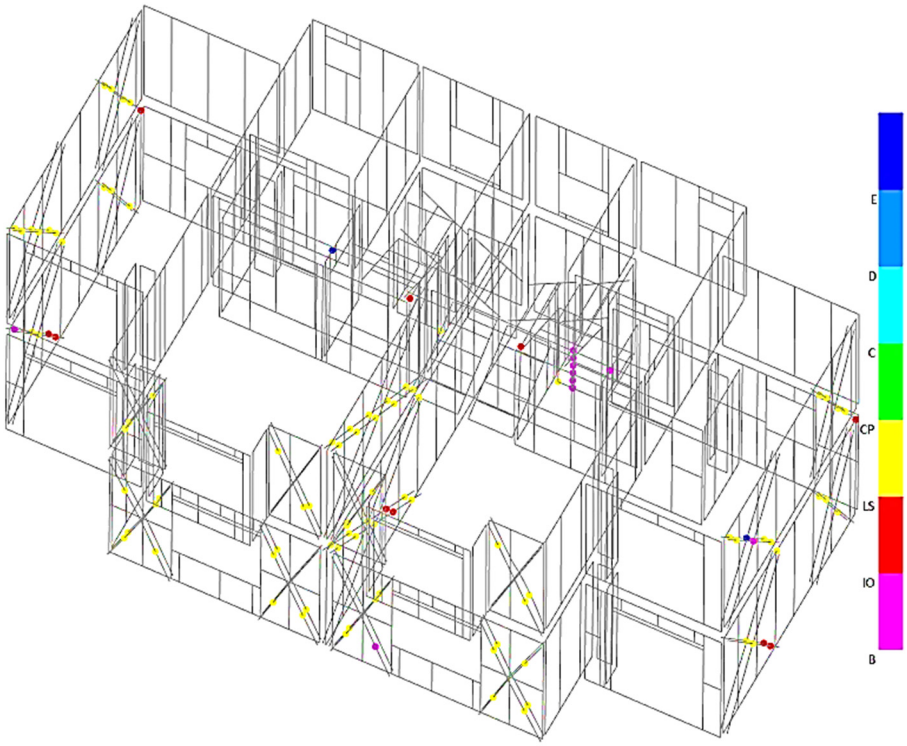

Figure E.9. Plastic hinge progression at the 127th step of the pushover analysis in Y-direction.

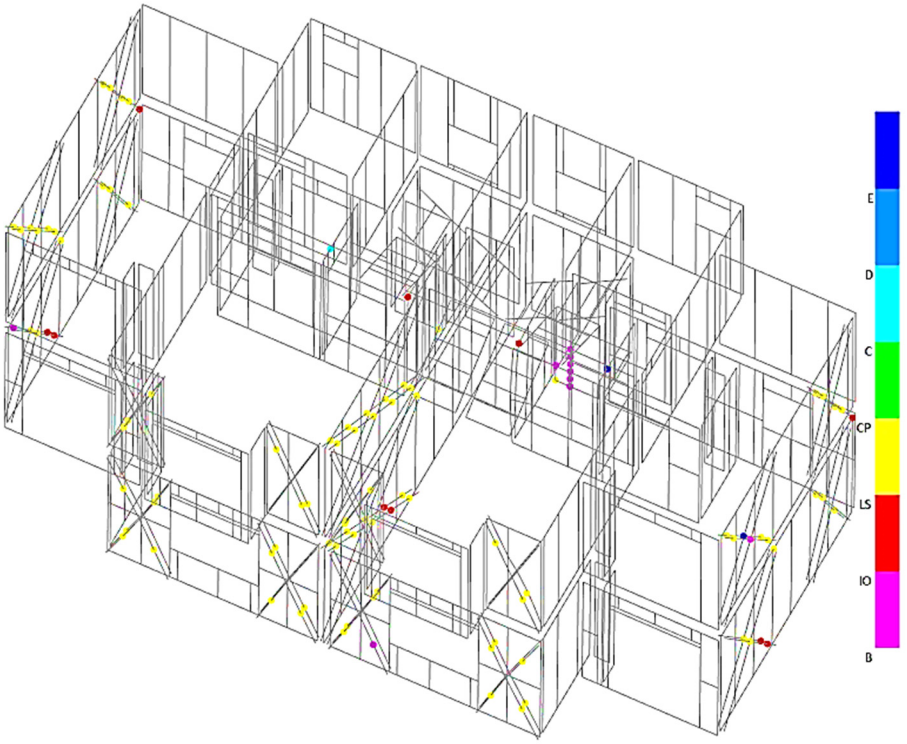

Figure E.10. Plastic hinge progression at the 160th step of the pushover analysis in Y-direction.

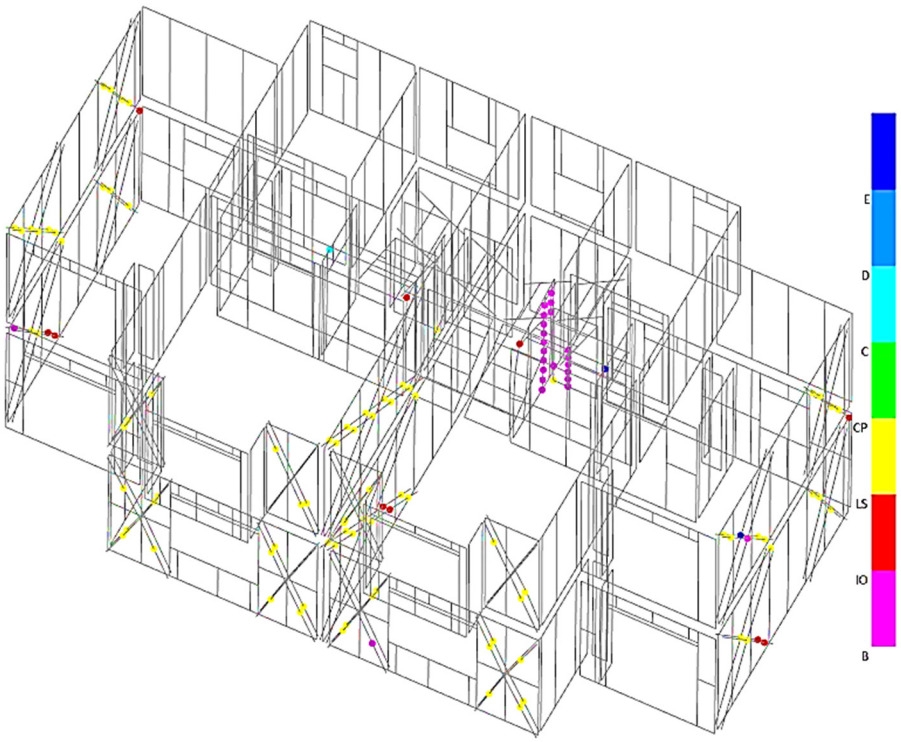

Figure E.11. Plastic hinge progression at the 161st step of the pushover analysis in Y-direction.

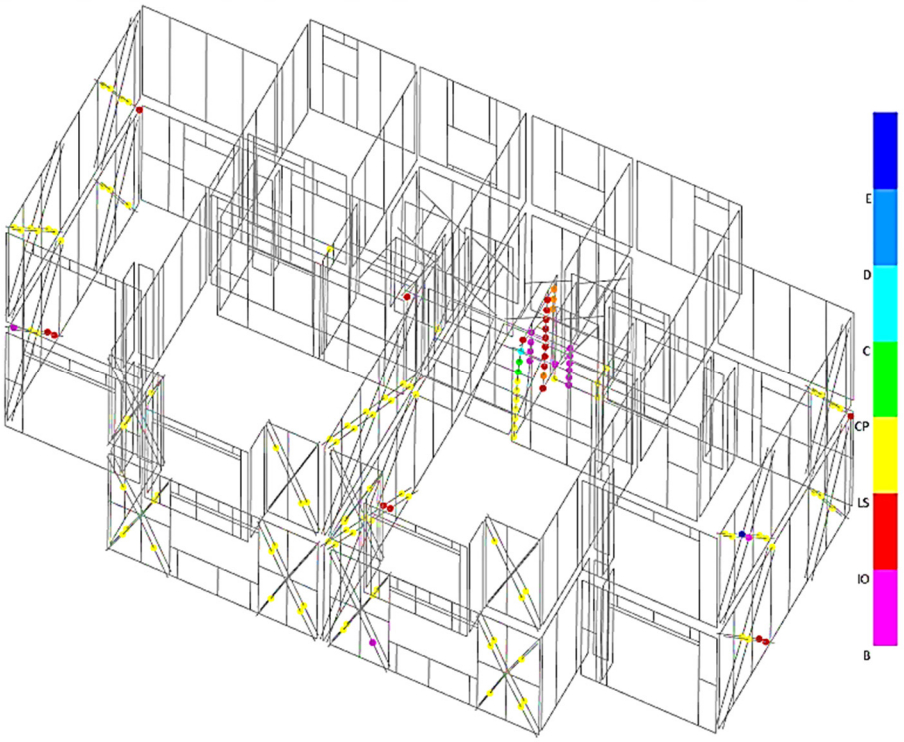

Figure E.12. Plastic hinge progression at the 162nd step of the pushover analysis in Y-direction.

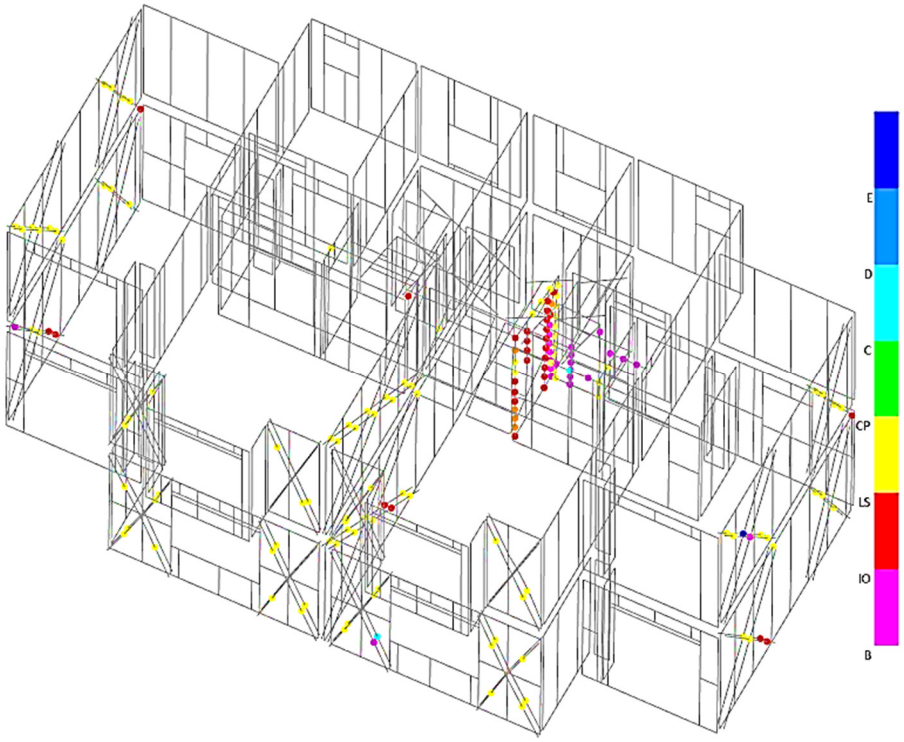

Figure E.13. Plastic hinge progression at the 163rd step of the pushover analysis in Y-direction.

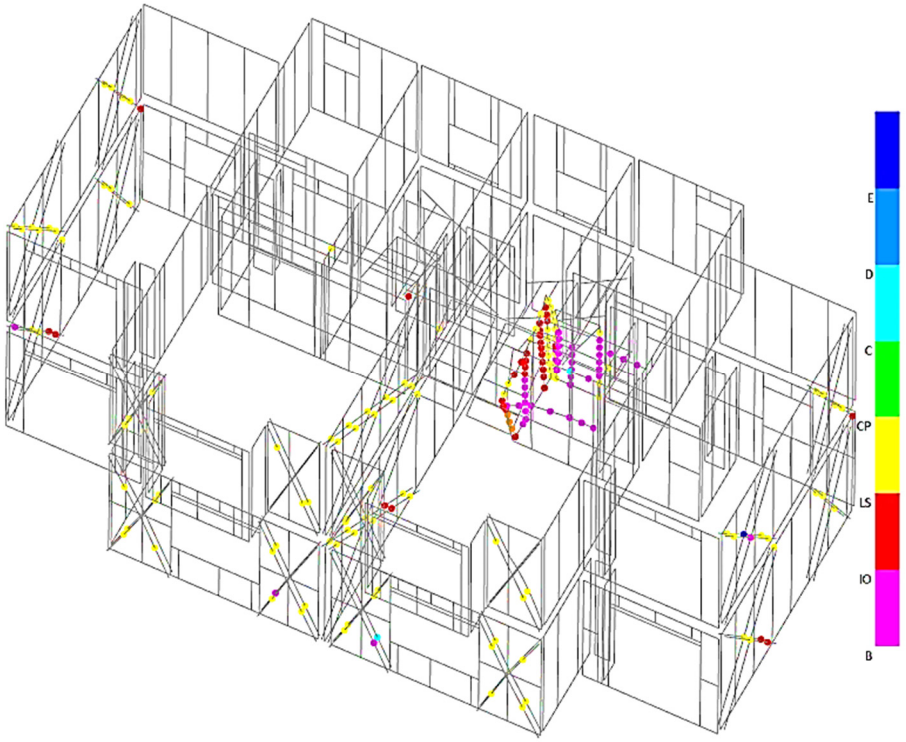

Figure E.14. Plastic hinge progression at the 170th step of the pushover analysis in Y-direction.

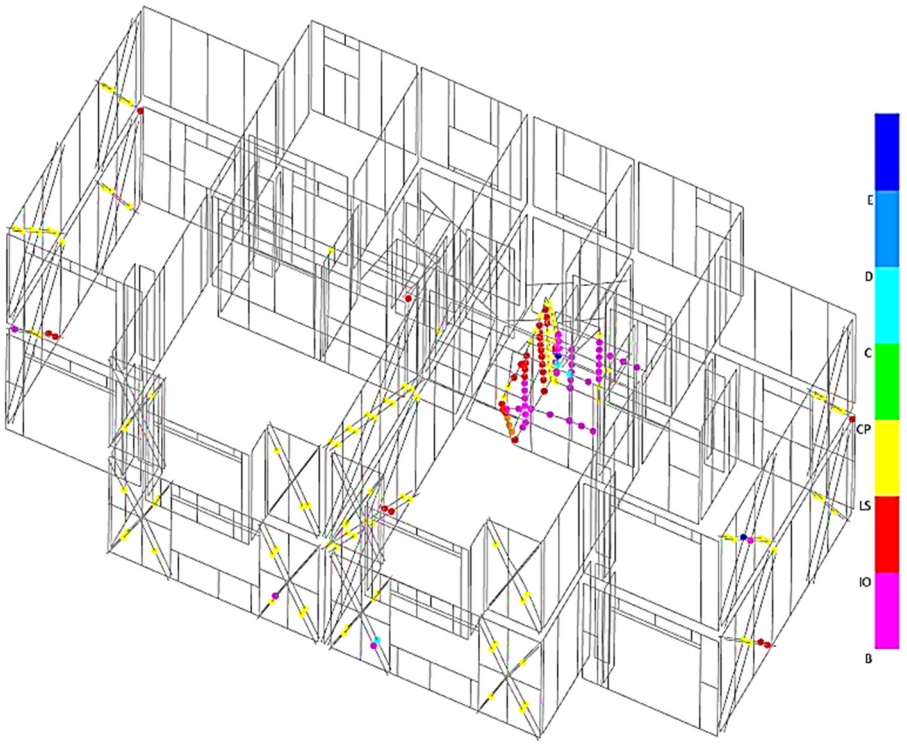

Figure E.15. Plastic hinge progression at the 178th step of the pushover analysis in Y-direction.

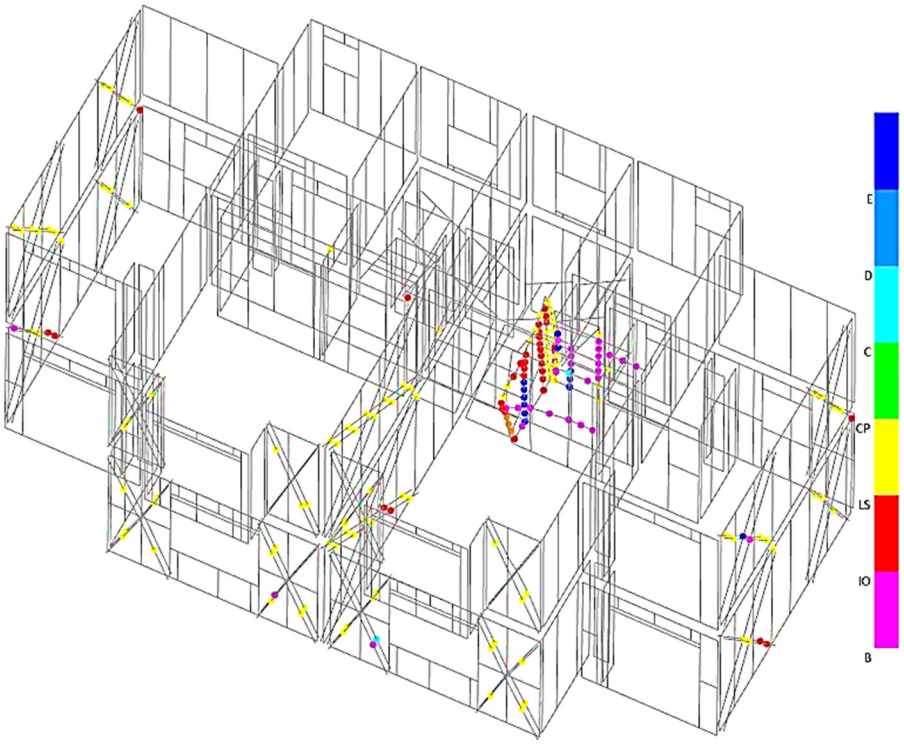

Figure E.16. Plastic hinge progression at the 180th step of the pushover analysis in Y-direction.

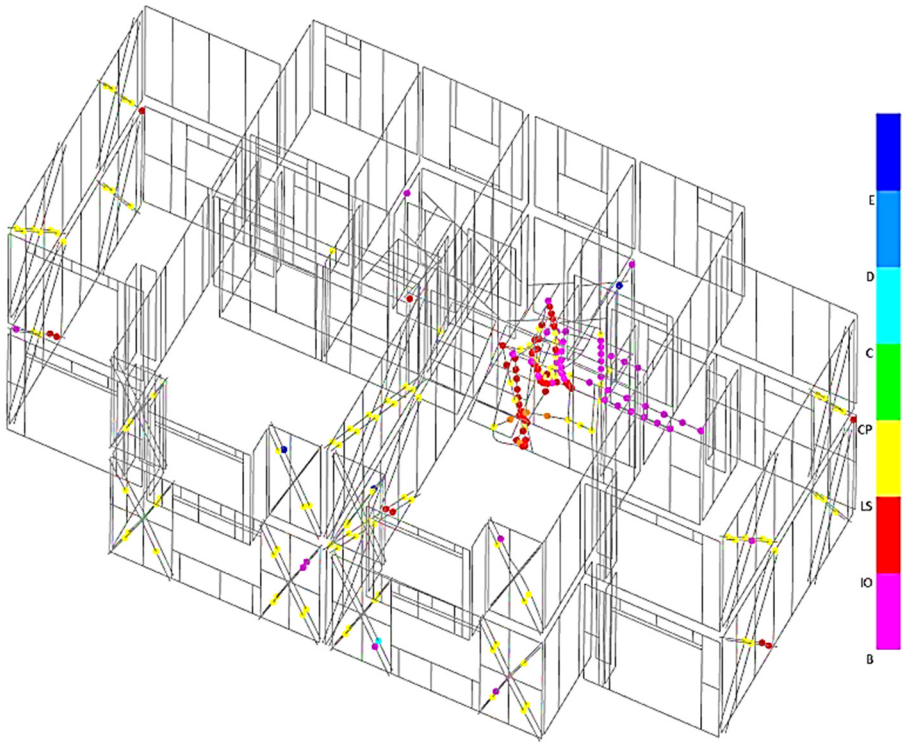

Figure E.17. Plastic hinge progression at the 186th step of the pushover analysis in Y-direction.

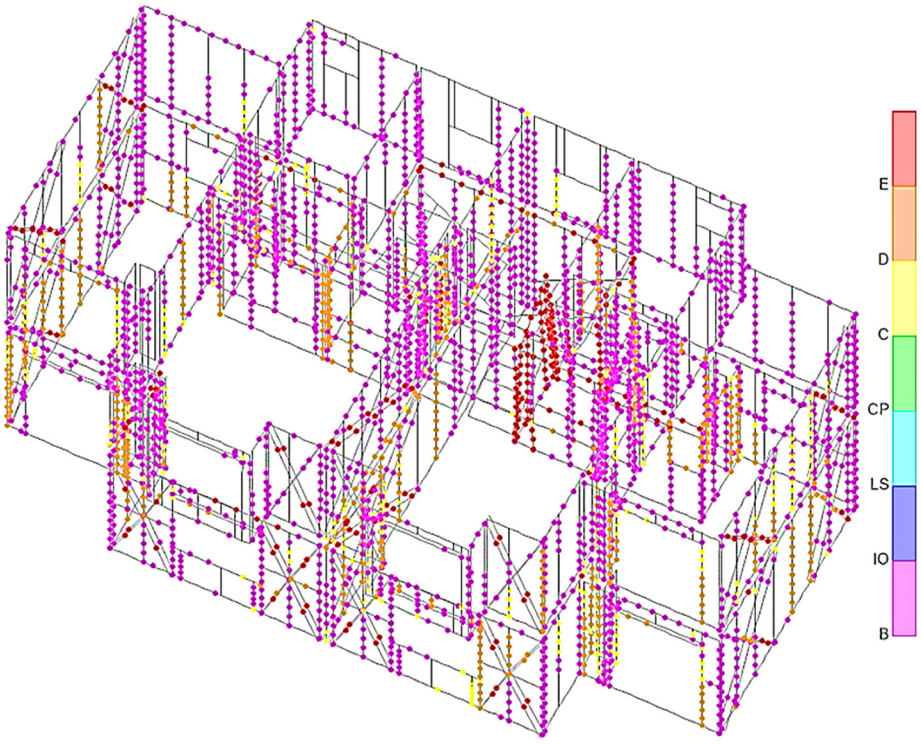

Figure E.18. Plastic hinge progression at the 188th step of the pushover analysis in Y-direction.

APPENDIX F: CAPACITY SPECTRA WITH LARGER SCALES

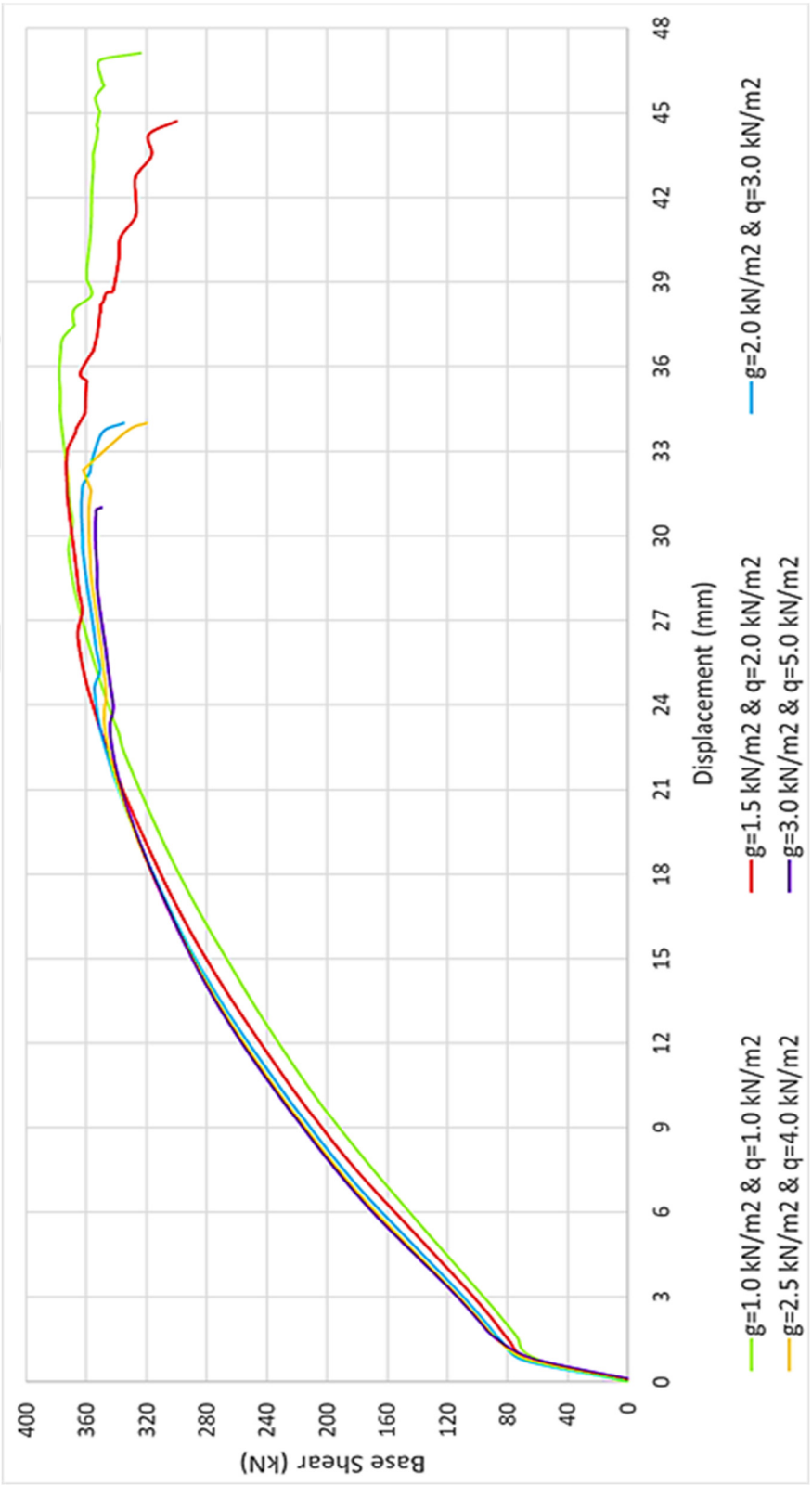

Figure F.1. Pushover curves of the analysis models with varying gravity loads.

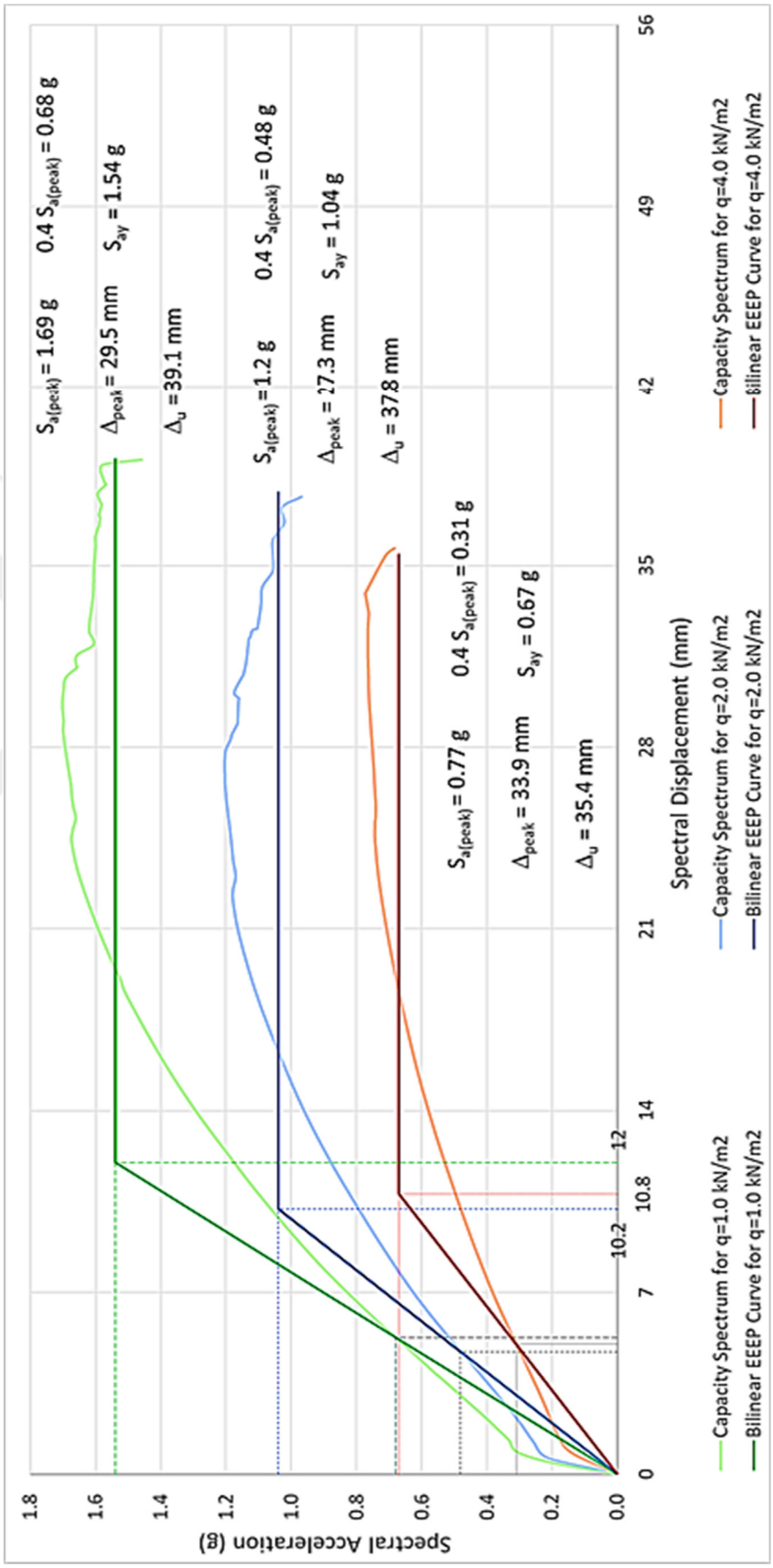

Figure F.2. Performance assessment for varying gravity loads.

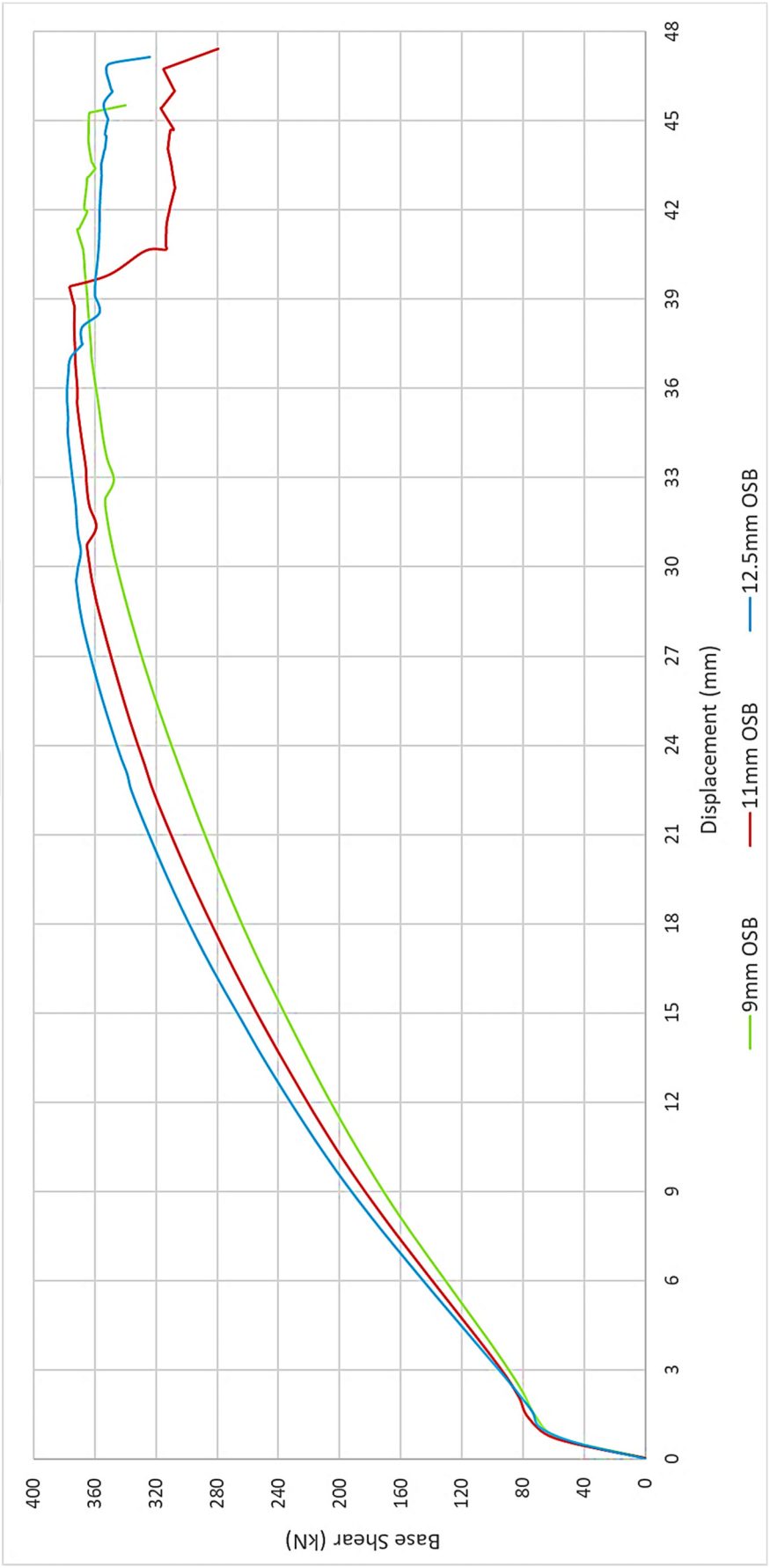

Figure F.3. Pushover curves of analysis models with varying OSB panel thickness.

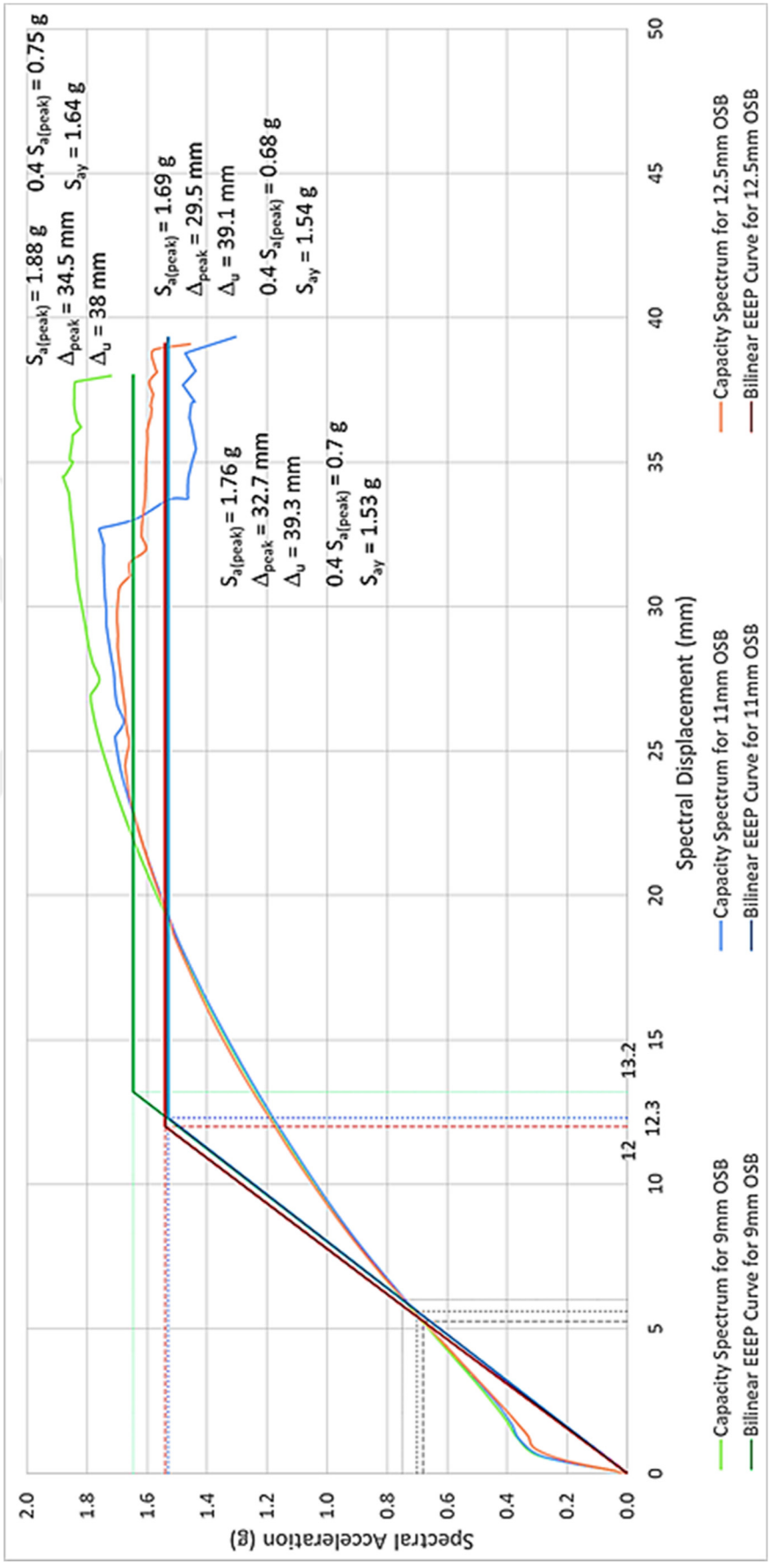

Figure F.4. Performance assessment for varying OSB panel thickness.

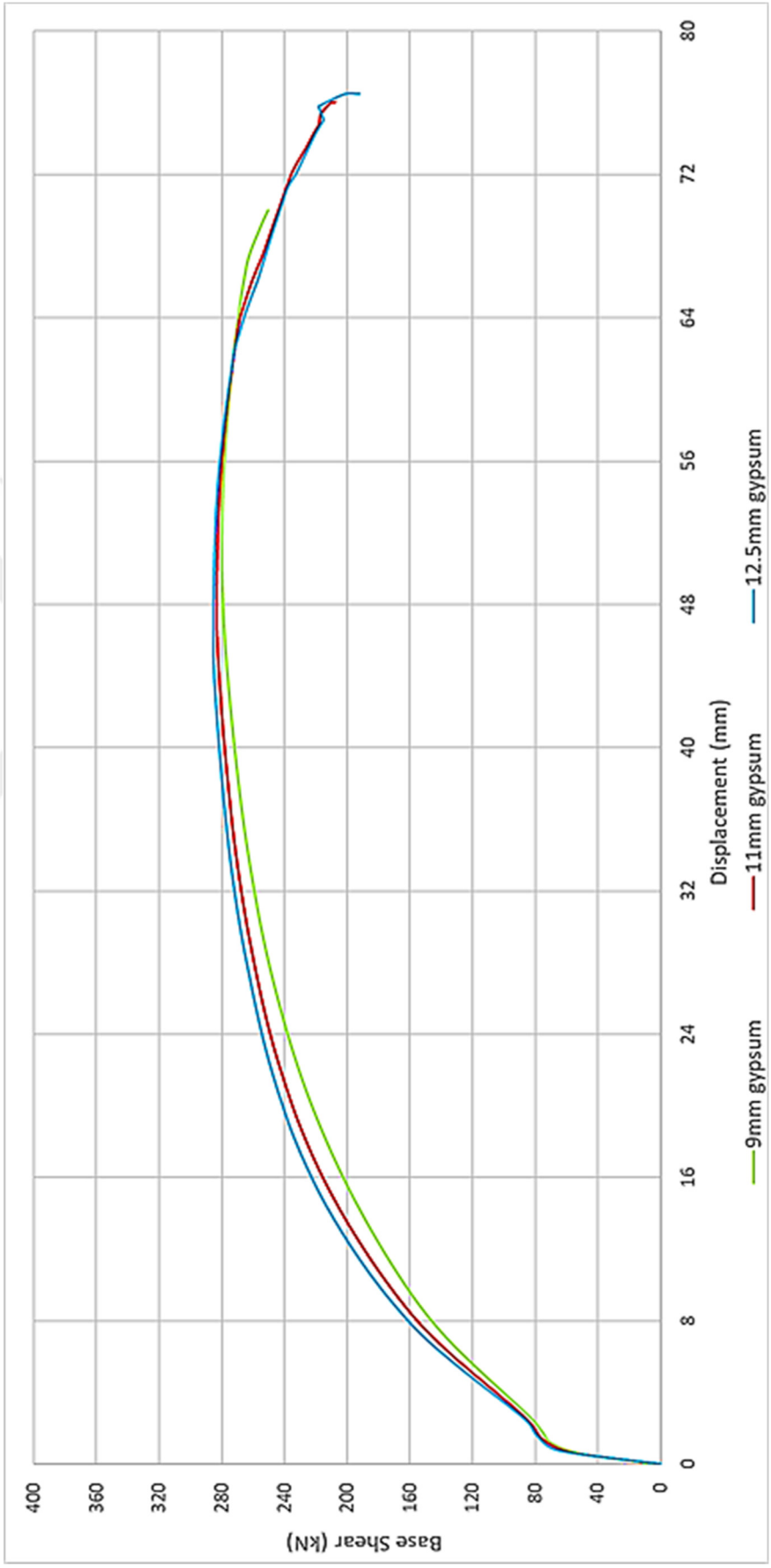

Figure F.5. Pushover curves of analysis models with varying gypsum panel thickness.

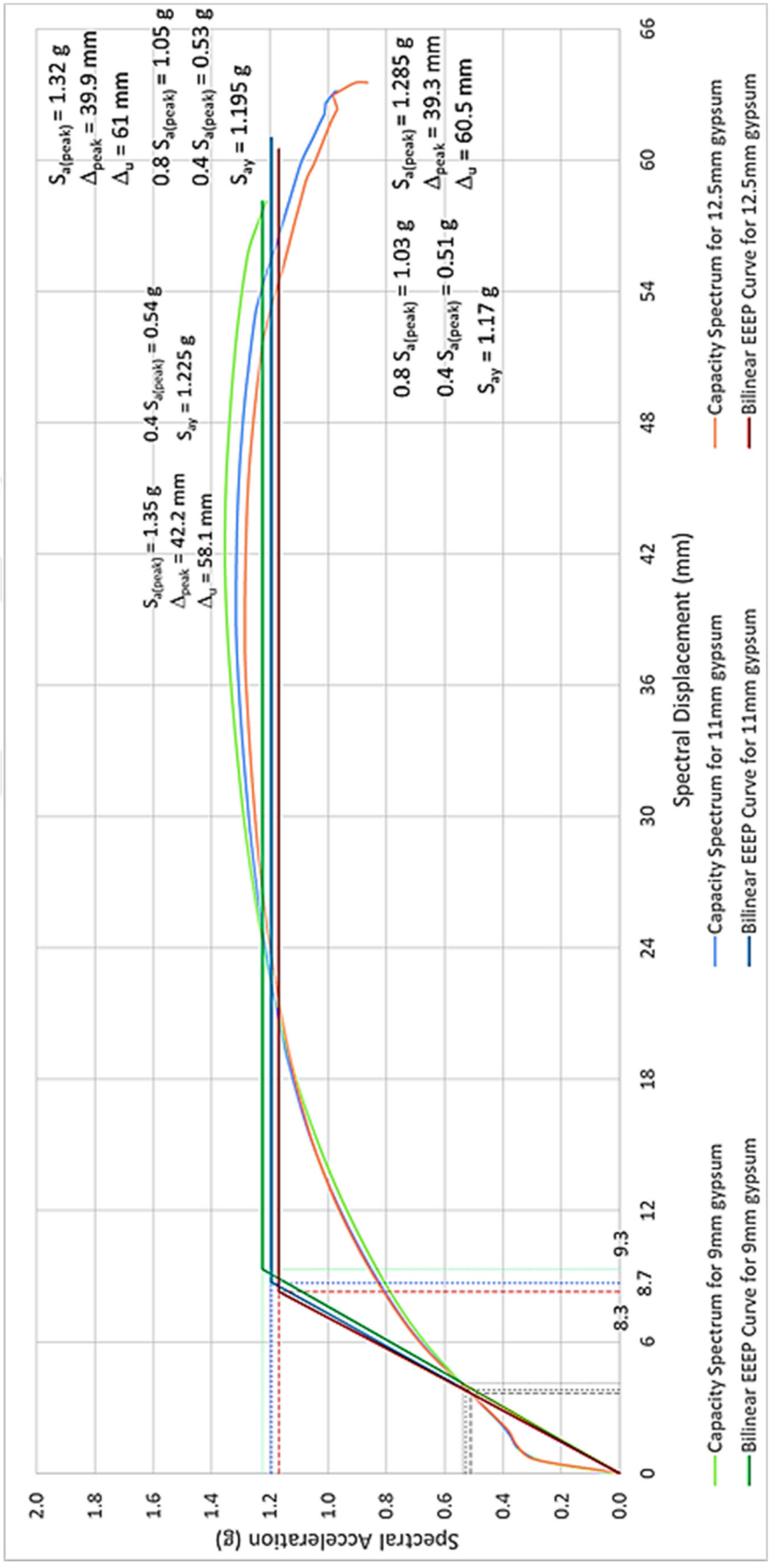

Figure F.6. Performance assessment for varying gypsum panel thickness.

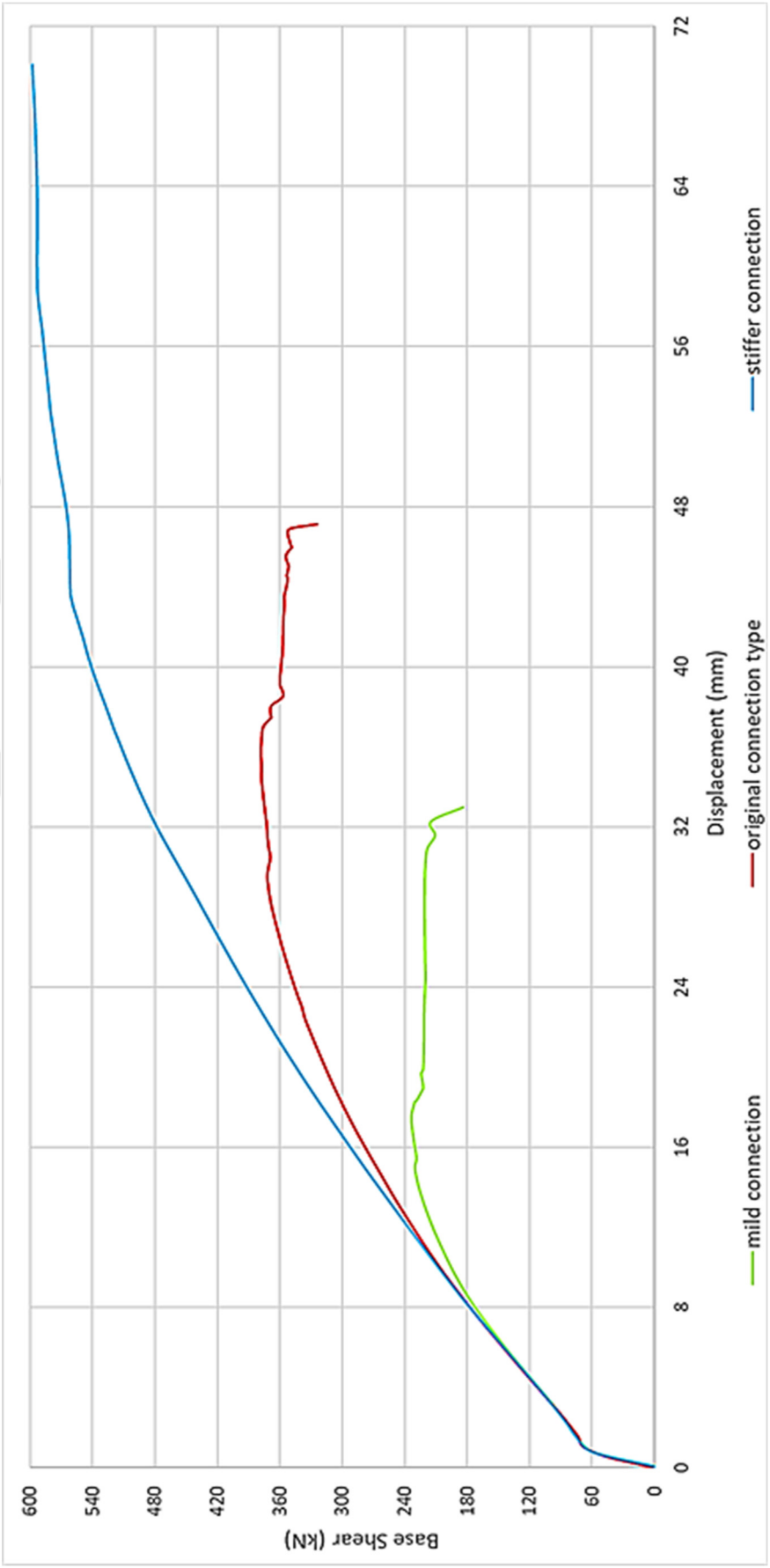

Figure F.7. Pushover curves of analysis models with varying screw thickness.

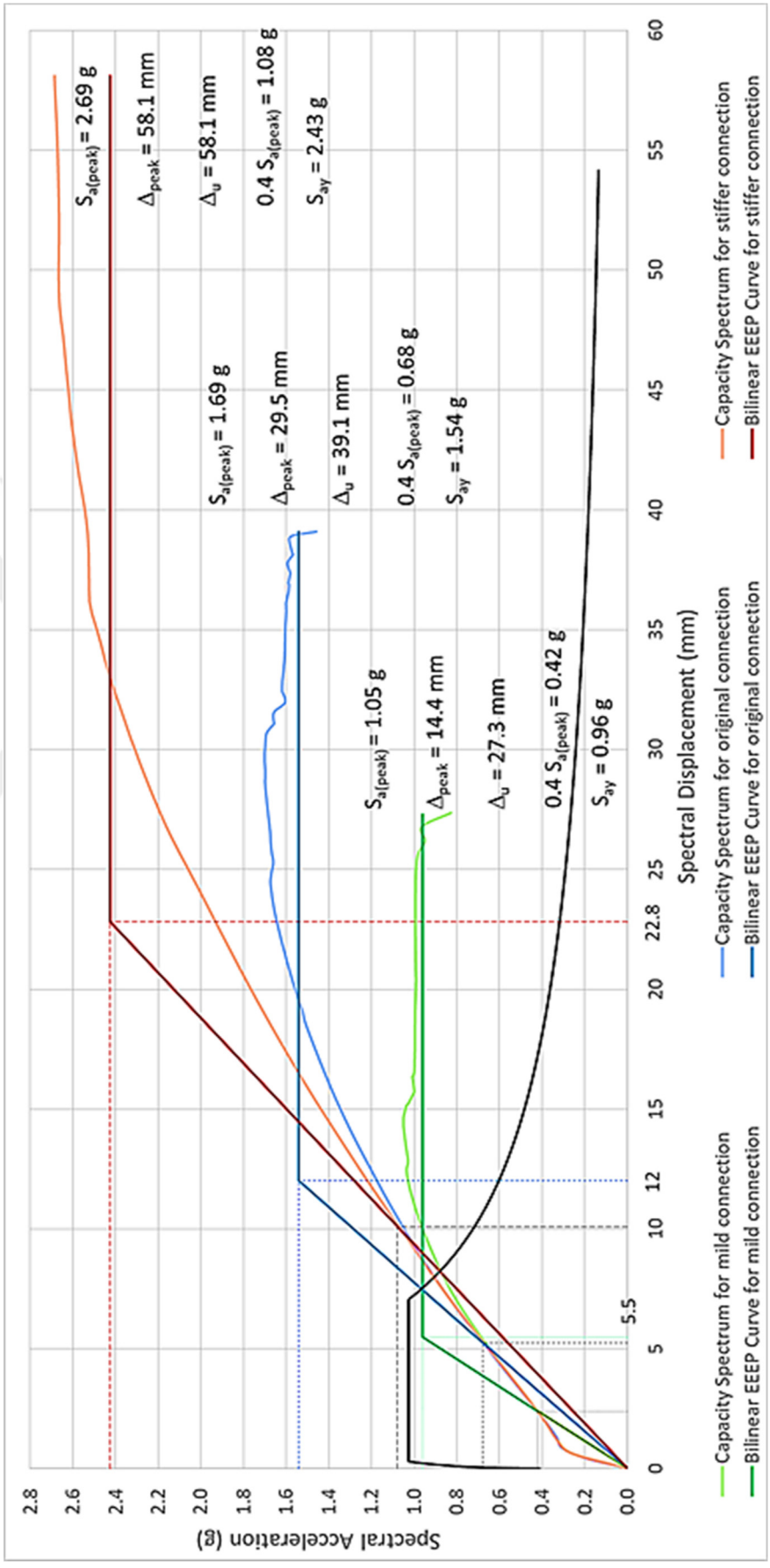

Figure F.8. Performance assessment for varying screw thickness.